Quantitative application of 4D seismic data for updating thin-reservoir models

Ilya Fursov

Submitted for the degree of Doctor of Philosophy

Heriot-Watt University

School of Energy, Geoscience, Infrastructure and Society

May 2015

Abstract

A range of methods which allow quantitative integration of 4D seismic and reservoir simulation are developed. These methods are designed to work with thin reservoirs, where the seismic response is normally treated in a map-based sense due to the limited vertical resolution of seismic. The first group of methods are fast-track procedures for prediction of future saturation fronts, and reservoir permeability estimation. The input to these methods is pressure and saturation maps which are intended to be derived from time-lapse seismic attributes. The procedures employ a streamline representation of the fluid flow, and finite difference discretisation of the flow equations. The underlying ideas are drawn from the literature and merged with some innovative new ideas, particularly for the implementation and use. However my conclusions on the applicability of the methods are different from their literature counterparts, and are more conservative. The fast-track procedures are advantageous in terms of speed compared to history matching techniques, but are lacking coupling between the quantities which describe the reservoir fluid flow: permeabilities, pressures, and saturations. For this reason, these methods are very sensitive to the input noise, and currently cannot be applied to the real dataset with a robust outcome.

Seismic history matching is the second major method considered here for integrating 4D seismic data with the reservoir simulation model. Although more computationally demanding, history matching is capable of tolerating high levels of the input noise, and is more readily applicable to the real datasets. The proposed implementation for seismic modelling within the history matching loop is based on a linear regression between the time-lapse seismic attribute maps and the reservoir dynamic parameter maps, thus avoiding the petro-elastic and seismic trace modelling. The idea for such regression is developed from a pressure/saturation inversion approach found in the literature. Testing of the seismic history matching workflow with the associated uncertainty estimation is performed for a synthetic model. A reduction of the forecast uncertainties is observed after addition of the 4D seismic information to the history matching process. It is found that a proper formulation of the covariance matrices for the seismic errors is essential to obtain favourable forecasts which have small levels of bias. Finally, the procedure is applied to a North Sea field dataset where a marginal reduction in the prediction uncertainties is observed for the wells located close to the major seismic anomalies. Overall, it is demonstrated that the proposed seismic history matching technique is capable of integrating 4D seismic data with the simulation model and increasing confidence in the latter.

This work is dedicated to

my wife Liliya

and my son Yaroslav

Acknowledgements

I would like to thank Prof. Colin MacBeth for his support and patience during my very long PhD work, for the opportunity to start the PhD with IPE, and for the opportunity to finish it after one year's leave. I appreciate Colin's nice job of running such a huge PhD group with so many sponsors, and well organised sponsor meetings. Thanks for the SEG Bellagio conference, it was a pleasant experience!

The ETLP sponsor companies are thanked for the financial support of the group and for their keen interest in the PhD student's work.

I am thankful to the SEG foundation and Ian Jack for receiving a scholarship.

All the ETLP folks are thanked for being around. I thank Reza Falahat and Hamed Amini for sharing their geophysical knowledge with the engineering guy. I thank Dennis Obidegwu and Yin Zhen for the energetic discussions on the engineering perspectives and the logic behind our works. I thank Yin Zhen and Veronica Omofoma for sharing their flat for a while with the homeless person.

I would like to thank my parents for their all-round support, and my wife Liliya for inspiring and motivating me.

ACADEMIC REGISTRY
Research Thesis Submission

Name*:*	ILYA FURSOV		
School/PGI:	SCHOOL OF ENERGY, GEOSCIENCE, INFRASTRUCTURE AND SOCIETY		
Version: *(i.e. First, Resubmission, Final)*	FINAL	Degree Sought (Award **and** Subject area)	PhD, RESERVOIR ENGINEERING

Declaration

In accordance with the appropriate regulations I hereby submit my thesis and I declare that:

1) the thesis embodies the results of my own work and has been composed by myself
2) where appropriate, I have made acknowledgement of the work of others and have made reference to work carried out in collaboration with other persons
3) the thesis is the correct version of the thesis for submission and is the same version as any electronic versions submitted*.
4) my thesis for the award referred to, deposited in the Heriot-Watt University Library, should be made available for loan or photocopying and be available via the Institutional Repository, subject to such conditions as the Librarian may require
5) I understand that as a student of the University I am required to abide by the Regulations of the University and to conform to its discipline.

* *Please note that it is the responsibility of the candidate to ensure that the correct version of the thesis is submitted.*

Signature of Candidate*:*		Date:	

Submission

Submitted By *(name in capitals):*	ILYA FURSOV
Signature of Individual Submitting:	
Date Submitted:	

For Completion in the Student Service Centre (SSC)

Received in the SSC by *(name in capitals):*			
Method of Submission (*Handed in to SSC; posted through internal/external mail*):	Handed to SSC		
E-thesis Submitted (*mandatory for final theses*)			
Signature:		Date:	

Please note this form should bound into the submitted thesis.

Updated February 2008, November 2008, February 2009, January 2011

Contents

List of tables

List of figures

Nomenclature

API	American Petroleum Institute oil gravity
BFGS	Broyden-Fletcher-Goldfarb-Shanno (algorithm)
BHP	Bottom-hole pressure
BOA	Bayesian optimisation algorithm
CMA-ES	Covariance matrix adaptation Evolution strategy
DE	Differential evolution
EnKF	Ensemble Kalman filter
FGIP	Free gas in place
FGOR	Field GOR
FOPR	Field oil production rate
FWIR	Field water injection rate
FWPR	Field water production rate
GOC	Gas oil contact
GOR	Gas-oil ratio
HM	History matching
i.i.d.	Independent and identically distributed (random variables)
IW	Intelligent well
LoFS	Life of field seismic
MAP	Maximum a posteriori (estimate)
MCMC	Markov chain Monte-Carlo
mean	Mean value
MD	Matrix decomposition
ML	Maximum likelihood (estimate)
mscf	Thousand standard cubic feet
mstb	Thousand stock tank barrels
NA	Neighbourhood algorithm
NRMS	Normalised RMS (measure of 4D seismic non-repeatability)
NTG	Net to gross ratio
OBC	Ocean bottom cable
OIP	Oil in place
OWC	Oil water contact
PDF	Probability density function
PLT	Production logging tool
PORV	Pore volume
psi	Pounds per square inch
PSO	Particle swarm optimisation
rb	Reservoir barrel
rm^3	Reservoir cubic meter
RML	Randomised maximum likelihood
RMS	Root mean square
Rs	Solution gas oil ratio
SA	Simulated annealing
scf	Standard cubic feet
SHM	Seismic history matching
sm^3	Standard cubic meter
SSS	Screening sequential simulation
stb	Stock tank barrel
std	Standard deviation
TVDSS	True vertical depth subsea

VFSA	Very fast simulated annealing
WCT	Water cut
WGOR	Well GOR
WIP	Water in place
WOPR	Well oil production rate
WWIR	Well water injection rate
WWPR	Well water production rate

Table of notation[1]

Symbol	Explanation	Context
$A, C, G, M,$ P, Y, Z	Matrix	
A	Seismic amplitude	*Chapter 1*
A	Seismic attribute	*Chapters 4, 5, 6, Appendix E*
A	Cross-sectional area of a tube	*Chapters 2, 3*
A_0	Baseline seismic attribute	*Chapters 4, 5, Appendix E*
$a_P, a_{Sw}, a_{Sg}, ...$	Coefficients linking 4D seismic with the pressure and saturation changes	*Chapters 4, 5, 6, Appendix E*
$a, b, c, d, f,$ g, x, y, δ	Column-vector	
B_g, B_o	Gas formation volume factor, oil formation volume factor	
d	Data (in Bayesian framework)	*Chapter 5*
$d_k^{obs}, d_k^{\mathrm{mod}}$	Observed data, modelled data	
$c(h), c(\vec{h})$	(Auto)covariance function: 1D, and 2D	*Chapters 5, 6*
Cov	Covariance	
C_P, C_S	Coefficients linking 4D seismic with the pressure and saturation changes	*Chapter 1*
C_s, C_w	Covariance matrices: for well data, for seismic data	
C_M, C_D	Covariance matrices: for prior model, for data	*Chapter 5*
$C^{(g)}$	Covariance matrix in CMA-ES	*Appendix B*
E	Normalised error	*Chapter 2*
E	(Mathematical) expectation	*Chapter 5*
e	Forecast error	*Chapter 6*
F	Flow rate between the grid cells	*Chapter 7*
f, f_1, f_2	Objective function	
f_w	Water fractional flow	
G	AVO gradient	*Chapter 1*
G	Matrix for linear forward modelling	*Chapter 5*
G	Specific gas gravity	*Appendix A*
g	Forward modelling procedure	*Chapter 5*
$\vec{g}, \vec{h}$	2D vectors	*Chapter 5, Appendix D*
h	Reservoir thickness	
I	Unit matrix	
I	Active set	*Appendix E*
K	Bulk modulus of a medium	*Appendix A*
K, k	Absolute permeability	*Chapter 1*
k_h, k_v	Horizontal permeability, vertical permeability	

[1] Note that there are some unavoidable multiple definitions of the same symbol due to widespread use in the different domains of application.

k_{rg}	Gas relative permeability	
k_{rog}	Relative permeability of oil in gas	
k_{ro}, k_{row}	Relative permeability of oil in water	
k_{rw}	Water relative permeability	
k_{rw0}	End point water relative permeability	
L	Likelihood function	
L	Lower triangular matrix in Cholesky decomposition	
m	Model (in Bayesian framework)	*Chapter 5*
m	Mean value	*Appendices B, D*
n, s	Nugget and sill of a variogram	*Appendix D*
$\vec{n}$	Normal (vector)	
$N(0, I)$	Multivariate normal distribution with independent standard normal components	
$N_a, a = 1,...,4$	Rectangular shape functions	*Chapter 2*
N_d, N_p	Number of data, number of parameters	*Chapters 5, 6*
N_o, N_w	Corey exponents for the phase relative permeabilities	
P	Pressure	
p	Ray parameter (horizontal slowness)	*Appendix A*
p	Saturation front slowness	*Chapter 1*
p	Probability density	*Chapter 5*
$p(m \mid d)$	Conditional probability (density) of *m* given *d*	
$p_c^{(g+1)}$, $p_\sigma^{(g+1)}$	Evolution path, conjugate evolution path in CMA-ES	*Appendix B*
P_i, P_{init}	Initial pressure	
$P_j, j = 1,2,...$	Pressure (maps)	
P_{bub}	Bubble point pressure	
Q, q	Source density	*Chapters 1, 3*
Q	Functional defined on the simulation model	*Chapter 5*
Q, q	Flow rate	
q	Prior probability density	*Chapter 5*
q	Quadratic function	*Chapter 7, Appendix E*
R	Correlation matrix	*Chapter 5*
R	Gas constant (8.3144621 $J \cdot K^{-}1 \cdot mol^{-1}$)	*Appendix A*
R	Reflectivity coefficient	*Appendix A*
R_0	AVO intercept	
R^2	Coefficient of determination	
r	Residual	
R_e, r_e	Major and minor ranges for the correlation ellipse	*Chapters 5, 6, Appendix D*
S	Water saturation	*Chapter 1*
S	Normalised water saturation	*Chapter 3, Appendix C*
S	Diagonal matrix with standard deviations	*Chapter 5*

S	Salinity	*Appendix A*
s	(2D) error in the seismic attribute map	*Chapter 5*
S_g	Gas saturation	
S_{gc}	Connate gas saturation	
S_{gcr}	Critical gas saturation	
$S_{g\max}$	Maximum gas saturation	
$S_j, j = 1,2,...$	Water saturation (maps)	
S_o	Oil saturation	
S_{orw}	Residual saturation of oil in water	
S_{res}, S_{tot}	Sum of squares of residuals, and the total sum of squares in the linear regression	
S_w	Water saturation	
S_{wc}	Connate (irreducible) water saturation	
S_{wcr}	Critical water saturation	
T	Transmissibility	*Chapter 7*
T	Temperature	*Appendix A*
$T_j, j = 1,2,...$	Time	
U_0	Relative saturation velocity	
U_r	Relative flow velocity	
V	Acoustic velocity of a medium	*Appendix A*
Var	Variance	
v_{Sw}	Velocity of a water saturation value	
$w(x)$	Horizontal thickness of a tube	*Chapters 2, 3*
$w(t)$	Wavelet	*Appendix A*
$w_i, i = 1,2,...$	Weights	
x, y	Spatial coordinates	
$x_k^{(g)}$	Individual sampled by CMA-ES	*Appendix B*
α, β	P, S wave velocities	*Chapter 1, Appendix A*
$\alpha, \gamma_i, \zeta_i$	Weights	*Chapter 3*
Γ	Gamma function	*Appendix B*
Γ_i, Z_i	Regularisation matrices	*Chapter 3*
Δ	Delta, change of some quantity	
ΔB	Right hand side of the equations linking 4D seismic with the pressure and saturation changes	
δ	(Infinitesimal) perturbation	
γ	Variogram	
ε	Threshold	
κ, λ	Total fluid mobility	*Chapters 1, 3*
λ	Generation size in CMA-ES	*Appendix B*
λ^*	Lagrange multipliers	*Appendix E*
λ_i	Kriging weights	*Appendix D*
μ	Shear modulus of a medium	*Appendix A*

μ_o	Oil viscosity	
μ_w	Water viscosity	
ρ	Density	*Appendix A*
σ, σ_k	Standard deviation	
σ, τ	Time of flight	*Chapter 2*
$\sigma^{(g)}$	Step size in CMA-ES	*Appendix B*
υ	Degrees of freedom of a χ^2 distribution	*Chapters 4, 5*
φ	Porosity	
χ	Rotation angle for the correlation ellipse	*Chapters 5, 6, Appendix D*
∂	Partial derivative	
∇	Gradient (or divergence) operator	
∇^2	Laplace operator	
$\|\cdot\|$	Euclidian norm	
$\in$	"Is an element of"	

Chapter 1 Introduction

1.1 Reservoir evaluation, monitoring and modelling

Development of oil and gas reservoirs is a process associated with a wide range of uncertainties in geology, rock property distribution and other subsurface characteristics. Poor estimation of the reservoir properties and insufficient monitoring of the current reservoir state may result in improper planning and management of hydrocarbons production, and therefore, worsened economical performance. The need to better estimate the reservoir properties and the current reservoir state, as well as to forecast its future behaviour, has led to the development of a number of practical tools and procedures, like well coring, logging and testing, geophysical surveying, and mathematical modelling of the reservoir dynamic behaviour.

Well and production logging provide data associated with very sparse locations in the reservoir – well locations, and hence may not give appropriate reservoir picture, leaving the numerous uncertainties unresolved. Both static and dynamic reservoir characteristics are accessible from the wells. The former are provided by the well logs, which evaluate lithology, porosity, and saturation. The latter are provided by the routine well production data, production logging, well testing, which show the dynamic performance of the well and the reservoir in its vicinity. Well cores supply a wide range of static and dynamic rock properties – anything that can be studied in laboratory conditions. However, due to small sample numbers, core data is usually unrepresentative to be extrapolated reliably to the whole reservoir.

Geophysical surveying, which is *seismic surveying* in most cases of petroleum reservoirs, gives a good spatial coverage of the area in question, although with poor vertical resolution compared to the well logs. One of the most common techniques used is the 3D seismic surveying, which helps to create reservoir structure and distribute the rock properties in the static reservoir models. The other technique used for increasingly more oil fields is time-lapse seismic surveying. It aims to look at the subtle differences between several 3D seismic surveys taken at different moments of the field life, interpreting these differences as the elastic response to the changes in the reservoir which occurred during the field development activities. By interpreting the time-lapse

seismic, one may be able to estimate changes of the reservoir pressure and saturation, their location and magnitude.

Forecasting the future reservoir behaviour is performed either by extrapolation of the currently observed trends, or by using mathematical models of varying degrees of complexity – from the simple material balance to the full physics reservoir simulations. Any such model will inevitably suffer from the lack of correct input data (e.g. distribution of facies, rock properties, flow barriers) as a consequence of the uncertainty, thus depreciating the forecasts. To narrow down the uncertainty range of the input data, the mathematical model is usually calibrated to be consistent with a possibly wider amount of the available information. This includes *both* the data used to build the initial static model – well logs, core data, 3D seismic data, *and* the dynamic data used to calibrate the existing simulation model – well performance data, well logs, time-lapse seismic surveys. The process of the model calibration to the dynamic reservoir data is referred to as *history matching*.

1.2 Outline of the thesis

In this thesis I will consider the general question of the reservoir behaviour forecasting – in the context of applying time-lapse seismic data for tackling this problem. A number of techniques which quantitatively employ the 4D seismic data (or its products, like the estimated pressures and saturations) will be elaborated and tested, ranging from some fast-track procedures, to more computing intensive history matching workflows. The seismic data will be essentially considered in the form of 2D attribute[2] maps, which is an appropriate approach for the case of thin reservoirs. The seismically thin reservoirs are those for which seismic cannot resolve vertically the different sub-layers, generally because the reservoir thickness is below the tuning thickness, which equals the seismic wavelength divided by four. Whenever "thin" reservoirs are mentioned in the text below, seismically thin reservoirs are implied in most cases. Although the methods and approaches elaborated in the thesis are meant to work with the thin reservoirs, I do not take the definition of being *thin* too strictly. For example, for Schiehallion field considered in Chapter 6 the seismic cubes provided by the operator show the coloured inversion seismic, which typically resolves one reservoir unit within

[2] Seismic attribute map is any map calculated from the 3D seismic cube, e.g. root mean square amplitude over certain window within the cube, sum of amplitudes within the window, etc.

the main reservoir layer T31. Occasionally, two sublayers within T31 are resolved (cf. Figure 6.3). However, by taking the 2D attribute equal to the sum of negative amplitudes between the reservoir top and base horizons it is possible to account for all the sublayers without differentiating them, and essentially treat the reservoir as a single, "thin" one. From the engineering perspective, a reservoir can be considered thin if the fluid flow takes place predominantly in the horizontal directions (and in the same direction in different stacked sublayers), with little vertical flow, so that a 2D flow simulation model adequately describes the reservoir behaviour. Such reservoirs will be usually referred in the text as the reservoirs exhibiting 2D fluid flow, rather than just "thin" reservoirs. Assumption of the 2D nature of the fluid flow behaviour will be essential for the fast-track methods of Chapters 2 - 3, but will be irrelevant for the seismic history matching method introduced in Chapter 4. It should also be noted that a seismically thin reservoir can, depending on the seismic wavelength, have thickness 30 – 70 m. At the same time, a common geologist or reservoir engineer would consider a reservoir to be *thin* if its thickness does not exceed 5 – 15 m. Thus, the definition of *thin reservoir* used in this thesis is different from the ubiquitous definition of thin reservoir used in the industry, and the reader should not be confused by this discrepancy.

The brief and full scheme of the thesis is depicted in the flowchart in Figure 1.1, where the logic of development for the whole study is shown, as well as how certain approaches follow from the findings obtained for the previous ones.

The starting point of my study is to pose and solve the *problem of the reservoir state prediction avoiding conventional reservoir simulation and history matching*. The incentive to avoid the conventional model building and history matching stems from the significant demand of effort and time needed for this process. Instead, if I am able to invert the time-lapse seismic data to pressure and saturation maps (as discussed in below section 1.3), then I may use these maps to seed a simple 2D flow simulation, which finally will give a forecast. It was found that such a simulation is feasible by adopting the streamline formulation of the fluid flow. Only two-dimensional simulation is considered, which is appropriate for the reservoirs that are thin in the engineering sense. I also assume that the reservoir is thin in the seismic sense, so that seismic lacks the vertical resolution necessary for inverting the 3D cubes of pressure and saturation, and essentially gives the 2D maps of certain attributes associated with the reservoir.

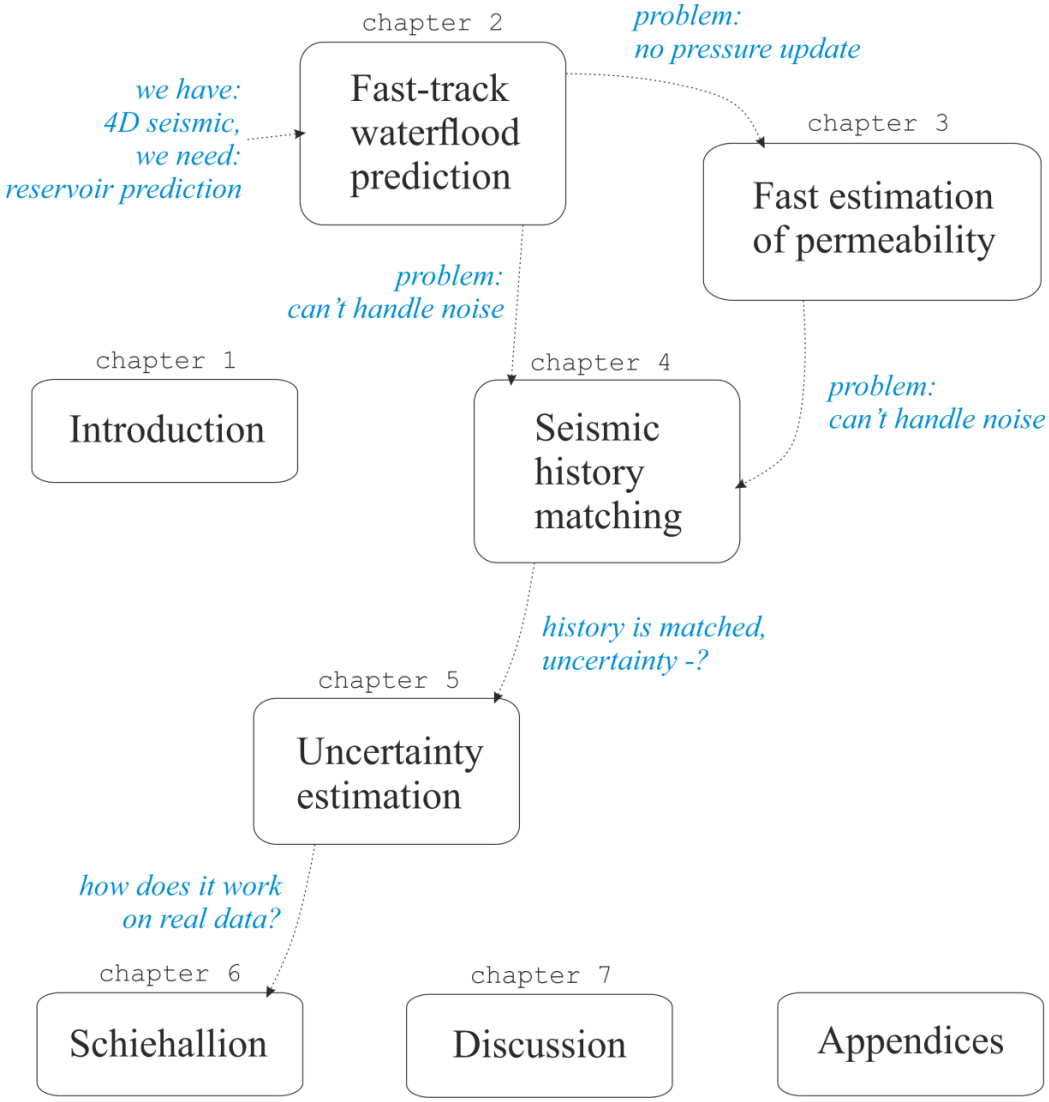

Figure 1.1 The general scheme of this thesis.

In the proposed 2D simulator, which is described in Chapter 2, the streamlines are tracked using the input pressure map. Then, the historical saturation progress along each streamline is analysed, saturation propagation velocities are calculated, and finally the saturations are moved forward, forming the forecast saturation map (Figure 1.2). To ensure that the streamlines in question do not change their trajectories during the saturation prediction step, the reservoir pressure is assumed to roughly follow the steady or semi-steady state scenario.

Although this method works well for noiseless input from simple 2D synthetic models, it was found to have too high forecast errors for more realistic input – one obtained from the 3D models or having noise. Besides, the method only gives predictions of the saturation maps, and cannot forecast pressure.

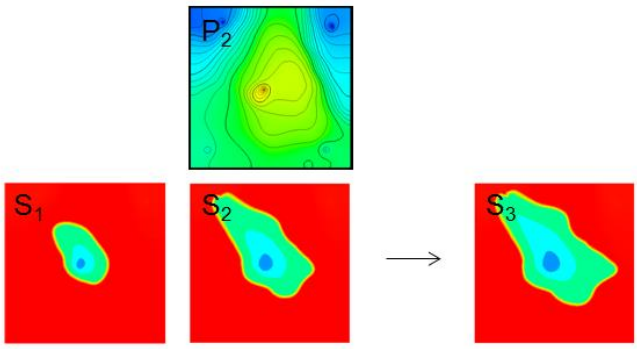

Figure 1.2 Simple waterflood prediction: *left and middle columns* – the input maps of pressure and saturation, *right column* – predicted saturation.

Pressure forecasting, on the other hand, is feasible if one knows the distribution of permeability in the reservoir and the well controls – the flow rates or the bottom-hole pressures. Pressure maps calculated in this way are more reliable and hydrodynamically consistent than the pressure maps estimated from the time-lapse seismic. If the former is used as input for the simplified streamline simulation mentioned above, a more robust saturation prediction may be expected. Then, if the reservoir pressure is highly variable and does not follow the semi-steady state scenario, the original streamline tracking method may not work properly, but the ability to recalculate pressure alleviates this restriction and adds more flexibility to the saturation forecasting procedure. Finally, pressure prediction *per se* is a valuable output one may be looking for.

The need to calculate pressure from the permeability distribution and well data led to posing the *problem of permeability map estimation using the time-lapse seismic data (or its products)*, which is considered in Chapter 3. Again, the problem is posed in the 2D domain because I am dealing only with thin reservoirs with insufficient seismic vertical resolution, so the 2D permeability maps are to be determined. A number of relatively fast techniques of permeability estimation are examined, which take the input of either a pressure map, or saturation map, or both. It was found that favourable results can be expected only if the pressure map is used *as one of inputs*, and the data itself contain very little noise. The cases where the fluid flow has highly three-dimensional character, i.e. where it cannot be effectively substituted by a 2D flow, also produce poor results.

It was further found that introduction of significant perturbations in permeability (like high permeable channels, or low permeable areas on the map) has rather moderate impact on the resulting pressure, from 20% to 70% of the average time-lapse pressure

signal. Of course, the high or low permeable patches will affect the *average reservoir permeability* which in turn will impact the pressure drops between the wells, or the well flow rates, and thus can be estimated. But if the average permeability is put aside, and the higher frequency component of the areal permeability distribution (permeability heterogeneity) is examined, it will be seen that the imprint of the high or low permeability patch on the pressure map is generally 20% to 70% for the realistic cases. Even for pressure maps with the error level of 20% it will be challenging to infer any permeability information, except for the average permeability value, and for errors exceeding 70% the lateral permeability estimation becomes almost impossible. Thus, the pressure maps inverted from seismic data (and hence having quite high noise) are generally not suitable for assessing the permeability heterogeneity, however they may provide information on the boundaries of the sealed compartments present in a reservoir, and help with estimation of the associated transmissibility multipliers.

Due to the abovementioned reasons, it is concluded that the fast-track methods of permeability estimation studied in Chapter 3 are not particularly suitable for application on the real cases. There exists an opportunity to estimate permeability using the alternate, slower procedure of history matching, with the observed data like pressure/saturation maps and well measurements. However, history matching has a wider applicability which goes far beyond permeability estimation, and for this reason a history matching approach which employs the time-lapse seismic is considered in detail in three chapters: 4, 5, 6. The approach integrates the 4D seismic measurements into the history matching loop by estimating the simple seismic-simulation correlations. This means, firstly, that the algorithm does not perform inversion from seismic to impedances or to the simulation model domain (pressures and saturations). Thus the uncertainties which could be inadvertently lost or ignored during such inversion are retained. Secondly, the approach does not use full-physics petro-elastic or seismic modelling, avoiding the need to handle the associated parameters. It uses ideas similar to the data-driven equation (1.3) below, i.e. the first-order relationships between the time-lapse seismic amplitudes and the dynamic parameters (pressures, saturations) from the simulation model. Such relationships, albeit simplistic and rough, appear to be sound from the engineering point of view. The automation of the history matching loop is achieved with a stochastic algorithm CMA-ES (evolution strategy with covariance matrix adaptation), which should be certainly familiar to the *black box optimisation* community. This algorithm works with generations of models, sampling each generation using a multivariate normal distribution with certain mean value and

covariance matrix. After calculating the objective function values for the given generation, the algorithm updates the mean and the covariance so as to increase the probability of objective function decrease in the subsequent generations. The advantages of CMA-ES include good invariance properties (see Appendix B), freely available code, and reasonable performance in the history matching setting, which will also be compared with the other popular choices of the stochastic methods.

An approach for uncertainty estimation is introduced in Chapter 5. It uses Monte-Carlo integration with weights to estimate the *mean values* and *standard deviations* of the uncertain parameters and the modelled data. This algorithm works in conjunction with CMA-ES, and exploits the knowledge of the PDF used by CMA-ES to generate new models. It has a simpler implementation than the *neighbourhood-Bayes algorithm* (see the literature review for details), and does not require the storage of the output of all the evaluated models, since the necessary statistics are accumulated "on-the-fly". The approach, however, was found to work reliably only for very small dimensionality of the problem, and is not applicable for realistic problems. This drawback is deemed to be the consequence of the insufficient exploration of the search space by CMA-ES.

For tackling the uncertainty estimation, the Randomised Maximum Likelihood method is taken aboard. Its implementation is simplified in that only the uniform prior distributions are considered. For defining the likelihood function, the correlated Gaussian errors are taken. The estimation of the correlation ranges and standard deviations which describe the Gaussian error model is performed by examining the errors in the well data (or seismic data) after some preliminary history matching. In the case of seismic data the correlations are defined by an ellipse with a specific rotation angle, major and minor ranges. The estimation of the standard deviations and the overall check of the correctness of the objective function are achieved by applying what I call the χ^2-criterion which describes the expected value of the objective function after optimisation, based on the total number of the data and the number of parameters.

The proposed procedure of history matching and uncertainty estimation is then tested on a synthetic model, where it is shown that introduction of the time-lapse seismic data to the history matching loop allows reducing the prediction uncertainty of the history matched model, compared to the conventional well history matching where only well data is used. This demonstrates the value of 4D seismic for the purposes of better reservoir characterisation and improved forecast modelling. Another result of this study

is in highlighting the importance of the correct definition of the error model used in the uncertainty estimation. This is demonstrated by comparing history matching with the diagonal covariance matrices for seismic error, and the estimated non-diagonal ones, where the latter give notably less biased results.

In Chapter 6 these history matching techniques are applied to a sector of Schiehallion field, which is located in the UK continental shelf in the North Sea. Schiehallion reservoir is made of turbidite sandstones and features complex connectivity between the stacked channels and the sheet-like sands. The reservoir connectivity was one of the key issues in the field development as it controlled the operator's decisions on the optimal well placement. The main simulation model parameters used for history matching in this chapter are the permeability and transmissibility multipliers, controlling the connectivity between the different sand geobodies.

Prior to setting up the history matching, the available data and the preliminary steps are described, e.g. the simulation model upscaling, the noise estimation in the 4D seismic data, selection of the parameters, and the objective function definition. Two history matching cases are considered and compared: conventional well history matching and well-seismic history matching. Both cases are shown to reasonably *reproduce* the actual observations over the chosen historic period, and *forecast* the observations on the subsequent prediction period. Finally, I demonstrate that addition of the 4D seismic data to the history matching loop reduces the forecast uncertainties for certain wells and well data types (water cuts, GOR's, bottom-hole pressures), especially those associated with the distinct signal seen on the time-lapse seismic attribute maps. The reduction of the uncertainties is rather marginal, which is consistent with the high levels of noise in the 4D seismic, but it is in line with the qualitative information contained in the seismic (water saturation signals, gas signals, pressure-up signals), so the application of the history matching workflow devised above to the North Sea dataset can be deemed successful.

The thesis is concluded by Chapter 7 where the main results are recapitulated and the recommendations for the further research are set forth. The subsequent appendices A – E describe some technical questions and algorithms which are used throughout this work.

In the subsequent three sections I will review the literature which is relevant to the topics discussed in the thesis. First, I start from the brief overview of the methods of

pressure and saturation inversion, because the procedures studied in Chapters 2, 3 are supposed to rely on the results of such inversion. Then, I proceed to the review of the time-lapse seismic application to permeability estimation, which is relevant to Chapter 3. Finally, the literature on the different aspects of history matching and uncertainty estimation is considered, as these aspects will be of interest for the seismic history matching procedure of Chapter 4 and its subsequent application in uncertainty studies of Chapters 5, 6.

1.3 Inversion of pressure and saturation from 4D seismic

From the seismic point of view, the basic changes which occur in the reservoir are the **saturation change** (e.g. water replacing oil in a waterflood, gas replacing other fluid phases during depressurisation), and the **pressure change**. Their effect on the rock elastic properties manifests itself as either reservoir hardening (increase of impedance), or reservoir softening (decrease of impedance), see Table 1.1, plus velocity changes.

Change in the reservoir	**Acoustic response**
pressure increase	reservoir *softening*
pressure decrease	reservoir hardening
saturation increase of a denser fluid	reservoir hardening
saturation increase of a lighter fluid	reservoir *softening*

Table 1.1 Basic changes in a petroleum reservoir, and their effect on the rock elastic properties.

However, in real reservoirs the pressure and saturation changes occur mostly simultaneously, leading in general to some sort of superposition of the rock softenings and hardenings. The common examples are:

1. Reservoir softening due to the pressure increase near the injection well combined with reservoir hardening due to the water saturation increase.
2. Reservoir hardening due to the pressure decrease near a production well combined with reservoir softening due to the gas coming out of solution, arising from pressure falling below the bubble point.
3. Reservoir hardening due to water front propagation towards a producing well combined with the reservoir softening due to gas which might have been liberated at some stage because of the excessive depletion caused by the well.

Decoupling of different effects which constitute the observed time-lapse seismic response is a challenging problem, which is often far from being resolved uniquely and with a good precision. One of the key moments in such a decoupling is usage of the multiple seismic attributes which respond differently to the pressure and saturation changes; such attributes, as found from the literature, are often based on the AVO effects.

Studies addressing the qualitative and quantitative estimation of the saturation and pressure changes emerged at the end of 1990's. Brevik [1] presents inversion of pressure and saturation from the time-lapse travel times of the P and S waves. The least-squares inversion scheme uses the derivatives of these seismic attributes with respect to the pressure and saturation change, which are calculated either analytically or numerically. The author reports good inversion results for a synthetic model for the seismic input with 20% noise.

Landrø [2] considers AVO analysis to discriminate the pressure and saturation effects simultaneously taking place in the reservoir in Gullfaks field. Prior to making the inversion, a rock physics model is calibrated. Dependence of the rock properties on the saturation changes is established using the well-log measurements, and this dependence was found to be close to a linear one. Sensitivity to the pressure changes was derived from the ultrasonic lab measurements on the core samples taken from various formations. The resulting dependence is non-linear, and was approximated by a quadratic polynomial. Although the author trusts the laboratory measurements, he poses two concerns: whether it is valid to use the velocities measured at high frequencies (laboratory) for the lower-frequency seismic analysis, and whether it is appropriate to use the measurements made on a dry core sample, that has gone through reloading and loading several times, to infer the actual reservoir rock stress sensitivity.

The inversion technique proposed by the author considers a two-layered subsurface model consisting of the inactive caprock and the active reservoir. The time-lapse change of the reflectivity coefficient on the interface between the two layers is calculated analytically, as a function of P, S velocities, density, their changes, and the angle of incidence. The sensitivities of density and P, S velocities with respect to the reservoir dynamic parameters are calibrated by the well logs and lab measurements, as mentioned above, which finally allows expressing the AVO intercept R_0 and gradient G changes as functions of the pressure and saturation change:

$$\Delta R_0 \approx \frac{1}{2}(k_\alpha \Delta S + k_\rho \Delta S + l_\alpha \Delta P + m_\alpha \Delta P^2),$$
$$\Delta G \approx \frac{1}{2}(k_\alpha \Delta S + l_\alpha \Delta P + m_\alpha \Delta P^2) - \frac{4\beta^2}{\alpha^2}(l_\beta \Delta P + m_\beta \Delta P^2), \quad (1.1)$$

where k, l, m are the empirically calibrated coefficients, α, β are the P and S velocities, $\Delta P, \Delta S$ are the reservoir pressure and saturation changes. From these equations, explicit solution for $\Delta P, \Delta S$ can be obtained using the observed AVO intercept and gradient changes.

Application of the technique to Gullfaks field gave pressure and saturation which are generally consistent with the pressure measurements at wells and the saturation estimates. However, some unphysical values exist, which may be due to either incorrect rock physics model calibration, spatial variability of this model (which was not accounted for in any way), or lack of repeatability between the seismic surveys.

Cole et al. [3] suggest an algorithm of pressure/saturation inversion from the time-lapse P and S impedances. They apply a full physics PEM which uses Gassmann equation [4], harmonic averaging of the fluid bulk moduli, Batzle-Wang equations [5], etc. The pressure dependence is taken from the laboratory measurements on core samples. The inversion algorithm itself is rather simplistic and requires multiple forward modelling to be performed to explore the 3D parameter space consisting of the values of pressure change, saturation change and porosity change. However, the algorithm provides a convenient means for uncertainty estimation of the inverted reservoir parameters.

MacBeth et al. [6] present another approach for the pressure and saturation inversion, in which all the necessary calibration is done based on the available data at the well locations. The changes of pressure and oil saturation $\Delta P, \Delta S_o$ are linked to the time-lapse seismic attribute ΔA by a simple relationship

$$\frac{\Delta A(x,y)}{\bar{A}_b} \approx C_S \frac{\Delta S_o(x,y)}{\bar{S}_{oi}} + C_P \frac{\Delta P(x,y)}{\bar{P}_i}, \quad (1.2)$$

where the quantities in denominators (with bars) are the average properties at the initial time moment, i.e. the average of the baseline seismic attribute, the initial oil saturation and pressure. Such linear relationship is said to be generally valid for typical pressure and saturation changes in a petroleum reservoir. The authors start calibrating the coefficients by considering first the average quantities of what is given in equation (1.2), i.e.

$$\frac{\Delta\overline{A}}{\overline{A}_b} = C_S \frac{\Delta\overline{S}_o}{\overline{S}_{oi}} + C_P \frac{\Delta\overline{P}}{\overline{P}_i}. \tag{1.3}$$

Here the averages are calculated over the entire reservoir, or its sub-volume, in either case with the pore-volume weighting. The mean reservoir pressure and saturation can be found e.g. from a simulation model, or material balance. If the well data consisting of the pressure and saturation estimates at wells are used, then averaging of the relevant quantities is done over the specific wells and intervals. Coefficients C_S, C_P can be found if equation (1.3) is written for at least two different time-lapse monitors, and the appropriate linear system is solved.

If coefficients in (1.3) are calibrated independently for two or more seismic attributes, e.g. A, A', which respond differently to the pressure and saturation change, then it is possible to invert for pressure and saturation in each bin location x, y by solving the system

$$\begin{aligned} \frac{\Delta A(x,y)}{\overline{A}_b} &= C_S \frac{\Delta S_o(x,y)}{\overline{S}_{oi}} + C_P \frac{\Delta P(x,y)}{\overline{P}_i} \\ \frac{\Delta A'(x,y)}{\overline{A}_b'} &= C_S' \frac{\Delta S_o(x,y)}{\overline{S}_{oi}} + C_P' \frac{\Delta P(x,y)}{\overline{P}_i}. \end{aligned} \tag{1.4}$$

If multiple attributes are used, then the above system is to be solved in the least-squares sense. The suggested candidate attributes, which are likely to respond differently to the dynamic reservoir changes are: restricted offset stacks, AVO attributes like intercept and gradient, P and S impedances, instantaneous frequency, phase shift or time shift. In order to account for the areal lithology variation in the reservoir, the authors suggest to normalise the left-hand side of equation (1.2) by $\tilde{A}_b(x,y)$, which is the baseline survey attribute adjusted to the mean of unity and the standard deviation guided by the porosity distribution from the well data:

$$\frac{\Delta A(x,y)}{\overline{A}_b \tilde{A}_b(x,y)} = C_S \frac{\Delta S_o(x,y)}{\overline{S}_{oi}} + C_P \frac{\Delta P(x,y)}{\overline{P}_i}. \tag{1.5}$$

In general, this normalisation procedure is said to be case-dependent. The proposed method was applied to a synthetic dataset, with favorable results, and to the North Sea Schiehallion reservoir, where the inversion results looked rather unphysical and not consistent with the history matched simulation model, probably because of the 4D noise or the gas effects which were not taken into account.

A similar algorithm is proposed in [7], however the considered dependence of the time-lapse seismic attributes on the dynamic reservoir parameters was more complex, viz. linear dependence on ΔS_w, quadratic dependence on ΔP, exponential dependence on ΔS_g.

Pressure and saturation distribution inverted from the time-lapse seismic can be used for the purposes of reservoir monitoring. Another usage will be illustrated in the subsequent chapters, where the pressure and saturation maps are used for simple waterflood forecasting and reservoir permeability estimation (see also section 1.4). Yet another application of these maps finds its way as an additional constraint in history matching, see section 1.5. Relationships between the seismic and the dynamic reservoir parameters of the form (1.2) will be used in Chapter 4, where a simplified seismic modeling procedure avoiding full-physics petro-elastic modeling is proposed.

1.4 Estimation of permeability from 4D seismic

Time-lapse seismic has been found to give improved reservoir characterisation compared to the conventional 3D seismic. From this perspective, there are a number of studies relevant to this thesis, which attempt to estimate the reservoir permeability distribution using the time-lapse seismic, or the pressure and saturation maps estimated from it, as input.

Vasco [8] proposes a method of permeability calculation using the reservoir pressure estimate, which can be in turn derived from time-lapse seismic observations. The method is based on the steady state flow equation

$$\nabla \cdot (K\lambda \nabla P) = Q, \tag{1.6}$$

where $K(x)$ denotes absolute permeability; Q is the source density term associated with the wells; λ is the total fluid mobility which depends on the current saturation, and can be estimated if one has an estimate of saturation. The author subtracts two equations of type (1.6) taken at two distinct time steps T_0 and T_1, arriving at the linear equation for permeability of the form

$$\nabla K \cdot \Phi + k \nabla \cdot \Phi = Q_\Delta. \tag{1.7}$$

(From the perspective of the following calculations, taking this time-lapse difference of (1.6) looks as unnecessary complication; a better option might be to simply consider

(1.6) at a specific time moment). Variable Φ used in the equation is the quantity expressed by $\Phi = 0.5(\lambda_1 + \lambda_0) \cdot \nabla(P_1 - P_0) + 0.5(\lambda_1 - \lambda_0) \cdot (2\nabla P_0 + \nabla(P_1 - P_0))$, and $Q_\Delta = Q_1 - Q_0$, with the subscripts 0, 1 denoting the two time steps. The boundary conditions with the predefined constant permeability values are imposed for this problem. Then, equation (1.7) is discretized using the finite differences, resulting in a system of linear equations

$$Ak = q, \tag{1.8}$$

where vector k is the unknown permeability field, the coefficients of the sparse matrix A are obtained from the input pressure and the total mobility estimate, and the right hand side q is determined by the original well source terms. Equation (1.8) is solved in the least-squares sense. To avoid numerical instabilities, the regularisation is applied by means of introducing a term which penalises abrupt changes of the permeability field. The weighting coefficient for the penalty term is selected based on a set of test runs.

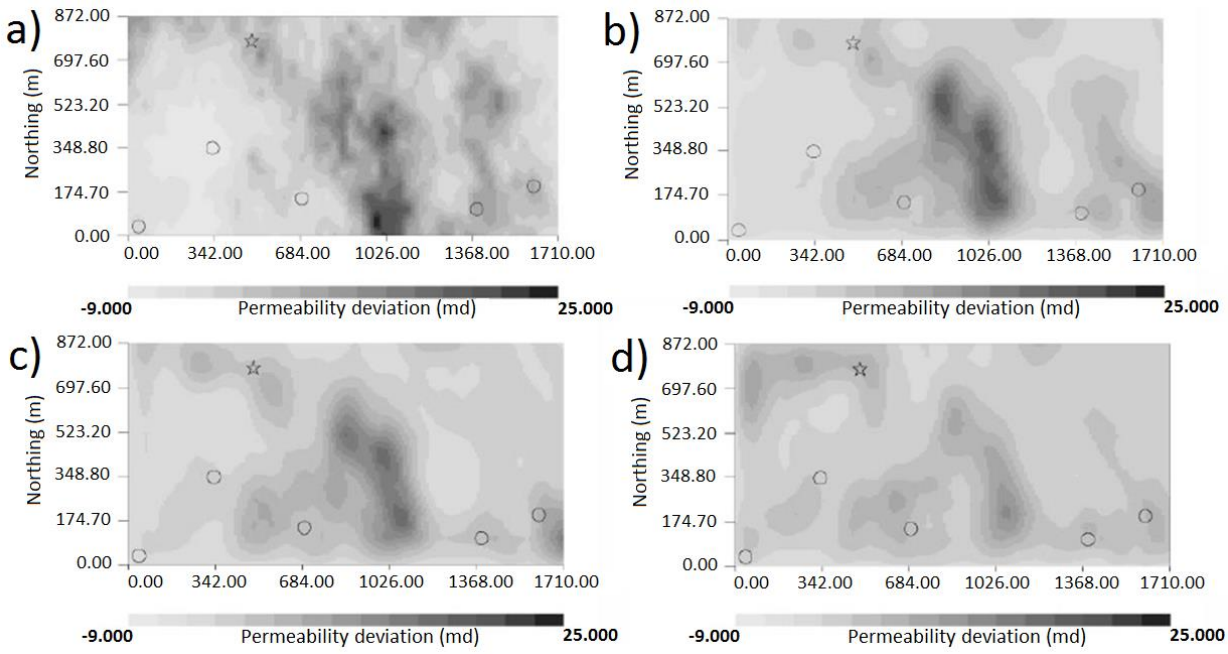

Figure 1.3 Reference permeability map (a); and the maps resolved with the Gaussian noise added to Φ, with the noise standard deviation equal to a percentage of $\max(\Phi)$: (b) 10%, (c) 30%, (d) 60%. The maps display the permeability deviations from the background value of 10 mD. Adopted from [8].

The method was tested on a 2D areal synthetic model, and the author reports successful resolution of the underlying permeability map when the exact input (pressure, permeability boundary conditions, total fluid mobility) is used. Addition of the

Gaussian random noise to Φ decreases the resolution capabilities of the method, but still the general features of the permeability map are resolved, see Figure 1.3. Finally, the method was applied to estimate the permeability of a real reservoir at Lost Hills field, California, where the pressure and saturations were estimated from the time-lapse cross-well seismic and the electro-magnetic surveys.

Another approach to the reservoir characterisation proposed in [9], [10], is based on the streamlines formulation. The authors start by deriving the sensitivities of the seismic amplitudes A to the reservoir properties – porosity and permeability. This is done in steps, essentially using the chain rule. Among the reservoir dynamic parameters which may affect the time-lapse amplitudes, the pressure effects and reservoir compaction are neglected, so the time-lapse amplitude is considered to depend only on the saturation change. For the vertical column of the 3D model grid cells with coordinate i, j the perturbation of the time-lapse amplitude can be written as

$$\delta A_{ij}^1 - \delta A_{ij}^0 = \sum_k \left(\frac{\partial A^1}{\partial S_{ijk}} \delta S_{ijk}^1 - \frac{\partial A^0}{\partial S_{ijk}} \delta S_{ijk}^0 \right). \tag{1.9}$$

The partial derivatives of the amplitude with respect to the saturation are calculated *numerically*, using certain petro-elastic model (Gassmann equation, stress sensitivity relationships calibrated on the lab measurements).

The next step is estimation of the sensitivity of saturation in a particular grid cell to the static reservoir parameters – porosities and permeabilities. For this, the streamline trajectories are calculated from the known pressure field. The saturation history along each streamline can be expressed as

$$S(t,\sigma) = S(\sigma / t), \tag{1.10}$$

where σ is the travel time along the streamline found as the integral of the front slowness $p(r,t)$:

$$p(r,t) = \frac{\varphi(r)}{\kappa K(r) \mid \nabla P(r,t) \mid} \tag{1.11}$$

$$\sigma = \int_{\Sigma} p(r,t) dr. \tag{1.12}$$

Here t is time, r is distance along the streamline, κ is the total mobility, K - absolute permeability, φ - porosity, ∇P - pressure gradient. Perturbing the porosity and permeability in the equations above, the authors arrive at

$$\delta p(r,t) = \frac{\partial p}{\partial \varphi}\delta\varphi(r) + \frac{\partial p}{\partial K}\delta K(r) + \frac{\partial p}{\partial |\nabla P|}\delta |\nabla P(r,t)| \tag{1.13}$$

$$\delta\sigma = \int_{\Sigma} \delta p(r,t)dr \tag{1.14}$$

$$\delta S(\sigma / t) = \frac{1}{t} S'(\sigma / t)\delta\sigma. \tag{1.15}$$

The authors ignore the shift of the streamline trajectories induced by perturbations of the porosity and permeability. Also, in equation (1.13) the pressure gradient at each point along the streamline depends on porosity and permeability, but it is not mentioned how to account for this dependence while calculating the sensitivities. Nevertheless, the authors claim that the streamlines approach gives quite accurate sensitivities as compared to the reference sensitivities calculated using the finite differences. This is illustrated by a 31 x 31 cells synthetic model with one injector in the middle, and four producers at the corners. Sensitivities of the seismic amplitude at some observation point with respect to the porosity or permeability change can be seen in Figure 1.4. This conclusion on the accuracy of the sensitivities from the streamlines approach will be questioned in Chapter 3.

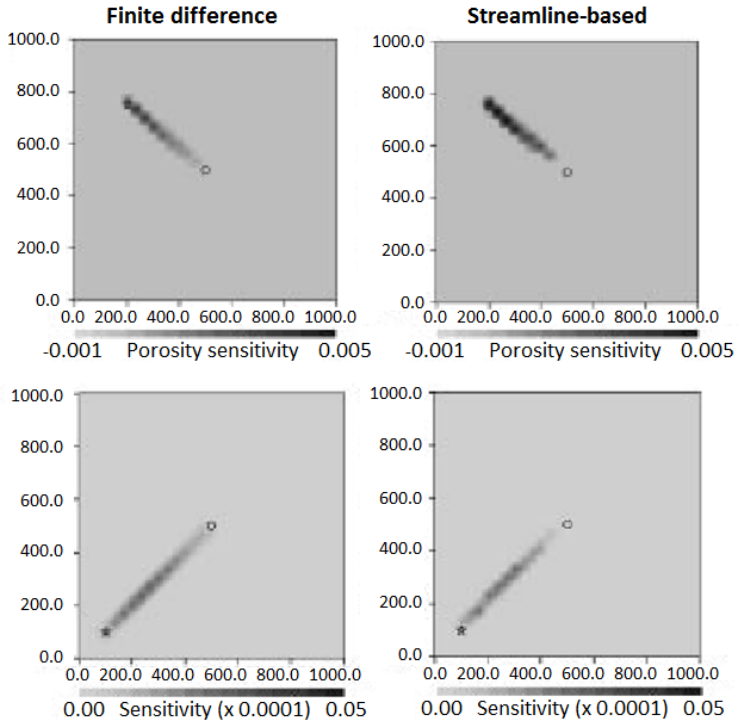

Figure 1.4 Sensitivity of the amplitude at certain observation point (denoted by *star*) to the changes in porosity (*top row*), and permeability (*bottom row*). Numerical finite difference result is on the *left*, streamline-based result – on the *right*. Adopted from [10].

The implemented sensitivity calculation algorithm allows inverting for the reservoir properties from the time-lapse amplitude changes. Since there is a trade-off between porosity and permeability in equation (1.11), it is suggested to fix porosity, and invert only for permeability. The process is started from some initial reservoir model, and permeabilities are iteratively updated to obtain a better fit to the observed time-lapse seismic. On each step a linear system can be produced from the equations (1.9), (1.11), (1.13), (1.15)

$$\delta A^{1-0} = M\delta k^{-1}, \tag{1.16}$$

where the left hand side is the time-lapse amplitude, M is the sensitivity matrix, δk^{-1}-vector of the reciprocal permeabilities. The system is solved in the least-square sense, after adding two regularisation terms: the first one which forces permeability updates to be smoother, and the second one which biases the result in the direction of the prior permeability model. Equation (1.16) is solved for the reciprocal permeabilities, but the authors do not describe how they treat the situation when δk^{-1} approaches zero which may lead to the unphysically high permeability values. At each iteration of the algorithm, a reservoir simulation is performed to redefine the pressure and saturation, and recalculate the streamline trajectories.

Permeability update within each iteration minimises the time-lapse amplitude misfit, however the updated permeability is not coupled with the pressure field (pressure and streamlines are kept fixed within the single iteration). Therefore, after the model is re-run and pressure is recalculated for the new permeability, the amplitude misfit may increase. Such increases can be seen in Figure 1.5, where the progress of the misfit function is shown. This behaviour shows that the algorithm proposed by the authors is not a rigorous gradient optimisation method, although it may seem to be such a method because of the use of "sensitivities" for the model updates. Hence, there is generally no guarantee that the algorithm should converge and minimise the misfit of the time-lapse seismic.

The quality of the permeability inversion for a synthetic model can be found in Figure 1.6. As we see, the quality is rather low; the permeability values are smeared along the flow paths. Besides, the area where permeability was updated is limited to the region covered by the streamlines. Finally, the inversion algorithm was applied to the time-lapse seismic from Bay Marchand field. Although the amplitude misfit from the initial permeability model was somewhat reduced by the iterations, no evidence is provided

which could indicate that the updated permeability gives a better reservoir characterisation, or whether the new model is consistent with the well data.

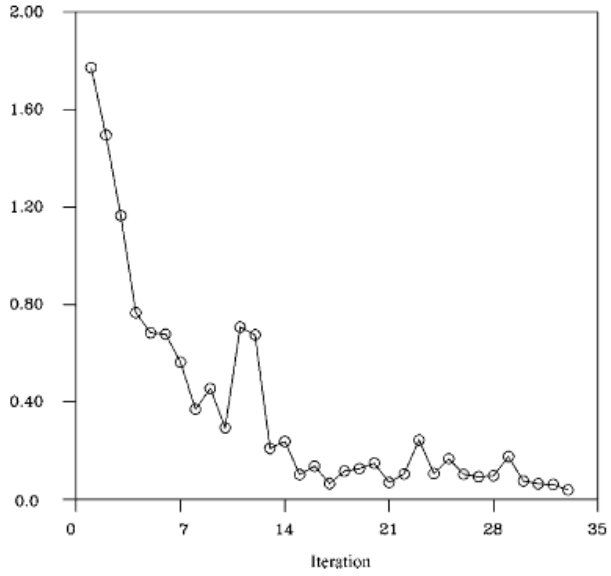

Figure 1.5 Misfit vs. iterations: the reduction is not monotonic. Adopted from [10].

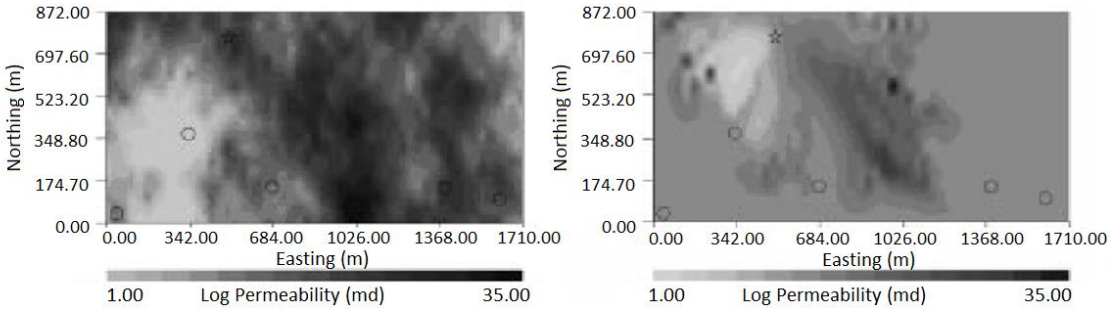

Figure 1.6 Reference permeability map for the synthetic model (*left*), and the inverted one (*right*). Adopted from [10].

1.5 Time-lapse seismic for history matching

One of the widespread quantitative applications of time-lapse seismic lies in its integration with the reservoir simulation model by means of history matching. History matching *per se* – both well data based, and well plus 4D seismic data based – is a very broad field of research, so let me briefly consider the existing approaches and techniques as found in the literature. History matching works with the full physics fluid flow simulation model of the reservoir, calibrating this model with the past behaviour of the reservoir, so as to improve the overall reservoir characterisation and make more

confident forecasts of the future reservoir behaviour. It aims at finding the unknown reservoir model parameters such that the resulting model maintains the physical realism and satisfies the different kinds of the measured data.

Maintaining the physical realism of the model should be taken care of when the model parameterisation is proposed. Model parameters (which may include e.g. porosities, NTG ratios, permeabilities, relative permeability curves, fluid contact depths, fault transmissibilities, aquifer parameters, *etc*) should be restricted to vary within certain *ranges* which are deemed appropriate for the given reservoir and consistent with the data from other sources: core samples, well logs and well tests. Gridblock-based or *volumetric* parameters like porosity and permeability are also required to have realistic spatial variations so as to properly approximate the geology of the reservoir.

Since the simulation model typically has too many volumetric parameters, it may be beneficial to reduce their number by re-parameterising the model. In the simplest case this can be done by defining the coarse regions in the model and parameterising the volumetric properties region-wise [11]. The other approach is to parameterise only the values at some selected points of the model – the *pilot points* – and then make an interpolation between them, using e.g. kriging [12]. Volumetric properties can also be defined by different kinds of basis functions like splines [13] and wavelets. Apart from the volumetric properties, parameterisation may define the geometry and outline of the different regions within the reservoir, like the facies boundaries. Landa et al. [14] considered a simple synthetic case study where eight parameters define the location and shape of a sand channel embedded in a shaley layer. They reported improved history-matching performance as compared to the region-wise permeability parameterisation. The same authors consider a model with fault, where a fault is modelled by a narrow low permeable rectangle which changes position, azimuth and length.

One of the methods to reduce the number of parameters is sensitivity analysis whereby a sensitivity matrix is calculated which consists of the partial derivatives of the modelled data with respect to the model parameters. Then, in the simplest procedure, the parameters are ranked depending on their relative importance to matching the data, and the least influential are excluded. In a more advanced approach, some kind of spectral analysis is performed based on the sensitivity matrix, see e.g. [15]. It should be noted, however, that the sensitivity matrix depends on the current values of the parameters. So, the matrix computed for the initial parameter values may become unreliable as the parameters assume different values during the history matching.

It should also be noted that excessive reduction of the parameters list may not be beneficial. As discussed and summarised in [16], such a reduction may cause the decreased efficiency of history matching, underestimated uncertainties and less plausible resulting parameter distributions. A more appropriate procedure might be to maintain a larger number of parameters with certain *regularisation*.

Practically, history matching is either done manually, or in automated (computer aided) manner. The latter approach is focused in this thesis, as well as in the majority of technical literature on history matching. While manual history matching allows soft, or *qualitative* definition of the data-match criteria, the automated history matching is only feasible with some *quantification* of the mismatch between the modelled and measured data.

The measured data used for history matching in most practical cases may include the routine well production or injection data, including well rates, water cuts, GOR's, and bottom-hole pressures. By adding more dynamic data, more constraints can be imposed on the reservoir model, which allows reduction of the model uncertainties and more reliable predictions of the reservoir performance. Additional dynamic data may include e.g. the well test measurements [17] and tracer data [18]. All these data, however, lack the spatial resolution because they are associated with rather sparse well locations. Well data are usually incorporated into the objective function in the least squares form, with appropriate normalisation of the data mismatch for the different data types in order to account for their different magnitudes.

Another type of the additional dynamic data which may be available to a reservoir engineer is the time-lapse seismic data. It has good spatial coverage and resolution compared to the well data. Among the downsides which can be pointed out is rather poor vertical resolution of seismic, which prevents monitoring the thin sub-layers of the reservoir, instead giving some response averaged over a thickness of ¼ of the wave-length. If the time-lapse seismic data is to be used qualitatively, the difficulties of using it may arise from the interpretation side: the different reservoir effects, like the changes of rock stress, water or gas saturation, which control the time-lapse seismic response, may not always be differentiated or properly interpreted from the observed time-lapse rock *softening* or *hardening*. If the time-lapse seismic is to be integrated into history matching on quantitative basis, a problem then emerges of how to convert the data from the seismic domain to the simulation model domain or vice versa, so that comparison of the modelled and measured data could be performed.

Conversion from the seismic to the simulation model essentially means estimation of the pressure and saturation changes (maps or volumes) based on the 4D seismic, for which a number of approaches have been reported in the literature (see section 1.3). This estimation can also be done by passing through the intermediate domain of impedances, i.e. the seismic is firstly inverted into impedances, and then pressure and saturation changes are estimated from the impedance changes. The drawback of history matching using the time-lapse seismic converted to the *simulation model domain* (i.e. to pressures, saturations) is that the *inversion* made to prepare the data for history matching is a non-unique procedure, however this non-uniqueness is usually treated inappropriately, or not treated at all, so the history matching very likely just gets an input of a single specimen of pressure and saturation, which are likely to be incorrect, with no uncertainty information additionally provided.

The literature examples of the 4D seismic history matching in the *simulation model domain* often deal with the synthetic models. Landa et al. [14] used the water saturation maps (supposing they were interpreted from the 4D seismic) in a synthetic history matching case study. It was shown that even treating these maps in a binary (black and white) manner, which is fairly qualitative, still keeps the information valuable for the history matching. Jin et al. [19] used the water-front patterns inferred from 4D seismic for history matching of the water-flooded West-African offshore reservoir. Davolio et al. [20] used the pressure and saturation maps inverted from P and S-impedances for history matching of a synthetic model.

Conversion from the domain of simulation model to the *seismic domain* is usually done with the petro-elastic modelling of the reservoir rock impedances and velocities, and subsequent modelling of the seismic wavefield. Although no inversion is done here, the petro-elastic model itself introduces a substantial number of new uncertain parameters, e.g. the elastic properties of the mineral matrix and shales, the rock stress sensitivities. While these properties can be estimated in the laboratory, there is no guarantee that these estimates will appropriately describe the *in situ* reservoir rock (see e.g. the concerns posed in [2]). Moreover, the elastic behaviour of the reservoir depends on the distribution of porosity and shales, and this distribution is also uncertain, although it can be calibrated to some extent using the 3D seismic modelling. If the petro-elastic model parameters are deemed to be unreliable, they can be added to the full list of the history matching parameters, however such an expansion of the parameter list will make the entire problem more difficult to solve. An illustration of the 4D seismic history

matching in the *seismic domain* can be given by [21], where the time-lapse seismic amplitudes were used for history matching of a Gulf of Mexico turbidite reservoir.

History matching can also employ the intermediate domain – i.e. the *domain of impedances*, such that the seismic volumes are inverted to the impedances, which are compared with the impedances obtained from the simulation model through the petro-elastic modelling. This approach, albeit visually compelling, has drawbacks of the previous two: inversion to the impedances is likely to ignore the uncertainties, and petro-elastic modelling for the simulation model will need reliable petro-elastic model parameters. However, the domain of impedances appears to be the most popular in the history matching literature, see e.g. [22], [23], [24], [25], [26]. While there are reports of better history matching performance in this domain rather than e.g. in the amplitudes domain [27], it is still not clear whether the popularity of history matching in the impedances domain is due to its robustness, or because this domain is an acceptable compromise which is understood by *both* engineering and geophysical communities.

There are also approaches which avoid the direct comparison (e.g. in the least-squares sense) of the observed and modelled time-lapse reservoir signatures, calculating instead some correlation measures between the quantities in question. Usually they are employed for the reservoirs where petro-elastic modelling is challenging. For example, Waggoner et al. [28] used the normalised cross-correlation between the observed and modelled maps of acoustic impedance for history matching of a Gulf of Mexico gas condensate reservoir. Kjelstadli et al. [29] employed the correlation between the observed and modelled attribute maps to history match a North Sea compacting chalk reservoir, where adequate seismic modelling was problematic.

A range of optimisation algorithms have been found by the researchers and engineers to be appropriate for automated history matching. No algorithm exists which is universally efficient for all conceivable problems. For a particular history matching problem, which is characterised by its parameters and the shape of the objective function, some techniques may be more suitable than the others. The optimisation algorithms for history matching can be split into the stochastic group and the deterministic group.

Optimisation algorithms from the stochastic group are typically the black box optimisers, i.e. they only require the values of the objective function, but no information on the derivatives. These algorithms have relatively slow convergence, but are believed

to be less prone to getting stuck in the local minima. The number of parameters which can be handled by them is typically a few tens to one hundred. Quite popular stochastic algorithms include: simulated annealing [21], genetic algorithms [29], evolution strategies, particle swarm optimisation [30], [31], and colony optimization [32], neighbourhood algorithm [33], Bayesian optimization algorithm [34]. A few benchmark studies can be found in the literature comparing these procedures. Jin et al. [19] compared particle swarm optimization (PSO), very fast simulated annealing (VFSA) and neighbourhood algorithm (NA). They report good convergence behaviour of PSO provided that enough parallel resources are available, and relatively cheaper convergence of VFSA if computing resources are very limited. Hajizadeh et al. [35] compared differential evolution (DE), PSO, ant colony optimization (ACO) and NA on the well-known synthetic PUNQ-S3 model with 45 parameters, reporting faster convergence for DE and PSO, and slowest convergence for NA.

Deterministic optimisation algorithms commonly used for history matching include the *Newton-like methods* [36], like Gauss-Newton [14], Levenberg-Marqardt methods [22] and *quasi-Newton methods*[3] like BFGS [37], [11]. These *gradient-based* algorithms have fast convergence provided that the necessary derivatives (gradients, Hessians) are readily available, and the objective function is smooth enough. The Newton-like methods converge faster than quasi-Newton methods, but they require more derivatives calculation. This overhead in the additional derivatives calculation for the Newton-like methods becomes very pronounced for the problems with a large number of the observed data and a large number of the model parameters. In such situation the Newton-like methods may become inefficient, but the quasi-Newton methods keep working because they rely merely on the gradient of the objective function, for which there are efficient calculation approaches. Although the gradient-based algorithms are believed to get prematurely stuck in a local minimum which is *far* from a global minimum, this is not necessarily the case as discussed in [16] and confirmed by my experience.

All gradient-based methods require the derivatives of the objective function to work. The simplest derivative calculation can be done with the finite differences. The drawback here is that the number of the full simulation runs required grows linearly with the number of the model parameters, so the history matching may consume too much computational resources. Although, in some cases the objective function can be

[3] Also known as *variable metric methods.*

split into the local components, and the model perturbations can be designed more efficiently, reducing the overall number of simulations [38]. One more concern of the finite difference derivative estimates is that the resulting precision may become unsatisfactory, leading to the degraded convergence of the optimisation methods [39].

The other two methods for the derivatives calculation are the *forward*[4] method and the *adjoint* method which should be coupled with the numerical simulator [40]. Their advantage is the high precision and the smaller calculation effort compared to the finite differences mentioned above. The drawback is the small flexibility, because the procedure of the derivatives calculation for the specific parameters should be hard coded in the numerical simulator.

The computing costs for the *forward* method are linearly proportional to the number of parameters, and practically do not depend on the number of the objective functions or the data functions for which the derivatives are calculated. So, this method may be not appropriate for the history matching problems with large number of parameters. For the *adjoint* method the situation is reverse: the computing costs practically do not depend on the number of parameters (the full gradient of the objective function is calculated at the additional cost of one simulation run), but are linearly proportional to the number of the objective functions (or number of data, if the data sensitivities are to be evaluated). This makes the adjoint method a good choice for calculating the gradients of a single objective function with high number of parameters. However, this advantage of the adjoint method has its cost: since this procedure needs to start from the last time step of the simulator and proceed back to the first time step, all the model states throughout the simulation should have been kept in the memory, so the memory consumption becomes significant. Alleviation of the memory usage can be done at the expense of additional calculation [16]. Since the adjoint method gives a very cheap estimation of the objective function gradient, it is very well suited to work with the optimisation algorithms which require only these gradients, e.g. the conjugate gradients or the quasi-Newton methods.

History matching means solving an inverse problem, and it has two inherent major challenges. Firstly, finding even a single plausible model requires a significant computational effort, since all the history matching approaches to date bear some trial and error elements. The second challenge is that the problem is ill-posed and its

[4] Also known as the *gradient simulator method*.

solution is notably non-unique. This means that multiple combinations of the parameters can satisfy the data-match criteria equally well. Ignoring such a feature of the inverse problem and selecting just a single model out of a whole range of the plausible solutions may result in a poor quality decision-making based on the model. A more sound practice to handle this challenge would be history matching with estimation of the associated uncertainties and making output of multiple models instead of a single one. Uncertainty estimation is more readily performed if history matching is done in the automated manner rather than the manual one.

There are approaches of uncertainty estimation that work with a single best model, and characterise uncertainty based on the objective function Hessian or its estimates like the Gauss-Newton approximation. Such approaches are more natural for the gradient-based optimisation algorithms [41], [42]. Uncertainty estimation based on the Hessians is precise when the modelled data are related to the model parameters linearly. However it is not the case for the typical history matching problems which are non-linear and have multiple local minima in the search space. Using the Hessian-based methods for such problems usually results in the uncertainty underestimation. An illustration of the uncertainties underestimated by the gradient algorithms (as compared to the better estimates by the stochastic algorithms) for synthetic model PUNQ-S3 can be found e.g. in [35].

The other group of methods for uncertainty quantification samples multiple models from the posterior distribution or its approximation. The following approaches can be pointed out: Metropolis-Hastings Markov chain Monte-Carlo, randomized maximum likelihood method, neighbourhood-Bayes algorithm. The principles and limitations of these methods are as follows. Metropolis-Hastings algorithm builds a Markov chain of models, such that in each iteration a new candidate model is proposed, simulated, and its likelihood is evaluated. The model is then accepted or rejected based on certain criteria, which ensure that the accepted models will be asymptotically sampled from the desired posterior distribution. However, in practice a long burn-in period is required before the sampled models start following the posterior distribution. Besides, the fraction of the accepted models is usually small, leading to impractically high computation costs.

Randomised maximum likelihood [43] also utilizes the MCMC principles. It first draws a model from the a priori distribution, perturbs the data according to the data error covariance matrix, and then applies *an arbitrary* optimisation algorithm to condition the

model to the perturbed production data. Finally, the acceptance criterion is checked, and the model is either kept or rejected. The resulting acceptance rates are high, but rigorous estimation of the acceptance probability is very computationally costly, so it is proposed [43] to accept all models. Such an approach exactly samples from the posterior distribution when the modelled data linearly depend on the model parameters. For highly nonlinear problems it is not the case, but still, for a few simple non-linear examples the models sampled by the RML are reported to follow the posterior distribution reasonably well [42]. Reasonable performance of the RML is also reported for a 1D synthetic non-linear model with multimodal PDF [44], and for PUNQ-S3 synthetic model [45].

The Neighbourhood-Bayes algorithm (*NA-Bayes, NAB*) is flexible in that it can work with arbitrary ensemble of models for which the likelihood values were estimated [46] , [35]. It works naturally in conjunction with the stochastic optimisation algorithms, since they produce lots of models with the estimated objective functions as they search the parameter space. The algorithm re-samples the new models from a distribution which is piecewise-constant on Voronoi cells defined by the input ensemble of models. However, if the input ensemble is of poor quality, which is quite likely for the high-dimensional parameter spaces, the resulting uncertainty estimate by the NA-Bayes algorithm will be unreliable.

Finally, an increasingly popular technique for history matching and uncertainty estimation is the ensemble Kalman filter, which is quite effective in terms of the computational costs. EnKF is a data assimilation technique, which sequentially updates the ensemble of models at each time step whenever the observed data are available, without the need to re-run models from time zero. Update at each time step is done in two parts – *forecast*, moving each model forward in time with a simulator, and *analysis*, updating the variables based on the covariances estimated from the ensemble. While the traditional history matching techniques examine the sensitivities of the model data to the parameters (e.g. porosities, permeabilities) and estimate these parameters, the EnKF estimates both the parameters and the state variables (e.g. pressures and saturations). It correctly samples from the posterior density if the modelled data linearly depend on the model parameters, the prior density is Gaussian, and the ensemble is sufficiently large. In this case the EnKF becomes equivalent to the randomised maximum likelihood method [47].

EnKF can handle huge numbers of the model parameters (hundreds of thousands), and is reported to work well on the realistic reservoir problems [16], while it may fail to reliably characterise the uncertainty on the simple problems [47]. The estimates of the EnKF performance in the literature tend to be contradictory, e.g. Liu et al. [48] report EnKF to outperform gradient methods in history match quality, while Emerick et al. [49] remark that the history match quality of EnKF is much worse than that of the gradient-based methods. This difference may be due to the nature of the problems being history matched. The main challenges of EnKF method include: rank deficiency of the covariance matrix estimated from the ensemble, non-Gaussian prior distributions, strongly non-linear relationship between the parameters and the modelled data [50]. Rank deficiency in the covariance matrix leads to the spurious correlations which can be suppressed e.g. by some kind of covariance localisation: distance-dependent [51], streamline-based [52], or making thresholding in the Kalman gain estimation [53]. EnKF can be used in combination with other techniques, e.g. Emerick et al. [49] propose a combined EnKF-MCMC for which they report the improved uncertainty estimate compared to the EnKF with covariance localisation.

1.6 New findings and practical value of the thesis

Let me outline the main findings of the thesis, which improve, complement, or criticise the results published in the literature. The fast-track waterflood forecasting using the streamline tracking has not been to my knowledge essentially done anywhere, except very briefly in the PhD thesis of Oldenziel [54]. The procedure proposed there was not tested sufficiently, and besides the description of its technical details is rather confusing, as the streamlines are calculated only based on the saturation profiles. In my work the saturation forecasting algorithm is considered in more rigour and detail, followed by more intensive testing. The general conclusion of its restricted applicability is drawn because of increased sensitivity to the input noise.

A permeability estimation procedure (#1) which uses the input of pressure and saturation maps is implemented. To my knowledge, such a procedure has not been considered elsewhere. The algorithm relies on the streamlines formulation of fluid flow and suffers from the same drawbacks as those found for the fast-track waterflood forecasting method. The permeability estimation approach suggested in [8] (see equations (1.6) – (1.8) above) is implemented with some minor modifications and tested

on a range of models (approach #2). The conclusions of its applicability reported by the author have not been confirmed, and a stronger dependence of the method on the input noise is established in my work (although the direct comparison with the noise considered by the author was not possible due to the lack of the details provided). Another permeability estimation method (#3) is implemented, which is close, from the perspective of the ideas, to the method proposed by the same author (equations (1.9) – (1.16)). The method has been found to experience problems with convergence, raising some doubts on whether the said author actually achieved plausible results from the reservoir engineering point of view. The main conclusion of my work with respect to the fast-track saturation prediction and permeability estimation approaches is that one should exercise caution when using them, and that the approaches are not likely to work reliably in realistic settings.

The major part of the thesis is devoted to the implementation and testing of a seismic history matching workflow. The following aspects of the workflow are elaborated:

1. Application of CMA-ES optimisation algorithm, benchmarking with other stochastic black box optimisers. CMA-ES has almost[5] not been used for history matching, and from my results it can be reported that the algorithm has moderate performance in the HM setting.
2. Implementing the objective function using the correlations between the time-lapse seismic and the reservoir dynamic parameters. This approach adopts the ideas proposed e.g. in [6] for pressure and saturation inversion from the time-lapse seismic data. However, in my work no such inversion is performed, and the ideas are further developed for application in a seismic history matching setting. To my knowledge, such an approach has not been considered in the history matching literature. The proposed method is tested on a synthetic model, and is also applied to a North Sea field, where it shows the decrease of the model forecasts uncertainty compared to the conventional well history matching.

[5] The only two applications of CMA-ES for history matching which I found among the reservoir engineering papers are: a hybrid HM method which uses both EnKF and CMA-ES [93], and application of CMA-ES for optimising the kriging proxies in history matching of a carbonate reservoir [92]. In both cases the different aspects of CMA-ES, including its performance, are not addressed, and the papers essentially only report the fact of using this optimisation algorithm. A more extensive application of CMA-ES in reservoir engineering can be found for the problems of the well placement optimisation, see e.g. [94].

3. Implementing and testing an uncertainty estimation algorithm based on Monte-Carlo integration. The poor performance achieved here is a warning that one should exercise caution with the uncertainty estimation approaches which rely on exploration of the search space. A sensible performance is obtained for the RML uncertainty estimation method. The different ways of defining the covariance matrices in terms of the correlation ranges for the seismic errors are studied, and it is found that this aspect may greatly affect the uncertainty estimation. By this observation I emphasise that one should be careful at defining the error model.

The ideas and approaches briefly outlined in this introductory chapter are now to be discussed in the full-fledged fasion throughout the core Chapters 2 – 6 of the thesis, followed by recommendations for the future development given in Chapter 7.

Chapter 2 Fast-track waterflood forecasting

In this chapter I will consider a procedure for fast forecasting of the reservoir saturation based on the input maps of pressure and saturation, which are processed by the streamlines technique. The pressure and saturation maps required by the method in the practical setting can be obtained from time-lapse seismic, but in this chapter only the maps taken from the simulation models will be used. The procedure will be tested on a number of synthetic models of different complexity and the range of its applicability will be discussed. We will see that the method works reasonably well for 2D models, but lacks accuracy for 3D models because of the 3D flow effects.

2.1 Fast track predictions in a nutshell

One of the directions of quantitative 4D seismic interpretation is estimation of the underlying reservoir dynamic parameters – pressures and saturations. While this may be a useful monitoring tool *per se*, it also opens a possibility for making fast-track prediction of waterflood development, or, simply speaking, forecasting of the saturation fronts. I will consider this problem in the situation of thin reservoirs for which 4D seismic and the reservoir dynamic parameters (pressures, saturations) can be treated in a 2D map sense. The idea of fast-track saturation prediction is based on the streamline representation of the fluid flow in the reservoir. At every moment the fluids are moving along the paths defined by the streamlines, and for any streamline one can analyse the saturation front propagation along it. To do this, two consecutive saturation fronts can be considered, the front velocity is then estimated from them, and finally the front is propagated forward based on the inferred velocity, giving the saturation prediction in the future, see Figure 2.1.

To implement this idea, the assumption of steady-state pressure should be made, i.e. the reservoir pressure map is assumed to be constant (or subject to semi-steady state conditions) so that the direction of the streamlines and the flow velocities along them do not change. I will consider the input consisting of two saturation maps S_1, S_2 taken at time moments T_1, T_2 and one pressure map P_2 at the moment T_2. The third saturation S_3 at some future moment T_3 is the output of the method. The pressure steady-state assumption is quite strong and may be more appropriate for the reservoirs where

frequent seismic monitors are available, from which pressure and saturation maps could be estimated.

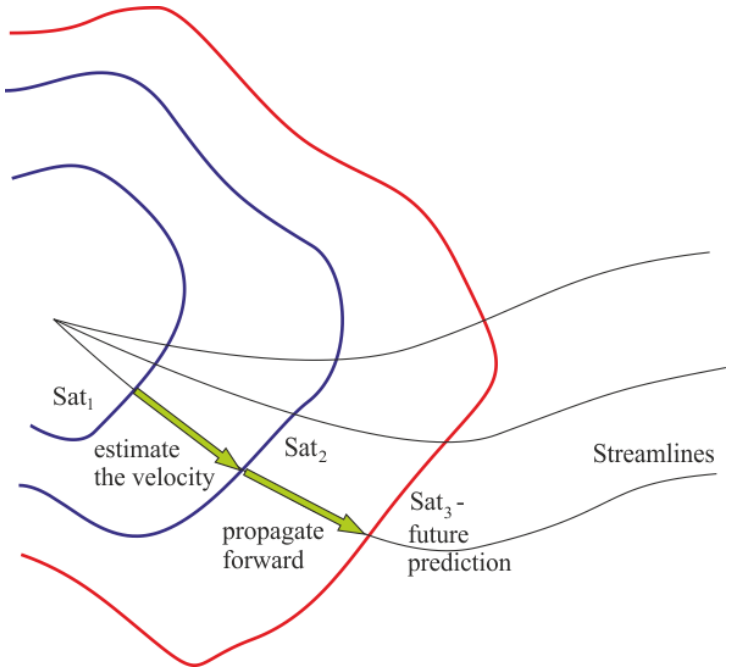

Figure 2.1 Idea of the fast-track saturation prediction. Sat_1, Sat_2 (blue contours) denote two historic saturation fronts, Sat_3 (red contour) denotes the predicted saturation front.

The input required by the method can be slightly reduced by taking the initial time T_1 to be the time of the reservoir production start, and using the initial saturation map as S_1. Numerical testing has shown however that this approach leads to some decrease of the forecasting quality. Apart from the dynamic maps, the method would require the map of $\varphi \cdot h \cdot NTG$ which is the pore volume per unit area. This map is needed to estimate the cross-sectional area of the stream tubes, cf. equation (2.3). In practice such a map can be estimated e.g. using the maps of amplitude-based seismic attributes calibrated to the data at well locations.

2.2 Streamline tracking

The first step of the procedure is calculation of the streamlines which can be done based on the input pressure map. The streamlines are tracked as the lines starting at some point on the map, which are tangential to the vectors of the fluid flow velocity at every point. Since the vector of fluid flow velocity is parallel to the pressure gradient (by virtue of Darcy's law), one essentially only needs the pressure map to calculate a streamline trajectory.

Addressing the question of the starting point of a streamline, it can be noted that only those streamlines are required which pass through the regions of some visible saturation change, because the subsequent estimation of the saturation front velocity is only feasible if there is a saturation change between times T_1 and T_2. So, the starting point for a streamline is any point on the map where the saturation difference $S_2 - S_1$ exceeds a predefined "visibility" threshold ε, where the value of ε can equal e.g. 0.01 (this value was found based on a few trial runs of the algorithm with different thresholds). In this way, all the streamlines for which the saturation front velocity can be inferred will be considered, whereas the other possible streamlines – which are useless for the method – are not calculated.

Given the starting point, the streamline is tracked in both directions by adding small line segments parallel to the pressure gradient, until it reaches a termination point. The termination of the streamline occurs once it hits an injection well (for upstream tracking), a production well (for downstream tracking), map boundary, or a local minimum/maximum on the pressure map. The minima and maxima points on the pressure map which are not associated with wells may occur because of the presence of noise. In the case of a pressure map inverted from 4D seismic, the noise results from both seismic noise and inaccuracies of the inversion procedure. In the case of pressure maps obtained by averaging the pressure cubes of a 3D simulation model the noise emerges because usually the 3D flow cannot be described by 2D flow mechanics, and the average pressure maps obtained in this way may exhibit "unphysical features" including local peaks or troughs. Whatever is the origin of the noise, it should be removed to acceptable levels by the input map smoothing before the streamlines can be tracked.

Since the pressure map is represented as a grid of pressure values attached to a mesh, and it is beneficial to be able to keep the elementary streamline segment below the mesh resolution, pressure interpolation between the mesh nodes is required. To do this interpolation, the rectangular shape functions were adopted. Interpolation on the rectangle [-1, 1] x [-1, 1] from the nodal values P_a corresponding to the rectangle's vertices has the form

$$P(x,y) = \sum_{a=1}^{4} N_a(x,y) P_a, \tag{2.1}$$

where the shape functions N_a are defined by

$$
\begin{aligned}
N_1(x,y) &= (1-x)(1-y)/4, \\
N_2(x,y) &= (1+x)(1-y)/4, \\
N_3(x,y) &= (1+x)(1+y)/4, \\
N_4(x,y) &= (1-x)(1+y)/4.
\end{aligned}
\tag{2.2}
$$

Each shape function equals 1 at its node, and equals 0 at the other three nodes, see the example in Figure 2.2. This interpolation is then transferred to an arbitrary mesh rectangle by a linear transform.

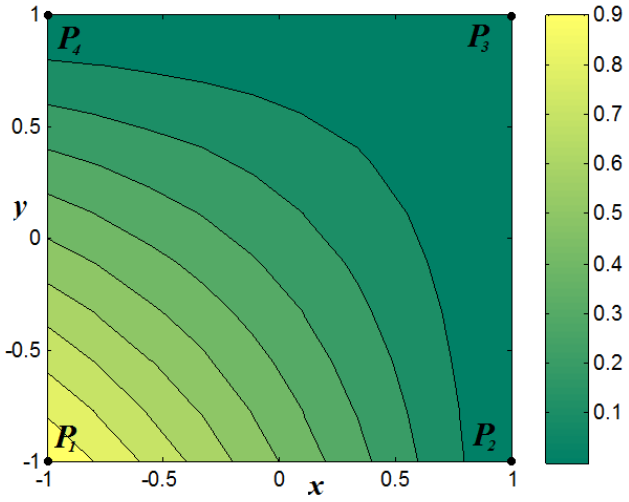

Figure 2.2 Plot of the shape function N_1. For each node of the rectangle the corresponding nodal value $P_1 - P_4$ is displayed.

One of the possible termination points for a streamline is the well location, which theoretically should coincide with the local minimum or maximum of pressure. Because of the pressure noise discussed above there may be some misalignment of the well position and the pressure peak. To treat this, a small neighbourhood around each well is surrounded by circles (for vertical wells) or ellipses (for horizontal wells) so that the well and the local pressure peak are completely contained within the ellipse. The streamlines are then terminated once they reach the ellipse boundary. Introduction of these regions around the wells also proves useful because the streamlines near the vertical wells converge to a single point. Calculation of some quantities like "distance between the streamlines" in the immediate well vicinity may lead to the computational problems, which are avoided if the well vicinities are not considered.

An example of streamline tracking is given in Figure 2.3, where the implemented method is compared with the streamlines from FrontSim[6] simulator. The model considered here is a 2D heterogeneous model with 5 wells which is referred to in the subsequent sections as "Model 2". The pressure map for the streamlines tracking was taken directly from the model without adding any noise.

A good agreement between the two streamline versions is seen, with the difference being due to lack of smoothness in the FrontSim streamlines, and different sets of starting points of the streamlines in FrontSim and my calculation.

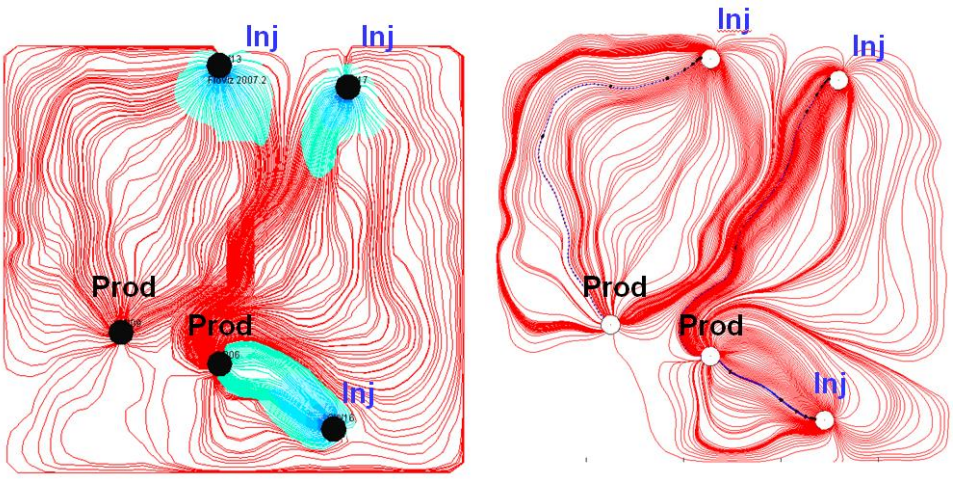

Figure 2.3 Picture of the streamlines for a 2D model, *left* – FrontSim (the blue color shows the water saturation front), *right* – the implemented method.

2.3 Inferring the flow velocity and propagating the saturation forward

To analyse the velocities of the flowing fluids, the streamline will be treated as a tube of variable cross-section, where one-dimensional fluid flow takes place. Assuming that the flow is incompressible, immiscible and involves two phases (oil and water), and also neglecting the capillary and gravity effects, the Buckley-Leverett equation can be considered:

[6] FrontSim (trademark of Schlumberger) is a recognised commercial streamline-based simulator, which is taken here for reference. The major difference of FrontSim with the method proposed here is that FrontSim performs simulation in 3D (not 2D), it implicitly solves the pressure equation (in my method the pressure map is an input), and FrontSim calculates flow velocities using pressure (in my method flow velocities are inferred from the saturation fronts).

$$v_{Sw} = \frac{q}{A\varphi}\frac{\partial f_w}{\partial S_w}\bigg|_{S_w}, \tag{2.3}$$

where q is the total flow rate along the tube, A is the cross-sectional area of the tube, φ is porosity, f_w is fractional flow of water which is a function of water saturation S_w and also depends on the phase relative permeabilities and fluid viscosities. This equation describes the velocity of movement of the given "saturation value" S_w along the streamline.

Due to the incompressibility assumption the total flow rate q is constant along the streamline. The other quantities which affect the saturation velocity are variable along the streamline, and two components can be formed from them: the one that relates to geometry U_r, and the other one that relates to the fractional flow U_0:

$$\begin{aligned} U_r &= \frac{1}{A\varphi}, \\ U_0 &= q\frac{\partial f_w}{\partial S_w}. \end{aligned} \tag{2.4}$$

Given that, the saturation velocity equals $v_{Sw} = U_r \cdot U_0$. This definition is consistent with the classical streamline equations that can be found elsewhere in the literature, see e.g. [55]. To show this, introduce the *time of flight* $\tau(x)$ which is the time it takes for a particle to travel to a specific position x along the streamline. Time of flight is one of the variables commonly used in the streamline equations. Given the definition of U_r, time of flight τ can be found by integration of the reciprocal flow velocity:

$$\tau = \int_0^x \frac{dl}{qU_r(l)}. \tag{2.5}$$

Next, calculate the derivative of the fractional flow with respect to time of flight by the chain rule

$$\frac{\partial f_w}{\partial \tau} = \frac{\partial f_w}{\partial S_w}\cdot\frac{\partial S_w}{\partial x}\cdot\frac{\partial x}{\partial \tau} = \frac{U_0}{q}\cdot\frac{\partial S_w}{\partial x}\cdot qU_r = U_0U_r\frac{\partial S_w}{\partial x}, \tag{2.6}$$

where the substitutions after the second equality sign are made by virtue of definitions (2.4), (2.5). To express the velocity of propagation of some fixed saturation value S_w, consider that it passed the distance *dx* over time *dt*. During this movement the value of saturation itself did not change, and the whole differential of S_w can be equated to zero:

$$dS_w = \frac{\partial S_w}{\partial t} dt + \frac{\partial S_w}{\partial x} dx = 0. \tag{2.7}$$

Dividing this equation by *dt*, and noting that the saturation velocity is *dx*/*dt*, one arrives at

$$\frac{\partial S_w}{\partial t} + \frac{\partial S_w}{\partial x} v_{Sw} = 0. \tag{2.8}$$

On the other hand, using the adopted definition of v_{Sw}, it can be written

$$\frac{\partial S_w}{\partial t} + \frac{\partial S_w}{\partial x} U_0 U_r = 0. \tag{2.9}$$

Finally, applying (2.6), the well-known equation describing the fluid transfer along the streamline in terms of time *t* and time of flight τ is obtained

$$\frac{\partial S_w}{\partial t} + \frac{\partial f_w}{\partial \tau} = 0. \tag{2.10}$$

Now let us turn to the estimation of U_r, U_0 and the other quantities involved. The cross-sectional area of the tube *A*(*x*) depends on the position along the line *x* and is expressed as $A = NTG \cdot h \cdot w$. Here *h* is the gross thickness of the reservoir, and the factor $NTG \cdot h$ (effective reservoir thickness) can be regarded as the vertical thickness of the tube. The factor *w* is the horizontal thickness of the tube and is estimated by tracking a neighbour streamline close to the original one and finding the distance between the two along the whole length, see Figure 2.4. The quantity *w* calculated in this was is only defined up to a constant factor (multiplier), however this will not affect the subsequent discourse.

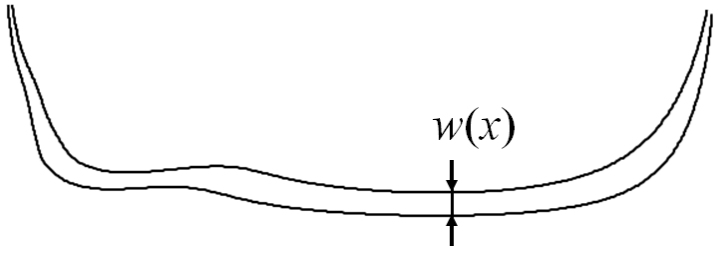

Figure 2.4 Concept of the horizontal thickness of a tube.

$U_r(x)$ accounts only for the effective reservoir thickness, porosity, and the geometrical spread of the streamlines. It will also be referred to as the *relative flow velocity*. This quantity depends on the position along the streamline *x*, but does not depend on

saturation S_w. The absolute flow velocity at each point of the streamline is equal to $q \cdot U_r$, and this fact was already used in equation (2.5). The term $U_0(S_w)$ accounts for the relative movement of the two phases within the total flow, and will be termed the *relative saturation velocity*. It depends on saturation, but does not explicitly depend on the position along the streamline *x*. To estimate U_0, consider two consecutive saturation profiles along the streamline Sat_1, Sat_2 which are found from the inupt saturation maps S_1, S_2.

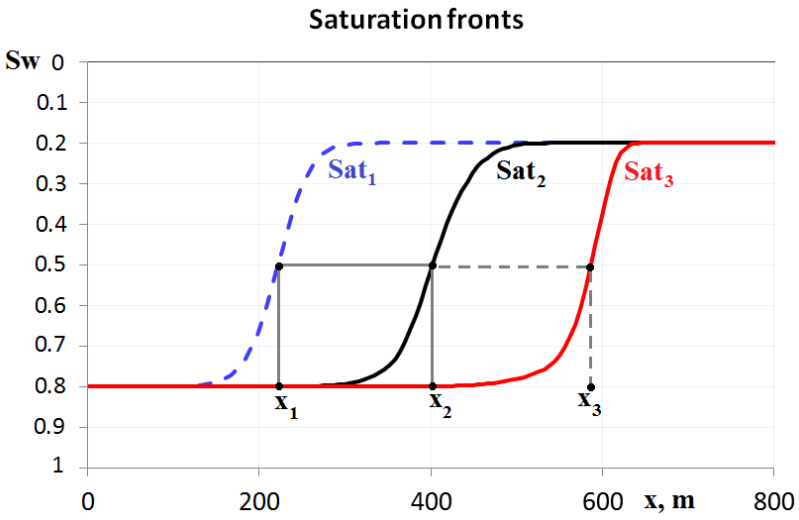

Figure 2.5 Water saturation profiles along the streamline: Sat_1 and Sat_2 are the input to infer the flow velocity, Sat_3 is the future prediction. *X axis* is the distance along the streamline.

Taking an arbitrary saturation point S_w on the profile Sat_2 at position x_2, one can find its position on profile Sat_1, which is denoted by x_1, see Figure 2.5. Then, integrate the reciprocal velocity v_{Sw}^{-1} (i.e. slowness) of saturation S_w between x_1 and x_2, finding the total travel time of S_w between the two positions, as shown by (2.11). Since this travel time is just the time lag between the consecutive saturation maps, which is known, $U_0(S_w)$ can be calculated from this formula. The procedure is then repeated for all points along the streamline where displacement of the saturation profile can be picked.

$$T_2 - T_1 = \Delta T_1 = \int_{x_1}^{x_2} \frac{dx}{U_r(x) \cdot U_0(x_2)} \tag{2.11}$$

An example of velocity analysis for a single streamline from a 2D heterogeneous synthetic model with two wells (producer and injector) is shown in Figure 2.6. The saturation fronts for this streamline are those shown in Figure 2.5.

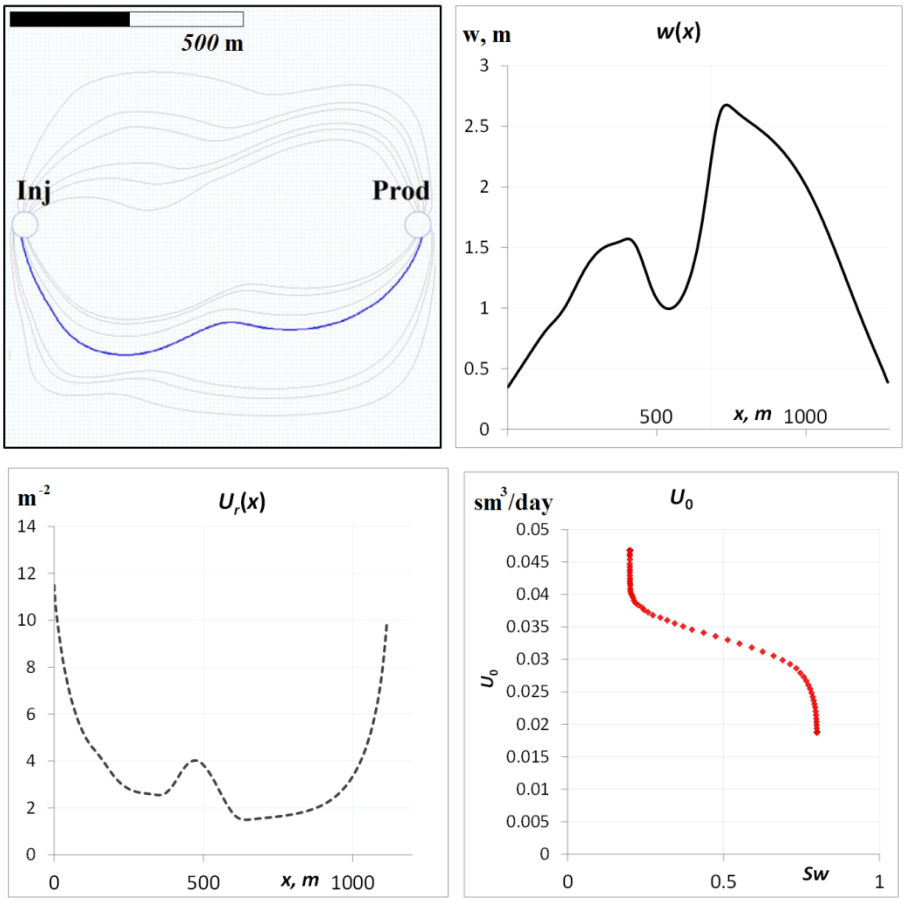

Figure 2.6 Velocity analysis for a streamline. *Top left*: some selected streamlines between the two wells, the streamline under consideration is highlighted with blue colour. *Top right*: horizontal thickness of the tube, *bottom left*: relative flow velocity, *bottom right*: relative saturation velocity.

Once both the relative flow velocity and relative saturation velocity have been estimated, the saturation value S_w can be propagated forward, making the time step $\Delta T_2 = T_3 - T_2$. To do this, an expression similar to (2.11) is written for another time interval, which allows us to find the new position x_3 of saturation S_w from the following equation:

$$\Delta T_2 = \int_{x_2}^{x_3} \frac{dl}{U_r(l) \cdot U_0(x_2)}. \tag{2.12}$$

The forward propagation is then repeated for all saturation values on the profile Sat_2 for which the estimation of velocity U_0 was successful. This step is performed under

assumption that the flow velocities found do not change with time, which is the case if the streamlines and their associated flow rates are constant.

After moving the saturation fronts for all the streamlines a new saturation map S_3^* can be formed from the predicted profiles. In situations where the exact saturation S_3 at time T_3 is known, e.g. from the simulator output, it can be compared with the estimated saturation map to assess the quality of prediction. To do this in a quantitative manner, introduce the following measure of the prediction quality, referred to as *normalised error*:

$$E = \frac{\int | S_3^* - S_3 | \, dxdy}{\int | S_3 - S_2 | \, dxdy}. \tag{2.13}$$

Obviously, the normalised error E equals 0 when prediction is exact, and it equals 1 when no prediction is made, i.e. the new saturation is taken from the previous step: $S_3^* = S_2$. Since the predicted saturation map can contain arbitrarily high errors, the normalised error can become higher than 1.

2.4 Testing the procedure on synthetic models

A number of synthetic models were considered to check the algorithm of fast-track saturation prediction described above. The models range in heterogeneity and complexity as follows:

Model 1 – a very simple 2D homogeneous model with two wells, which is a quarter of the 5-spot well pattern element.

Model 2 – 2D heterogeneous model with 2 producers and 3 injectors (the streamlines for this model are shown in Figure 2.3).

Model 3 – 3D heterogeneous model with 1 producer and 2 injectors, which has channelised fluvial geology.

Model 4 – 3D heterogeneous model which is a segment of Schiehallion field simulation model (this field will be discussed in detail in Chapter 6). The well schedule of the original model was adjusted for this exercise to meet the steady-state pressure assumptions of the saturation prediction algorithm.

To test the procedure more thoroughly, for each of the models I considered different degrees of grid refinement, and different time intervals between the input and the estimated saturation maps $S_1 - S_3^*$. All the input maps required by the method – i.e. pressure, saturations, porosity, NTG and thickness – were obtained by averaging the corresponding 3D properties of the models. An example of the saturation front propagation for Models 1 and 2 is given in Figure 2.7 and Figure 2.8, where the estimated future prediction can be compared with the exact prediction from the simulator. As can be seen, the prediction is quite accurate for the very simple Model 1, with the normalised error E = 0.055, despite the fact that the prediction time step ΔT_2 = 4600 days is notably longer than the analysis time step $\Delta T_1 = 870$ days.

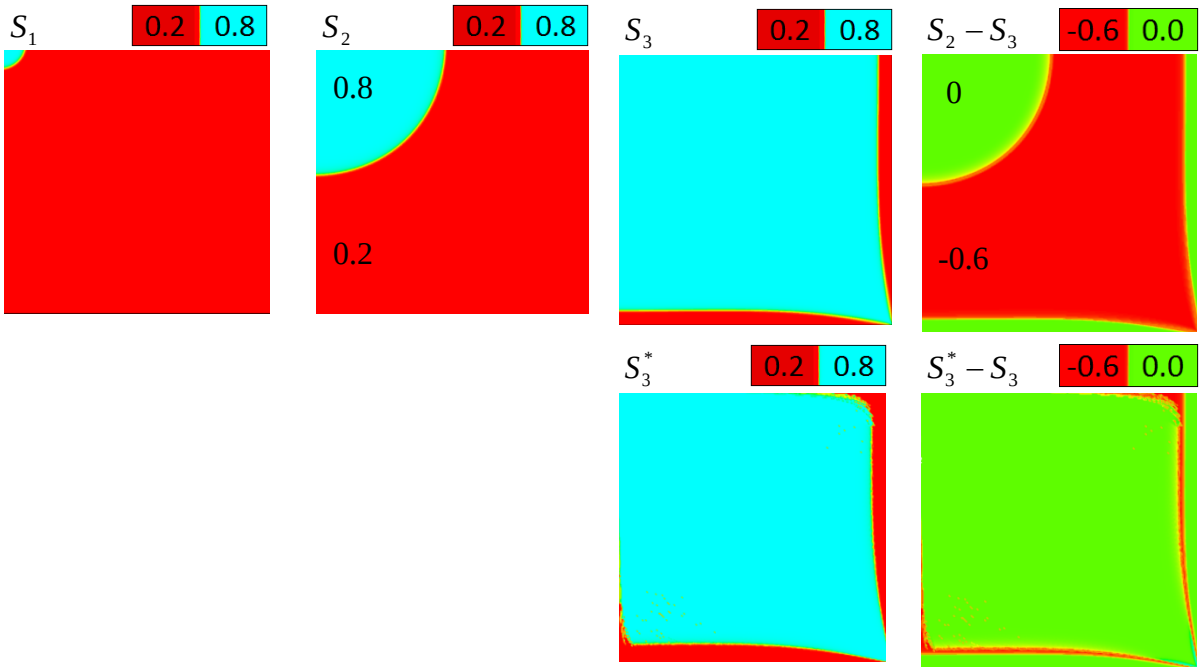

Figure 2.7 Saturation prediction for Model 1. *Top, left to right*: input water saturation maps S_1, S_2, exact future map S_3, difference $S_2 - S_3$. *Bottom, left to right*: estimated future map S_3^*, and its difference with the exact one S_3. Time steps are $\Delta T_1 = 870$ days, $\Delta T_2 = 4600$ days. Normalised error = 0.055. The numbers on the maps show the map values for the given colours. The colours in column 4 are different from columns 1 – 3.

For Model 2 (Figure 2.8), where the flow pattern is more complex, more errors emerge, leading to E = 0.474. The pressure maps P_1 (not used as input) and P_2 (used as input) are provided in the same figure, and it can be seen that the semi-steady state conditions hold for pressure, with the average reservoir pressure gradually increasing. The

normalised error of the saturation prediction is rather high despite the fact that the input maps were provided by the exact 2D flow equations. The factors which contribute to the errors here are the following (refer to Figure 2.9 for the illustration).

First, some streamlines may intersect the saturation fronts at small angles, which leads to smearing of the saturation front when it is mapped onto the streamline. The most favourable situation in this respect is when the streamline goes perpendicular to the front. If it becomes nearly tangential, then all the inaccuracies existing in the front due to numerical or other reasons will be magnified during projection to the streamline. This will in turn adversely affect the velocity analysis.

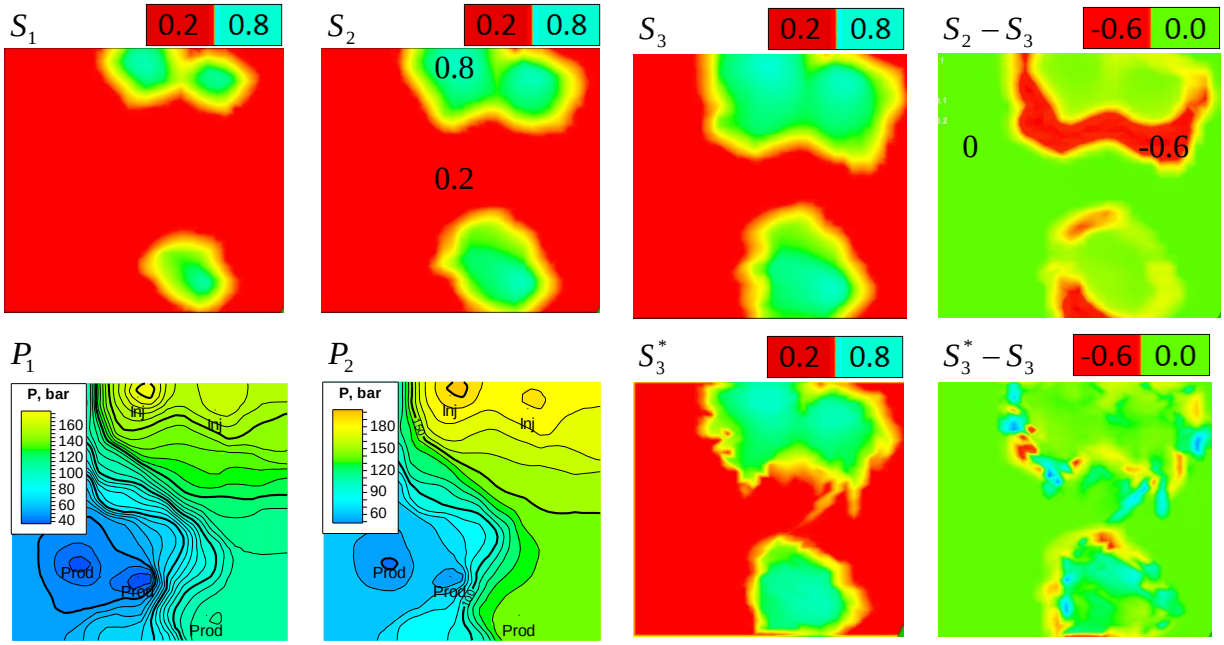

Figure 2.8 Saturation prediction for Model 2. *Top, left to right*: input water saturation maps S_1, S_2, exact future map S_3, difference $S_2 - S_3$. *Bottom, left to right*: pressure maps P_1, P_2, estimated future saturation map S_3^*, and its difference with the exact one S_3. Time steps are $\Delta T_1 = 184$ days, $\Delta T_2 = 181$ days. Normalised error = 0.474. The numbers on the maps show the map values for the given colours. The colours in column 4 are different from columns 1 – 3.

Second, the actual fluid flow may occur in the direction transverse to the streamline. This situation is recognised in the literature, see e.g. [55] where a streamline simulation approach with a correction to transverse fluxes is introduced. Transverse fluxes take place whenever the flow steady-state conditions are violated, so that the "frozen" streamlines do not capture all the fluid movement involved. This may happen for instance if the reservoir pressure changes due to the changes of the well controls, or as a

result of the areal fluid mobility change as the saturation front moves forward. The latter phenomenon will take place almost in every reservoir encountered in practice, so the true steady-state flow is hardly attainable. One more reason of the transverse saturation movement is the numerical dispersion which occurs in the finite difference reservoir simulator used for generating the input maps.

An illustration of the transverse flows is given in Figure 2.9, with their locations indicated by the arrows. This figure shows the same Model 2, although for the time moments different from those in Figure 2.8. For the sake of clarity, only one streamline is displayed here, and for the complete streamlines picture see Figure 2.3. In this work I attempted to preserve the steady-state flow conditions as closely as possible, so the most prominent transverse flow cases were associated with the streamlines which pass close to the no-flow boundary. This may be a real no-flow boundary, e.g. the grid boundary, or imaginary one, where two bundles of streamlines originating from different injectors come into contact, which is the case for the streamline plotted in Figure 2.9. In this situation the leading source of the transverse flow is deemed to be the numerical dispersion.

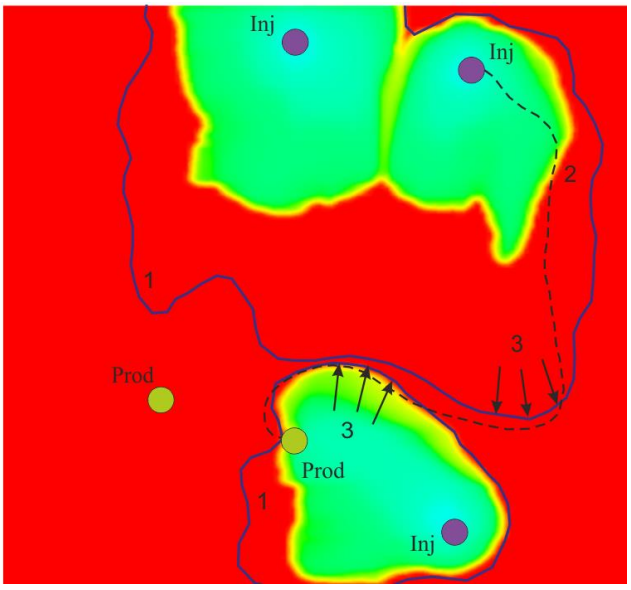

Figure 2.9 Sources of error in saturation prediction. The coloured map shows the saturation S_2 at time T_2. The blue contours (**1**) are the exact saturation front at time T_3. The *dotted* streamline intersects the saturation S_2 at a small angle (**2**). Direction of the front movement transverse to the streamline is shown by the arrows (**3**).

Waterflood prediction testing for the complex 3D models revealed even higher errors. The input pressure and saturation maps for these models were obtained by vertical averaging of the 3D property grids. Since the *average pressure* and *saturation maps* do not follow exactly the physics of the 2D fluid flow used by the algorithm, these maps can be regarded as a *sum* of the exact maps from some effective 2D fluid flow *plus* some noise. By the effective 2D flow I mean a 2D flow giving the pressure and saturation maps that are as close as possible to the corresponding average maps from the 3D flow, over a range of time steps. The discrepancy between the 3D flow and the effective 2D flow increases if there is substantial vertical fluid movement in the 3D model, or the fluid flow in different layers occurs in the different directions. The discrepancy, or *noise*, "generated" in this way for the models of realistic 3D complexity turned out to be critical for the prediction quality, making it notably degrade.

Among the noisy input maps provided by the 3D models, the most essential one is the pressure map since it defines the trajectories of the streamlines. A noisy pressure map will almost certainly contain numerous local minima and maxima not associated with the wells. Considering the example of Model 3, the average pressure map with numerous local peaks is shown in Figure 2.10, *top left map*. If the streamlines are tracked with such a map, they will be too short, terminating at these local peaks and troughs (*top middle map* on the figure). As a consequence, it will not be possible to make a reliable velocity analysis and further saturation propagation. For Model 3 the usage of the rough pressure map resulted in the normalised error of prediction equal to 0.90. The corresponding saturation estimate S_3^* is shown in the *bottom middle map* on the figure. As can be seen, the true saturation front propagation (marked by the black dotted line) was notably underestimated, as the saturation map S_3^* is essentially equal to the map from the previous step S_2.

To ensure that the streamlines are long enough, the pressure noise should be removed, which is achieved in the most straightforward way by the map smoothing. Depending on the original noise level quite a high degree of smoothing may be required, which may in turn shift the streamlines, again leading to prediction errors. The map smoothing applied to the "noisy" average pressure of Model 3 resulted in the streamlines shown in the *top right map* on the figure (the smoothed pressure map can be found in Figure 2.11, *middle*). The streamlines became long and continuous, which does not mean however that they capture the underlying fluid flow correctly. The

resulting predicted saturation is shown in the *bottom right map*, and the associated normalised error is 0.62, which is also quite large.

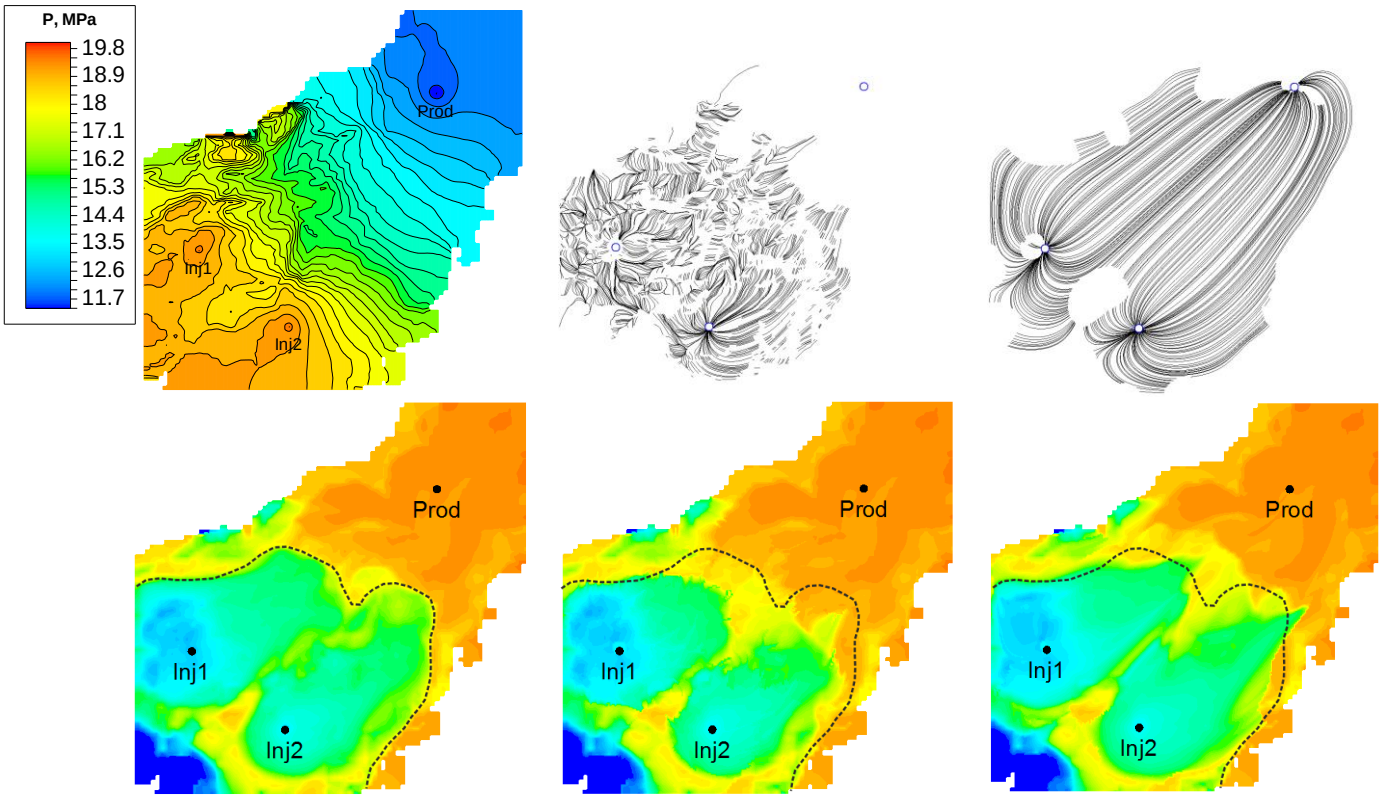

Figure 2.10 Saturation forecasting for Model 3. *Top, left to right*: average pressure map from the 3D simulation model, streamlines tracked using this map, streamlines tracked using a smoothed pressure map. *Bottom, left to right*: exact S_3, prediction with the rough pressure, prediction with the smoothed pressure. The dotted contours show the position of the exact saturation front (picked from exact S_3).

It is worth mentioning that a pressure map has local peaks and troughs at the well locations, and these features will be affected by the ordinary smoothing algorithms, resulting in the amplitude decrease of the peaks, and also in the lateral shift of those peaks which have skewed (non-symmetrical) shape. To avoid both these effects, a smoothing algorithm was implemented which performs *diffusion* of the input pressure map by solving the diffusivity equation. The diffusion starts with the initial map equal to the input noisy map. It applies the "no-flow" conditions at the grid boundaries, and constant value conditions at the wells. Thus, the diffused map becomes smoother between the wells, and the original peaks existing at the well locations are preserved. The degree of smoothing is controlled by the time the diffusion takes place; this parameter is set by the user. The larger diffusion times result in more smooth diffused maps. The example of the algorithm's application to the input pressure from Figure

2.10 is shown in Figure 2.11 (*middle*), where we can observe that the local peaks at the wells are preserved. For comparison, the simple map smoothing performed in Petrel[7] software shown in the same figure (*right*) has removed the peaks from the wells, so the map does not look like the pressure map related to the wells.

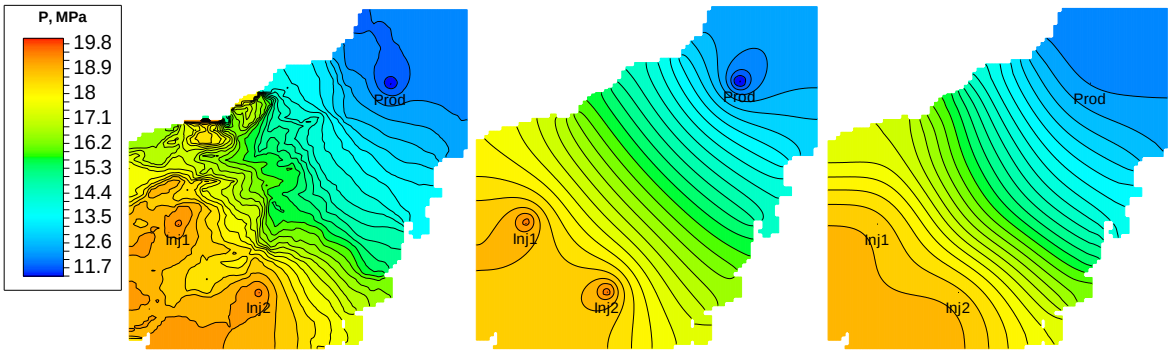

Figure 2.11 Pressure map smoothing. *Left*: the input pressure (same as in Figure 2.10, top left), *middle*: pressure smoothed by diffusion (corresponds to the streamlines in Figure 2.10, top right), *right*: pressure smoothed by the Petrel map smoother.

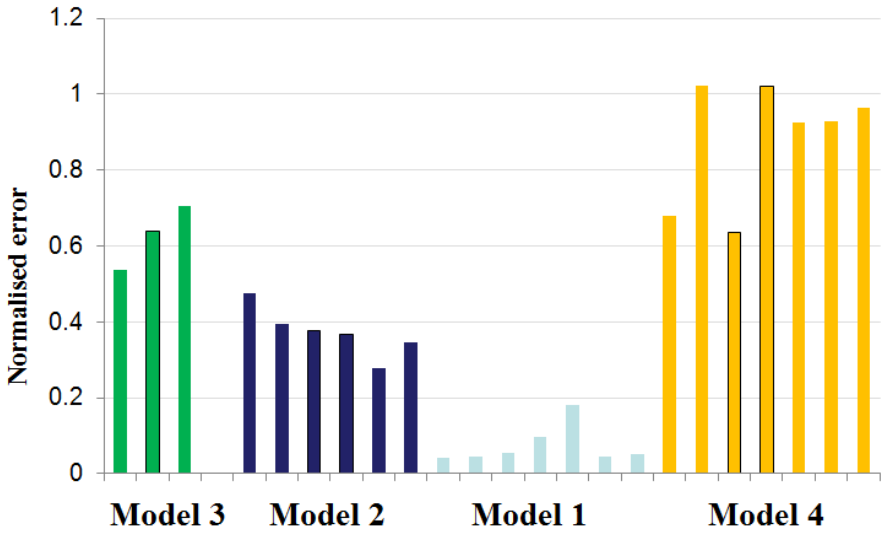

Figure 2.12 Normalised errors for the considered four models. For each model the results for different grid refinement and different time intervals are displayed.

The summary of the normalised errors of predictions for all the models considered is shown in Figure 2.12. As can be seen, the errors are small to moderate for the two-dimensional Models 1, 2, and significant for the three-dimensional Models 3, 4. For each model I considered different cases of (1) grid refinement and (2) the length of the

[7] Schlumberger trademark.

time steps $\Delta T_1, \Delta T_2$. However, no particular dependence of the normalised error on any of these two parameters was observed. So, the main factor controlling the forecast quality is the *noise* which may result from different sources, including the 3D complexity of the fluid flow; non-repeatability noise existing in the 4D seismic; and errors in the seismic-to-pressure-and-saturation inversion procedure.

2.5 Summary and discussion

An algorithm of the fast map-based saturation forecasting was proposed, which employs the principles of the streamlines flow representation. The associated technical issues were discussed, namely how the streamlines are calculated, how the flow velocities along them are analysed, and how the saturation fronts are moved forward. The method was tested on a range of models of different complexity and was shown to work reasonably well for the input maps of pressure and saturation provided by the relatively simple 2D simulation models. However for the average maps obtained from more complex 3D models[8] the prediction errors appear to be quite high. This results from the high sensitivity of the proposed procedure to the input noise, and the fact that the procedure essentially relies on the 2D fluid flow dynamics, and perceives the dynamic property maps obtained from a 3D model as being noisy. In the situation of inverting the pressure and saturation maps from the 4D seismic attributes I would expect even higher levels of noise coming both from the seismic noise and inaccuracies of the inversion procedure. (E.g. for the North Sea field considered in Chapter 6 the 4D noise to 4D signal ratio is estimated to be around 80%). This means that the considered prediction procedure is hardly applicable for the present day input which can be provided by the 4D seismic.

One way of removing the input noise is smoothing the pressure and saturation maps, however this leads to losing the information content of these maps which also adversely affects the prediction quality. E.g. smoothing a rough pressure map leads to more continuous and longer streamlines, which is favourable for velocity analysis and saturation front propagation. But at the same time these streamlines divert from the

[8] Here, the distinction between the 2D and 3D models is made in the fluid flow sense (absence or presence of the vertical flows, or flows in different directions in the different layers), rather than in the seismic sense (smaller or larger reservoir thickness affecting the seismic resolution of different layers in the reservoir).

actual flow paths existing in the reservoir, and approach the streamlines picture which might be produced by the flow simulation with a homogeneous permeability map. An open question remains as to what degree of smoothing should be applied. For the considered synthetic models different degrees of map smoothing were examined, and it was established that in each case an optimal smoothing can be found for which the normalised error is minimal. However no general guidelines could be formulated from these observations on how the optimal degree of smoothing could be estimated in advance. The information content of the pressure maps will be discussed in more detail in the next chapter, where it will be shown that the *features* of the pressure maps which are most critical from the point of view of streamlines calculation and permeability estimation *are subtle* and easily become contaminated by noise. This means that a noisy pressure map which can be estimated from the time-lapse seismic will almost certainly be not suitable for the streamline tracking.

The assumption of the steady-state flow conditions reduces the flexibility of the method as well, since for example the prediction cannot be properly done in the situation of the changing well controls. To address this situation one would need to consider the problem of producing fast estimates of a pressure map based on the well controls, so that the saturations could then be propagated forward using the updated pressures, which would increase the method applicability. The 2D pressure map calculation could be performed by solving the diffusivity equation if an estimate of the reservoir permeability map was available. This finally leads us to the subject of the next chapter where a number of ways of fast permeability estimation are discussed.

2.6 List of codes

For the studies described in this chapter the following programs were coded:

1. **Saturation prediction code**. The program works with the input maps of pressure, saturation, and $\varphi \cdot h \cdot NTG$ exported from Petrel. The other input are the time steps and the elliptic boundaries around the wells. The output is the predicted saturation map, the streamlines map, and the estimated velocities along each streamline.

   Coding language: Matlab, C++.

2. **Map smoothing by diffusion**. The program takes the input map, the elliptic boundaries around the wells and the diffusion time. The smoothed map is the output.

   Coding language: C++.

Chapter 3 Fast-track permeability estimation

In this chapter I will consider fast-track methods for permeability estimation based on pressure and saturation maps. As in the previous chapter I assume that the pressure and saturation maps employed by the methods can be inverted from the time-lapse seismic attributes. However, only the maps obtained directly from the synthetic simulation models will be used for testing purposes. While permeability map or grid could be estimated by history matching using the observed well data, 4D seismic data (or grid pressures and saturations), this procedure would require substantial computing and time resources. The suggested fast-track methods are less CPU-demanding as they typically solve a simpler system of equations. Performance of the methods will be tested on the synthetic models, and their limitations – in particular, high sensitivity to the input noise – will be discussed. The information content of pressure maps will also be examined.

3.1 Method #1, estimation of permeability using pressure and saturation maps

This method of permeability estimation is based on analysis of pressure and saturation profiles along the streamlines, and is the natural extension of the ideas discussed in the previous chapter. Equation (2.3) from Chapter 2 describes the saturation propagation velocity along a streamline as a product of the *relative flow velocity* $U_r(x) = (A\varphi)^{-1}$ which accounts for the variable "cross-sectional area" of the streamline, and the *relative saturation velocity* $U_0(S_w)$ which accounts for the movement of the saturation values relative to the total flow velocity. The latter quantity can be expressed via the total flow rate for the given streamline q and the derivative of the fractional flow with respect to saturation:

$$U_0(S_w) = q \cdot \frac{\partial f_w}{\partial S_w}(S_w) \tag{3.1}$$

In the absence of capillary and gravity forces the fractional flow can be determined from the phase relative permeabilities and fluid viscosities μ_o, μ_w. The phase relative permeabilities will be assumed unknown. Even if the relative permeability measurements from core are available, fluid flow in the reservoir simulation model (especially a two-dimensional one) takes place at the scale quite different from the scale of core. Hence, this flow is controlled by the *effective* relative permeabilities that are

unknown in advance. To handle the uncertain relative permeabilities, I adopt Corey parameterisation (see Appendix C, equation (C.1)), which results in the following expression for the fractional flow:

$$f_w = \left(1 + \frac{\mu_w}{\mu_o \cdot k_{rw0}} \cdot \frac{(1-S)^{No}}{S^{Nw}}\right)^{-1}. \tag{3.2}$$

As described in Chapter 2, the curve of velocity U_0 along the streamline can be inferred from the two consecutive saturation profiles. The same curve can also be analytically expressed as a function of parameters $q, S_{wcr}, S_{orw}, k_{rw0}, N_w, N_o$ by virtue of equations (3.1), (3.2). This allows us to perform a regression by adjusting the said parameters so that the analytical U_0 matches the original estimate from the streamline. While doing this, I provide the ranges for the Corey parameters to vary within. Alternatively, some parameters can just be kept fixed if they are known with reasonable accuracy. The regression is performed by an optimisation algorithm, e.g. CMA-ES (see Appendix B). The objective function (3.3) to be minimised takes the integral along the streamline of the squared difference between the analytical velocity and the estimated one U_0

$$f = w_1 \cdot E_1 \equiv w_1 \cdot \int \left(q \frac{\partial f_w}{\partial S_w}(S_w) - U_0(S_w) \right)^2 dS_w. \tag{3.3}$$

In this expression w_1 is a weight provided for flexibility, as more terms with their respective weights will be added to the objective function f in the text below. The estimate of the saturation velocity U_0 using the fractional flow derivative (3.1) is only applicable for the situation of smeared saturation fronts, e.g. in the case of high viscosity oils. In the typical case of light oils the large water saturation values move more rapidly than the small saturations, and a shock front in the saturation profile develops leading to the piston-like displacement. To treat this properly in estimating the analytical velocity U_0, the equation (3.3) is slightly amended to include the Rankine-Hugoniot conditions for the sharp saturation front which are based on the material balance across the front. The Rankine-Hugoniot conditions essentially replace (2.3) by $v_{Sw} = q \cdot (A\varphi)^{-1} \cdot (f_{w,L} - f_{w,R}) \cdot (S_{w,L} - S_{w,R})^{-1}$, where the fractional flows f_w and saturations S_w with subindices "*R*" correspond to the conditions ahead of front, and those with "*L*" correspond to the conditions behind the front. In particular, equation (3.5) below is obtained from the Rankine-Hugoniot front velocity.

The main goal of the regression is to estimate the total flow rate along the streamline *q*. It should be noted that rigorously speaking a streamline has no cross-sectional area, and the quantity *A*(*x*) used in definition of U_r can be defined up to a constant multiplier, resulting in that the flow rate *q* is also defined up to the same multiplier. This degree of freedom will not, however, affect the further ideas.

After estimation of *q* the absolute permeability can be found along the streamline using Darcy's law:

$$k = \frac{q\varphi U_r}{\left(\frac{k_{ro}}{\mu_o} + \frac{k_{rw}}{\mu_w}\right)\nabla P}, \tag{3.4}$$

where the relative phase permeabilities k_{ro}, k_{rw} are those already estimated by regression, ∇P is the pressure gradient along the streamline. Note that this formula only uses the first pressure derivatives. Unlike the saturation forecasting approach from Chapter 2 which only used the lumped map of $\varphi \cdot h \cdot NTG$, formula (3.4) also requires a separate map of porosity φ. Calculation of the flow rate *q* and the subsequent calculation of permeability *k* is performed independently for each streamline.

A problem was found when applying this approach for a situation of sharp saturation front. In such conditions the saturation front velocity

$$v_{Sw} = q \cdot (A\varphi)^{-1} \cdot (1 - S_{wcr} - S_{orw})^{-1} \tag{3.5}$$

does not depend on k_{rw0}, so the fluid mobility cannot be estimated from the observed front velocity. At the same time the difference of the fluid mobility at both sides of the saturation front affects the pressure gradient, so that straightforward application of (3.4) with incorrect k_{rw0} will result in a wrong estimation of the absolute permeability k, which will exhibit a step-like feature.

To fix this issue, a regularisation is introduced, which forces the permeability to change linearly across the saturation front. Thus a sharp step-like permeability change is avoided and the end point relative permeability k_{rw0} is estimated reasonably well. To do the regularisation, firstly for the given streamline detect the position of the sharp saturation front by taking the derivative of S_w and checking its value versus the predefined threshold ε. The area with $|\partial S_w / \partial x| > \varepsilon$ is regarded as the saturation front.

Then make a step away from the front at distance L_1, and consider two windows of width L_2 on both sides, see Figure 3.1. Within these windows a linear regression is performed for the points of the estimated permeability profile *k*. If permeability follows the same linear trend on both sides of the saturation front, it can be regarded as a plausible one, and this situation is indicated by the values of the coefficient of determination R^2 close to 1. Thus, the regularisation is implemented by adding the second term to the objective function (3.3):

$$f = w_1 \cdot E_1 + w_2 \cdot E_2 \equiv w_1 \cdot E_1 + w_2 \cdot (1 - R^2). \tag{3.6}$$

The values of the threshold and window parameters can be selected e.g. as follows: $\varepsilon = 0.02, L_1 = 20\,\text{m}, L_2 = 70\,\text{m}$ for the mesh cell size 15 m x 15 m, as was revealed from the numerical testing. Finally, by applying the algorithm to the simple synthetic models it was found that some simple prior information on permeability may favourably affect the estimation results. The prior data I use here is the mean value of the permeability logarithm μ and the standard deviation σ which are supplied to the objective function by

$$f = w_1 \cdot E_1 + w_2 \cdot E_2 + w_3 \cdot E_3 \equiv w_1 \cdot E_1 + w_2 \cdot E_2 + w_3 \cdot \frac{(\ln(\bar{k}) - \mu)^2}{2\sigma^2}, \tag{3.7}$$

where $\bar{k}$ is the mean estimated permeability along the streamline. The logarithm of permeability is used here, since it typically has normal distribution for petroleum reservoirs. The likely values for weights $w_1 - w_3$ which can be used are $w_1 = 25$, $w_2 = 1000, w_3 = 1$ (these are the weights used for the synthetic model shown in Figure 3.2).

The described procedure of permeability estimation was tested on a number of models, both 2D and 3D. In Figure 3.2 the results are reported for the 2D heterogeneous model which is referred to as Model 2 in Chapter 2. For this example I used the exact maps of pressure, saturation, porosity, *NTG* and thickness, without adding any noise.

As can be seen, in general all the permeability features are picked up by the method. One of the most notable mismatches are the areas with overestimated permeability near the wells. These erroneous values seeded in the parts of the streamlines close to the saturation fronts, where the velocities were estimated, and then propagated towards the wells, being amplified by the streamlines convergence at the wells. The sources of errors remain the same as were discussed in Chapter 2: the streamlines crossing the

saturation fronts at small angles, and movement of the saturation fronts transverse to the streamlines (the latter can be regarded as the extreme version of the former).

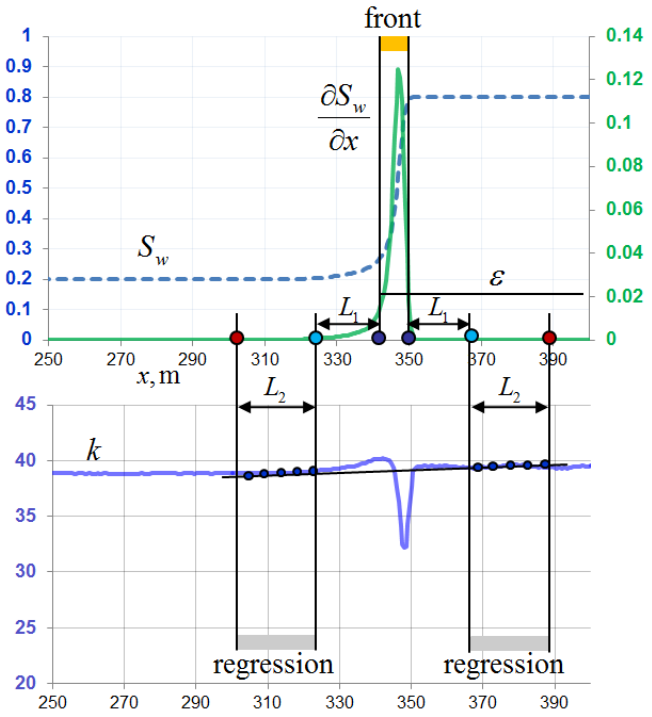

Figure 3.1 Regularisation for removing the permeability step across the sharp saturation front. *Top*: plot of saturation (*blue dotted line*) and its derivative (*green line*) vs. distance *x*. *Bottom*: calculated absolute permeability. The windows "L_2" used for regression are marked by the vertical lines.

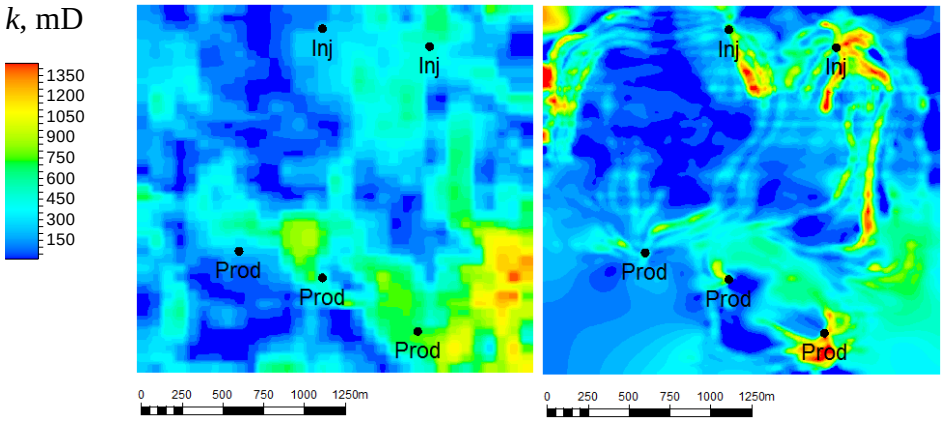

Figure 3.2 Permeability estimation for Model 2 by method #1. *Left*: exact underlying permeability, *right*: the estimate.

It can be also noted that some areas on the estimated permeability map are left blank. The streamlines covering these areas either did not cross the regions of saturation change to be able to assess the velocities, or the velocity analysis failed for them for some other reasons, e.g. because of the transverse flows.

Results of the method application to a 3D model are shown in Figure 3.3, where Model 3 from Chapter 2 is considered. Since the model is characterised by a complex 3D flow, direct application of the average maps for input does not allow tracking the streamlines of sufficient length, and hence the map smoothing is required. But even for the smoothed maps the results looks quite erroneous. Certainly, the estimated 2D permeability (right map on the figure) is not expected to reproduce the averaged 3D permeability (left map on the figure). Instead, the estimated 2D permeability should correspond to the effective 2D flow, and as such may be, for example, smoother than the averaged 3D permeability, and may also have a different mean value. The left hand side permeability map in Figure 3.3 was obtained by arithmetic averaging which is only rigorous for horizontal flow, and it gives the upper estimate for the effective 2D permeability map. The lower estimate for the effective 2D permeability might be given by harmonic averaging, corresponding to the vertical flow, however for the given model the harmonic average would equal zero almost everywhere due to the presence of numerous non-permeable shale interlayers.

We can also see that the estimated permeability map does not look geological: there are high permeable local features near the injectors (to the south); the zones close to the injectors (to the north) seem to have underestimated the permeability. Finally, there are two distinct high permeability stripes entering the producer, obviously associated with the streamlines having an erroneous velocity estimate and geometrical convergence.

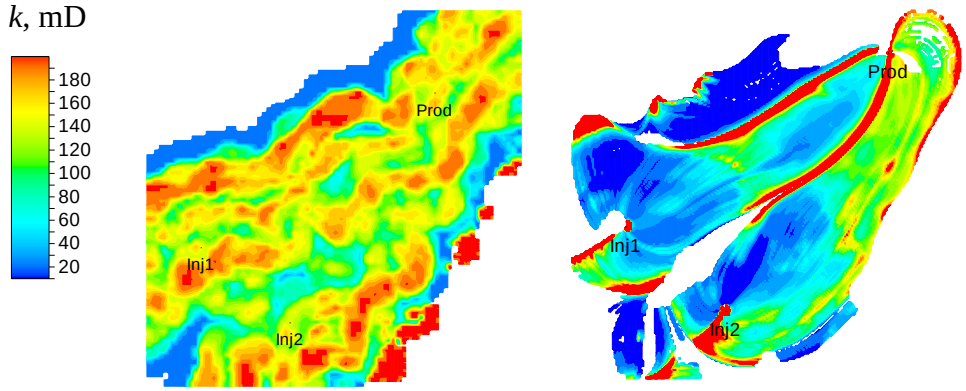

Figure 3.3 Permeability estimation for Model 3 by method #1. *Left*: exact underlying permeability, *right*: the estimate.

Roughly speaking, the proposed method of permeability estimation exhibits the same quality of estimation depending on the simulation model complexity as was reported in Chapter 2 for the saturation forecasting algorithm. Additional testing of the method in the presence of noise will be discussed below, in section 3.3.

3.2 Method #2, estimation of permeability using pressure map

The second method of permeability estimation I consider in this chapter follows the ideas suggested by [8], the brief review of this work can be found Chapter 1. The method is based on the steady state flow equation (3.8), which is discretised and solved numerically for permeability. In my work the implementation is generally consistent with the paper [8], however there are some differences, including the regularisation approach, and more details in treatment of the source terms.

$$\nabla \cdot (k\lambda \nabla P) = Q \tag{3.8}$$

The above equation is a steady-state one, and does not account for compressibility. Hence, errors associated with the transient flow effects may arise for the cases of rapidly changing well controls, high fluid compressibility, or small reservoir permeability. Note that method #1 of permeability estimation described above required the constant pressure conditions, or at least small pressure changes between the different time moments, which situation could be approximated if the time steps between the seismic monitors (pressure maps) are small. For the method considered in this section, pressure is allowed to change between the consecutive surveys, and the requirement here is that the instantaneous pressure maps should be subject to the steady-state flow, with little transient effects. However, the situation of frequently acquired 4D seismic also proves favourable for this approach, since information from all available multiple pressure maps is easily incorporated by it.

If equation (3.8) is applied to a 3D case, then variable *k* is the reservoir permeability. In two dimensions, if one wants to account for the variable reservoir effective thickness, the variable *k* gets the meaning of the permeability-thickness product $k_{abs} \cdot h \cdot NTG$ (this can be easily established by considering the conservation of mass for an elementary reservoir volume). In the subsequent discussion the latter use of *k* will be implied, since I consider the 2D method of permeability estimation. The variable λ is the total fluid mobility, $\lambda = k_{ro} / \mu_o + k_{rw} / \mu_w$. Since one can expect that the average saturation maps are available from the time-lapse seismic, the total mobility can be found by using the saturations and the phase relative permeabilities. In this section I will assume that the relative permeabilities are known. Otherwise, only the total product of $k\lambda$ can be resolved by the method. Quantity *Q* is the source density (volumetric density for 3D,

areal density for 2D), which represents the wells, and has positive sign for the producers and negative for the injectors. The variable P denotes pressure, however for the cases where the reservoir depth is variable and the gravity should be accounted for, P obtains the meaning of the *potential* – i.e. the pressure hydrostatically referred to a certain datum depth. Having made this note, I will refer to P as pressure in what follows[9]. The map of pressure along with the well flow rates converted to the reservoir conditions constitute the main input to the method. Expanding the left hand side of equation (3.8) one can write

$$k\nabla\lambda\nabla P + \lambda\nabla k\nabla P + k\lambda\nabla^2 P = Q. \tag{3.9}$$

The obtained equation can then be discretised using the finite differences[10], resulting in the linear problem

$$Ak = b, \tag{3.10}$$

where k is the unknown map of $k_{abs}\cdot h\cdot NTG$, and matrix A is formed by the values of pressure and total fluid mobility λ (see below). The right hand side is expressed via the well source density Q. Since matrix A is large and sparse, (3.10) is typically solved by an iterative linear solver for which it is sufficient to implement the matrix-vector multiplication $k \to A\cdot k$, instead of explicitly specifying all matrix entries. According to (3.9) the multiplication results in the map with the value at node (i, j) equal to

$$\begin{aligned}(Ak)_{ij} = &\left(\frac{\lambda_{i+1,j}-\lambda_{i-1,j\cdot}}{2\Delta x}\cdot\frac{P_{i+1,j}-P_{i-1,j}}{2\Delta x}+\frac{\lambda_{i,j+1}-\lambda_{i,j-1\cdot}}{2\Delta y}\cdot\frac{P_{i,j+1}-P_{i,j-1}}{2\Delta y}\right)\cdot k_{ij}+\\ &+\lambda_{ij}\frac{P_{i+1,j}-P_{i-1,j}}{2\Delta x}\cdot\frac{k_{i+1,j}-k_{i-1,j}}{2\Delta x}+\lambda_{ij}\frac{P_{i,j+1}-P_{i,j-1}}{2\Delta y}\cdot\frac{k_{i,j+1}-k_{i,j-1}}{2\Delta y}+\\ &+\lambda_{ij}\left(\frac{P_{i+1,j}-2P_{ij}+P_{i-1,j}}{\Delta x^2}+\frac{P_{i,j+1}-2P_{ij}+P_{i,j-1}}{\Delta y^2}\right)\cdot k_{ij}\end{aligned} \tag{3.11}$$

For the vertical wells, which act as points on the map, or horizontal wells, which act as lines on the map, the source density will be a delta function rather than a normal continuous function. It may be challenging to properly incorporate it into the discretisation (3.10). This problem is overcome by considering some neighbourhood around the wells and treating the source term in the integral sense. To do that, each well is surrounded by an ellipse, which is in turn discretised into a closed contour L

[9] The same thing is tacitly assumed for method #1 as well.

[10] Here, I used the central differences both for the first and the second derivatives.

consisting of the grid cell edges, see Figure 3.4. For any such contour the integral form of (3.8), or, equivalently, of mass conservation, can be written as

$$\int_L k\lambda \nabla P \vec{n} dl = Q, \tag{3.12}$$

where $\vec{n}$ is the outer normal to the contour. Assume that the value of k is constant on the considered contour L, and equals k_L. The left hand side of (3.12) can then be discretised as a sum of products of the nodal values of λ and P:

$$k_L \sum c_{ij,kl} \lambda_{ij} P_{i+k,j+l} = Q, \tag{3.13}$$

where $c_{ij,kl}$ are coefficients that depend on the grid cell dimensions, and indices $k,l = -1,0,1$. For example, for the contour segment between the nodes (i, j) and $(i, j+1)$ the corresponding discretised summand of (3.12) can be written as $k_L(\lambda_{ij}(P_{i+1j} - P_{i-1j}) + \lambda_{ij+1}(P_{i+1j+1} - P_{i-1j+1})) \cdot \Delta y / \Delta x / 4$, so the value $\Delta y / \Delta x / 4$ should be added to the coefficient $c_{ij,10}$ (the other coefficients are processed likewise). This addition to the coefficients is performed for each elementary contour segment. Equation (3.13) is a linear equation with one unknown, and it is added to the main system (3.10). The latter system, in turn, is considered only for the nodes outside the contours surrounding the wells, and thus has zero right hand side. Treating the well source terms by the contour integrals around the wells is also beneficial for the situation when the noise is present in the input pressure map, or the pressure map has been smoothed. In this case the peaks or troughs of pressure may not coincide with the actual well positions, however when calculation is done in some neighbourhood near the well, the slight perturbation or shift of the peaks can be tolerated.

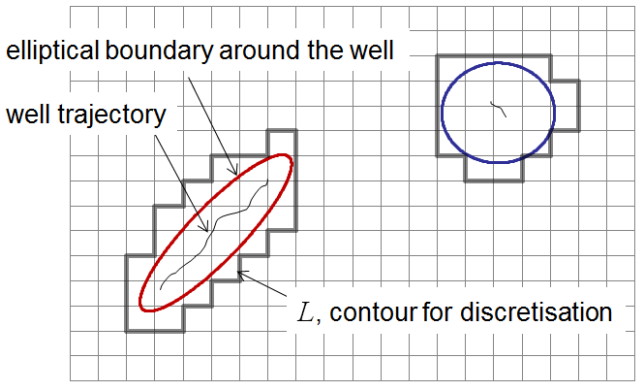

Figure 3.4 Contours for the integral treatment of the well source terms.

The boundary condition is also added to both continuous (3.8) and discrete (3.10) problems in the following form:

$$\nabla k \cdot \vec{n} = 0, \tag{3.14}$$

where vector $\vec{n}$ is normal to the grid boundary. This condition means that the map *k* has no "flux"[11] across the boundary.

Once the complete linear system of equations (3.10) is formed, which accounts for the boundary conditions and the source terms, it can be solved in the least squares sense (3.15). However, due to poor condition numbers a stable and practical solution is only reached if a regularisation of the system is made, which consists of imposing some additional conditions on the solution.

$$\| Ak - b \|^2 \to \min. \tag{3.15}$$

Among the simplest regularisation conditions one can think of are those of smoothness of the map *k*. Mathematically, the smoothness condition can be formulated in the form of minimising the spatial derivatives $\partial k / \partial x, \partial k / \partial y$ of the sought map. Denoting Γ_x and Γ_y the matrices resulting from the discretisation of the derivatives operators $\partial / \partial x, \partial / \partial y$, I arrive at the regularised least squares problem

$$\| Ak - b \|^2 + w_x \| \Gamma_x k \|^2 + w_y \| \Gamma_y k \|^2 \to \min, \tag{3.16}$$

where the weights w_x, w_y are subject to adjustment. If there are multiple pressure maps available for the different time steps, these are easily incorporated into the equation, e.g. for 3 input pressure maps the following expression should be minimised:

$$\| A_1 k - b_1 \|^2 + \| A_2 k - b_2 \|^2 + \| A_3 k - b_3 \|^2 + w_x \| \Gamma_x k \|^2 + w_y \| \Gamma_y k \|^2 \to \min. \tag{3.17}$$

The solution of this minimisation problem is equivalent to the solution of the linear system

$$(A_1^T A_1 + A_2^T A_2 + A_3^T A_3 + w_x^2 \Gamma_x^T \Gamma_x + w_y^2 \Gamma_y^T \Gamma_y) k = A_1^T b_1 + A_2^T b_2 + A_3^T b_3. \tag{3.18}$$

If the input maps have fine resolution (100 x 100, 500 x 500 points), then the final linear system (3.18) is solved iteratively, using the conjugate gradients solver.

---

[11] In the diffusivity equation describing the pressure diffusion or heat conduction the quantities like $\alpha \nabla P, \beta \nabla T$ are the fluid flux velocity and the heat flux density respectively (here the scalars α, β denote the medium conductivity, P, T - pressure and temperature). Thus, equation (3.14) essentially states the zero flux of the quantity *k*.

The described method was tested on the pressure maps obtained from a range of 2D models, with the focus on the following aspects: how the choice of weights w_x, w_y affects the performance, how the multiple pressure maps taken for input improve the results, and how the input noise impairs the estimate. The examples below illustrate these questions.

The first example is a simple quarter five-spot model with one producer and one injector located at the opposite corners. The model has background permeability of 100 mD, and two sharp permeability patches, one of 20 mD, another of 500 mD, see Figure 3.5, *left map*. The effective reservoir thickness is taken as 1 m, so that permeability is resolved directly. The algorithm was applied with different weights for regularisation.

For the moderate weight values $w_i = 10^{-7}$ all the general features of permeability are resolved, however the values for the high permeable patch are approximately 2 times underestimated (*middle map*). Also, some noisy wiggles start emerging on the map. This noise becomes even higher when regularisation is further weakened by taking the weights $w_i = 10^{-9}$ (*right map*). At the same time, the estimate of the high permeable patch becomes somewhat better, almost reaching the original value of 500 mD. As we see, there is a trade-off between the output noise suppression and resolution of the local permeability patches.

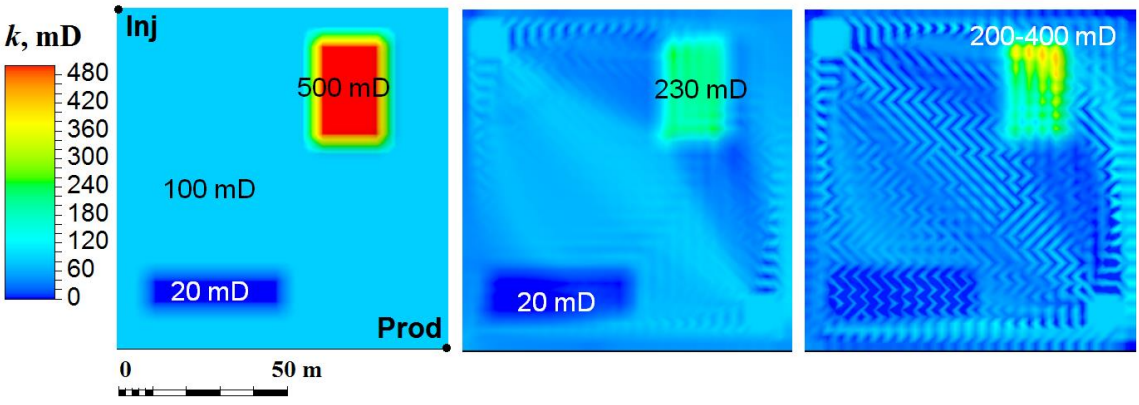

Figure 3.5 Permeability for a ¼ five-spot model. *Left* – underlying permeability, *middle* – estimate with weights $w_i = 10^{-7}$, *right* – estimate with weights $w_i = 10^{-9}$.

The second example is a 2D model with 6 producers and 2 injectors with alternating working regime. Three pressure maps P_1, P_2, P_3 corresponding to the different time moments T_1, T_2, T_3 are used for input. Each well works only at specific time steps:

- the left-hand side wells Prod1, Prod2, Inj1 are working at time T_1;
- the right-hand side wells Prod3, Prod4, Inj2 are working at T_2;
- finally, the wells in the middle Prod5, Prod6, Inj2 are working at T_3.

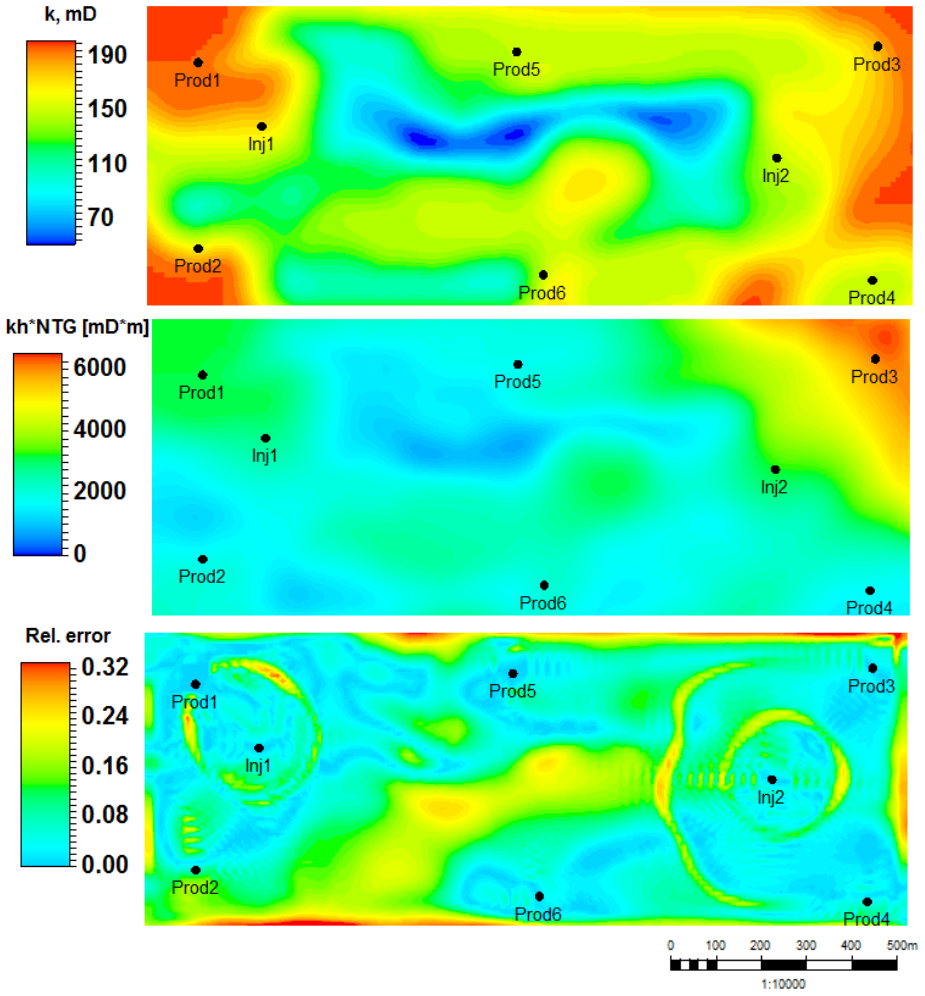

Figure 3.6 2D model with alternating wells. *Top*: exact permeability, *middle*: exact $k_{abs} \cdot h \cdot NTG$, *bottom*: relative error of $k_{abs} \cdot h \cdot NTG$ estimate.

To test the method, four inversions were done, three of them using only a single pressure map among P_1, P_2, P_3, and the last one using all three maps at once. The regularisation weights $w_i = 10^{-7}$ showed the most appealing results, as in the previous example. The underlying exact maps of permeability and $k_{abs} \cdot h \cdot NTG$ are shown in Figure 3.6. Since the reservoir thickness for this example is variable, these two maps

are quite different. Looking at the obtained estimates of *k* displayed in Figure 3.7, once again we can observe that it is permeability-thickness product, not just permeability, that is inverted by the method.

The impact of different pressure maps used for input is clearly seen in Figure 3.7. When a single pressure map is used, the pressure change illuminates only a specific part of the reservoir, where permeability-thickness is subsequently best resolved. Using all the available pressure maps in a single inversion gives the best estimate for the entire model (*bottom-right map* on the figure).

Comparing the results for the three-pressure-maps input (Figure 3.7, bottom right map) with the original $k_{abs} \cdot h \cdot NTG$ (Figure 3.6, middle map), the relative error $(= |k_{exact} - k_{estimate}| / k_{exact})$ can be found, see Figure 3.6, *bottom map*. The overall relative error is less than 20%. The higher error values are associated with the areas which are far from wells, or have little fluid flow. The ring-shaped features which can be seen on the error map are related to the sharp saturation fronts at different time steps. Comparing this model example with the previous one, it can be also seen that the method resolves the smooth permeability variations better than the sharp features, which is natural in view of the regularisation procedure applied.

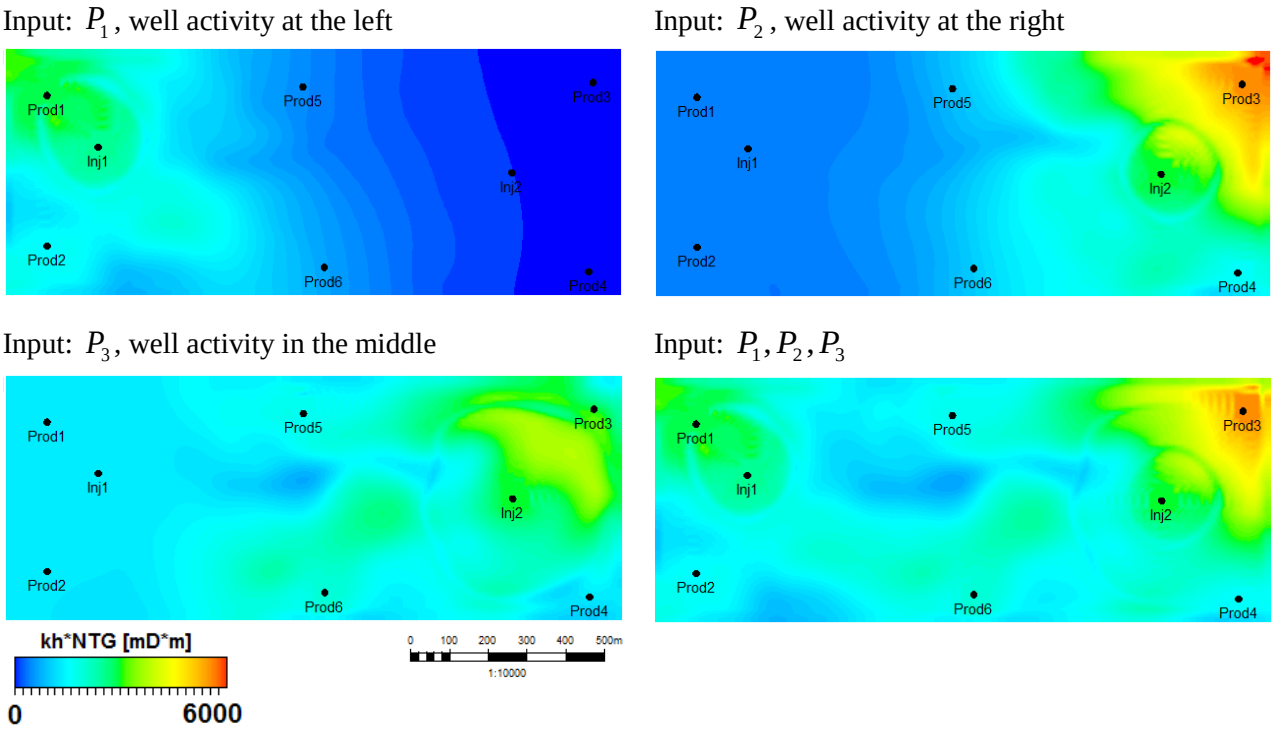

Figure 3.7 Estimates of *k* obtained for different input (the input is specified above each map).

3.3 Permeability estimation in the presence of noise

Testing of the two permeability estimation methods proposed above in the situation of noise present in the input pressure was performed on a range of simple 2D models. The models exhibit different kinds of permeability heterogeneity: high permeable channels, low permeable zones and partially sealing faults. Each model has two wells – producer and injector – located at the opposite edges of the grid, for which a constant BHP control is set. The initial reservoir pressure for all models is 15 MPa, and the BHP at producer and injector are 10 MPa and 20 MPa respectively.

The exact pressure maps taken from the simulation models were perturbed by adding the Gaussian correlated random noise shown in Figure 3.8. The noise peak values are within ± 1 MPa, and the RMS value is 0.31 MPa. Since both methods #1 and #2 failed to work with the perturbed pressure map, some map smoothing was done prior to running the procedures. The degree of smoothing was taken the same for all three cases.

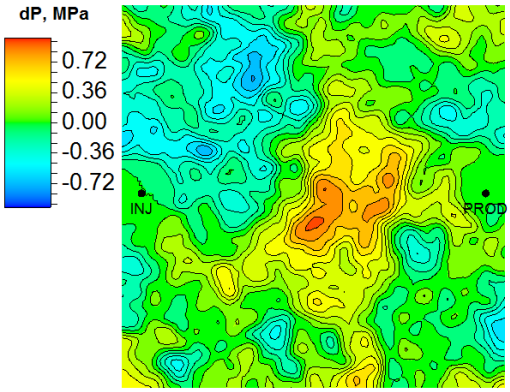

Figure 3.8 Correlated random noise added to the pressure maps.

The comparative performance of permeability estimation methods #1 and #2 for three simple models is shown in Figure 3.9 (these three models are also considered in the next section, so for consistent referencing they are labelled as Case 1, Case 9, Case 11 on the figure). When examining the different models, the magnitude of the pressure noise introduced should be compared with the magnitude of the total *pressure signal*. The total *signal* for each case equals the pressure map from the model minus the initial pressure, i.e. $P - P_{init} = P - 15\,\text{MPa}$, since it is *pressure difference* which is inferred from the time-lapse seismic.

Case 1 is a reservoir with a high permeable channel between the wells, which is not connected to them. The RMS of the pressure signal (signal = P – 15 MPa) equals 1.28 MPa, so the noise shown in Figure 3.8 constitutes 28% of the signal in terms of their RMS ratio. The high permeable channel is resolved reasonably well by method #1 using the exact pressure map, although some artefacts appear. Applying the method for the perturbed (and smoothed) pressure converts the channel into a feature that connects the two wells, has relatively small permeability, and inherits its geometry from the streamlines pattern. The method essentially failed here. Method #2 with the exact pressure input is good in resolving the channel geometry, however the overall permeability values become somewhat underestimated. This is likely to be the consequence of the regularisation, since the channel itself does not connect to the wells and has a small impact on the pressure map. Running algorithm #2 with the perturbed pressure input results in a failure to estimate permeability anywhere except for the wells vicinity.

Case 9 is a reservoir with a more complex channel picture, where the channels connect the two wells. The RMS of the pressure signal is 1.81 MPa, so the noise/signal ratio equals 17%. Method #1 with exact pressure resolves the part of channels connecting the wells, but does not resolve the remaining channels since there is almost no fluid flow taking place there, and consequently almost no streamlines. When the same method is run with the perturbed pressure, it also resolves the channel to a certain extent. The channel now takes its geometry from the streamlines bundle. Algorithm #2 with the exact pressure works well in estimating the permeability map. Since the high permeable feature connects the wells in this model, the algorithm resolves the channels even for the perturbed pressure input (*middle bottom map*). However, as will be shown below, a visually appealing picture does not mean a good reproduction of the historic fluid flow.

Case 11 is a homogeneous model with a sealing fault which baffles approximately 80% of the cross-sectional area between the wells. The RMS of the pressure signal for this model equals 2.49 MPa, which corresponds to 12% noise/signal ratio. Algorithm #1 with exact pressure produced a decent estimation for the part of the reservoir covered by the streamlines. Its application to the perturbed pressure also resulted in a sensible estimate for the lower part of the map. Again, the imprint of the streamlines geometry is clearly seen on the permeability features. The presence of the fault cannot be inferred from the estimated permeability map, instead, the map shows a channel going through the lower part of the map connecting the two wells. Method #2 with the exact input

gives a good quality permeability estimate, and the fault position can be inferred from it. Supplying the perturbed input pressure for the method led to poor permeability estimation, which is only valid in the immediate vicinity of the wells.

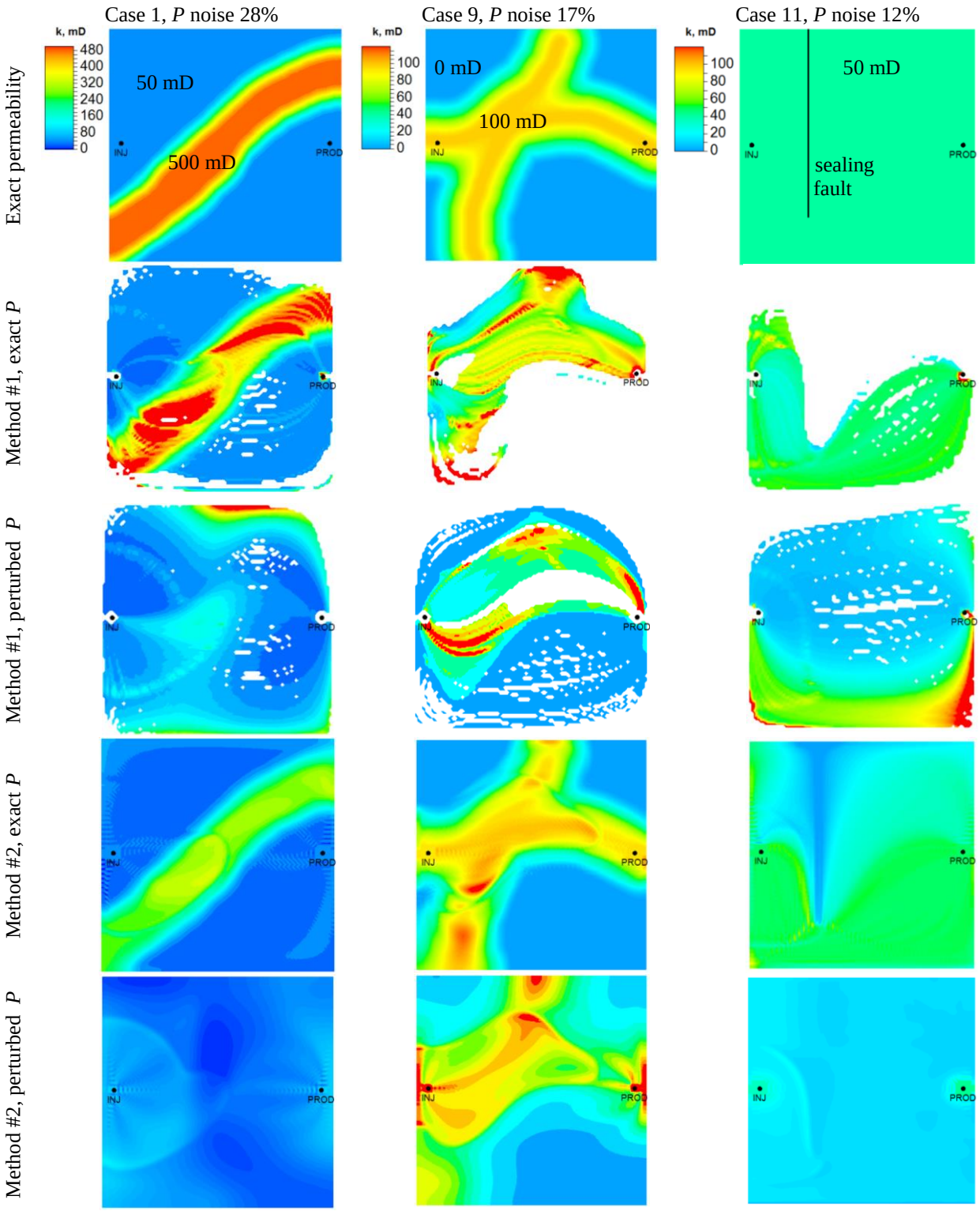

Figure 3.9 Testing of permeability estimation methods #1 and #2. *Columns*: different models. *Rows, top to bottom*: exact permeability, estimation #1 from the exact pressure, estimation #1 from the perturbed pressure, estimation #2 from the exact pressure, estimation #2 from the perturbed pressure.

Further testing of the permeability maps resulting from the noisy pressure input was conducted for Case 9 which gave the most favourable results above. To do the testing, the maps (rows 3, 5 in the middle column in Figure 3.9) were supplied to the simulation model which was run with the constant rate controls at wells to ensure the same injected and produced volumes as in the original exact model. By doing this, I look at how well the resolved lateral variations of permeability allow reproduction of the historic saturation front propagation, whereas reproduction of the historic well BHP's could then be achieved by adjusting the average reservoir permeability and the well skin factors. The simulation results are shown in Figure 3.10.

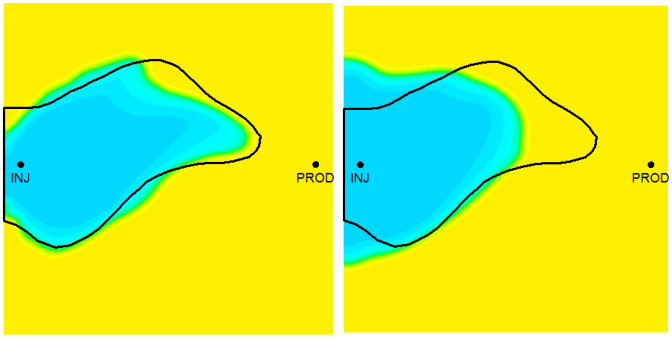

Figure 3.10 Saturation front prediction at step 2 using the permeability maps estimated from the noisy pressure for Case 9. *Left*: method #1, *right*: method #2. The maps show the predicted saturation, the solid black line shows the reference exact saturation front.

Method #2 which relies only on the pressure map produced a permeability map which visually resembles the underlying exact permeability, but gives a rather poor prediction of the saturation front. Method #1 also accounts for the saturation when making estimates, and despite the estimated permeability does not look quite similar to the underlying one, the saturation front prediction looks better, although there is space for further improvement. Thus, usage of the saturation information by method #1 results in better saturation forecasts, as opposed to method #2.

From the testing conducted, I can conclude the following. Method #1 with noiseless input works reasonably well, however errors may emerge in the velocity analysis, as was discussed in the previous chapter. A noisy pressure map requires smoothing for the method to work, and the stronger the smoothing applied, the closer the resulting map to the pressure map of a homogeneous model. In the noisy case method #1 can resolve the permeability features which follow the streamlines direction, as we saw for Cases 9 and

11. The map of permeability calculated in this way will however have a strong imprint of the streamlines geometry. The ability of the method to work in the "noisy" circumstances results from the usage of the saturation maps in addition to pressure. For the same reason one may expect better prediction of the saturation fronts compared to method #2. Method #2 is generally good for the exact input pressure taken from a 2D model, although it may somewhat fail in resolving the permeability features located far from the wells and not connected to them (cf. Case 1). For the perturbed input the method works notably worse. It either estimates permeability only close to the wells (cf. Cases 1, 11), or, even if the permeability estimation looks promising (cf. Case 9), it still proves un-sucessful in predicting the saturation fronts.

The levels of noise I considered in this exercise range from 12% to 28%, which is quite low compared to the errors one may expect for the pressure maps inverted from seismic. Method #2, as additional testing revealed, may start failing for the noise being as low as 5%. High sensitivity to the pressure noise could be a consequence of the implementation of this particular algorithm. On the other hand, this could be due to a more fundamental restriction of resolving the permeability map from a pressure map. In the following section I will examine the latter possibility and address the question of the information content of the pressure map.

3.4 Permeability impact on pressure

Consider decomposition of the permeability map into low frequency and high frequency components:

$$k = k_0 \cdot k_1. \tag{3.19}$$

The low frequency component k_0 can be e.g. just a constant map of average permeability, or a linear trend. The map of the average permeability can be estimated with reasonable confidence from the well data – namely, well flow rates and the bottom-hole pressures. Denote by P_0 the pressure map corresponding to the solution of the flow equations with constant permeability k_0. Then the total pressure response P for the original permeability k can be represented as P_0 plus some residual P_1 which results from the high frequency permeability component k_1:

$$P = P_0 + P_1. \tag{3.20}$$

Putting the "homogeneous" pressure P_0 aside, all the information content of the pressure map is covered by the residual P_1. To assess the magnitude of the latter for different permeability perturbations k_1, I performed a number of tests on synthetic models similar to those considered in the previous section in Figure 3.9.

The base case model is taken as a homogeneous one, with constant permeability equal to 50 mD, and other constant reservoir properties. The different cases with lateral permeability variations are obtained by introducing the following features to the permeability maps: high permeable channels, low permeable areas, local high permeability patches, non-permeable barriers (for Cases 10, 11). Permeability maps of all the perturbed Cases 1 – 11 are shown in Figure 3.11.

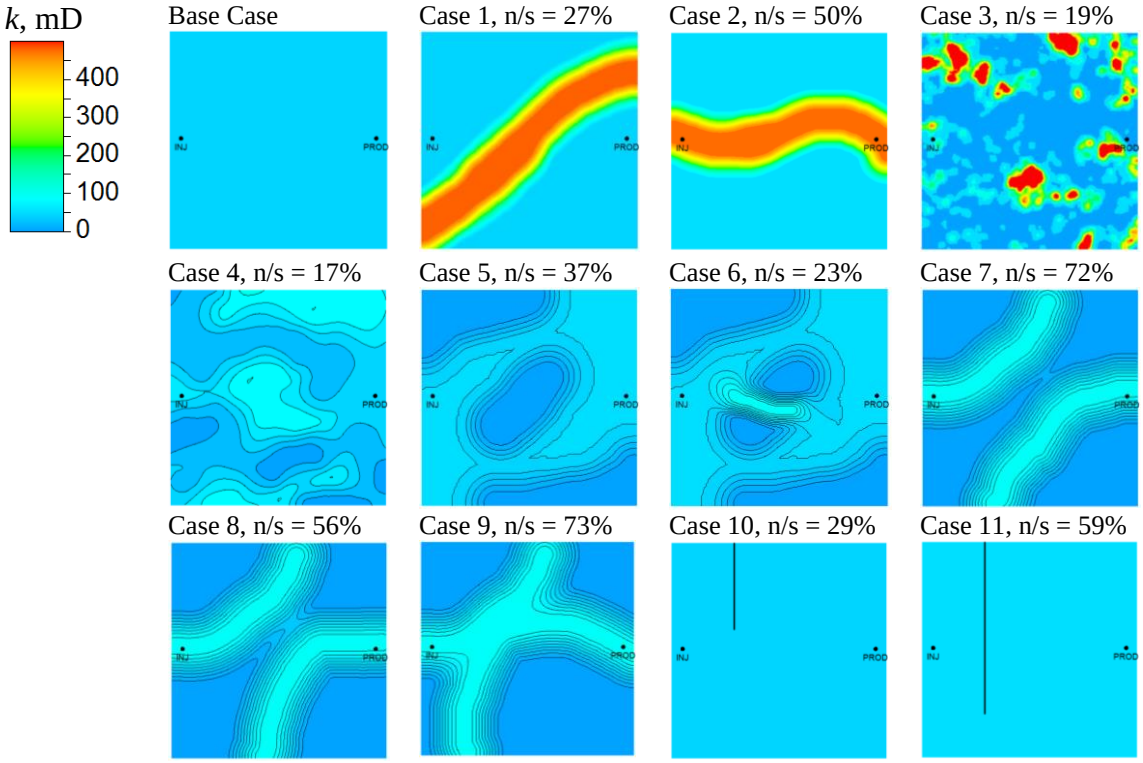

Figure 3.11 Permeability maps for the different perturbed cases. The RMS ratio of the pressure residual P_1 and the pressure signal ΔP is reported as "n/s".

To assess the values of the residual P_1 for each case, the pressure map of the base case P_{base} was subtracted from the pressure map of the given case P, so that $P_1 = P - P_{base}$. Certainly, for each case the average permeability map k_0 is different, but since the wells are controlled by the BHP, the pressure map P_0 resulting from k_0 will be the same for all cases, and it will equal P_{base}. The residual P_1 can be thought of as "noise" resulting

from the permeability heterogeneity introduced to the base case model. The magnitude of its RMS was compared with the RMS of the pressure signal ($\Delta P = P - 15\,\text{MPa}$), and their ratio is referred to as n/s (noise/signal) in Figure 3.11.

An example of the calculation of P_1 for case 5 is shown in Figure 3.12. As can be seen, visually the full pressure map P is very close to the pressure map P_0 found from the constant permeability. The difference between them ranges within ±1 MPa, and has RMS 0.62 MPa, which is 37% of the pressure signal RMS equal to 1.68 MPa.

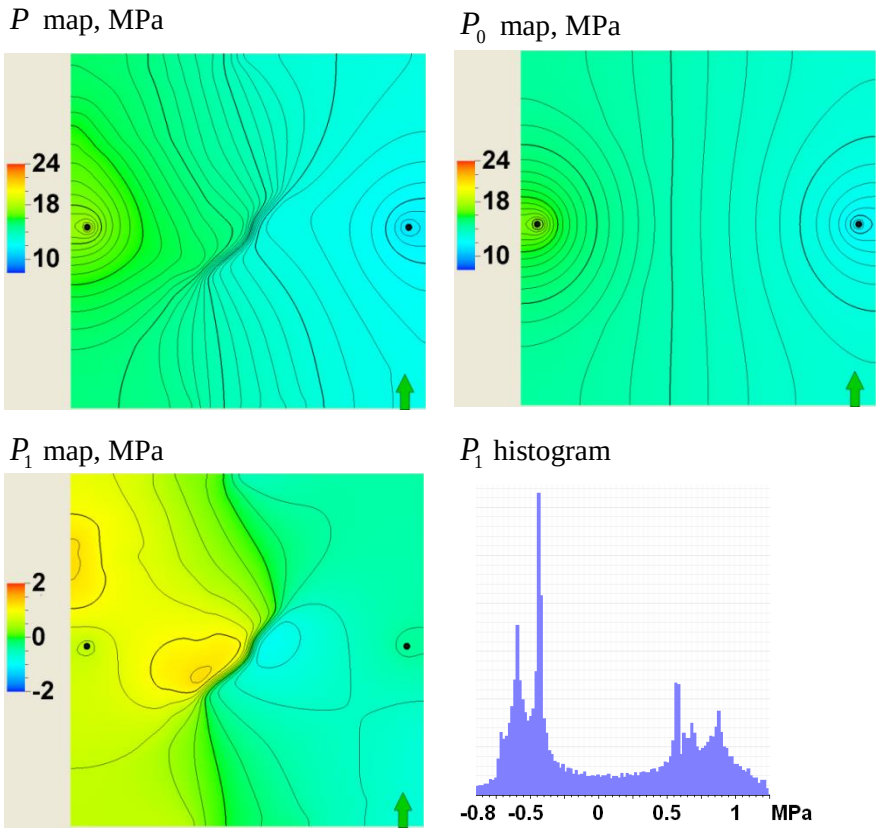

Figure 3.12 Decomposition of pressure response for Case 5. *Top, left to right*: pressure response P, "smooth" component P_0. *Bottom, left to right*: residual component P_1, and its histogram.

For the other cases considered the RMS ratio between the residual and the signal ranges from 17% to 73%, see Figure 3.11. For a pressure map inverted from the 4D seismic the error may well exceed these percentages due to the noise in the 4D seismic data itself and the inaccuracies of the inversion procedure, especially in the areas far from the wells. For example, for the Schiehallion dataset the estimated error in the 4D seismic signal is 50% to 90% or more, see Chapter 6 for the details. The pressure map

with such noise will not contain any useful information in terms of resolving the features on the permeability map like those in the examples considered here.

3.5 Method #3, estimation of permeability using saturation maps

As can be seen from the previous exercises, a pressure map can only be used for inferring the lateral permeability variations if it has little noise. At the same time, method #1 which uses both pressure and saturation maps for input showed somewhat better stability to the pressure noise and better capability for reproducing the historic saturation profiles. This brought me to the idea of the next method of permeability estimation where the pressure input is discarded and only saturation is used.

Consider a pressure map estimate, e.g. the one obtained from a model with constant permeability, or some other permeability approximation. When calculating the pressure map from the model, the wells are assumed to work with the constant flow rates corresponding to the average historic ones. The other option might be to take a noisy pressure map estimated from the seismic, and apply smoothing to it. If the smoothing is strong enough, the result *again* will be close to the pressure map calculated using the constant permeability model. From the pressure map the streamlines can be tracked and the pressure drop along each streamline can be analysed. The pressure drop ΔP along the streamline can be expressed in terms of the quantities considered in Chapter 2: the tube cross-sectional area *A*, total flow rate *q*, permeability *k*, which is unknown, and the total fluid mobility λ, which I assume I can estimate from the saturation maps and the relative permeability information. Using Darcy's law and integrating along the streamline Σ, one obtains

$$\Delta P = \int_{\Sigma} \frac{q dx}{A(x)\lambda(x)k(x)} \tag{3.21}$$

The flow rate *q* for each streamline is calculated from the estimated saturation velocity along the streamline, in the same manner as was explained in section 3.1. While doing this, I assume the phase relative permeabilities to be known. To discretise (3.21), for each grid cell *i* penetrated by the streamline the corresponding part of the integral can be found, where the integration is only performed over the streamline segment $[xi, yi]$ contained within the cell:

$$\beta_i = \int_{[xi,yi]} \frac{qdx}{A(x)\lambda(x)}. \tag{3.22}$$

Taking all the cells covered by the streamline, one can get the discrete formula

$$\Delta P = \sum_i \frac{\beta_i}{k_i}, \tag{3.23}$$

where permeability in cell *i* is considered constant, equal to k_i.

Since the streamlines mostly connect pairs of wells, the *observed pressure drop* along the streamline ΔP_{meas} can also be calculated from the pressure at well locations. More rigorously, in my approach the streamlines are terminated at the circles or ellipses surrounding the wells. It is reasonable to assume that permeability in the wells vicinity and the well skin factors are known, e.g. from the transient well testing. Given these, one can estimate pressure at some distance from the well for the current BHP and the flow rate, so the pressure values at the ellipses around the wells can be regarded known, and the total *observed pressure drop* along the streamline ΔP_{meas} can be found. Finally, comparing the observed pressure drop ΔP_{meas} and the one estimated by equation (3.23), one can adjust the unknown permeability values k_i along the streamline so as to match the pressure drops. Matching of the pressure drops for all the existing streamlines can be written in the form of the nonlinear[12] system of equations

$$B(k) = d, \tag{3.24}$$

where k is the whole grid of permeabilities, the column-vector $B(k)$ denotes the right hand sides of (3.23), and column-vector d denotes the measured pressure drops ΔP_{meas}. Each row in this system of equations is essentially equation of type (3.23) corresponding to a particular streamline. Upon solution of (3.24) one gets the updated permeability grid, for which the pressure map can be recalculated. The procedure consisting of the streamline tracking, formulating the system (3.24) and solving it is then repeated for a number of iterations, until the solution reasonably stabilises.

This algorithm is quite similar to that proposed by Vasco in [9], [10], see discussion in Chapter 1. In Vasco's approach it is examined how a perturbation of permeability

[12] The system of equations will become linear if one considers the unknowns $r = k^{-1}$, i.e. the reciprocal permeabilities, or hydraulic resistivities. Experiments with these new variables were not too successful however, because of the challenges of constraining r from approaching zero values, in which case the permeability values may become indefinitely large.

impacts the saturation velocities, and then how the perturbed velocities impact the saturation fronts (while doing this, the authors also use the pressure gradient, as opposed to my procedure). The quantity that is matched is essentially the saturation fronts which are linked directly to the 4D seismic by seismic modelling. The algorithm starts from some initial permeability approximation, tracks the streamlines, resolves the permeabilities that are then passed to the next iteration, and so on. In my method it is examined how a perturbation of permeability impacts the pressure drops along the streamline. The observed saturation fronts are used directly to estimate the saturation velocities. The matched quantity is the pressure drops.

The problem of adjusting the permeabilities to reproduce the pressure drops along the streamlines resembles the simple tomographic problem, where the attenuation coefficients of the medium are estimated from the observed attenuation of the rays illuminating the medium, see Figure 3.13. Likewise, for the fluid flow problem, the medium is characterised by its "attenuation coefficients" – reciprocal permeabilities that reduce the value of pressure along the "rays" – the streamlines, and the ultimate pressure drop along the "rays" is known from the observations.

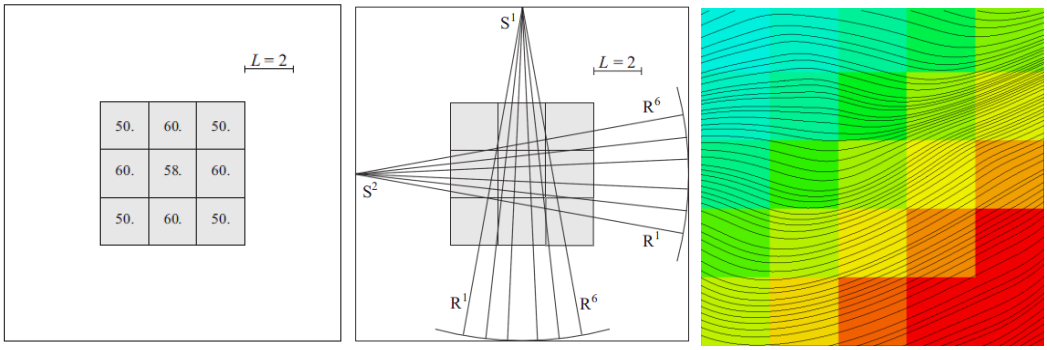

Figure 3.13 Simple tomographic problem versus pressure drop matching. *Left*: medium described by the attenuation coefficients, *middle*: attenuation of the rays is the measured quantity (adopted from [56]). *Right*: permeability grid with superimposed streamlines.

The system of equations (3.24) was firstly evaluated on the exact input taken from a few simple 2D simulation models. This testing involved taking the exact permeability map k to calculate the pressure map and the streamlines. The same permeability was substituted to the equations and the residue vector $r = B(k) - d$ was calculated. Its components show the discrepancy between the observed pressure drop along the streamline and that calculated by (3.21). Five models were considered altogether:

- heterogeneous Cases 1 (model with channel), 11 (model with fault) from section 3.4, Figure 3.11.
- homogeneous model with radial flow (Case 12);
- homogeneous model with linear flow (Case 13),
- heterogeneous model (Case 14) obtained from Case 5 by adding a high permeable channel, see Figure 3.14.

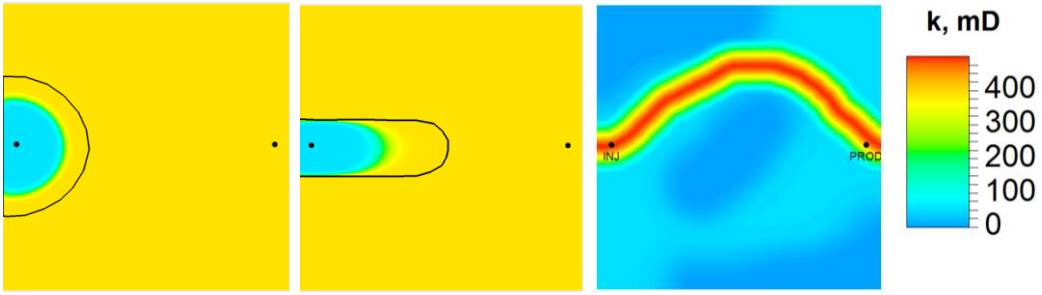

Figure 3.14 Illustration of Cases 12 – 14 used for estimating the residue *r*. *Left* – saturation for Case 12, *middle* – saturation for Case 13, two consecutive saturation fronts used to infer the velocities are displayed. *Right* – permeability map for Case 14.

The results of estimating the residue are shown in Table 3.1, where the mean and standard deviation of the residue are reported, as well as the average pressure drop ΔP for reference. As can be seen, for the basic homogeneous Cases 12, 13 the residue is small, within 1% of the total pressure drop, which just serves as a confirmation of the correct formulation of the system of equations. For Cases 11 and 14 the relative magnitude of the residue reaches 4 – 6%, and the standard deviation of the residue increases accordingly. This growth of the residue is related to the errors in velocity estimation which arise from the streamlines crossing the saturation fronts at small angles. Thus, any possible inaccuracies of the streamlines analysis discussed in Chapter 2 will affect the performance of this permeability estimation procedure.

To formulate system (3.24), the reservoir is required to flow under steady state conditions between time moments T_1, T_2, at which the maps of saturation S_1, S_2 are taken for velocity estimation. If there are more time intervals with the steady state flow, e.g. the interval T_3, T_4 with saturations S_3, S_4, then additional equations of type (3.24) corresponding to the new streamlines and dealing with the same permeability grid can be added. This will further constrain the unknown permeabilities.

model	mean(ΔP), MPa	mean(r), MPa	std(r), MPa	mean(r) / mean(ΔP)
Case 1	4.21	0.026	0.286	0.62%
Case 11	6.31	-0.39	0.44	-6.15%
Case 12	4.72	-0.024	0.04	-0.51%
Case 13	7.03	0.002	0.039	0.03%
Case 14	7.87	-0.34	0.693	-4.36%

Table 3.1 Residue in the pressure drop. The *columns* show: the mean total pressure drop ΔP along the streamlines, mean residue *r*, standard deviation of the residue, ratio of mean *r* to mean ΔP.

System (3.24) is solved in the least-squares sense (3.25), and practice revealed that to solve it some prior information and regularisation should be introduced. The following regularisation was considered:

1. Introduction of the known values of permeability k_*, essentially at the well locations. This can be done e.g. by using a diagonal "observations" matrix *A* which has *zero* values corresponding to the inter-well space, and *ones* in the vicinity of the wells.
2. Smoothing of the permeability grid by minimising the first derivatives. The derivatives are approximated by the same matrices Γ_x, Γ_y used in formula (3.16), section 3.2.
3. Smoothing of permeability grid by minimising the second derivatives which are approximated by matrices Z_x, Z_y.

$$\left\|B(k)-d\right\|^2+\alpha\left\|Ak-Ak_*\right\|^2+\gamma_x\left\|\Gamma_x k\right\|^2+\gamma_y\left\|\Gamma_y k\right\|^2+\zeta_x\left\|Z_x k\right\|^2+\zeta_y\left\|Z_y k\right\|^2\to\min. \quad (3.25)$$

The lowercase Greek letters in this formula denote the weights that are selected from the numerical testing. Since some streamlines may occasionally have a bad quality velocity analysis, additional weighting is introduced for the equations (3.24). Each equation is multiplied by factor *w*, which is higher in the case of a good velocity analysis, and lower for the bad one. This allows placing more emphasis on the streamlines with reliable velocities when minimising the objective function (3.25). The weight for a particular streamline is defined as

$$w=\Delta S_w\cdot\exp(-f/q^2), \quad (3.26)$$

where ΔS_w is the saturation range for which the relative flow velocity U_0 has been estimated. If a streamline did not cross a significant saturation front, ΔS_w is small and the velocity analysis is likely to be of low quality. The quantity f is defined by (3.3) in section 3.1 and measures the discrepancy between the velocity U_0 estimated from the maps and the same velocity calculated analytically. Normalising it by q^2 removes its dependence on the flow rate, so that only the quantities expressed via the fractional flow f_w are left. The smaller the discrepancy between the two versions of velocity U_0, the higher the confidence put on the streamline. Minimisation of the objective function (3.25) is done by conjugate gradients non-linear optimiser. Its implementation requires the derivatives of $B(k)$ with respect to k to be expressed, which is easily done using (3.23). The constraints $k_i > 0$ are imposed on the unknown permeability values, and these constraints are handled during optimisation by means of a barrier function.

The described permeability estimation approach was tested on a number of 2D models. Its performance was found to be rather poor, and the main findings will be illustrated below using the model of Case 1 described in sections 3.3, 3.4. The model has a high permeable channel between the wells, not connected to them, see Figures 3.9, 3.11. The first application of the procedure, with the results shown in Figure 3.15, compares the impact of different initial permeability approximations.

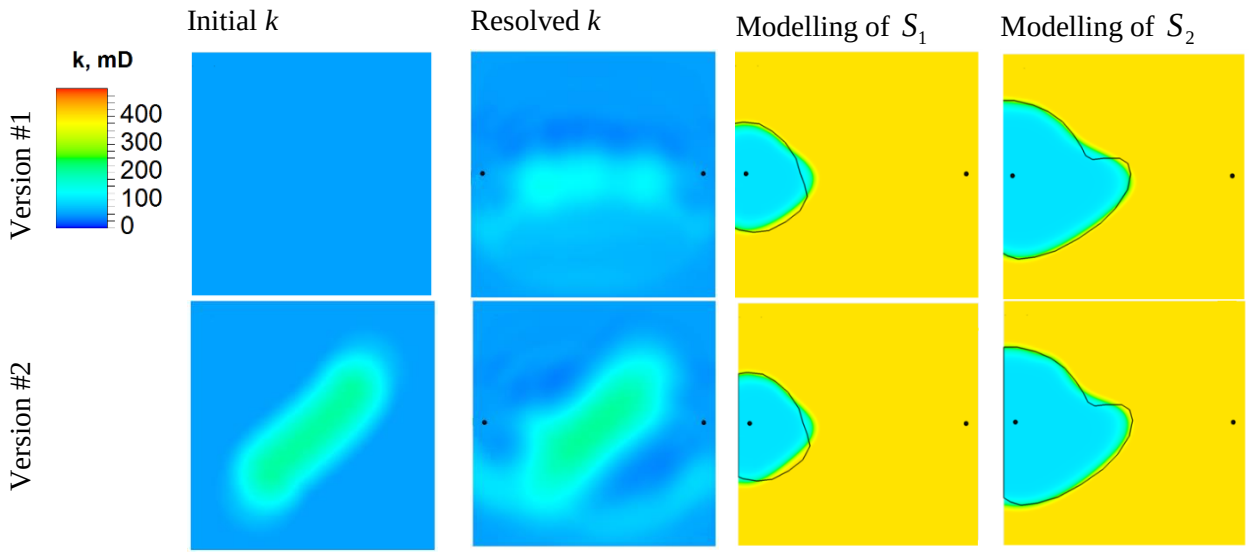

Figure 3.15 Permeability estimation by method #3 with two different initial approximations (*rows*). The *columns, left to right*, show: initial permeability, estimated permeability, saturation prediction with the estimated permeability (*cyan colour*) compared to the exact saturation contours S_1, S_2 (*black lines*).

As can be seen, the method mostly preserves the original features of the permeability map and introduces some smaller alterations to it. Some further studies also revealed that the method can give quite poor results if the initial permeability is selected inappropriately. Both versions of the resolved permeability in the figure above gave models[13] which reproduce the historic saturation fronts S_1 and S_2 reasonably well. These models also showed a good match to the historic well flow rates, with the relative error ranging within 3 – 5%. Although the *k* found cannot be said to resolve the underlying high permeability channel, both estimated maps of *k* can be regarded as acceptable, since they reproduce the saturations, whereas resolution of a channel located at a distance from the wells is a challenging problem which has large uncertainties.

The resolved permeability may not look geologically realistic, especially if the smoothness (regularisation) imposed is weak. An example of this is shown in Figure 3.16, left column. We can see that the estimated permeability map has a rectangular feature in the middle, and scattered small blue spots with very low permeability, which certainly does not look geologic. The corresponding saturation map S_2, however, reproduces the historic position of the saturation front with quite a good quality.

Apart from treating the permeability as an unknown variable in each grid cell (referred to as "continuous parameterisation"), two other parameterisation approaches were considered:

1. Parameterisation by regions, whereby the map is represented by a set of coarser regions with constant permeability. The simplest choice for the regions is the coarse rectangles. The permeability value of each region is to be resolved.
2. Parameterisation by kriging based on a set of pilot points (see also Appendix D). A relatively sparse set of pilot points with unknown permeabilities is considered, which allows calculating the whole permeability map by kriging with some predefined variogram model. Amendment for calculating the gradients required by the conjugate gradients solver is easily obtained since kriging interpolation for each grid point involves a linear combination of the values at pilot points multiplied by the pre-calculated kriging weights.

Comparison of the permeability calculation with *continuous* parameterisation with weak smoothing, *regions* parameterisation and *kriging* parameterisation is given in Figure 3.16. The latter two methods produced a somewhat more geological estimate of the

[13] The BHP control at the wells was used.

permeability map than the *continuous* parameterisation, but prediction of the saturation front S_2 degraded at the same time.

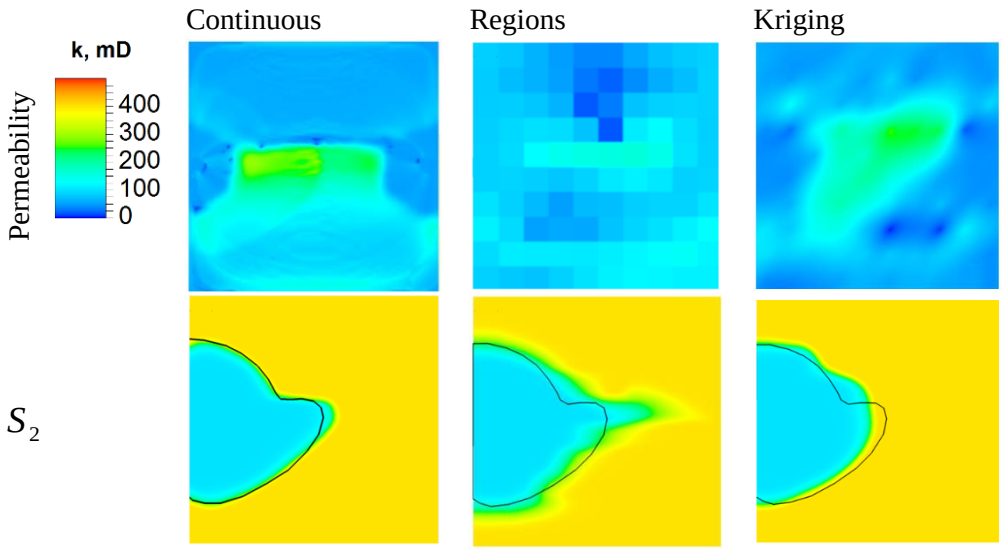

Figure 3.16 Permeability estimation with different parameterisations (*columns*): continuous with weak smoothing, coarse regions, kriging. *Top row*: estimated permeability, *bottom row*: prediction of the saturation front (*cyan colour*) compared to the exact one S_2 (*black contour*).

One of the major problems of the considered algorithm is that at each iteration permeability is updated based on the fixed streamlines, whereas the streamline trajectories actually depend on the permeability. As a result, after the objective function (3.25) has been minimised within the current iteration, pressure has been recalculated for the updated permeability, and new streamlines have been tracked, the objective function often shows a step increase of the value. Two examples of such behaviour are presented in Figure 3.17 which shows the plots of the objective function progress versus the total number of the internal iterations of the conjugate gradients solver (across all the iterations of the permeability estimation algorithm). The graphs consist of a series of intervals of a smooth monotonic function decrease (conjugate gradients perform the minimisation) with abrupt changes between them (pressure map is recalculated and new streamlines are tracked). As we see, the absence of coupling between the permeability and the streamlines adversely affects the convergence, so that the objective function may even become worse as the algorithm progresses, as illustrated by the right hand side plot on the figure. A similar convergence feature is reported for the algorithm proposed in [9], [10], see Figure 1.5.

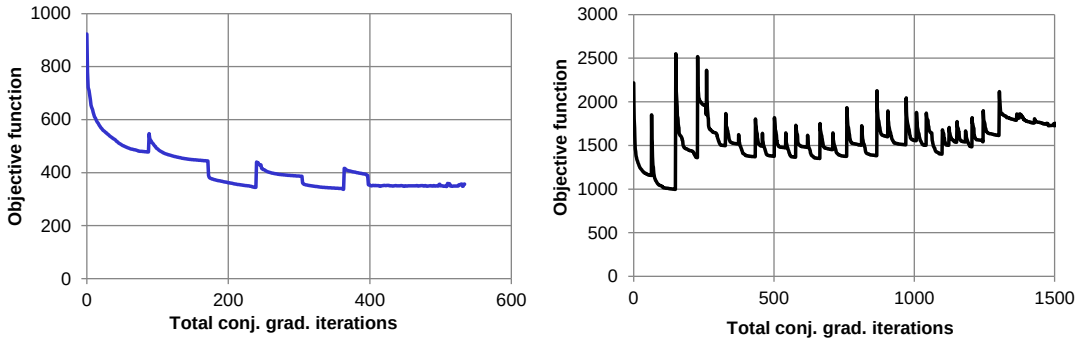

Figure 3.17 Two examples of the objective function progress over all conjugate gradients iterations.

The lack of coupling between the permeability grid and the streamlines is also admitted in the mentioned papers [9], [10]. However the author claims that the resulting sensitivities of the seismic amplitude with respect to the permeability or porosity changes calculated using the fixed streamlines are quite accurate compared to the reference sensitivities found by the finite differences (Figure 1.4 shows the sensitivities comparison for a synthetic 31 x 31 cells model). By saying this, the author implies that fixed streamlines do not impair much the final sensitivities.

My study of this question gave different results, see Figure 3.18. The figure shows the sensitivity of the water saturation S_w^* at an observation point with respect to the grid permeabilities k_{ij}, so each grid cell g_{ij} of the displayed grids shows the value $g_{ij} = \partial S_w^* / \partial k_{ij}$. The calculations were performed for a homogeneous 100 x 100 cells 2D model with one injector and one producer. The finite difference results were obtained with the simulator tuned up to very tight convergence to get a clear and noiseless sensitivity picture. The left hand side grid corresponds to the sensitivities calculated from the fixed streamline. Here the non-zero sensitivities are present only in the grid cells covered by the streamline, both in the upstream and downstream directions from the observation point. The right hand side grid with the sensitivities found by the central finite differences shows a notably different picture: the stripe of non-zero sensitivities is thicker, there are negative sensitivity values close to the observation point, and the sensitivities are zero almost everywhere in the downstream direction. Thus, the reasonable doubts arise with respect to the applicability of the fixed streamlines in assessing the fluid flow sensitivity to the permeability change.

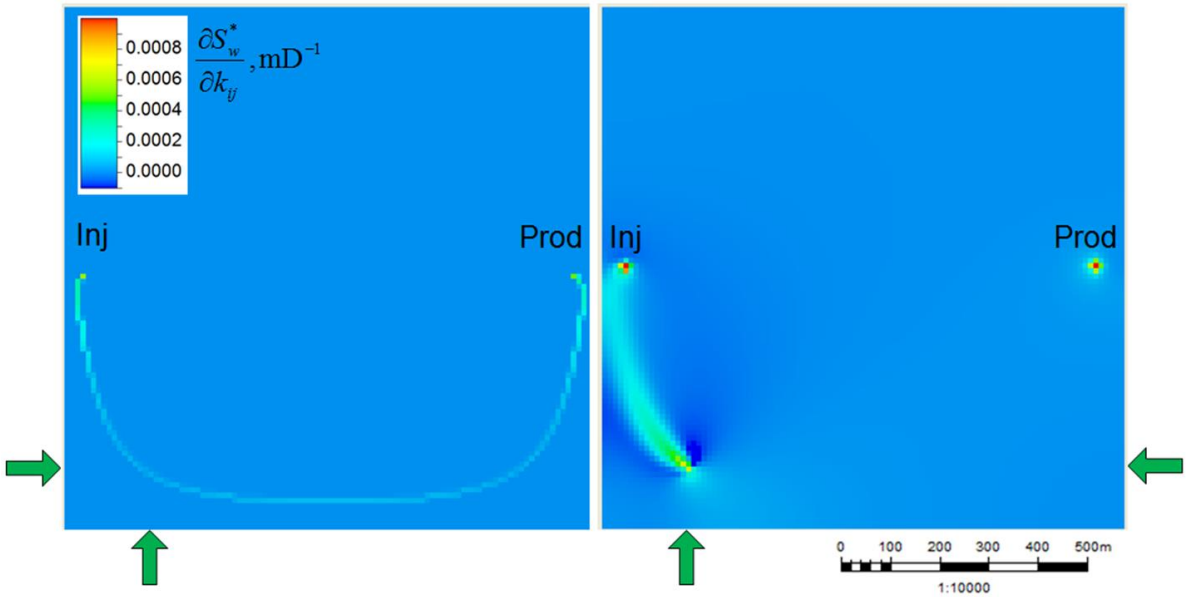

Figure 3.18 Sensitivity of water saturation at the observation point with respect to the grid cell permeabilities. *Left*: calculation using the fixed streamline, *right*: calculation by the finite differences. The arrows show the observation point's coordinates.

Getting back to the convergence issues of method #3, as a straightforward way to get rid of the abrupt changes of the objective function at the streamlines update, an additional term was introduced to the objective function. The term forces the permeability change between two successive iterations of the procedure to be within some predefined limits, so that both permeability and the streamlines change gradually. A reasonably monotonic decrease of the objective function was achieved, however the resulting permeability and the predicted saturations became worse, which means that the algorithm made its way to an unfavourable local minimum. Thus, convergence of the method is one of its weak points. It depends on the initial permeability approximation, the type of parameterisation used, and the settings used for regularisation. As was shown, the method may work if these prerequisites are properly selected, however no simple recipes were found on how to do this selection. Even when the method showed reasonably good matches of the saturation fronts, the associated permeabilities did not have a nice geological look. Some studies done towards making the algorithm behave better in this respect did not reveal any practical solution.

Leaping ahead to the subject of the next chapter, where seismic history matching is considered, I estimated permeability for the model of Case 1 by history matching based on the well data observations and saturation map observations. To do this, the permeability map was parameterised with 49 coarse regions, the initial permeability was

taken homogeneous, and assisted history matching was carried out using Schlumberger SimOpt software. The history matching results proved to be of higher quality than those of method #3, see Figure 3.19. As can be seen, the estimated permeability map shows the channel-like feature more clearly compared to the results of method #3 in Figures 3.15, 3.16. Then, prediction (calculation) of saturation front S_2 is also notably better than was observed in the two mentioned figures. Although the conducted seismic history matching took on average 4-8 times longer CPU time than the different applications of method #3, the improvement of the results quality is obvious. This improvement takes place because history matching employs the full physics reservoir simulation, and hence imposes more coupling on the fluid flow variables (permeabilities, pressures, saturations, flow rates) compared to the fast-track premability estimation method.

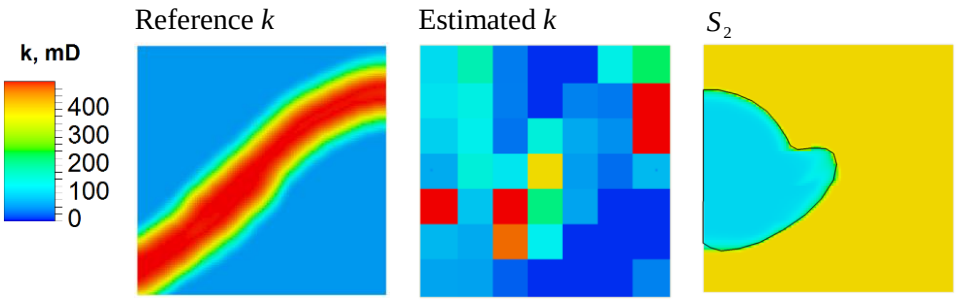

Figure 3.19 Permeability estimation for model of Case 1 by seismic history matching using SimOpt. *Left to right*: reference permeability map, estimated permeability map, prediction of the saturation front (*cyan colour*) compared to the exact one S_2 (*black contour*).

3.6 Summary and discussion

In this chapter I considered three algorithms of fast estimation of permeability maps. The first algorithm uses the input of two saturation maps and one pressure map. It is based on streamline tracking, estimating the saturation propagation velocities, calculating the flow rates for each streamline and finally finding the permeability from Darcy's equation. The method was tested on a number of 2D and 3D models. In general, its accuracy and problems are the same as were reported for the saturation propagation algorithm from the previous chapter. So, the algorithm reasonably works for 2D models (although there may be some problems due to the errors in the velocity estimation), and the errors increase for complex 3D models. In the presence of noise

the method is capable of resolving the permeability features which are aligned with the streamlines direction. However the resulting permeability map often does not look geological, as it carries a strong imprint of the streamlines geometry.

The second algorithm uses the input of a pressure map (or a few such maps) plus the information on the associated well flow rates. It is based on the discretisation of the steady-state flow equation, which is solved for the unknown permeability grid. The smoothing regularisation conditions are also introduced to suppress the numerical noise in the output. The tests of the procedure on simple 2D models allowed examination of the effect of the smoothing weights selection, the impact of using several input pressure maps, and influence of the input noise on the solution. For noiseless input, the method inverts for permeability with quite good precision, although it may not resolve well some permeability features which are far from the wells and are not connected to them. In the presence of noise the method often fails to estimate permeability anywhere except for the vicinity of the wells. The level of noise sufficient for the algorithm to start failing is case dependent, but may be as low as 5% – 10%. Even if the method does produce a permeability map which is visually appealing and resembles the exact one, this map is likely to give poor predictions of the saturation fronts, whereas the first method of permeability estimation gives better saturation predictions.

In [8] a higher tolerance to noise of the method similar to method #2 is reported, see the overview in section 1.4, Chapter 1. The direct testing of my procedure with the noise considered by the author is not possible however, since the author does not mention the spatial correlation ranges of the noise, whereas these are also important together with the noise RMS. E.g. the uncorrelated Gaussian noise can be removed relatively easily by smoothing, and the noise with the large correlation ranges may be impossible to filter out. Besides, the author applied the noise (10% to 60%) to the quantity Φ which is roughly equal to the pressure gradient times the fluid mobility, so this is different from the noise I considered, which is applied directly to the pressure map. Putting the noise percentages aside and analysing only the qualitative part of permeability inversion, another suspicious detail in this paper can be indicated. The author provides the permeability maps with reasonable inversion of the *high-permeable features* far from the wells even for the substantial input noise. From my experience, resolution of such features is the first thing that breaks down after the introduction of noise.

High sensitivity of the second procedure to the input noise led to a small study of how the lateral heterogeneity in the permeability map impacts the pressure response.

Expressing the permeability map as a product of a "low frequency" constant map and a "high frequency" heterogeneous map, it was found that the pressure signal corresponding to the high frequency component is rather low, ranging from 17% to 73% of the total pressure signal for the examples considered. This means that if the total pressure signal has errors exceeding these percentages, which may easily be the case for the pressure maps estimated from the time-lapse seismic, then this pressure is useless for resolving the permeability laterally. (For instance, for the Schiehallion dataset, as will be described in Chapter 6, the 4D noise to 4D signal ratio is estimated to be around 80%, and similar, or even higher levels of error can be expected in the pressures and saturations derived from such time-lapse seismic). Still, it should be noted that the noisy pressure map may be useful for estimation of compartmentalisation of the reservoir and assessing the fault transmissibilities, since the sealed or partially sealed compartments may produce quite a contrasting imprint on the pressure map. This is however not the subject of this work.

The third permeability estimation method discards the pressure input, and only works with the maps of saturations. It is an iterative procedure which starts from certain initial permeability approximation. In each iteration it calculates the pressure map and tracks the streamlines. By calculating analytically the pressure drop along each streamline and comparing it with the observed pressure drop, an equation for the permeabilities along the streamline can be written. A system of such equations with added regularisation conditions is then solved to give an updated permeability map, which is then passed to the next iteration. The algorithm was tested on simple 2D models to check the impact of the initial permeability approximation and the different parameterisation approaches (continuous, coarse regions, kriging). While the method occasionally showed reasonable results, its general performance was unfavourable for practical application: the resolved maps of permeability often look non-geological, or cannot predict the saturation fronts with sufficient quality. One of the major problems of the method is that the permeability and the streamlines are not coupled within each iteration, which results in the convergence problems. The key factors controlling the convergence and quality of the results are the initial permeability approximation map, the parameterisation approach and the regularisation settings. No simple recipe was found however on how these should be defined to make the method work properly. Thus, application of the third method may be more problematic than application of the first two approaches.

In general, the practical application of the three permeability estimation techniques considered here would require the 4D seismic data with small noise levels and a high precision procedure for the pressure and saturation inversion. Depending on the petro-elastic properties of the reservoir, the 4D seismic attributes may be dominated by either pressure or saturation signal. As a result, either pressure or saturation map will be inverted with higher confidence. If the more reliable map is that of pressure, then one may consider using method #1 or #2 for the fast-track estimation of permeability. In case of the reliable saturation, method #1 or #3 should be selected.

All three permeability inversion procedures apply some fast-track methods to analyse the flow mechanics. While these methods are fast, they lack coupling between the quantities describing the fluids flow – permeabilities, pressures, saturations. The first procedure does not have coupling between the estimated permeability and the streamlines, since the latter are tracked using the input pressure map. The second procedure does not account for the saturation, and only considers the pressure maps. The third algorithm does not couple permeability and the streamlines within each iteration. The lack of coupling naturally leads to higher sensitivity to the input noise and the impaired convergence, which was observed throughout this chapter. An analogous situation is known e.g. for the explicit numerical schemes for solving the differential equations. The explicit scheme uses simple ways to find the solution at the next time step, however the values of the variables at that step are not coupled, which leads to the amplified error propagation, poor stability, and may result in a complete divergence. As a contrast, implicit numerical schemes resolve the variables at the next time step in a coupled manner, which leads to high computational costs, however the scheme becomes stable, and the errors do not propagate. The same thing as for the implicit schemes can be expected for the problem of permeability calculation, i.e. if a permeability estimation method provides maximum coupling between the quantities describing the fluid flow, there may be a better tolerance to the input errors, and increased ability to produce the hydrodynamically consistent results. Such a coupled procedure for permeability estimation is *history matching*, which is indeed more computationally costly. Apart from high tolerance to the input errors, history matching is also a more flexible tool than just a permeability estimator, or a predictor of the future saturation fronts. Different aspects of history matching constitute the second major part of this thesis and are considered in detail in the next three chapters.

3.7 List of codes

For the studies described in this chapter the following programs were coded:

1. **Permeability estimation code #1**. The program is the extension of the saturation prediction code from Chapter 2. In particular, the extended code requires the additional settings for the phase relative permeability estimation, regularisation settings (Figure 3.1), and the objective function settings (3.7). Porosity map is also added to the input. The output is the estimated permeability map.

   Coding language: C++.

2. **Permeability estimation code #2**. The program works with the input of a few pressure maps, saturation maps (optional, needed to calculate the fluid mobility), the corresponding well flow rates in the reservoir conditions, the elliptic boundaries for the wells, phase relative permeabilities and fluid viscosities (optional), regularisation settings, conjugate gradients solver stopping criteria. The output is the estimated permeability map.

   Coding language: C++.

3. **Permeability estimation code #3**. The program takes the majority of input from the permeability estimation program #1 since it performs streamline tracking. However, the initial permeability approximation is supplied instead of the pressure map. The additional input includes the phase relative permeabilities and fluid viscosities, the reservoir thickness map, the regularisation settings, settings for the conjugate gradients nonlinear optimiser, and the total number of iterations. In case of using the kriging parameterisation, the variogram parameters (1D variogram type, 2D ellipse ranges and rotation angle) are supplied. In case of using the coarse regions parameterisation, the map with the regions indices is supplied. The sub-step of the pressure calculation from the permeability map is performed by using Schlumberger Eclipse simulator. The output of the program is the estimated permeability map.

   Coding language: C++.

Chapter 4 Time-lapse seismic history matching for thin reservoirs

In this chapter a seismic history matching procedure will be considered, with the following aspects discussed: model parameterisation, definition of the objective function, a few remarks on the optimisation algorithm, and finally incorporation of the time-lapse seismic data into the history matching loop. The latter aspect will be handled in the thesis in quite a novel way – by performing the regression between the 4D seismic attribute maps and the average maps of the dynamic reservoir properties, instead of performing the standard petro-elastic modelling and seismic trace modelling. In contrast to the fast-track algorithms considered in the two previous chapters, history matching relies on the full-physics reservoir simulator, and iteratively resolves the model parameters which provide the best possible match to the observed well and seismic data. This makes history matching a more time-consuming procedure, but on the other hand a more flexible one in terms of the input it can take, compared to the fast permeability and saturation estimation methods. Benckmarking of the different methods – from the fast-track ones to the full-fledged history matching – will be done for a simple synthetic 2D problem, showing that the fast-track methods are a better choice for the case with noiseless input, whereas the slower history matching workflows are more robust for the situation of noisy input.

4.1 Automated history matching loop

All the history matching jobs considered in this thesis are performed by an automated loop which couples two procedures: forward modelling and optimisation algorithm, see the workflow scheme in Figure 4.1. *Forward modelling*, or solution of the forward problem, converts the specified model parameters into the model response. It consists of the following major steps:

1. *Pre-processing step* takes the input vector of parameters and prepares the model dataset based on them.
2. *Simulation step* runs the prepared simulation model, which is done by Schlumberger black oil simulator Eclipse 100.
3. *Post-processing step* reads the model output consisting of well data and 3D grids of dynamic model properties (pressures, saturations). Based on that, the objective function is calculated.

Description of the postprocessing step – i.e. definition of the objective function – is done in sections 4.2, 4.4. At the moment let us make some comments on the preprocessing – i.e. parameterisation step. Firstly, for each model parameter x_i the lower and upper bounds are imposed: $l_i \le x_i \le u_i$. These are the primary constraints considered for the optimisation problem.

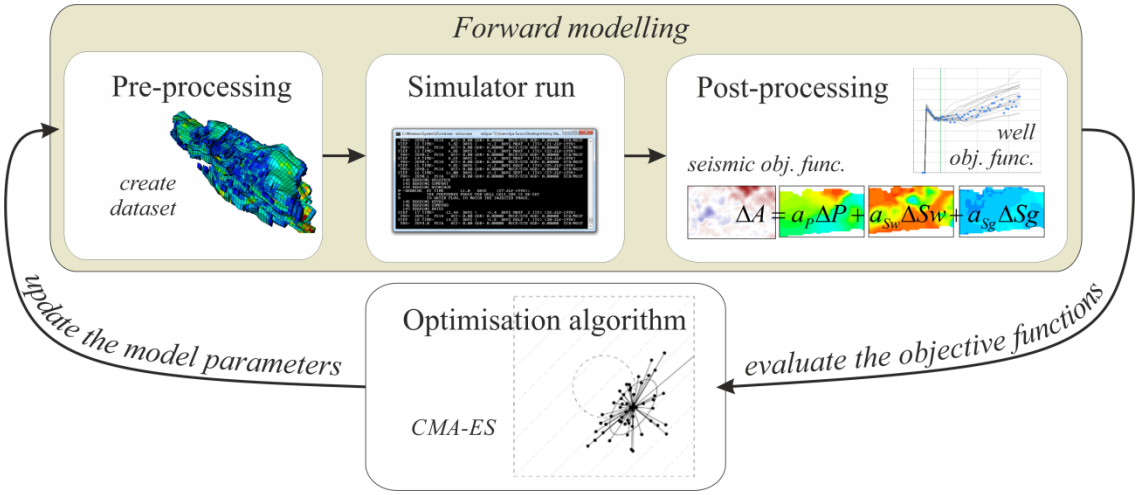

Figure 4.1 History matching workflow.

Secondly, from the point of view of optimisation algorithm performance it is beneficial to have all the parameters varying in approximately the same range. However, in the simulation model the parameters may be required to vary with totally different scales, e.g. porosity range may be 0.1 – 0.3, a fluid contact depth range may be 2000 m – 2010 m, fault transmissibility multiplier range may be 10^{-5} – 10^{-1}. To treat this situation, function transforms are applied to the parameters x_i handled by the optimiser to convert them to the parameters written to the model dataset y_i. The transforms include: linear $y_i = a_i x_i + b_i$ and exponential transform $y_i = 10^{a_i x_i}$.

The parameters which can be written to the simulation model dataset include:

1. Any number in the dataset file, e.g. fluid contact depth, permeability multiplier for a cell or a range of cells, well skin factor.
2. Tables defining the phase relative permeabilities based on some continuous parameterisation of the curves: Corey, Chierici or LET, see Appendix C for more details.

3. 3D grid of some property (porosity, permeability) calculated by kriging from the values at pilot points, see Appendix D for more details.

The *optimisation algorithm* that was chosen in this work is CMA-ES[14] - a black box optimiser with open source code, and this choice will be explained in section 4.3. The details on the algorithm can be found in [57], [58], as well as in Appendix B. The whole history matching procedure was coded as a parallel C++ MPI program, which can take advantage of the parallel computing resources.

4.2 Objective function

For *conventional well history matching* the objective function calculates the misfit between the modelled well data d_k^{mod} (bottom-hole pressures, production rates, water cuts, GORs, etc.) and the corresponding observations d_k^{obs}. The index *k* is this notation refers to a specific well, data type, and the time moment. The typical simple definition of the objective function is through the sum of squared differences with appropriate scaling:

$$f_1 = \sum_{k=1}^{N_d} \left(\frac{d_k^{obs} - d_k^{\text{mod}}}{\sigma_k} \right)^2, \tag{4.1}$$

where the sum is taken over all available observed data d_k^{obs}, and N_d is the total number of these data. The normalising constants σ_k allow handling data with the different magnitude. The other beneficial side of definition (4.1) comes from its application to uncertainty estimation, because it can be used to find the likelihood function $L = \gamma \exp(-0.5 f_1)$ for the situation where the errors $d_k^{obs} - d_k^{\text{mod}}$ are uncorrelated and have normal distribution with zero mean and standard deviation equal to σ_k. For a more general case with correlated errors, a full covariance matrix C_w should be introduced, resulting in the definition

$$f_1 = (\vec{d}^{\,obs} - \vec{d}^{\,\text{mod}})^T C_w^{-1} (\vec{d}^{\,obs} - \vec{d}^{\,\text{mod}}). \tag{4.2}$$

The latter approach will be discussed in detail in the subsequent Chapter 5. For the numerical tests considered in this chapter, definition (4.1) will be used.

[14] CMA-ES = Evolution Strategy with Covariance Matrix Adaptation.

For *seismic history matching* I will consider the objective function consisting of two parts which account for the model fit to both observed well data and seismic data:

$$f = f_1 + f_2, \tag{4.3}$$

where, leaping ahead, the value of the seismic part of objective function f_2 is found either as a sum of squares (4.11) or a more general quadratic form (4.12). The approach for calculation of f_2 I introduce here avoids the full-physics petro-elastic and seismic modelling, and the motivation behind it will be set forth in section 4.4. Note that definition (4.3) does not include any weights for the two components of the objective function. These weights could be included for the flexibility of the history matching workflow, so that an engineer can quickly put more emphasis on either component. However, for uncertaiunty estimation application no weights should be used, and the relative impact of both components is accounted for by their covariance matrices.

It is worth making a comment on the expected value of the objective function defined by (4.1), (4.2) or (4.3) after optimisation has finished. As discussed in [56], if the forward model – i.e. the link between the model parameters and the model data – was linear, and if the covariance matrix *C* correctly described the data errors, then f at its minimum would follow a χ^2 distribution with υ degrees of freedom, where $\upsilon = N_d - N_p$, the quantity N_d is the number of data, and N_p is the number of parameters. This statement is true if the inverse problem is not under-determined and the forward modelling matrix has full rank[15]. For this χ^2 the mean value is υ, and the variance equals 2υ, so the following estimate of the minimum of f can be considered, as suggested in [42]:

$$\upsilon - 5\sqrt{2\upsilon} \le f_{\min} \le \upsilon + 5\sqrt{2\upsilon}. \tag{4.4}$$

If, in addition, a Gaussian prior model was used, then, as discussed in [56], [42], the total misfit for the *maximum a posteriori* (MAP) estimate of the model would then follow χ^2 distribution with N_d degrees of freedom, independent of the number of model parameters used. However, in this thesis only simple priors are considered, viz. uniform priors defined over some regions in the parameter space, so the previous estimate with $\upsilon = N_d - N_p$ will be more relevant. These considerations are only

[15] The rank in this case is N_p.

rigorous for the case of linear forward modelling, and the quasi linear situations are to be treated with caution. However, Oliver et al. [42] report that for synthetic history matching problems the expected minimum value of misfit for MAP estimates is in reasonable agreement with the above theory. If the final value of the objective function after optimisation is not consistent with the estimate (4.4), this may mean failure of the optimisation algorithm to find the global minimum, or incorrectly defined standard deviations of the data errors. Too low values of $f_{\min}$ will mean overestimated std's, too high values will correspond to underestimated std's. Since in this work priors with uniform distribution over some region are used, if this region happens to be too small and restrictive, this may also lead to higher values of f at the global optima. It is well known that as the number of degrees of freedom υ increases, the χ^2 distribution converges[16] to a normal distribution with mean υ and standard deviation $\sigma_0 = \sqrt{2\upsilon}$. Because of this, if the minimum objective function value $f_{\min}$ follows χ^2 distribution with large υ (e.g. there is a large number of data), then one can also consider $f_{\min}$ to be distributed according to $N(\upsilon, \sigma_0)$, and the estimate (4.4) can be rewritten as

$$\upsilon - 5\sigma_0 \le f_{\min} \le \upsilon + 5\sigma_0. \tag{4.5}$$

4.3 Optimisation algorithm testing on a synthetic model

In order to test the history matching workflow outlined in section 4.1, and to assess performance of CMA-ES optimisation algorithm for history matching purposes, the PUNQ-S3[17] synthetic model was considered. This model was used in [35], [34] for benchmarking with a few stochastic optimisation algorithms, e.g. neighbourhood algorithm, ant colony optimisation, differential evolution (DE), particle swarm optimisation (PSO), Bayesian optimisation algorithm (BOA). I treated PUNQ-S3 as close to what was done in these papers as possible. To parameterise the model, 45 regions of constant porosity were selected – 9 regions per each of the 5 model layers. The corresponding porosity values were then used as 45 model parameters. Horizontal

[16] Due to the central limit theorem.

[17] The dataset is available at www3.imperial.ac.uk/earthscienceandengineering/research/perm/punq-s3model. This model is reasonably known in the literature and is used for benchmarking different history matching and uncertainty estimation algorithms.

permeabilities k_h and vertical permeabilities k_v were calculated from porosities φ, as shown in Figure 4.2.

The ranges for the porosities were taken as in the quoted papers:

- $\varphi \in [0.15, 0.30]$ for layers 1, 3, 5;
- $\varphi \in [0.05, 0.15]$ for layer 2;
- $\varphi \in [0.10, 0.20]$ for layer 4.

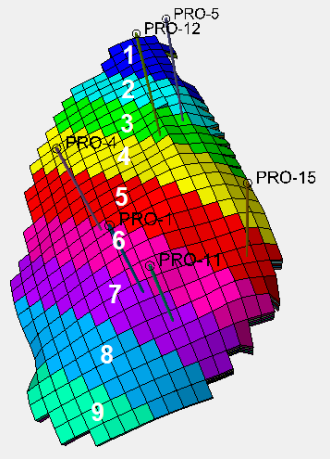

$$\ln(k_h) = 0.77 + 9.03\varphi$$
$$k_v = 3.124 + 0.306 k_h$$

Figure 4.2 Parameterisation of PUNQ-S3 model. *Left* – regions of constant porosity, *right* – formulae for calculation of permeabilities.

The objective function was defined as in (4.1) with the only difference that it was then divided by 117 – the total number of measurements. Data measurements of bottom-hole pressures, GORs and water cuts, together with the associated σ_k's were taken from the PUNQ-S3 website. CMA-ES, which is a population-based algorithm, was compared with the three other population-based algorithms: DE, PSO and BOA. The other optimisation procedures which can be found in the cited papers were not considered here because they converge more slowly. To run the three mentioned algorithms, a proprietary software developed by a Heriot-Watt University spin-off company[18,19] was used. All the meta-parameters of the algorithms, except for the number of models per generation, were taken as the defaults provided by the software. For each algorithm, a single optimisation run consisted of 3000 forward modelling runs, with 50 forward modelling runs per one generation of models, and 60 generations

[18] www.epistemy.com

[19] The authors of the two quoted papers worked very closely with the company which developed the software.

altogether. Since all the considered algorithms are stochastic, for a fair comparison five history matching runs were performed for each algorithm. The results in terms of the objective function progress can be found in Figure 4.3.

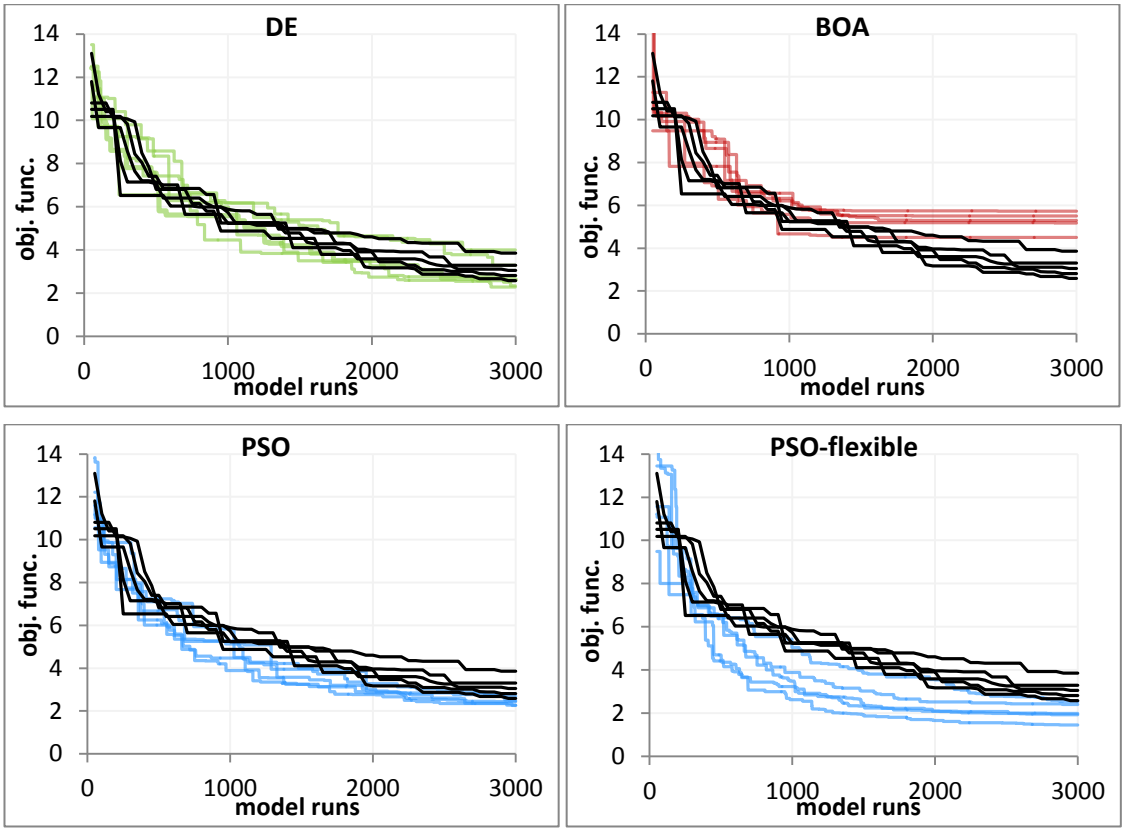

Figure 4.3 Objective function (best-so-far value, on *y* axis) vs. forward modelling runs number (*x* axis). Black lines correspond to CMA-ES, coloured lines correspond to the other algorithms. *Top row, left to right*: DE/best/1/exp, BOA, *bottom row, left to right*: PSO, PSO-flexible.

As can be observed, CMA-ES convergence behaviour approximately matches that of the DE[20]. BOA convergence is similar to CMA-ES in the beginning, but then it stops prematurely, resulting in history matching finishing with relatively high values of the objective function. PSO outmatched CMA-ES both in terms of the final values of the objective function, and in terms of the convergence speed which was on average 1.5 times higher than for CMA-ES. Another flavour of the particle swarm optimisation called PSO-flexible performed even better, giving two times convergence speed-up compared to CMA-ES. Although CMA-ES is not the fastest algorithm among those

[20] The type of DE algorithm used here is denoted DE/best/1/exp, which means that it uses the **best** vector for mutation, **one** difference vector and **exponential** crossover scheme. The other type of DE available from the software, called DE-random, converges more slowly.

considered, it still can be regarded as a sensible choice for history matching, and will be used for that purpose in this thesis. This choice is based on the algorithm's availability, easy setup of the meta-parameters, good invariance properties (see Appendix B), and ability to converge to the reasonable solutions (albeit slower than the PSO). The study and development of the optimisation algorithms appropriate for history matching is not among the primary goals of this work, and any deficiencies in the convergence speed will be compensated by considering bigger numbers of the forward modelling runs.

Finally, it is worth mentioning that different modifications of CMA-ES also exist as can be found in the literature, e.g. active CMA-ES [59] and (1+1)-CMA-ES [60] for which up to 2 times speed-up is reported compared to the original CMA-ES configuration.

4.4 Seismic history matching approach for thin reservoirs

To incorporate 4D seismic into the history matching loop, a procedure is proposed in what follows, which allows quantitative estimation of the agreement between the measured seismic and the reservoir simulation model. The procedure is designed to work with 2D maps of the time-lapse attributes, so it is suitable essentially for thin reservoirs, where the map-based approach can be used with confidence, and there is no need to deal with seismic in the volumetric terms. To compare a time-lapse seismic attribute map with the simulation model, I start from considering a linear relationship between the seismic and the average maps[21] of the reservoir dynamic properties: pressure, water and gas saturations.

$$\Delta A = a_P \Delta P + a_{Sw} \Delta Sw + a_{Sg} \Delta Sg. \tag{4.6}$$

In this equation ΔA, ΔP, ΔSw, ΔSg represent the time-lapse *maps* of the corresponding quantities (seismic attribute, pressure, water saturation and gas saturation respectively), a_P, a_{Sw}, a_{Sg} are the *constant numbers*, and the equation is treated in the point-wise sense. Generally, the coefficients $a_i, i \in \{P, Sw, Sg\}$ would vary laterally depending e.g on the reservoir porosity and NTG. This variation will be accounted for below by multiplying the right hand side by a scaling map, however the coefficients themselves will still be treated as constants. When seismic data for the given reservoir is available from *multiple* monitors, then all these data can be used in the equation. In this case the

[21] In this work averaging of 3D grid properties to get the maps is done with pore volume weighting.

left hand side will include all the points of time-lapse attribute maps from all monitors, the right hand side will include the points of the reservoir dynamic property maps from the corresponding time steps. Relationships of this sort were considered in [6], [7], [61], where the constants a_i are typically estimated by linear regression from the data at well locations, or using a calibrated petro-elastic model. Once a_i's are found, one can calculate the seismic response using this formula, thus avoiding the full physics seismic modelling.

In [62] the authors analytically derive the equation of type (4.6) for a water-oil system by considering the reflectivity on the interface between the cap-rock shale and the reservoir sand. Their equation reveals how the coefficients a_P, a_{Sw} depend on the underlying reservoir parameters such as porosity, the petro-elastic parameters, and the offset range. The coefficient a_P embraces the rock stress sensitivities and fluids response to the pressure change, and the coefficient a_{Sw} takes account of the difference in the bulk modulus and density between oil and water. Both coefficients are functions of porosity[22] and the AVO effects.

In application to history matching, relationship (4.6) can be used to estimate the agreement between the seismic (left hand side) and the simulation model (right hand side) even without calculating the unknown constants a_i in advance. For that, the *linear regression* is performed with the points from the map ΔA being the dependent variables, the corresponding points from ΔP, ΔSw, ΔSg being the independent variables, and constants a_i being the regression coefficients. High quality regression can then be regarded as a sign of good agreement between the seismic and the simulation model, and the *coefficient of determination* R^2 can be used as a quantitative measure of it[23]. Since R^2 is close to 1 for high quality regression, and close to 0 (or even becomes negative) for poor quality regression, it is natural to consider $1-R^2$ as the seismic part of objective function f_2. At the end of this section a slightly different definition of the seismic part of objective function will be introduced which allows a more sensible

[22] Dependence of *a*'s on NTG and the reservoir thickness is not considered in the quoted paper, but, generally speaking, it exists along with the dependence on porosity.

[23] R^2 is a coefficient indicating how well a statistical model (obtained by regression) fits the data, and is defined as $R^2 = 1 - \sum (y_i - f_i)^2 / \sum (y_i - \bar{y})^2$, where the y_i are the data values, $\bar{y}$ is their mean, and f_i are the values predicted by the model.

treatment of the seismic data errors, with f_2 equal to $1-R^2$ multiplied by a constant. The definition will be further refined in Chapter 5 and will account for the spatial correlations in seismic data errors. At the moment, however, I keep considering simply R^2 because of easiness of its perception.

The use of (4.6) for the linear regression with full maps to find the unknown coefficients a_i and the coefficient R^2 is better than first calculating a_i's from the well data and then using (4.6) as just a simulator-to-seismic procedure, the reasons are as follows:

1. The seismic data is usually noisy, so the linear regression with large amount of data (maps) is more robust than the regression with little data (wells).
2. In the real case, to find a_i's from the well data, one would require knowledge of the pressure, water and gas saturations at wells. Such data may not be available in the form of measurements, e.g. the measurements of water[24] or gas saturations at wells are not very common. Treatment of the reservoir pressure is also not trivial, since pressure has a very sharp peak near the wells, so seismic "sees" some average of this peak, and it definitely does not see the *bottom-hole pressure*, which is usually measured at the wells[25]. Besides, the available measurements may miss the time of the seismic monitor acquisition. Thus, in most cases, to estimate a_i's from the well data, a history matched model is necessary.

The basic formula (4.6) is a very rough tool, and it may require some modifications in order to provide a better link between the seismic and the simulation model. Two modifications will be examined here: firstly, point-wise multiplication of the right hand side by some scaling map A_0

$$\Delta A = (a_P \Delta P + a_{Sw} \Delta Sw + a_{Sg} \Delta Sg) \cdot A_0, \tag{4.7}$$

and secondly, introduction of the quadratic terms of the reservoir dynamic properties, like ΔP^2 or $\Delta P \cdot \Delta Sw$

[24] Determination of the water saturation in a cased well requires the pulsed neutron logging.

[25] The same thing applies to the *pressure differences*: the reservoir pressure differences between the monitors have sharp peak at the wells, and 4D seismic does not see the differences of the bottom-hole pressure.

$$\Delta A = (a_P \Delta P + a_{Sw} \Delta Sw + a_{Sg} \Delta Sg + a_{PP} \Delta P^2 + a_{PSw} \Delta P \Delta Sw + ...) \cdot A_0. \quad (4.8)$$

Multiplication by the scaling map allows accounting for the lateral variations of the static reservoir properties such as thickness, porosity and NTG, which affect the time-lapse seismic response of the reservoir. In [61] it is essentially proposed to use the *pore volume map* as A_0. In [6] the left hand side of equation (4.6) is divided by the map A_0 equal to the *baseline seismic attribute map*. However it should be noted that division operation is ill-posed compared to multiplication, and numerical problems may emerge at the points where A_0 is close to zero. Instead, multiplication of the right hand side by A_0 is deemed to be a more appropriate treatment of the reservoir lateral heterogeneities, as proposed in equation (4.7). In what follows I will use the scaling map A_0 equal to the baseline attribute map, and the reasons for that will be briefly discussed below. Multiplication of the right hand side of equation (4.6) by the baseline attribute map is also appealing from the point of view of the physical "dimensionality" of both sides of the equation, since in this way the *seismic* in the left hand side is equated to the *seismic* in the right hand side (while the term in the brackets can be deemed dimensionless).

Introduction of the quadratic terms for pressure was considered in [7]. In the present work I also introduce the quadratic terms for the other parameters like water or gas saturation, and the mixed terms like $\Delta P \cdot \Delta Sw$. All the three formulae considered above use the linear (or at most quadratic) gas term, whereas in the literature it is often believed that gas impact on the 4D seismic is nonlinear, e.g. in [7] the exponential dependence on ΔSg is used. In this work linear treatment of gas is adopted, as established in [61].

To illustrate the effect of both modifications (4.7) and (4.8) on the linear regression quality, first consider the three-phase 3D heterogeneous synthetic model which is discussed in more detail in Chapter 5[26]. There are two wells working in the reservoir: an injector which partially penetrates the water-saturated zone, and a producer which penetrates the small gas cap. For this model the time-lapse maps of the seismic attribute, pressure, water and gas saturations were created (see Figure 4.4). To model the synthetic seismic I employed the procedure and the associated settings as described in Appendix A. The seismic attribute used is the sum of negative amplitudes between the reservoir top and base horizons.

The regression was performed between the time-lapse seismic and the reservoir dynamic parameters with the different options for scaling and quadratic terms. The

[26] This is the only model considered in Chapter 5, so the reference has no ambiguity.

basic equation (4.6) resulted in R^2 = 0.65, as shown in Table 4.1. Using the baseline seismic attribute map for scaling in (4.7) improved it to R^2 = 0.726. A smaller enhancement takes place when two quadratic terms $\Delta Sw^2, \Delta Sg^2$ are introduced, leading to R^2 = 0.74. These two terms had the maximum contribution, and once these were added, introduction of any other quadratic term only gave a marginal improvement. Cross-plots demonstrating the regression quality for the basic equation (4.6) and equation with the scaling and quadratic terms (4.8) are shown in Figure 4.5.

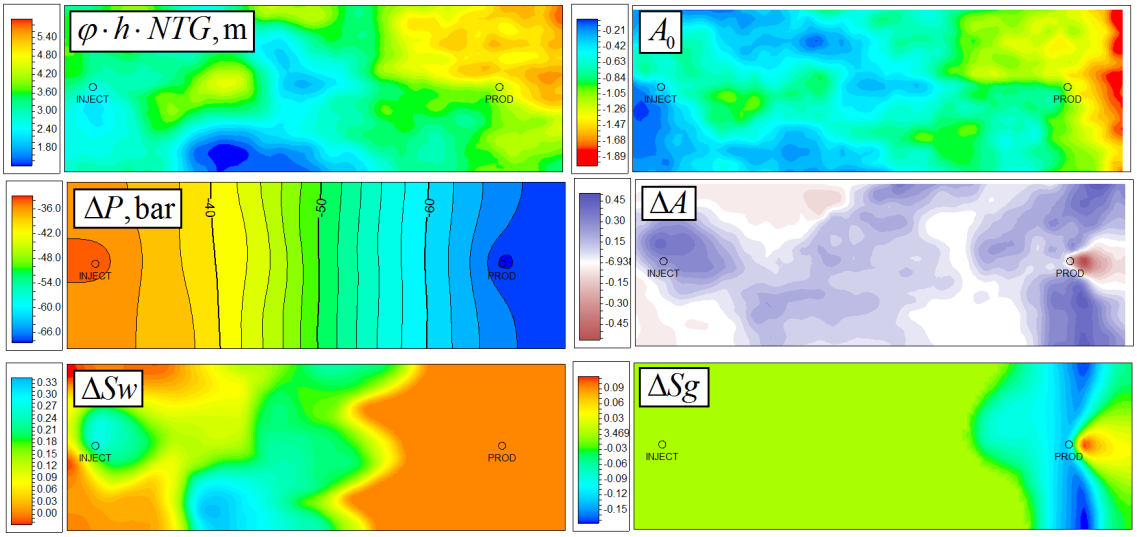

Figure 4.4 Maps for the three-phase 3D heterogeneous model: $\varphi \cdot h \cdot NTG$, baseline attribute map (A_0), time-lapse attribute map (ΔA), and the corresponding time-lapse average maps of pressure (ΔP), water saturation (ΔSw), gas saturation (ΔSg). The figure replicates Figure 5.7.

	no scaling	scaling (A_0 = baseline seismic)
non-quadratic	0.650	0.726
quadratic ($\Delta Sw^2, \Delta Sg^2$)	0.661	0.740

Table 4.1 Values of R^2 for different equation modifications: (4.6) - (4.8). The results are based on the synthetic model from Chapter 5.

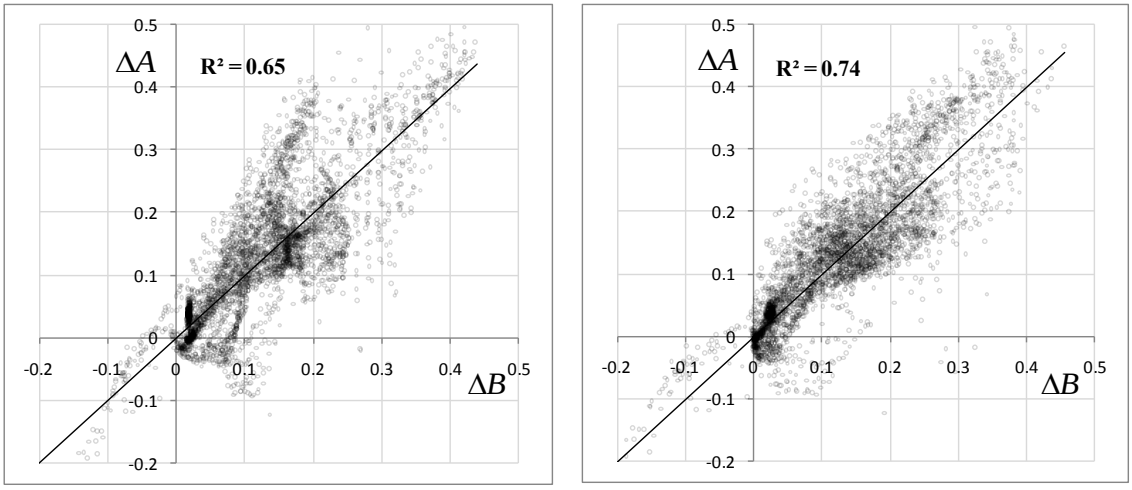

Figure 4.5 Cross-plots of the measured 4D seismic attribute versus that calculated by equations (4.6), (4.8). *X* axis is the attribute calculated in the right hand side of the equations (ΔB). *Y* axis is the measured attribute given by the left hand side (ΔA). *Left*: basic equation (4.6), *right*: equation with scaling and quadratic terms $\Delta Sw^2, \Delta Sg^2$ (4.8). The results are based on the synthetic model from Chapter 5.

Now, let us give another example of regression based on a small region of the 3D simulation model of Schiehallion field[27]. Two versions of the permeabilities and transmissibility multipliers were considered for the model, resulting in the corresponding two versions of the reservoir dynamic parameters. The major difference can be observed in the pressure map: for version #1 the pressure changes are large, for version #2 they are moderate. Porosity, NTG and reservoir geometry are identical for both cases. Figure 4.6 shows the resulting time-lapse maps of pressure, water and gas saturation, along with the maps of $\varphi \cdot h \cdot NTG$, baseline seismic and the time-lapse seismic attribute ΔA. Synthetic seismic was generated by the same procedure as mentioned above. For the selected petro-elastic model and the seismic attribute type (sum of negative amplitudes) the attribute increase (e.g. from -2.0 to -1.0) corresponds to the reservoir hardening, displayed with blue colours. The attribute decrease corresponds to the reservoir softening, displayed with red colours.

It can be seen on the picture that in version #1 the time-lapse seismic ΔA is dominated, depending on location, by either pressure (notable reservoir softening near well INJ2) or saturation. In version #2 ΔA is dominated by saturation, showing the reservoir hardening almost everywhere. Linear regression with equations (4.6), (4.8) was

[27] The simulation model was provided by the operator company. Schiehallion field will be considered in more detail in Chapter 6. The small region of the model examined here is from a different segment of the field than the segment history matched in Chapter 6.

performed for these maps, and the results for version #2 are presented in Figure 4.7 in the form of cross-plots. For equation (4.8), with the results shown on the right cross-plot, I used the *baseline attribute map* for scaling and the quadratic term ΔSw^2. As can be seen, this led to the notable improvement in the coefficient R^2. Addition of other quadratic terms almost did not enhance the regression quality. A wider picture presenting the different combinations of the scaling options and quadratic terms for both versions #1 and #2 is given in Table 4.2. The table shows R^2 for the situation with no scaling, scaling with the baseline attribute map and scaling with $\varphi \cdot h \cdot NTG$ map. The latter map is no more than the map of pore volume per unit area. As can be seen, the usage of $\varphi \cdot h \cdot NTG$ for scaling gives somewhat worse results than the use of the baseline attribute map. Besides, in the case of a real reservoir, one is not likely to have a reliable map of $\varphi \cdot h \cdot NTG$, whereas the seismic attribute maps are readily available. For this reason I will only consider scaling with the baseline attributes in this work.

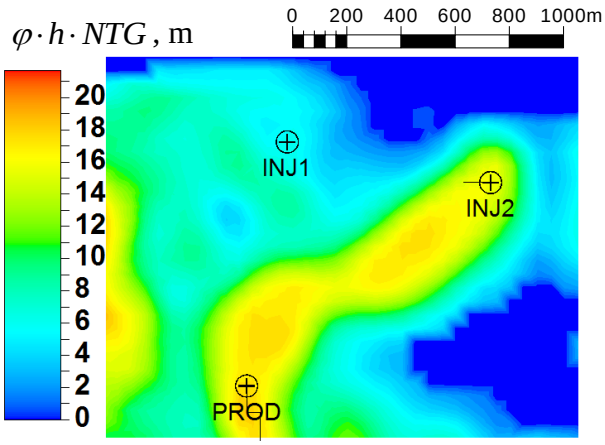

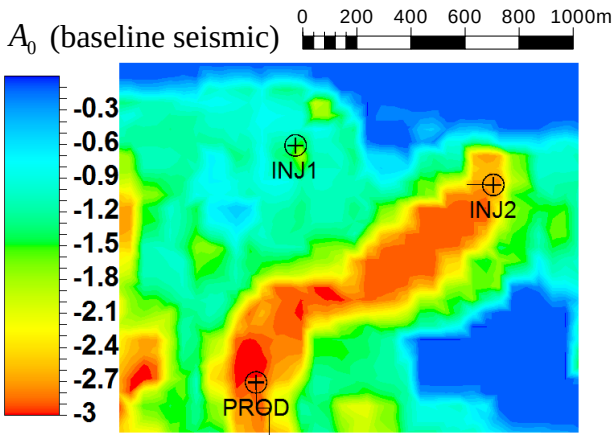

version #1 **version #2**

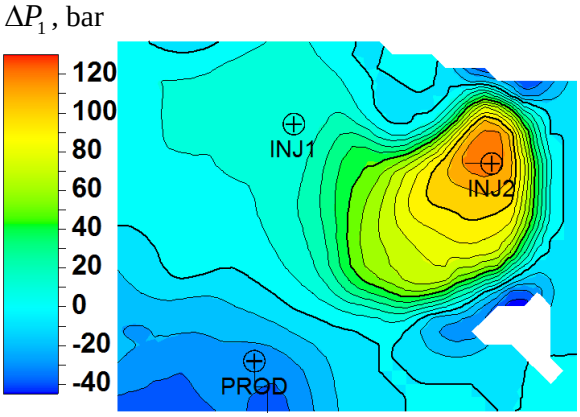

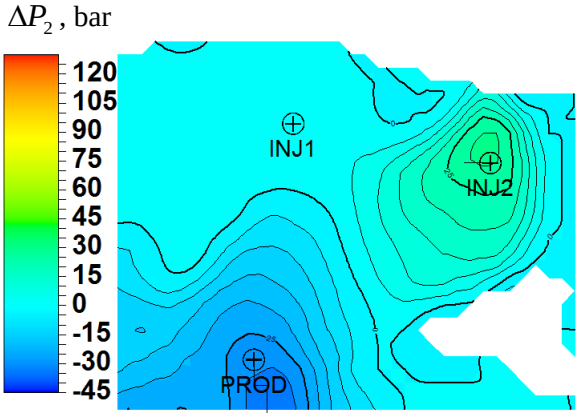

continued on the next page

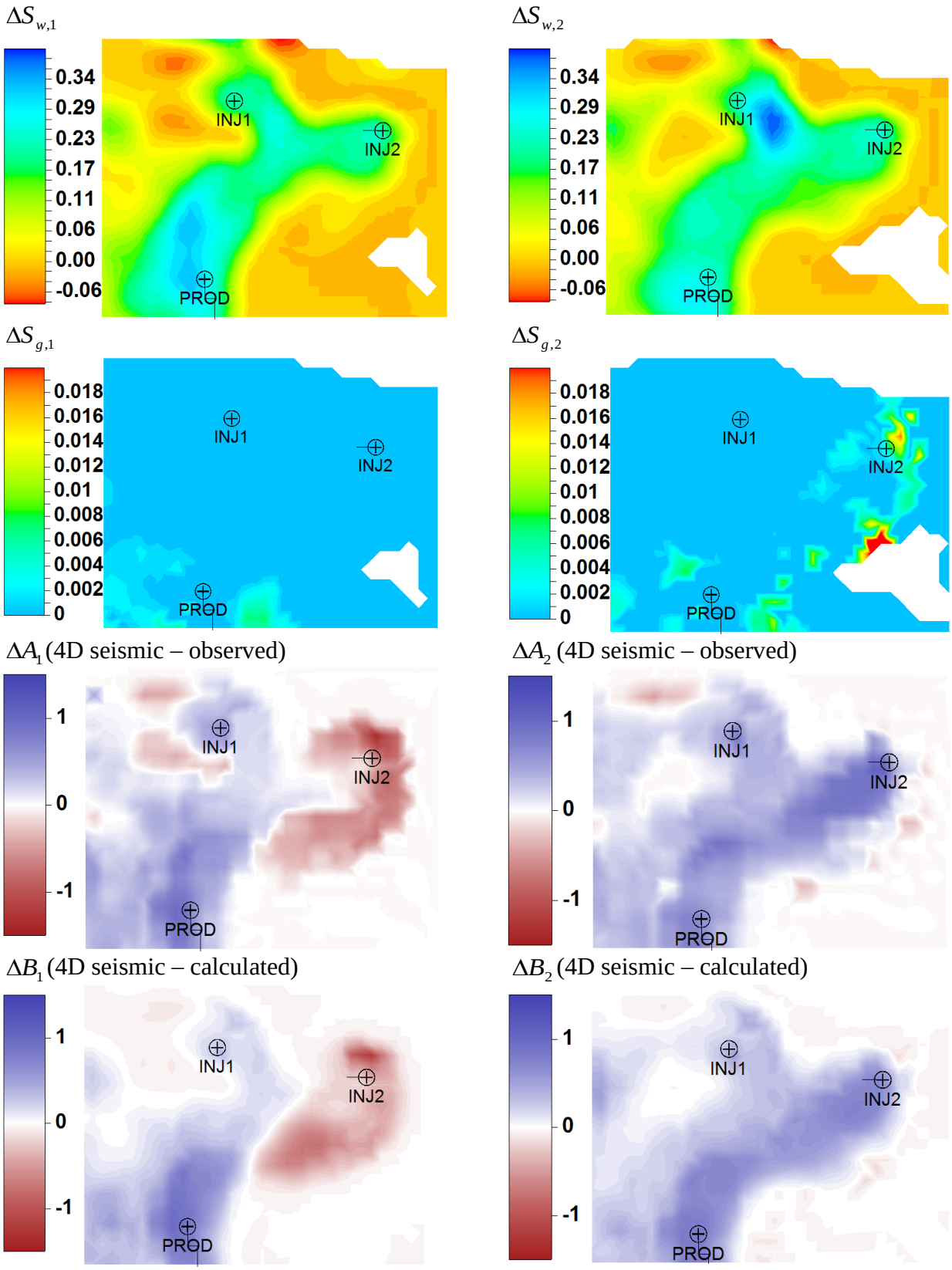

Figure 4.6 Maps obtained from a small region of Schiehallion simulation model. *Top row*: $\varphi \cdot h \cdot NTG$ (pore volume per unit area), baseline seismic attribute. *Subsequent rows:* time-lapse maps of pressure, water saturation, gas saturation, observed seismic attribute, calculated seismic attribute. The time-lapse maps in the *left column* are for version #1, in the *right column* - for version #2.

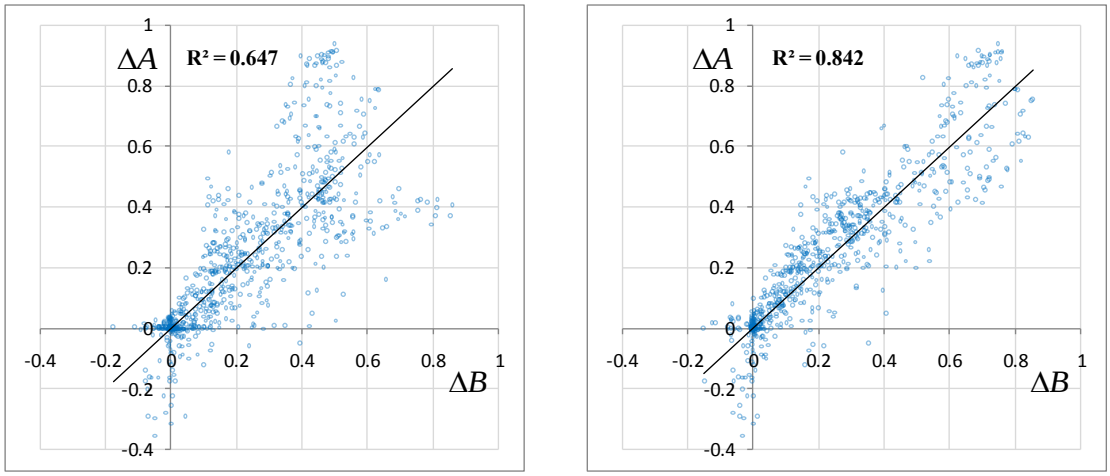

Figure 4.7 Cross-plots of the measured 4D seismic attribute versus that calculated by equations (4.6), (4.8) for version #2. *X* axis is the attribute calculated in the right hand side of the equations (ΔB), *Y* axis is the measured 4D attribute given by the left hand side (ΔA). *Left*: basic equation (4.6), *right*: equation with scaling and quadratic term ΔSw^2 (4.8).

For version #1 application of the scaling map resulted in some decrease of R^2. However, subsequent introduction of terms ΔP^2, $\Delta P \Delta Sw$ improved the regression quality. For version #2, which is saturation-dominated, the scaling map A_0 had a pronounced positive effect, and quadratic terms resulted in a further smaller enhancement. Among all the quadratic terms ΔSw^2 had the strongest impact.

version #1		A_0 map	
quadratic terms	no scaling	baseline attribute	$\varphi \cdot h \cdot NTG$
no	0.791	0.755	0.733
ΔP^2, $\Delta P \Delta Sw$	0.814	**0.804**	0.782
all possible	0.815	0.813	0.791

version #2		A_0 map	
quadratic terms	no scaling	baseline attribute	$\varphi \cdot h \cdot NTG$
no	0.647	0.826	0.792
ΔSw^2	0.679	**0.842**	0.801
all possible	0.681	0.845	0.804

Table 4.2 Values of R^2 for different combinations of scaling maps and quadratic terms. *Left table*: version #1, *right table*: version #2. The *rows* show the different combinations of the quadratic terms used. The *columns* correspond to the different scaling options: no scaling, baseline attribute scaling, pore volume per unit area scaling. The two cases displayed in Figure 4.7 are highlighted with green. The two cases with the modelled 4D attribute (ΔB) displayed in the bottom row in Figure 4.6 are highlighted with bold font.

The maps of the seismic attributes calculated using the seismic-simulator equation (4.8) with the calibrated coefficients a_i are shown in Figure 4.6, *bottom row*. For version #1 calculation of the seismic attribute involved the baseline attribute scaling, and quadratic

terms ΔP^2, $\Delta P \Delta Sw$, resulting in $R^2 = 0.804$. For version #2 I used the same scaling, and quadratic term ΔSw^2, resulting in $R^2 = 0.842$. As can be seen, in both cases the calculated 4D attributes reproduce the observed 4D attributes with rather high quality. The considered examples showed that both scaling operation in equation (4.7) and quadratic terms in equation (4.8) improve the quality of the considered relationship between the time-lapse seismic and the simulation model. In what follows, primarily these two equations will be used.

It may happen that the reservoir in question will consist of several regions with sufficiently different geological properties so that a single equation of the form (4.7), (4.8) will not be able to capture this variability with a single set of coefficients a_i. In this case it may be appropriate to make linear regression separately in each region, finding its own set of a_i's, and calculating the corresponding right hand side of the equation. Then, combining all the "regional" right hand sides, one can get the global right hand side, which can be compared with the left hand side to give the global coefficient of determination R^2.

Practice has also revealed that simply solving either equation (4.7), (4.8) does not always result in the physically meaningful signs of values of the coefficients a_i. Consider, for example, a simple situation when the reservoir pressure decreases $(\Delta P < 0)$, leading to the reservoir hardening. Suppose that the selected time-lapse seismic attribute reacts on the reservoir hardening by increasing its value ($\Delta A > 0$). It is obvious that the resulting derivative $\partial \Delta A / \partial \Delta P$ should be negative. If, for example, one is dealing with equation (4.7), then one arrives at $\partial \Delta A / \partial \Delta P = A_0 \cdot a_P < 0$. If linear regression (usually because provided poor quality input) results in positive $A_0 \cdot a_P$, the numerical link between the seismic and the simulation model becomes quite meaningless. To treat this, the constraints are introduced when solving equations (4.7), (4.8) in the least squares sense, which allow maintaining the proper signs of the derivatives of ΔA with respect to the pressure, water and gas saturations. The resulting constrained least squares problem is then solved by the active set method of quadratic programming, see Appendix E for more details. In all seismic history matching problems in this thesis the following derivative signs are maintained:

$$\partial\Delta A/\partial\Delta P \le 0, \qquad (4.9)$$
$$\partial\Delta A/\partial\Delta Sw \ge 0,$$
$$\partial\Delta A/\partial\Delta Sg \le 0.$$

These signs are defined according to the petro-elastic model and the seismic attribute used. For the selected PEM the reservoir sands have lower impedances than the overburden and underburden shales, so the sands correspond to the negative amplitudes on the seismic traces generated with the selected wavelet[28]. Consequently, the sum of negative amplitudes attribute which I employ increases[29] its value in the case of the reservoir hardening (e.g. for the water saturation increase) and decreases its value in the case of the reservoir softening (e.g. the pressure increase, or the gas saturation increase).

Now that the different aspects of the linear regression have been considered, let us draw the line and give the definition of seismic part of the objective function f_2. After either of the map-based equations (4.7), (4.8) has been solved in the least squares sense, denote its right hand side by ΔB. Then, the resulting $1 - R^2$ can be written as ratio of *the sum of squares of residuals* and *the total sum of squares*:

$$1-R^2 = \frac{S_{res}}{S_{tot}} \equiv \frac{\sum_k (\Delta A_k - \Delta B_k)^2}{\sum_k (\Delta A_k - \Delta\bar{A})^2}, \qquad (4.10)$$

where the sums are taken over all points of the maps, for all time-lapse monitors, and $\Delta\bar{A}$ is the mean value of $\{\Delta A_k\}$. As can be seen, this is essentially the sum of squared differences formula. Assuming (for the moment) that the errors in the seismic data are uncorrelated and have standard deviation σ, the seismic part of the objective function can be defined as

$$f_2 = \sum_k \left(\frac{\Delta A_k - \Delta B_k}{\sigma} \right)^2 = \frac{1}{\sigma^2}(1-R^2)\cdot S_{tot}. \qquad (4.11)$$

Since S_{tot} is constant for the given seismic measurements, the proposed f_2 definition is just the scaled $1 - R^2$. In reality the errors in the seismic data are likely to be correlated, so the definition of f_2 would require application of the full data error covariance matrix C_s. This will be performed in detail in the next chapter, converting f_2 into

[28] The Schiehallion wavelet is used throughout the thesis. It was extracted from the coloured inversion full-stack seismic of this field.

[29] Note that this means the absolute value decrease, consider e.g. the change -1500 → -1000.

$$f_2 = (\Delta A - \Delta B)^T C_s^{-1} (\Delta A - \Delta B), \tag{4.12}$$

where the *modelled*[30] time-lapse seismic ΔB is again given by the right-hand side of either equation (4.7), (4.8), and is calculated by finding the unknown coefficients a_i which minimise the value of f_2 in (4.12).

4.5 Benchmarking of different methods

As discussed in Chapter 3, history matching is a procedure that imposes substantial coupling on the variables describing the fluid flow. This makes the procedure rather slow, but at the same time tolerant to the input noise. The fast-track algorithms of the waterflood prediction and reservoir characterisation introduced in Chapters 2 - 3 run faster, but their performance notably degrades with addition of noise to the input data. To check whether seismic history matching is more advantageous than the fast-track algorithms, all these workflows were benchmarked in the same environment, using a simple synthetic 2D model. This allowed analysing the behaviour of these methods and identifying which of them are superior in the situation of either present or absent noise in the input data.

The synthetic 2D model considered here is "case 9" model from Chapter 3 (see Figure 3.9 – Figure 3.11) which has two phases (oil and water), and features high permeable channels connecting the injector and producer (see Figure 4.10, *left*). Three time steps are analysed: step 1 (at 1500 days) and step 2 (at 3500 days) are used as historical steps, providing the data necessary for the further estimation. Step 3 (at 5500 days) is used to control quality of the future forecasts of the saturation front. The input data for the fast-track procedures of Chapters 2 - 3 consist of the pressure and saturation maps which are assumed to have been inverted from the time-lapse seismic data. For seismic history matching, the input of time-lapse attribute maps is required. The attribute I consider here is the sum of negative amplitudes between the reservoir top and base horizons, calculated from the seismic cubes. In turn, generation of the seismic cubes involved the petro-elastic model and the seismic modelling procedure which can be found in Appendix A. The resulting time-lapse seismic maps for three time steps are shown in Figure 4.8. These maps are dominated by the water signal, and only faint pressure signal exists near the wells.

[30] The words *modelled* and *calculated* (time-lapse seismic) are used as synonyms here.

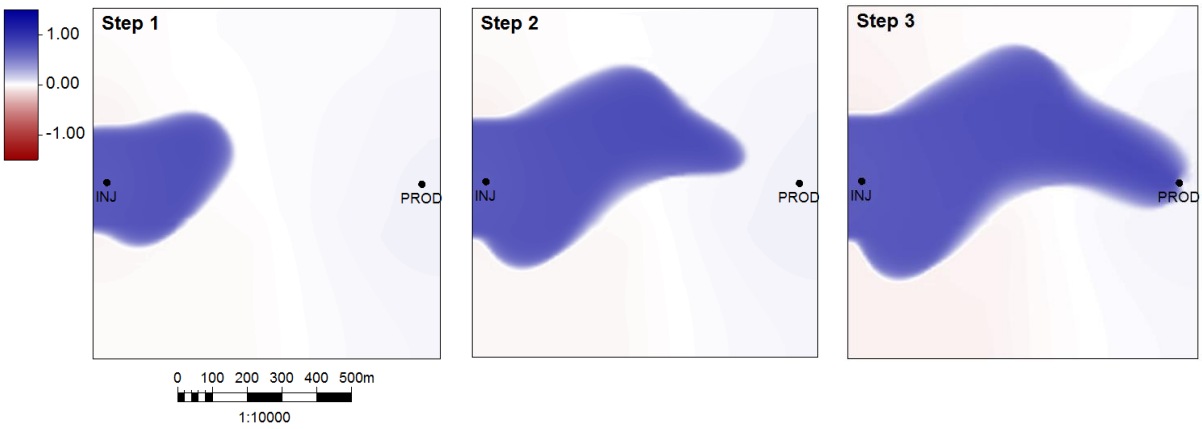

Figure 4.8 Time-lapse seismic attributes (sum of negative amplitudes) for steps 1-3.

The key question in this benchmarking study is investigation of how noise affects performance of the different methods. The following noise was considered for the input data. For the pressure map, the correlated random noise ε_P shown in Figure 3.8 was added, resulting in the pressure displayed in Figure 4.9. Its relative magnitude, i.e. RMS of the noise map divided by RMS of the pressure signal map, equals 17%. For the saturation noise map ε_{Sw}, the same relative magnitude was considered. After the saturation noise was added, the resulting saturation map (see Figure 4.9) was assigned the connate water saturation value in the oil-saturated zones far from the water front. This is a natural step of noise reduction that can be performed for the saturation maps estimated from 4D seismic. Finally, to obtain the seismic attribute noise consistent with the pressure and saturation noise introduced, I considered equation (4.6), dropping out the gas saturation term: $\Delta A = a_P \Delta P + a_{Sw} \Delta Sw$. Given the maps on the right hand side and the left hand side, the constant coefficients were estimated as $a_P = -0.00136\,\text{bar}^{-1}$, $a_{Sw} = 1.274$. From these, the time-lapse seismic noise ε_{dA} was found as $\varepsilon_{dA} = a_P \varepsilon_P + a_{Sw} \varepsilon_{Sw}$, see Figure 4.9.

The different fast-track procedures and seismic history matching were tested for both noiseless and noisy versions of the input data. For the waterflood prediction method, the saturation at step 3 was produced as output. For the permeability estimation methods, as well as for seismic history matching, the output is a permeability map. Furthermore, this permeability map is employed in the simulation model for modelling water saturation at steps 2 and 3. While doing this, the flow rates at wells are maintained equal to the average flow rates in the original simulation model. This allows keeping the same injected and produced volumes, and concentrating the analysis on the

lateral patterns of the predicted saturation fronts. The list of the input and output data for all the methods is shown in Table 4.3.

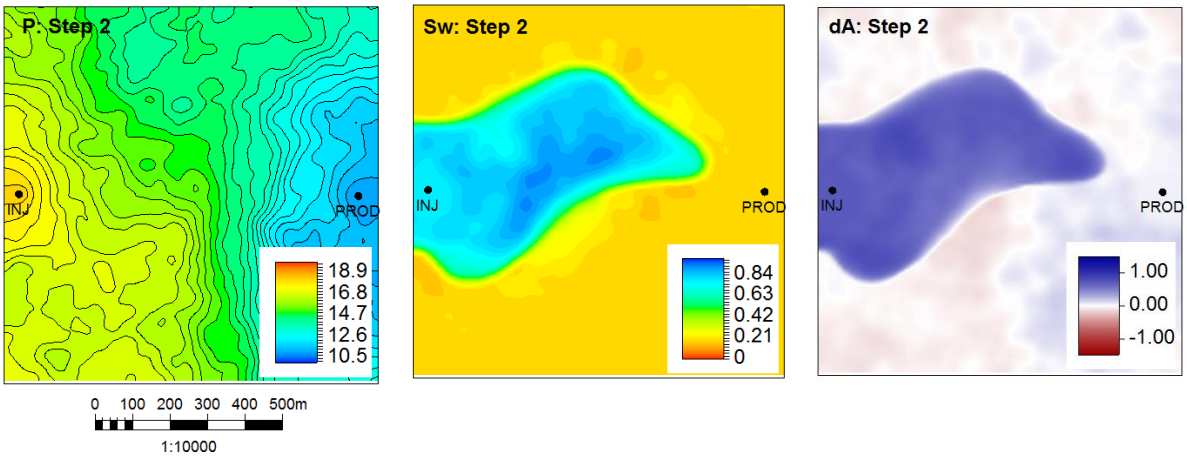

Figure 4.9 Examples of noisy input maps at step 2 used for the fast-track methods, and for the seismic history matching workflow. *Left to right*: noisy pressure, noisy saturation, noisy time-lapse seismic attribute.

For the permeability estimation method #3 kriging parameterisation of the grid was used, with 68 pilot points altogether (see Figure 4.10, *right*) and both variogram ranges equal to 200 m. The same permeability grid parameterisation was employed in the seismic history matching workflow.

	Method	Input	Output
fast-track proceudres	Saturation front prediciton	P_2, S_1, S_2	S_3^*
	Permeability estimation #1	P_2, S_1, S_2	Permeability map, S_2^*, S_3^*
	Permeability estimation #2	$P_1, P_2,$ well flow rates	Permeability map, S_2^*, S_3^*
	Permeability estimation #3	$S_1, S_2,$ well BHP	Permeability map, S_2^*, S_3^*
	Seismic history matching	Simulation model, well production history, A_1, A_2	Permeability map, S_2^*, S_3^*

Table 4.3 Input and output data for the different methods tested. P denotes pressure maps, S – saturation maps, A – time-lapse seismic attribute maps. Subscripts denote the time steps. The star superscript indicates the estimated maps rather than the exact maps from the original model.

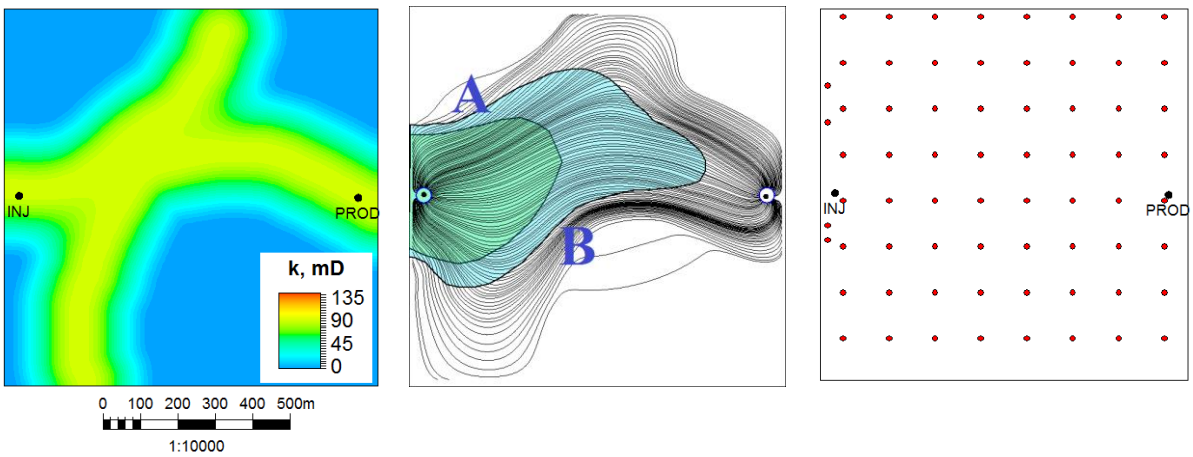

Figure 4.10 *Left*: reference permeability for the Case 9 test model. *Center*: streamlines pattern for permeability estimation method #1 (noiseless). The contours show the saturation fronts for steps 1, 2. Letters A and B show the locations where the streamlines become nearly tangent to the saturation fronts. *Right*: pilot points used in kriging parameterisation (red circles).

The running CPU time for the fast-track waterflood prediction is the smallest among all the methods: 0.3 sec. For the fast-track permeability estimation the CPU time equals 59 sec, 82 sec, and 7 sec for methods #1, #2, and #3 respectively. For seismic history matching the running time is 40,300 sec, however this could be reduced two times by running only half of the total iterations, which would slightly reduce the quality of the final result. As can be seen, in terms of running time the fast-track procedures are 3 orders of magnitude faster than the SHM. Let us however look at the quality of the permeability estimation and saturation prediction made by the different methods.

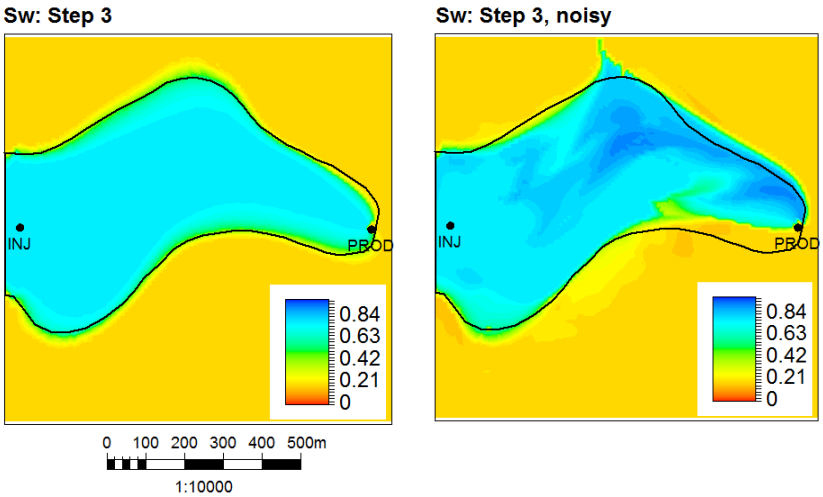

Figure 4.11 Water saturation at step 3 estimated by the fast-track waterflood prediction method. *Left*: for noiseless input, *right*: for noisy input. The black line shows the exact position of the water front.

The resulting saturation maps at step 3 for the fast-track waterflood prediction are shown in Figure 4.11. In order to estimate precision of the saturation prediction, the normalised error introduced in Chapter 2 was employed, see equation (2.13). The normalised errors for the saturation maps at steps 2 and 3 estimated by the different procedures are listed in Table 4.4. Saturation at step 3 is the future prediction, whereas saturation at step 2 belongs to the input data. However, the estimates of the latter are reported for the permeability inversion methods – to check how the corresponding permeability maps allow reproducing the input saturation maps.

Method	**Normalised error for**	
	S_2^*	S_3^*
Waterflood prediction	-	0.236
Waterflood prediction, noisy	-	0.858
Permeability #1	0.313	0.528
Permeability #1, noisy	0.350	0.600
Permeability #2	0.107	0.256
Permeability #2, noisy	0.737	1.553
Permeability #3	0.728	1.397
Seismic history matching	0.080	0.314
Seismic history matching, noisy	0.088	0.320

Table 4.4 Normalised error for the estimated saturation at step 2 (*middle column*), and forecasted saturation at step 3 (*right column*).

Figure 4.12 shows the maps of permeability and water saturation at steps 2 and 3 for the different fast-track methods, as well as for seismic history matching. As can be observed for the case of noiseless input, the best quality saturation forcast is provided by the fast-track waterflood prediction method (Figure 4.11), slightly worse forecasts are done by the permeability estimation method #2, and by seismic history matching (Figure 4.12). Permeability estimation method #1 shows higher normalised error for the saturation because of the high permeable spikes on the permeability map. Saturation prediction for permeability estimation method #3 is rather poor, although the calculated saturation maps have some resemblance with the reference water fronts. Because of the poor prediction here, permeability estimation procedure #3 was not tested with the noisy input.

Now if we look at how introduction of noise to the input data affects behaviour of the different methods, we can see its adverse effect on performance of permeability estimation method #2, which now becomes one of the worst saturation predictors. Permeability estimation method #1 is not affected much by the noise, and retains approximately the same intermediate error levels as before. The fast-track waterflood prediction method shows increased normalised error, which is mainly due to the fluctuations of the water saturation values behind the front, whereas prediction of the front position itself works reasonably well. Finally, introduction of noise has a very small effect on the SHM performance, which becomes the best saturation predictor for the noisy case, notably outperforming all the other methods.

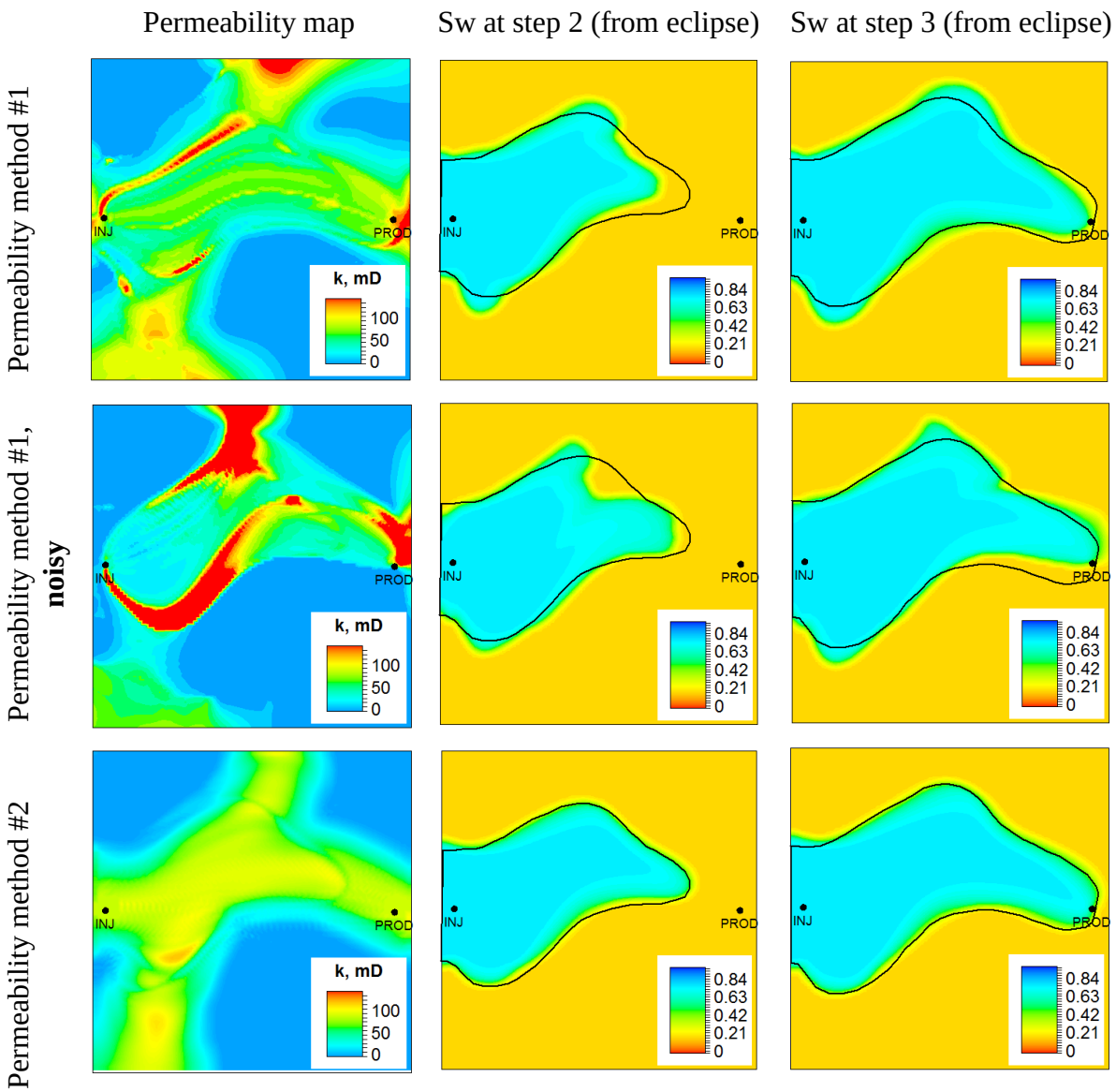

continued on the next page

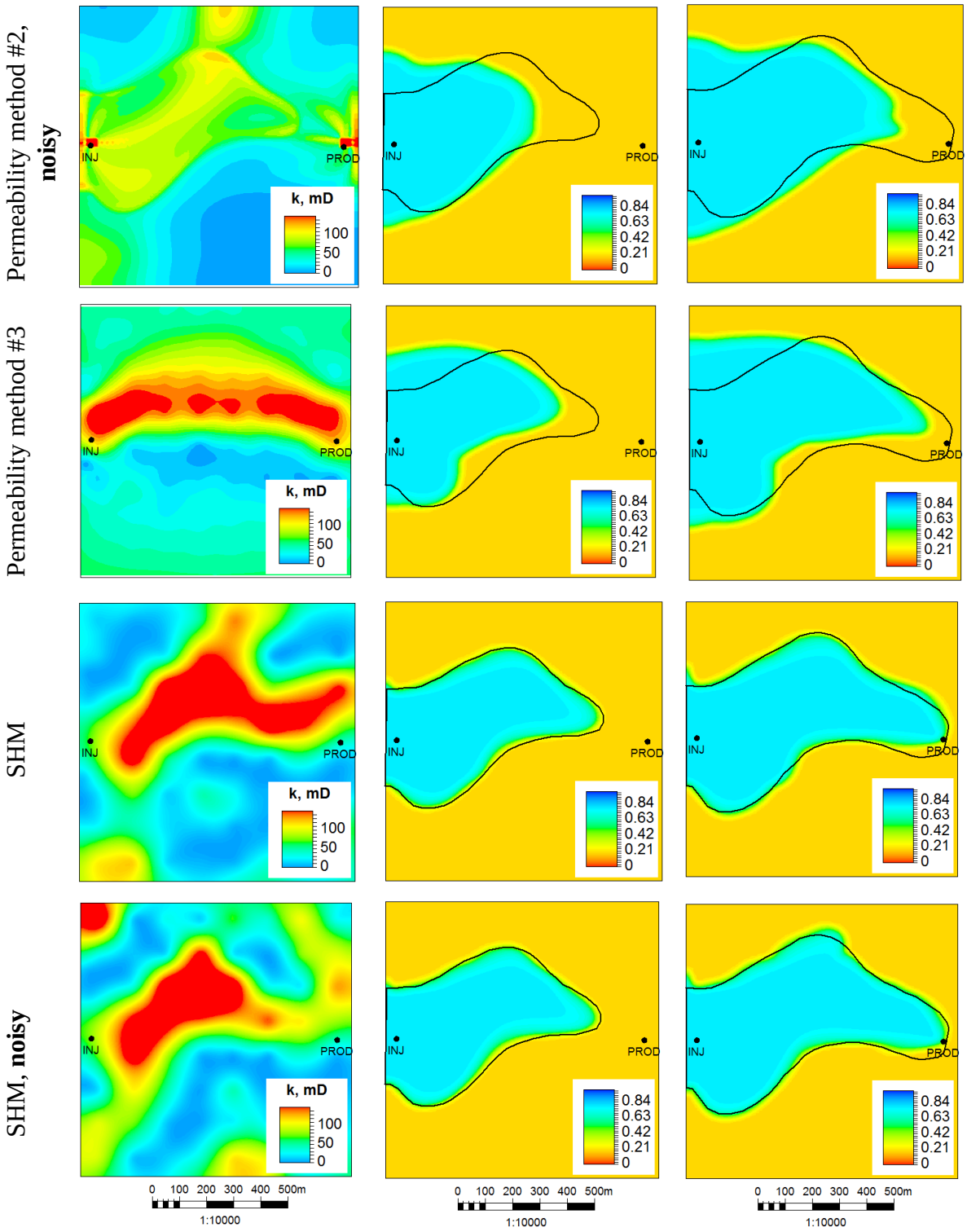

Figure 4.12 Benchmarking of fast-track procedures and SHM. *Columns, left to right*: estimated permeability map, saturation calculated for step 2, saturation forecasted for step 3. *The rows* show different permeability estimation methods and SHM.

Considering the problem of permeability map estimation, the main features of the reference permeability map (see Figure 4.10, *left*) are reproduced by the majority of the procedures considered, except for permeability estimation method #3. However, permeability estimation

method #1 introduces some non-geological high-permeable artefacts associated with streamlines going nearly tangent to the historical saturation fronts (see Figure 4.10, *center*). There errors become even higher when noise is added to the input data. Permeability estimation method #2 with the ideal noiseless input produces the permeability estimate remarkably close to the reference one. When noise is introduced, the resulting permeability becomes distorted, and leads to poor saturation prediction. The seismic history matching both with noiseless and noisy input resolves to certain extent the channel pattern on permeability map. Although the resolved permeability maps show too high values in the area between the wells, it should be noted that the permeability inversion problem may have a highly non-unique solution, so exact resolution of permeability far from the wells may be challenging.

As demonstrated by the tests conducted, the fast-track procedures are considerably faster than the full-fledged history matching. The former work with good precision (even somewhat better than the SHM) both for permeability map estimation and saturation map forecasting, provided the input is noiseless. However, their performance deteriorates even after addition of a moderate 17% noise to the input data. On the other hand, seismic history matching predictive capabilities are almost not affected by the presence of noise, and SHM saturation prediction for the noisy input turns out to be 2 – 5 times more precise than that of the fast-track methods. For a more realistic situation where the noise would be higher, the gap in accuracy between the fast-track procedures and SHM would be progressively larger, making the fast-track routines inacceptable despite their small running times. We should also keep in mind that the fast-track procedures considered lack flexibility in that they require the reservoir steady-state conditions. Given that, the fast-track methods introduced in Chapter 2 and Chapter 3 should only be applied for a very good quality input, with the input noise not exceeding probably 5% - 10% of the signal magnitude (although the tolerable noise levels are deemed to be case-dependant). For the situations with a stronger noise, which means for almost all present-day practical cases, the seismic history matching workflow elaborated in this chapter should be preferred.

4.6 Summary

In this chapter a history matching workflow was outlined, including the approach to parameterisation and the objective function definition. It was suggested to define the

well part of the objective function either as the sum of squared differences of the residuals, or as a quadratic form with a full covariance matrix. The seismic part of objective function is also defined by calculating the sum of squared differences (or a full quadratic form) – after solving a simple map-based equation linking the observed time-lapse seismic with the simulation model. The likely values of the minimum of the objective function were discussed - the χ^2 criterion considered provides a means to control whether optimisation converged to the acceptable level, and whether the overall error standard deviations specified for the history matching problem are correct.

The CMA-ES optimisation algorithm adopted to automate the loop was tested in the history matching environment, where it showed reasonably good behaviour compared to a few other stochastic algorithms. The map-based equation between the seismic and the simulation model was considered in detail, and two enhanced modifications for it were suggested: multiplication of the right-hand side by a scaling map and introduction of the quadratic terms. This equation is based on certain ideas found in the literature and applies them to the seismic history matching, allowing us to avoid the full physics seismic modelling. The question of the physical sense of the constituents of the equation was also touched upon, and it was suggested to impose the constraints to maintain the physically meaningful signs of the derivatives of the 4D seismic attribute with respect to the reservoir dynamic properties.

The link of the considered map-based seismic-simulator equations with the concepts found in the 4D seismic literature, and their successful testing on the synthetic case studies underpin the potential of the proposed seismic history matching algorithm. A small study for a simple 2D model was performed for testing the SHM algorithm and benchmarking it with the fast-track techniques introduced in the previous two chapters. For the noiseless input maps the latter techniques were shown to work with a good precision, and significantly faster than the SHM, however in the situation of moderate to high levels of noise the proposed seismic history matching workflow turned out to be a more accurate and robust procedure, albeit a slow one. Although the simple test conducted demonstrated the ability of the SHM to constrain the simulation model, in practice, performing just a single history match may not reveal the value of 4D seismic data (e.g. a conventional well history matching may *occasionally* result in a model which is better than a model produced by the seismic history matching). However, it is anticipated that 4D seismic data can reduce the *uncertainties* of history matching, which can be regarded as a proof of its value. For this reason more case studies of time-lapse

seismic history matching are dealt with in the two subsequent chapters, after introduction of the uncertainty estimation approach.

4.7 List of codes

For the studies described in this chapter the following programs were coded:

1. **Seismic-simulator regression code**. The program takes the input of the time-lapse maps of the following quantities: seismic attribute, reservoir pressure, water saturation, gas saturation. The other input includes the scaling map, the list of the quadratic terms in equation (4.8), and the list of the derivative constraints (4.9) to be used. The output is the coefficient of determination R^2, the coefficients a_i, and the modelled time-lapse attributes obtained after regression.

   Coding language: C++.

2. **Automated seismic history matching**. The program can perform a range of tasks:
   a. Forward modelling run for an Eclipse dataset based on the model parameters. The input data for this procedure is described below. The output is the calculated objective function with breakdown into the separate components corresponding to the different well data vectors and the seismic part. If seismic data is employed in the objective function, the output also includes the coefficients a_i, and the modelled time-lapse seismic attribute maps.
   b. Finite difference calculation of the objective function gradient and sensitivities for the well data. The input consists of the forward modelling input plus the list of perturbations used for each parameter. The output is the gradient vector and the sensitivity matrix.
   c. Calculation of a 2D plot of the objective function over an arbitrary 2D plane in the parameter space. The input consists of the forward modelling input, the 2D plane definition (3 points in the parameter space), and the mesh size. The output is the 2D map showing the objective function values.

d. Optimisation (history matching) loop using CMA-ES algorithm. The input consists of the forward modelling input and the CMA-ES settings: the stopping criteria (e.g. the maximum number of iterations), the generation size λ, etc. The output is the history matched model and the files with the optimisation record (progress of the objective function values, progress of the parameters vector, etc).

The last three procedures involving the massive numbers of the forward modelling runs were implemented using the MPI to take advantage of the parallel computing resources available.

The forward modelling run consists of:

a. Preprocessing step (parameterisation), for which the user should provide the ranges of the parameters, their functional transforms, and how the parameters are used (written) in the Eclipse dataset.
b. Eclipse run of the dataset.
c. Postprocessing step calculating the objective function, for which the user should provide the list of the well data vectors with their historic values, standard deviations, and temporal correlation ranges. The input for the seismic part of the objective function includes the observed maps of the 4D attributes, the scaling map, the 3D cube of weights for averaging the modelled dynamic property cubes, the list of quadratic terms in equation (4.8), the list of the derivative constraints (4.9), the value of the standard deviation, variogram type, variogram ellipse azimuth and semiaxes.

Coding language: C++.

Chapter 5 Uncertainty estimation

In this chapter I will consider a framework for uncertainty estimation and definition of the posterior probability in application to the history matching. History matching with estimation of uncertainties can be regarded as a more advanced and proper way of calibrating the simulation model to the observed data, because of the inherent non-uniqueness of such calibration. In this and the subsequent chapter, history matching with uncertainty estimation will be applied to validate the seismic history matching method introduced in the previous chapter. The primary expected indication of success of the SHM will be the ability of the resulting calibrated models to produce the forecasts of reasonable precision with uncertainties decreased compared to a conventional well history matching.

In what follows a method for making estimates based on the posterior distribution will be discussed, and procedures for assessing the data error covariance matrices will be outlined. Different history matching setups will be tested on a synthetic reservoir simulation model to examine the effect of introducing 4D seismic data into history matching loop, and the effect of using the non-diagonal covariance matrices.

5.1 Definition of posterior probability

If the history matching procedure results in a single model satisfying all measurements, it may be inappropriate to rely on this single model in the reservoir management decisions. This is because in most situations a wide range of models can satisfy the measurements, and the single model will typically lack the predictive power. The simplest approach to resolve this problem – i.e. to account for uncertainties – is to produce multiple models from history matching. More rigorously, one would need to work in terms of the probability densities: the prior probability of model, and the posterior probability of the model conditioned to the measured data. The final goal is to make some practically useful estimates based on the posterior probability, e.g. generate different models which follow the posterior distribution, or estimate mean values and standard deviations of some quantities using the posterior distribution.

In this work the widely used Bayesian approach is adopted. It establishes the link between the posterior probability density $p(m \mid d)$ of model m given the measured data

d and the prior probability density $q(m)$ of the model m by means of the likelihood function $L(d \mid m)$:

$$p(m \mid d) = \frac{L(d \mid m) \cdot q(m)}{p(d)}. \tag{5.1}$$

In practice, the data marginal probability density $p(d)$ from the denominator is not calculated directly, and can be regarded as a normalization constant which makes the integral of the posterior density $p(m \mid d)$ equal one. Assuming the probability densities $L(d \mid m)$ and $q(m)$ to be Gaussian leads to the formulation of the least-squares techniques. These techniques emerge when one is to find a model which maximises the likelihood function (ML estimate), or maximises the a posteriori probability density (MAP estimate). In this work I only consider prior distributions that are uniform over a certain region in the parameter space. The likelihood functions are taken to be Gaussian, with either simple diagonal covariance matrices, or full covariance matrices accounting for the correlations between the different data points. In terms of the objective function f defined in Chapter 4 it can be written

$$L(d \mid m) = \frac{1}{(2\pi)^{n/2} \mid C \mid^{1/2}} \exp\left(-\frac{1}{2}(d - g(m))^T C^{-1} (d - g(m)) \right) \equiv \gamma \exp\left(-\frac{1}{2} f(m) \right), \tag{5.2}$$

where $g(m)$ is the forward modelling procedure, C is n x n covariance matrix, γ is a normalising constant. I consider two sources of uncertainties, following the concepts set forth in Tarantola [56]. These are the imperfections in the theory (forward modelling procedure), and inaccuracies in the data measurements. If the forward modelling procedure was exact, i.e. did not introduce any *modelling*[31] or *theoretical* errors, then the covariance matrix C would equal the covariance matrix of the data measurement errors C_d. If the modelling errors were Gaussian, described by covariance matrix C_t, and the measurement errors were absent, then C would equal C_t. Now, if both error sources – measurement and modelling are present, then, as discussed in [56], the two Gaussian covariance matrices are simply added, giving

$$C = C_d + C_t. \tag{5.3}$$

In history matching problems both sources of errors exist. Formula (5.3) suggests that it is not necessary to separate the two sources, and one can only deal with the total covariance matrix C, that can be loosely treated as the "covariance matrix of observational uncertainties". This matrix can be represented as

[31] In [56] the term *modelization errors* is used.

$$C = SRS, \tag{5.4}$$

where S is a diagonal matrix containing the standard deviations for all data points, and R is the correlation matrix which accounts for the temporal (in the well data) or spatial (in the seismic data) correlations, and contains 1's on the main diagonal. In this work matrix R is calculated from the autocorrelation function fitted to the actual data errors. Estimation of the elements of matrix S – i.e. the standard deviations of the data observational errors – is done based on the engineering judgement, overall shape and scatter of the observations. Besides, the validity of the considered C is checked to a certain extent with the criterion outlined in Chapter 4, stating that the minimum of the objective function (after history matching) is expected to follow the χ^2 distribution with the known degrees of freedom.

5.2 Statistical estimates made from the posterior distribution

Once the posterior distribution is defined, one may want to make different estimates based on it, e.g. percentiles P_{10}, P_{50}, P_{90} of some quantities, like the total oil production from the reservoir, or *mean values* and *standard deviations* (**std**) of these quantities. In this work an approach for estimation of **mean**'s and **std**'s was designed, which makes use of the way the new models are sampled by CMA-ES optimisation algorithm. The approach showed appropriate results for small dimensions of the search space, e.g. n = 2, 3, but failed for the larger dimensions arising in the realistic history matching problems, e.g. n = 10 – 100. In particular, the latter failure was observed on a linearised history matching problem with parameter space dimension n = 24, where the exact theoretical expression for the posterior PDF was known due to the linear nature of the problem.

Although the approach will not be used in what follows, the brief outline of the main idea is given below. For a given reservoir model m having posterior density p (cf. (5.1)), consider the estimation of the **mean** and **std** of different *functionals* Q defined on the model:

$$\begin{aligned} &\text{mean}(Q) = EQ(m) = \int Q(x)\,p(x)dx, \\ &\text{std}(Q) = \sqrt{EQ^2(m) - (EQ(m))^2}\,. \end{aligned} \tag{5.5}$$

Examples of the *functionals* can be as follows: some well quantity, like oil production rate of certain well at certain date; some model parameter, like porosity value at certain

point; or any other quantity uniquely calculated from the given reservoir simulation model. To find the **mean** and **std** in (5.5), the first and second moments of $Q(m)$ are estimated by Monte-Carlo integration with weights.

$$EQ(m) = \int Q(x)\, p(x) dx = \int Q(x) \frac{p(x)}{h_g(x)} h_g(x) dx \approx \frac{1}{N} \sum_{k=1}^{N} Q(u^{(k)}) \frac{p(u^{(k)})}{h_g(u^{(k)})}. \tag{5.6}$$

Here N is the total sample size, and the models $u^{(k)}$ are those sampled by CMA-ES from the normal[32] distribution $h_g = N(m^{(g)}, \sigma^{(g)^2} C^{(g)})$ at each generation of models g, cf. equation (B.1). Since the prior density q is constant, the posterior density p is proportional to the likelihood L, for which the exact expression is known. The corresponding proportionality coefficient can be estimated by the Monte-Carlo approach along with the other quantities calculated by the algorithm. The other normalising coefficient arising from the truncation of normal distribution h_g is estimated similarly. Occasionally the value of density h_g in (5.6) may become very low leading to the extremely high weight for the corresponding term. To circumvent this problem a criterion was formulated to reject the models with extremely low h_g, leading to rejection of ~ 10% of the total number of the sampled models. Formula (5.6) can be applied for a single CMA-ES run, as well as for multiple runs provided they use the same likelihood function.

The likely reasons why the considered approach does not work properly for the realistic dimensions are that the CMA-ES is designed to converge to a minimum, and not to extensively explore the search space, whereas estimate (5.6) relies on exploration of the part of the search space where the posterior distribution is concentrated. As an uncertainty estimation algorithm to be used further in the thesis I took aboard the *randomised maximum likelihood* method, which is described in the next section.

5.3 Randomised maximum likelihood

The *randomised maximum likelihood* (RML) method allows sampling[33] models from the posterior distribution, and the details of its application to an inverse problem with

[32] Actually, *truncated normal distribution*, because the models are constrained to some region in the parameter space.

[33] This sampling is only exact for the linear forward modelling, but for a few non-linear examples, including the history matching problems, it is also reported to be reasonably accurate, see also Chapter 1.

Gaussian prior and Gaussian data errors can be found e.g. in [42]. The method starts from sampling a model m_{uc} from the prior distribution (the unconditional model), and perturbing the observed data d_{obs} by adding Gaussian noise ξ which is sampled according to the data error covariance matrix C_D, so that the perturbed data is $d_{uc} = d_{obs} + \xi$. Then, the following objective function is minimised by some optimisation algorithm

$$f(m) = (m - m_{uc})^T C_M^{-1} (m - m_{uc}) + (g(m) - d_{uc})^T C_D^{-1} (g(m) - d_{uc}), \tag{5.7}$$

where C_M is the covariance matrix of the prior distribution, $g(m)$ is the forward modelling procedure. If the forward modelling is linear, i.e. $g(m) = Gm$, then the RML procedure will exactly sample from the posterior PDF, which is demonstrated in the quoted literature. Such a demonstration will be sketched below for a simpler case where the prior information is absent.

For the linear inverse problem with no prior information and Gaussian data errors with covariance matrix C_D the posterior PDF is proportional to the likelihood:

$$p_a(m) = \gamma \exp\left(-\frac{1}{2} f_a(m)\right) \equiv \gamma \exp\left(-\frac{1}{2}(Gm - d_{obs})^T C_D^{-1} (Gm - d_{obs})\right), \tag{5.8}$$

where the normalising constant equals $\gamma = (2\pi)^{-n/2} |C_D|^{-1/2}$, cf. (5.2). This PDF is actually also a normal distribution, with covariance matrix $C^* = (G^T C_D^{-1} G)^{-1}$ and mean $m_{MAP} = C^* G^T C_D^{-1} d_{obs}$. This can be checked if one calculates the expression $f_b(m) = (m - m_{MAP})^T C^{*-1} (m - m_{MAP})$ which differs from $f_a(m)$ defined in (5.8) by an additive constant. Thus, after taking the exponents of f_a, f_b and normalising them, one will arrive at the same normal PDF. Model m_{MAP} is the maximum a posteriori estimate which maximises $p_a(m)$ and minimises f_a. Since no prior information was considered here, m_{MAP} is also the maximum likelihood estimate.

For the situation with no prior data the RML algorithm for sampling from the posterior PDF (5.8) can be formulated as follows:

1. Perturb the observed data: $d_{uc} = d_{obs} + L_D Z$, where $L_D L_D^T = C_D$, and vector Z is a random vector with i.i.d. components having the standard normal distribution $N(0, 1)$.

2. Find model m_c which minimises $f_a(m) = (Gm - d_{uc})^T C_D^{-1} (Gm - d_{uc})$. The samples m_c obtained in this way will follow the desired PDF $p_a(m)$.
3. Repeat steps 1 and 2 as many times as needed to produce the necessary number of samples.

To demonstrate the statement from step 2 about following the PDF $p_a(m)$ by m_c, one can write $m_c = C^* G^T C_D^{-1} (d_{obs} + L_D Z) = m_{MAP} + C^* G^T C_D^{-1} L_D Z$. Obviously, m_c will have normal distribution with mean m_{MAP} and covariance matrix which can be written as $E[(m_c - m_{MAP})(m_c - m_{MAP})^T] = E[C^* G^T C_D^{-1} L_D Z Z^T L_D^T C_D^{-1} G C^*] = C^*$, by virtue of $E[ZZ^T] = I$.

The minimum value of f_a found at step 2 of the algorithm is subject to the same considerations with χ^2 distribution as in Chapter 4, and its expected range can be assessed by the expression similar to (4.4). However, since d_{obs} is already a random normal vector with covariance matrix C_D, and an independent random vector with the same covariance is added to it to obtain d_{uc}, the quantity that should follow the χ^2 distribution is now $½ f_a(m) = (Gm - d_{uc})^T (2C_D)^{-1} (Gm - d_{uc})$, so the following estimate should apply:

$$\upsilon - 5\sqrt{2\upsilon} \le \frac{1}{2} f_{a,\min} \le \upsilon + 5\sqrt{2\upsilon}. \tag{5.9}$$

The algorithm above can be applied to non-linear problems by substituting the forward modelling expression Gm with $g(m)$, however in this case it is not guaranteed to produce the samples from the true posterior PDF. In this thesis the history matching problems are considered that have Gaussian observational errors, and a prior distribution that is uniform over some region *R*. Thus, the posterior PDF equals

$$p_R(m) = \beta \exp\left(-\frac{1}{2} (g(m) - d_{obs})^T C_D^{-1} (g(m) - d_{obs}) \right) \cdot I_R(m), \tag{5.10}$$

where the indicator function $I_R(m)$ is 1 inside region *R*, and 0 outside it, and β is a normalising constant to make the integral of p_R equal one. To sample from this PDF, the following procedure should be applied:

1. Produce a model by the RML algorithm, ignoring the prior information (region *R*).
2. Accept the model if it falls into region *R*, and reject it otherwise.

However, I will use a *less rigorous scheme*, such that the minimisation step of the RML algorithm is performed with constraints given by the region *R*, and all the resulting models are accepted.

In order to perform the minimisation step of the RML the CMA-ES algorithm will be used because of its accessibility and reasonable performance. Of course, gradient based methods like BFGS or Gauss-Newton could considerably outperform CMA-ES in terms of the speed, and normally these methods are used with RML as reported in the literature, however they would require a simulator with the derivatives calculation, which is not available to me. The use of CMA-ES will affect only the speed of calculations, but not the results and conclusions. That is, according to the testing of the different optimisation algorithms conducted in Chapter 4, CMA-ES is expected to find the plausible minima of the objective function after the sufficient number of iterations, thus delivering the models of approximately the same history match quality as would be achieved with the other stochastic optimisation procedures. Compared to the gradient-based methods, CMA-ES may result in even better minima, since the stochastic optimisation algorithms are typically more robust at finding the global optima than the gradient procedures.

5.4 Definition of covariance matrix for the well data

I will consider the total covariance matrix C (cf. (5.2), (5.4)) to be block diagonal, consisting of the two major blocks: C_w corresponding to the well data, and C_s corresponding to the seismic data, so that the objective function is split into the wells and seismic parts, as defined in (4.3).

$$C = \begin{pmatrix} C_w & 0 \\ 0 & C_s \end{pmatrix}. \tag{5.11}$$

Matrix C_w will be considered to be also block diagonal, with each block corresponding to a separate **well data vector** (the data vectors in the simulator output are the functions of different quantities vs. time, e.g. of water cut for a well or group of wells, GOR, BHP, etc). By adopting this block structure, I am making a simplifying assumption that the data points between the different vectors are not correlated. In practice C_w is commonly taken as just a diagonal matrix, implying that the errors in the well data are

not correlated, and only the standard deviations $\sqrt{C_{wii}}$ should be accounted for. E.g., in [63] the authors claim that the correlation length in the well data is around 10-20 days, so if the well data are reported at monthly rate, which is usually the case, these correlations can be ignored. In Schlumberger SimOpt user guide [64] roughly the same statement about the correlations in well data is made.

It seems that in the above considerations only the measurement errors were addressed by the authors. I think that a more appropriate approach will be to consider both measurement and modelling errors, as discussed in section 5.1. The total covariance matrix is then obtained by (5.3), where the Gaussian assumption is made on both types of errors. For the modelling errors such an *assumption* may be not suitable, but I believe that making *it* would lead to a better uncertainty quantification than just ignoring the modelling errors. A detailed study of this issue is however beyond the scope of this thesis.

If one considers the modelled well data $g_{well}(m)$ from a reservoir simulation model history matched to the observed well data d_{obs}^{well}, then in most cases the resulting error $r = d_{obs}^{well} - g_{well}(m)$ will show correlations with ranges notably exceeding 10 – 20 days reported for the measured well data. These long range correlations seem to be the consequence of the modelling errors existing in the total error *r*. To estimate the correlations range, the (auto)covariance function of *r* is considered:

$$c(h) = \frac{1}{N}\sum r(x)r(x+h), \tag{5.12}$$

where summation takes place over all available pairs of the data points separated with lag *h*, and $N = N(h)$ is the total number of such pairs. In this definition it is assumed that the residue *r* has zero mean, however for the real simulation models it is not always the case due to the modelling errors. Examples of the autocovariance functions for the well bottom-hole pressure, water cut and GOR are shown in Figure 5.1, where I took wells D2, D5, D7 from a history-matched simulation model of Schiehallion field, segment 4, which is to be considered in detail in the next chapter.

The statistical estimates of the covariance functions are more reliable at small lags (0 - 400 days on the plots above), since there are more pairs of points existing at such lags. In the ideal situation the shape of the covariance would look like that shown in Figure 5.2. In the examples considered, covariances for well D2 BHP and well D7 water cut

follow that shape quite closely. Covariance of well D2 GOR is somewhat worse, as it plunges into negative domain for the medium lags. Finally, the calculated covariance function of well D5 GOR is likely to be affected by the strong modelling errors.

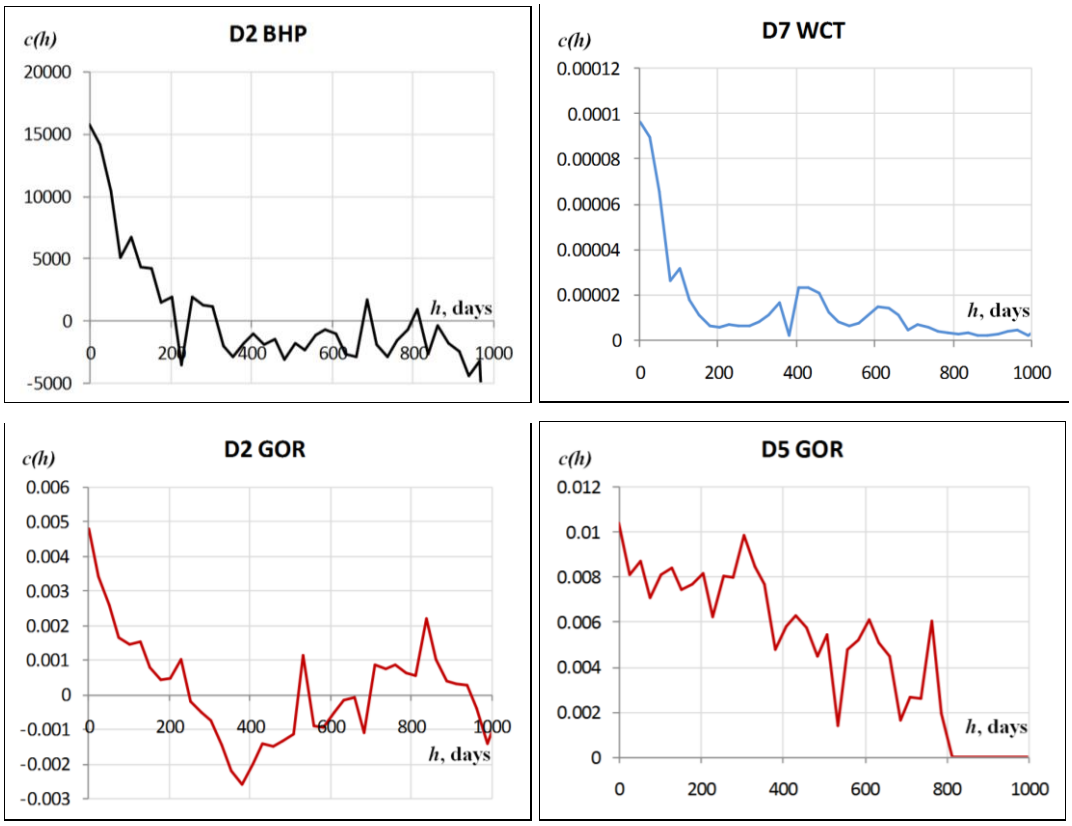

Figure 5.1 Autocovariance functions calculated from the well data errors of a history matched Schiehallion model, wells D2, D5, D7. *X* axis is time lag in days *h*, *Y* axis is the autocovariance function *c*(*h*).

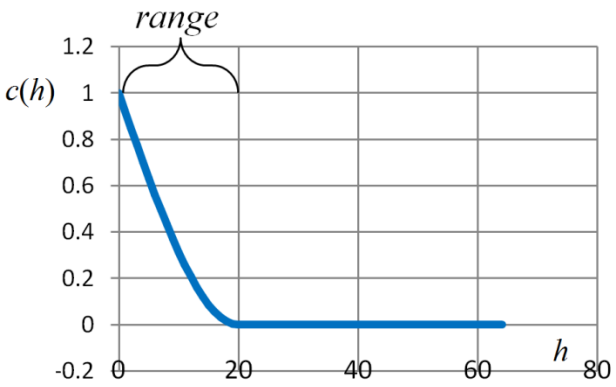

Figure 5.2 Spherical covariance function c_{sph} with range 20.

It should be noted that the statistical estimates of the autocovariances may look weird even if the input random vectors were precisely generated with the known covariance function. To illustrate this, I generated the random normal vectors with zero mean and

covariance matrix $C = \sigma^2 R$, where the correlation matrix R was calculated via the spherical[34] covariance:

$$R_{i,j} = c_{sph}(i - j) \equiv c_{sph}(range, i - j), \tag{5.13}$$

where i and j denote the vector indices (can be regarded as time). The resulting random vectors and the (auto)covariance functions estimated from them are shown in Figure 5.3. As can be seen, the autocovariances at large lags are far from the ideal underlying one (Figure 5.2).

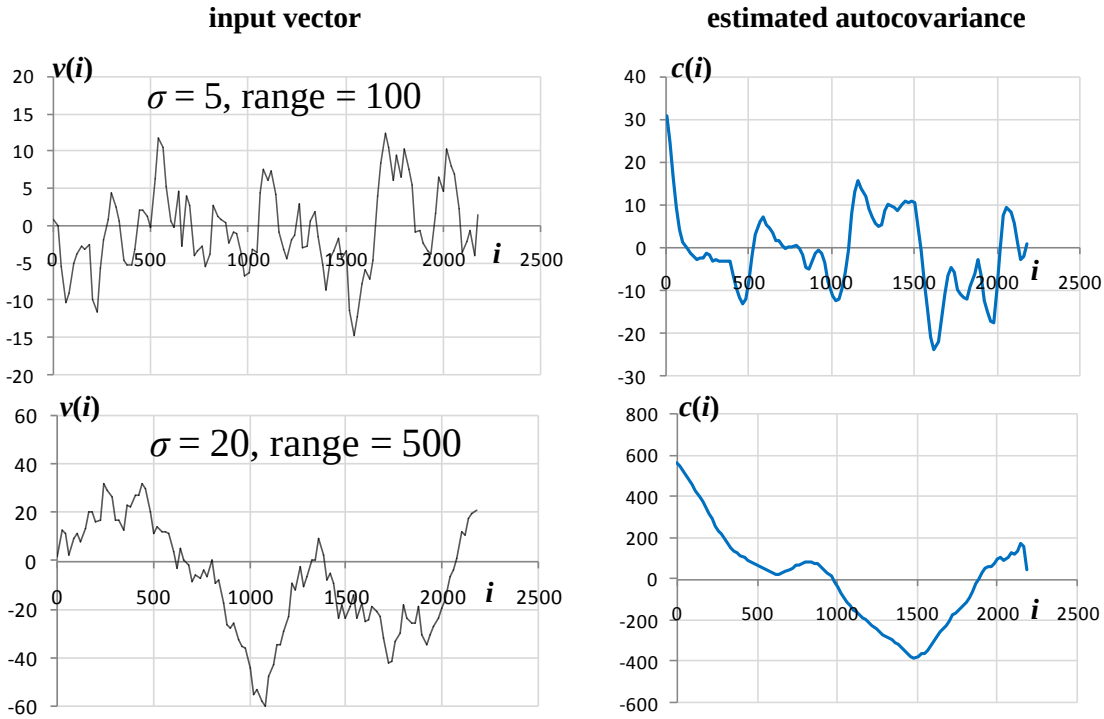

Figure 5.3 Random normal vectors sampled using the spherical covariance function c_{sph}. *Top row*: vector with σ = 5, correlation range = 100; *bottom row*: vector with σ = 20, correlation range = 500. *The left column* is the input vector, *the right column* is the statistically estimated autocovariance. *X axis* in the left column displays the index (can be regarded as time), *X axis* in the right column is the index lag, *Y axis* is for the vector (or covariance) value.

Returning to the example from Schiehallion field given in Figure 5.1, one can visually infer the correlation ranges of the autocovariance functions by superimposing the spherical covariance function (Figure 5.2) appropriately stretched horizontally and

[34] Whereas different covariance functions could be used, in this thesis only the spherical one is considered for convenience. The spherical covariance (or the corresponding variogram) is one of the most commonly used in the geostatistical applications. The formula for the variogram, i.e. $\gamma(h) = c(0) - c(h)$, can be found in Appendix D, where the obvious correction for the correlation range should be made.

vertically. The resulting ranges are of the order of 200 – 400 days, and this is obviously greater than 1 month. So, if the well data measurements are reported at monthly rate, the full non-diagonal covariance matrix should be used for the proper treatment of uncertainty.

For the purposes of history matching and uncertainty estimation the following procedure will be applied to estimate the covariance matrix C_w:

1. History match the model using the diagonal covariance matrix. In this preliminary history matching the model parameterisation is taken the same as in the subsequent "final" history matching. The only difference between the two HM versions is in the objective function: the preliminary HM uses diagonal covariance matrices, and the standard deviations which are quite rough and approximate (usually inferred from the absolute magnitude of the observed well data vectors and engineering judgement).

2. For each data vector estimate the error $r = d_{obs}^{well} - g_{well}(m)$ between the observation data and the modelled data. The data vectors participating in the objective function are BHP, water cut, GOR for a simulation model controlled by the well liquid production rate and the well water injection rate. These vectors reasonably cover the conventional field historic data, and there are essentially no correlations between them. I do not consider the cumulative quantities like the total water production (WWPT) because the corresponding vectors have more complicated covariance functions, and are also correlated with the other vectors (e.g. WWPT is correlated with water cut).

3. Calculate the *autocovariance* function $c(h)$ for r. Visually find the *range* by superimposing the spherical covariance function. If the autocovariance function looks suspicious, the range should be defined by analogy with the similar data vectors, and by engineering judgement. Once the range is found, the correlation matrix R can be calculated for each vector using the spherical covariance function, see (5.13).

4. Define the standard deviation σ for each data vector. Although σ can be specified separately for each vector at each time step, a more unifying approach is used here – one σ is defined for a whole *group* of similar vectors, e.g. for all well GOR vectors. In the first approximation the sigmas are defined from the magnitude of the vectors and engineering judgement. Then, for each *group* of vectors the χ^2 criterion set forth in Chapter 4 is applied, i.e. sigma for the group is selected such that after history matching the objective function for the group approximately equals $\upsilon = N_d^{group} - N_p^{group}$, where

N_d^{group} is the number of data in the group of vectors, N_p^{group} is the number of parameters "allocated" for that group. I define roughly N_p^{group} as the total number of parameters used in history matching divided by the number of groups. Strictly speaking, χ^2 criterion is formulated for the whole set of data, and is not applicable to the data subgroups, at least because it is not known how parameters should really be allocated between the subgroups. However I consider the groups of data vectors with relatively large number of data (well exceeding the total number of parameters), so that the χ^2 criterion is believed to be applicable. To define σ's with this algorithm it is required to run a few additional history matching runs. Once σ's are defined for each data point of a data vector, the diagonal matrix *S* can be found which contains these sigmas on its diagonal.

5. The covariance matrix for each vector is then $C = SRS$, and the total well covariance matrix C_w is block-diagonal, with blocks corresponding to the matrices of the vectors.

For uncertainty estimation using the RML procedure outlined above one will also require to generate the perturbation for the observed well data. The perturbation is a normal random vector with zero mean and covariance matrix C_w, and is calculated using Cholesky decomposition of each matrix sub-block of C_w. More details on generating the normal random vectors and fields will be given in the next section.

5.5 Definition of covariance matrix for the seismic data

When the time-lapse seismic data is introduced into history matching, the uncertainty model for it usually accounts for the spatial correlations, see e.g. [63]. The approach introduced in Chapter 4 for calculation of the seismic part of objective function is the least squares approach by nature, so it allows use of arbitrary covariance matrices, see (4.12). Since in this work the seismic data is treated in a 2-dimensional (map) form, the 2D spatial correlations are of interest. The errors in seismic data (measurement + modelling) will be assumed to be 2D Gaussian stationary random fileds/maps with zero mean and some covariance matrix C_s. I will use covariance matrices of the form $C_s = \sigma_s^2 R_s$ where the standard deviation σ_s defines the magnitude of the seismic errors, and correlation matrix R_s defines the spatial range and orientation of the

correlated features on the error map. Matrix R_s has size $N_{gr} \times N_{gr}$ where N_{gr} is the total number of defined values on the seismic attribute map (2D grid). It is calculated from the correlation ellipse and 1D covariance function $c_{sph}(\cdot)$. The ellipse in its turn is described by the rotation angle χ, and the major and minor semiaxes R_e, r_e corresponding to the correlation ranges. For each pair of points *k*, *l* of the 2D grid separated at lag $\vec{h} = (h_1, h_2)^T$ the correlation matrix value is given by

$$(R_s)_{kl} = c_{sph}(\|\bar{g}\|), \tag{5.14}$$

where 2D vector $\bar{g}$ is obtained from $\vec{h}$ by the linear transform which maps the ellipse to the unit circle (D.14), and indices *k*, *l* range from 1 to N_{gr}. Now, to define the covariance matrix C_s one only needs to set the value of standard deviation σ_s, which is usually done in this thesis based on the χ^2 criterion described in Chapter 4.

If multiple seismic monitors are used in the objective function, the corresponding covariance matrix $C_{s,tot}$ is built from the single-monitor matrix C_s by its replication on the diagonal blocks, e.g. for two monitors one would have

$$C_{s,tot} = \begin{pmatrix} C_s & 0 \\ 0 & C_s \end{pmatrix}. \tag{5.15}$$

This is rather rough treatment of the seismic errors of the different monitor surveys, and a higher degree of finesse would be reached if this procedure employed for each monitor its own correlation matrix and standard deviation.

When handling the correlation matrices and the correlated random fields, three procedures will be of interest for us:

1. Given the 1D covariance function and the correlation ellipse, generate (sample) the correlated random field. This procedure is needed when the RML uncertainty estimation algorithm is applied, since that algorithm requires perturbing the observed data according to the data error covariance matrix.
2. Given the correlated random field, calculate the 2D covariance map.
3. Given the 2D covariance map, estimate the parameters of the correlation ellipse: rotation angle, major and minor semiaxes. Procedures 2 and 3 are necessary to find the seismic correlation matrix from the correlated "random" maps of seismic errors that are obtained from the preliminary history matching with the

diagonal covariance matrices. The logic in this estimation is similar to what is done for the well data.

The problem of generating a correlated random field given a covariance matrix has a variety of solutions [65]: spectral method, matrix decomposition method (MD), turning bands method, screening sequential simulation method (SSS), multigrid method (which is a combination of MD and SSS). In this work the MD method is used which involves Cholesky decomposition of the covariance matrix into the lower and upper triangular matrices: $C = L \cdot L^T$. The required random field η is then produced by multiplying L by a vector of the uncorrelated standard normal variables: $\eta = L\xi$. Because of the Cholesky decomposition step the method is costly and may even become infeasible for the large matrices. However the seismic maps considered in this work have the number of points of the order of 1000, resulting in 1000 x 1000 covariance matrices for which the MD approach is computationally affordable. Having Cholesky decomposition at hand also proves useful for the fast inversion of the covariance matrix which is required when the objective function is calculated, and when matrix G and vector g used in the constrained regression (E.5) are estimated. For handling the seismic maps that contain substantially larger number of points, the *multigrid method* [65] can be taken for generating the correlated random fields, and *discrete convolution inverse method* [63] can be used for inverting the large covariance matrices.

Moving to the second procedure mentioned above, to estimate the 2D covariance map $c(\vec{h})$ from the correlated random map $s(\vec{x})$, use the straightforward statistical calculation:

$$c(\vec{h}) = \frac{1}{N(\vec{h})} \sum_{x,x+h} s(\vec{x}) s(\vec{x} + \vec{h}), \tag{5.16}$$

where summation takes place over all pairs of points $\vec{x}, \vec{x} + \vec{h}$ found on the map, their number being $N(\vec{h})$. The above formula works under assumption that the random map/field $s(\vec{x})$ is stationary and has zero mean. The assumption of zero mean is reasonable since $s(\vec{x})$ is supposed to be the map of seismic errors which arises in history matching.

Once the 2D covariance map is formed, it typically demonstrates an ellipse-like feature, and in my work this feature will always be approximated by an ellipse with parameters assessed by the following steps:

i. Visually find the direction of the major and minor axes of the ellipse seen on the input map of the 2D covariance. This allows estimating the rotation angle χ.

ii. Consider two 1D plots of the covariance map taken along the two axes. Visually superimpose the covariance function graph (Figure 5.2), stretching it appropriately to find the major and minor semiaxes R_e, r_e.

Procedures 1 – 3 were tested on generating the random fields with certain correlation ellipses and then solving the inverse problem – i.e. estimating the parameters of the underlying ellipse taking the random field as input. An example of this is given below. A random field was generated with the 1D spherical covariance function and the correlation ellipse rotated at 30^o, with the major semiaxis equal to 30 grid cells[35], and the minor semiaxis – 15 cells, as shown in Figure 5.4. From the random field the 2D covariance map was found using (5.16), with an ellipse distinctly seen on it. The major and minor axes were drawn visually, resulting in rotation angle 32^o, which is quite close to the original angle. Then two 1D plots along the axes were examined, the plot along the major axis is displayed in the same figure. By superimposing the sample covariance function graph (red line), we can see that the estimated covariance follows quite closely the sample covariance, and the major correlation range equal to 27 cells can be inferred. In the same way the minor correlation range was estimated as 15 cells.

From this and the other examples studied it was found that the ranges, which are small compared to the total grid size, are usually precisely recovered, e.g. 5 – 15 cells ranges for a 100 x 100 cells grid. The larger ranges (30 – 40 cells or more for 100 x 100 cells grid) tend to be 10 – 15% underestimated. This was the case for the example above, where the major range was estimated as 27 cells instead of the underlying value 30 cells. This situation is of no surprise since the 2D covariance values at large separation distances (lags) are estimated based on much fewer number of points than the covariance values at small lags, and hence are not quite reliable.

[35] In this example 1 grid cell = 5 m.

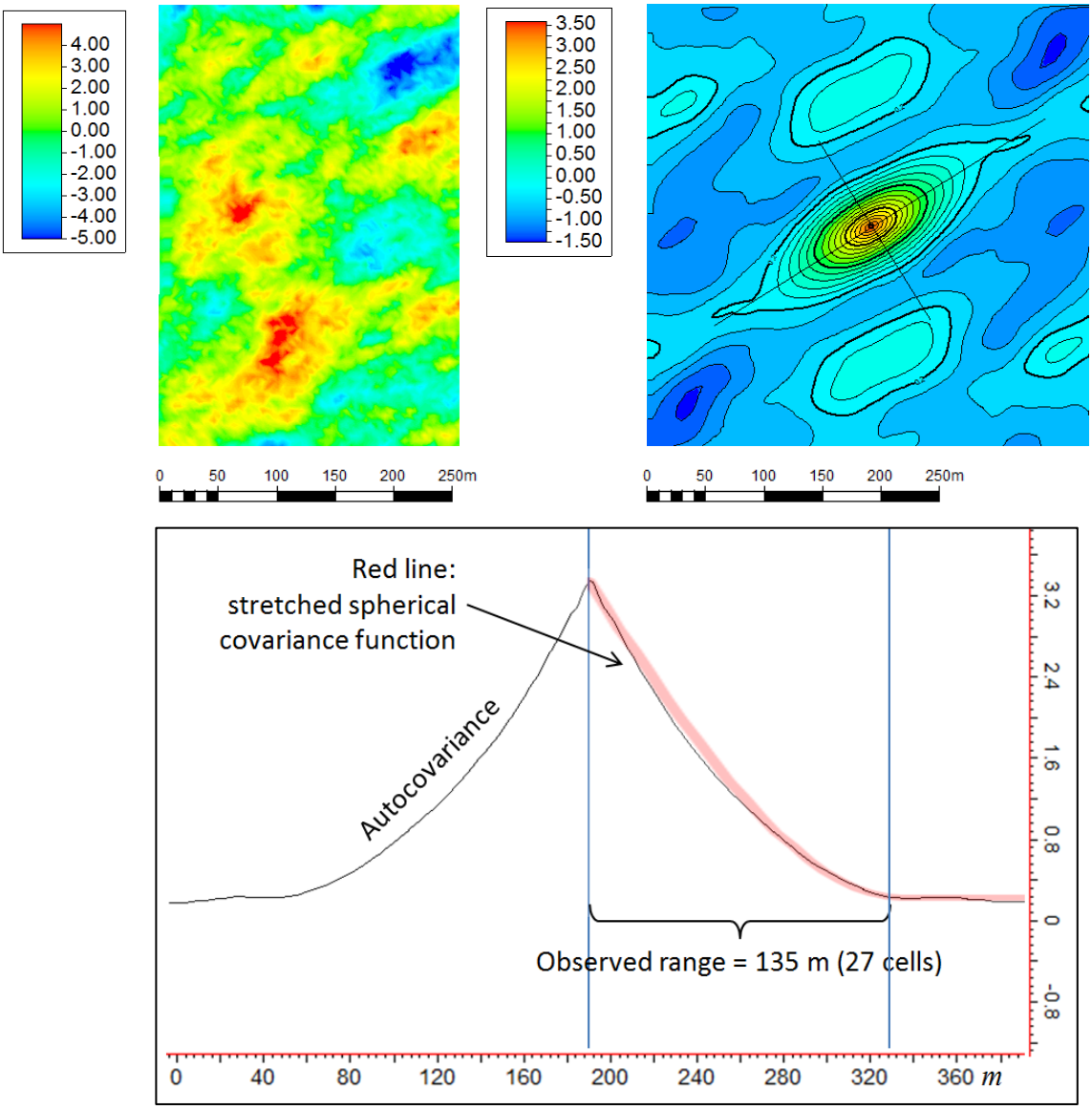

Figure 5.4 Correlated random normal field (*top left*), 2D covariance map estimated from it, with major and minor axes shown by the lines (*top right*), and 1D plot of the covariance map taken along the major axis (*bottom*).

Now the steps taken to estimate the seismic error covariance matrix C_s can be summarised (here it is assumed that the covariance matrix for the well data C_w has been properly calculated, and is used where appropriate):

1. Perform a preliminary history matching with diagonal C_s.
2. Estimate the error in the seismic map $s = d_{obs}^{seis} - g_{seis}(m)$ where d_{obs}^{seis} is the observed 4D seismic attribute, m – the history matched model, $g_{seis}(\cdot)$ – the forward modelling procedure for seismic.
3. Calculate the (auto)covariance map c (5.16), estimate the parameters of the underlying ellipse, calculate the corresponding correlation matrix R_s (5.14).

4. Define the standard deviation σ_s using the χ^2 criterion. Viz., sigma is selected such that the seismic part of the objective function after optimisation approximately equals $\upsilon = N_d^{seis} - N_p^{seis}$, where N_d^{seis} is the number of seismic data (number of points on the attribute maps summed for all monitors), N_p^{seis} - number of parameters "allocated" for seismic. N_p^{seis} can be roughly estimated from the total number of parameters N_p used in history matching, dividing N_p between *wells* and *seismic* proportionally to the total number of well data and the total number of seismic data. When making this estimation of σ_s a few additional history matching runs are required.
5. Finally, the covariance matrix sought is $C_s = \sigma_s^2 R_s$. In case of multiple seismic monitors one would need to follow the scheme outlined in (5.15) to form the total block-diagonal covariance matrix.

5.6 Uncertainty estimation for a synthetic model

Testing of the history matching approach proposed in Chapter 4 together with the uncertainty estimation by RML will be done on a synthetic model. The model is a three phase reservoir penetrated by two vertical wells – producer and injector, that are controlled by the constant bottom-hole pressure. The reservoir has the average thickness of 35 m, and heterogeneous properties (porosity, permeability, NTG), see Figure 5.5. There is a small water saturated zone penetrated by the injector which is completed over the whole thickness, and a small gas cap penetrated by the producer which is completed below the gas cap. The initial reservoir pressure is 250 bars, the bubble-point pressure is 205 bars.

Production history covers 500 days: for the first 50 days only the producer is working, followed by 50 days of shut-in period, followed by 400 days of the producer and injector working together. The resulting well rates and the controlling BHPs can be found in Figure 5.6. The historic period is followed by 2000 days of prediction period which will be used for checking the predictive capabilities of the history matched models. For this period the controlling BHPs at wells are inherited from the preceding historic period.

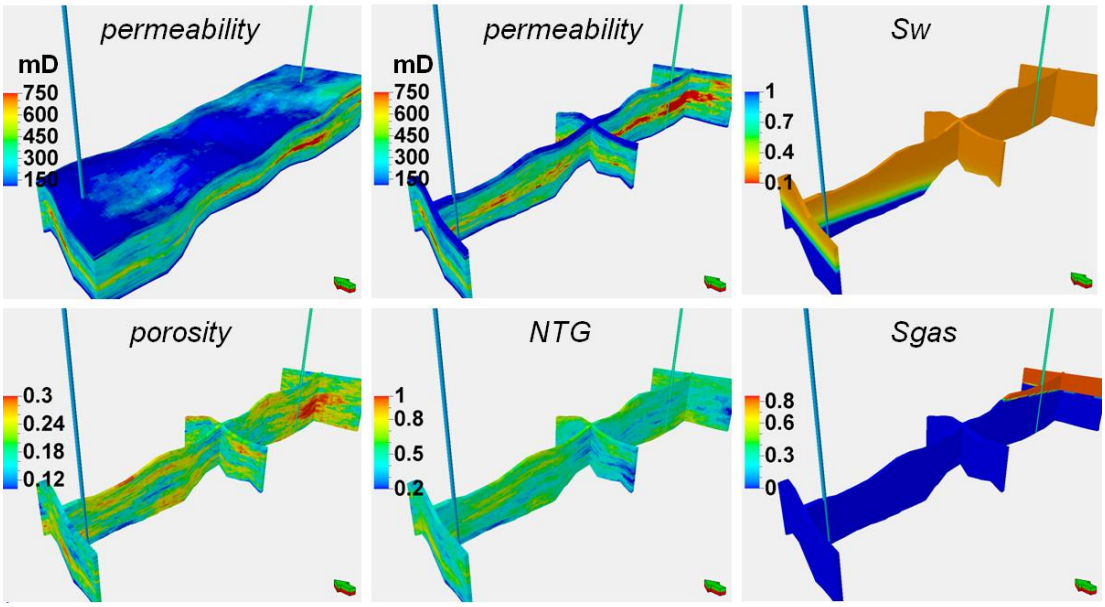

Figure 5.5 3D properties of the synthetic model: permeability, initial water saturation (*Sw*), porosity, NTG, initial gas saturation (*Sgas*). The injector is on the left, the producer is on the right.

Two seismic surveys were made: a baseline survey prior to the production start, and a monitor survey at the end of the historic period, i.e. at 500 days. Seismic modelling was done according to the procedure described in Appendix A, using the petro-elastic properties and the wavelet suggested there. The seismic attribute was taken to be the sum of negative amplitudes between the reservoir top and base horizons. The resulting time-lapse map of the attribute between the monitor at 500 days and the baseline is shown in Figure 5.7, along with the corresponding maps of the pressure change, water saturation change and gas saturation change.

As can be seen on the maps and the well production data (Figure 5.6), water breakthrough does not occur by the end of the historic period. However, the approximate position of the water saturation front can be guessed from the time-lapse seismic map, so it is anticipated that adding the seismic information to the history matching loop should reduce the uncertainty in predicting the water breakthrough and the water cut development. Figure 5.8 which shows the cross-sections between the two wells allows us to look at the reservoir from another perspective. For instance, from the cross-section with water saturation at 500 days we can see that the saturation tongue develops, which occupies only the lower half of the reservoir, following the high permeable middle zone seen in Figure 5.5, and also subject to the water gravity slumping.

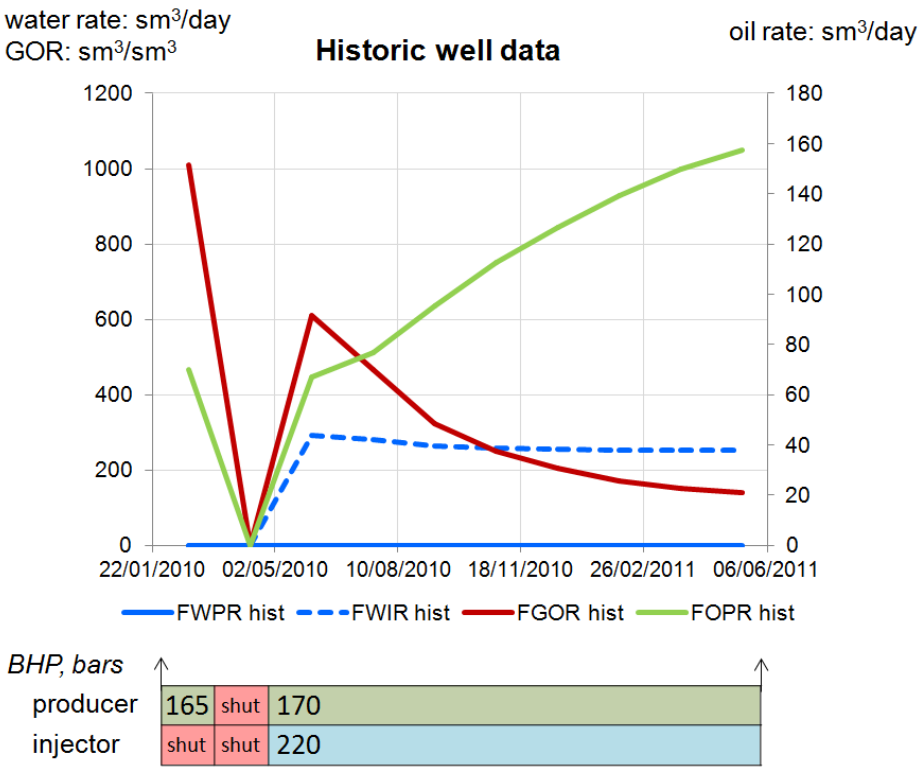

Figure 5.6 Production history of the synthetic model. *Above*: the plots of oil production rate (FOPR), water production rate (FWPR), water injection rate (FWIR), gas/oil ratio (FGOR). *Below*: schedule of changing the bottom-hole pressure (in bars) controlling the wells.

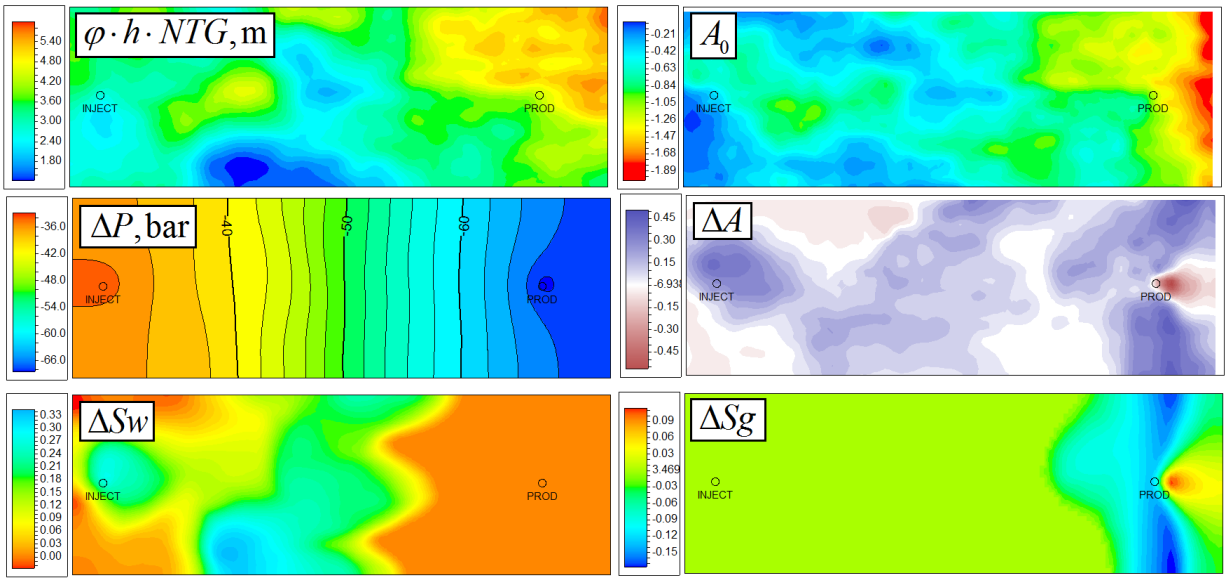

Figure 5.7 Map of $\varphi \cdot h \cdot NTG$, baseline attribute map (A_0), time-lapse attribute map (ΔA) at 500 days, and the corresponding time-lapse average maps of pressure (ΔP), water saturation (ΔSw), gas saturation (ΔSg).

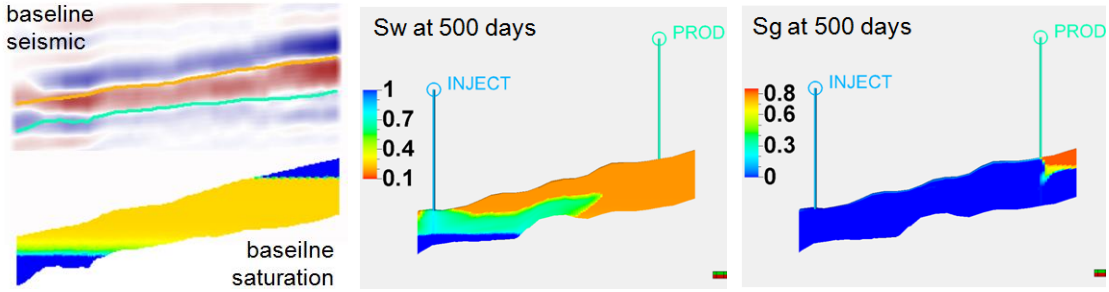

Figure 5.8 Cross-sections along the line connecting the two wells. *Left to right*: 1) baseline seismic with the reservoir top and base horizons and the corresponding oil saturation, 2) water saturation (*Sw*) at 500 days, 3) gas saturation (*Sg*) at 500 days.

The original 114 x 38 x 30 cells model used to produce the well data and seismic was upscaled, resulting in a 57 x 19 x 4 cells coarse model used for history matching. The upscaling essentially involved rebuilding the grid structure using a coarser mesh, whereas the grid properties in the coarse model were specified as follows. NTG and porosity were taken constant, equal to 0.75 and 0.25 respectively. Horizontal permeability was taken constant for each of the four layers, equal to 100 mD, 200 mD, 400 mD, 150 mD respectively for layers 1 – 4, and the vertical permeability was set equal to the horizontal one. The upscaled model is thus laterally homogeneous. It was parameterised by 24 variables capturing the main reservoir uncertainties, with ranges shown in Table 5.1, as follows:

1. The water-oil relative permeability curves were parameterised with S_{wcr}, k_{rw0} and the 6 parameters from LET parameterisation – see Appendix C for more details.
2. The gas-oil relative permeability curves were parameterised with S_{gcr}, k_{rg0} and the 6 parameters from LET parameterisation.
3. The other 8 parameters were used for:
    a. One pore volume multiplier for the whole model (both porosity and NTG are considered unknown).
    b. Four multipliers of horizontal permeability – one per layer.
    c. One k_v/k_h ratio to calculate the vertical permeabilities from the horizontal ones.
    d. Two skin factors – one per each well.

The considered parameterisation put more emphasis on the phase relative permeabilities, and less emphasis on the 3D grid properties. The use of the well skin factors as the parameters is reasonable because the original fine scale model is

heterogeneous and the well completions might pass through the local high or low permeable spots. The resulting effect for the coarse model which has the laterally homogeneous permeability can be captured by the well skin factors.

parameter	S_{wcr}	k_{rw0}	L_o	E_o	T_o	L_w	E_w	T_w
min	0.1	0.3	1	0.5	0.1	0.1	0.5	0.3
max	0.3	1	5	3	3	2	10	3
parameter	S_{gcr}	k_{rgo}	L_o, E_o, T_o, L_g, E_g, T_g	*mult* $k_{x1}...k_{x4}$	*mult* k_z	*mult PV*	*skin PROD*	*skin INJ*
min	0	0.4	0.05	0.2	0.01	0.5	-1	-2.5
max	0.01	1.2	10	3	1	2	10	1

Table 5.1 Ranges of the parameters considered for the synthetic model.

For the purposes of history matching the original well data shown in Figure 5.6 were perturbed by adding the *measurement errors*, taken as uncorrelated Gaussian noise with the standard deviations defined below:

- For Q_{OPR} (oil production rate) $\sigma_{OPR} = 0.1 \cdot Q_{OPR}$, so that σ_{OPR} ranges from 7 m^3/day to 16 m^3/day.
- For Q_{WPR} (water production rate) $\sigma_{WPR} = 5$ m^3/day before water breakthrough, and $\sigma_{WPR} = 0.1 \cdot Q_{WPR}$ after water breakthrough.
- For Q_{WIR} (water injection rate) $\sigma_{WIR} = 0.05 \cdot Q_{WIR}$,
- For GOR (gas/oil ratio) $\sigma_{GOR} = 0.2 \cdot GOR$.

On the other hand history matching would involve the modelling errors. To estimate these, seven history matching runs were made with the 2500 days of the original unperturbed history. The resulting models turned out to reproduce the well data very closely, despite not quite flexible parameterisation and the fact that the models are laterally homogeneous and coarser than the original heterogeneous model. For the model with the smallest final value of the objective function, the standard deviations of the well data errors were estimated. These modelling errors can be compared with the measurement errors introduced above, as shown in Table 5.2. As can be seen, the modelling errors have standard deviations 4 – 8 times smaller than those of the measurement errors. For this reason the modelling errors, which generally have non-diagonal covariance matrix, can be neglected, and the objective function will only account for the introduced measurement errors that are not correlated.

	WOPR	WWPR	WWIR	WGOR
estimated **std** of modelling errors	1.5	1.3	1.7	16.8
average **std** of measurement errors	11.2	5.0	13.4	74.3

Table 5.2 Standard deviations of the modelling and measurement errors for the well data.

The synthetic seismic to be used in history matching (see Figure 5.7) was not artificially perturbed, so there will be no measurement error. However the modelling error is likely to exist due to the roughness of the upscaled simulation model, roughness of the parameterisation, and roughness of the seismic modelling within the history matching loop (regression between the maps). To estimate these errors the steps outlined in section 5.5 were undertaken.

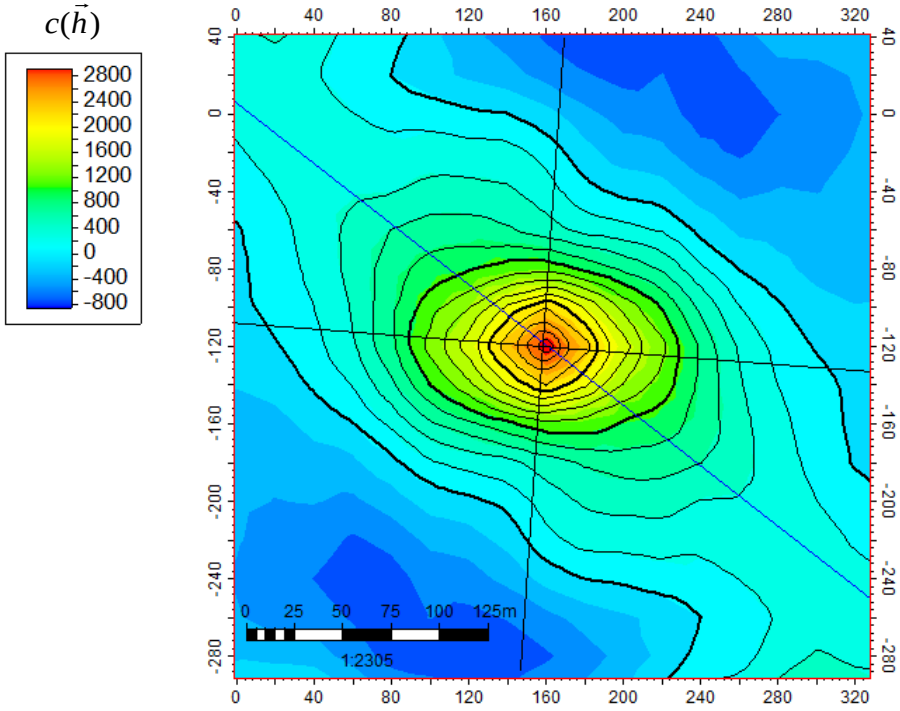

Figure 5.9 Estimated 2D covariace map with the major and minor axes of the ellipse shown by the black lines. The outer thick contour line corresponds to zero value on the map.

Twenty four preliminary SHM cases with diagonal C_s were run instead of just a single case – to gather more statistics. For each of the cases a 2D (auto)covariance was estimated and then I took the final covariance (Figure 5.9) as the arithmetic average of the 24 covariances, which is a statistically valid operation. The major and minor axes were picked visually and are shown by the black lines on the figure. To pick them only the inner – most reliable – contours of the ellipse were considered. The outer contours

seem to be somewhat distorted compared to the inner ones, and the direction picked from the outer contours is displayed by the blue line. This direction was not used however. The estimated ellipse parameters are as follows: rotation angle $\chi = -4^o$, major correlation range R_e = 140 m = 7 cells, minor correlation range r_e = 80 m = 4 cells.

To examine the effect of 4D seismic on the history matching uncertainty, six different HM setups were considered:

1. Well data (conventional) HM. The perturbed well data and the diagonal covariance matrix are used.
2. Seismic + well data HM, seismic without correlations. The well data are treated as in setup #1. The seismic part of the objective function f_2 uses the diagonal covariance matrix. The regression equation between the seismic and simulation model maps involves six (all possible) quadratic terms $\Delta P^2, \Delta Sw^2, \Delta Sg^2$, $\Delta P\Delta Sw, \Delta P\Delta Sg, \Delta Sw\Delta Sg$, and scaling by the baseline attribute map A_0. Taking into account the number of seismic data (points) equal to 1083, I estimated $\sigma_s = 60.2$ from the χ^2 criterion. The RMS of the observed 4D attribute map itself equals 171.4.
3. Seismic + well data HM, seismic *with* correlations. The difference with setup #2 is in the seismic covariance matrix C_s, which was calculated from the covariance ellipse of the seismic modelling errors, having the semiaxes 7 x 4 cells, rotated at -4^o. From χ^2 criterion the estimated $\sigma_s = 46.2$.
4. Seismic-only HM, seismic without correlations. The same definition of f_2 as in setup #2. The well data are not used.
5. Seismic-only HM, seismic *with* correlations. The same definition of f_2 as in setup #3. The well data are not used.
6. Unconstrained models. The models are simply sampled from the prior distribution – i.e. a uniform distribution in a rectangular area in the parameter space.

For each history matching setup I am interested in its predictive capabilities and the resulting uncertainty estimate. Both of these are assessed by firstly running the RML procedure for the 500 days historic period, thus producing a number of models which can be regarded as the samples from the posterior distribution. These models will be

referred to as the *RML-matched models*. The CMA-ES optimisation settings for a *single RML run* involve the population size $\lambda = 15$, and 400 generations altogether, resulting in the total 6000 forward modelling runs. The starting point for each CMA-ES search is taken as a uniformly distributed random point within the ranges of all parameters to maximise the diversity of the found local minima. Next, each RML-matched model is run by the simulator for another 2000 days of the prediction period, where the BHP controls at wells are inherited from the preceding historic period. The resulting well data forecasts can then be compared with the data from the original fine scale model, so that the predictive power of each HM setup can be assessed. The scatter of the well data forecasts among the bundle of models will in turn indicate the degree of uncertainty present therein.

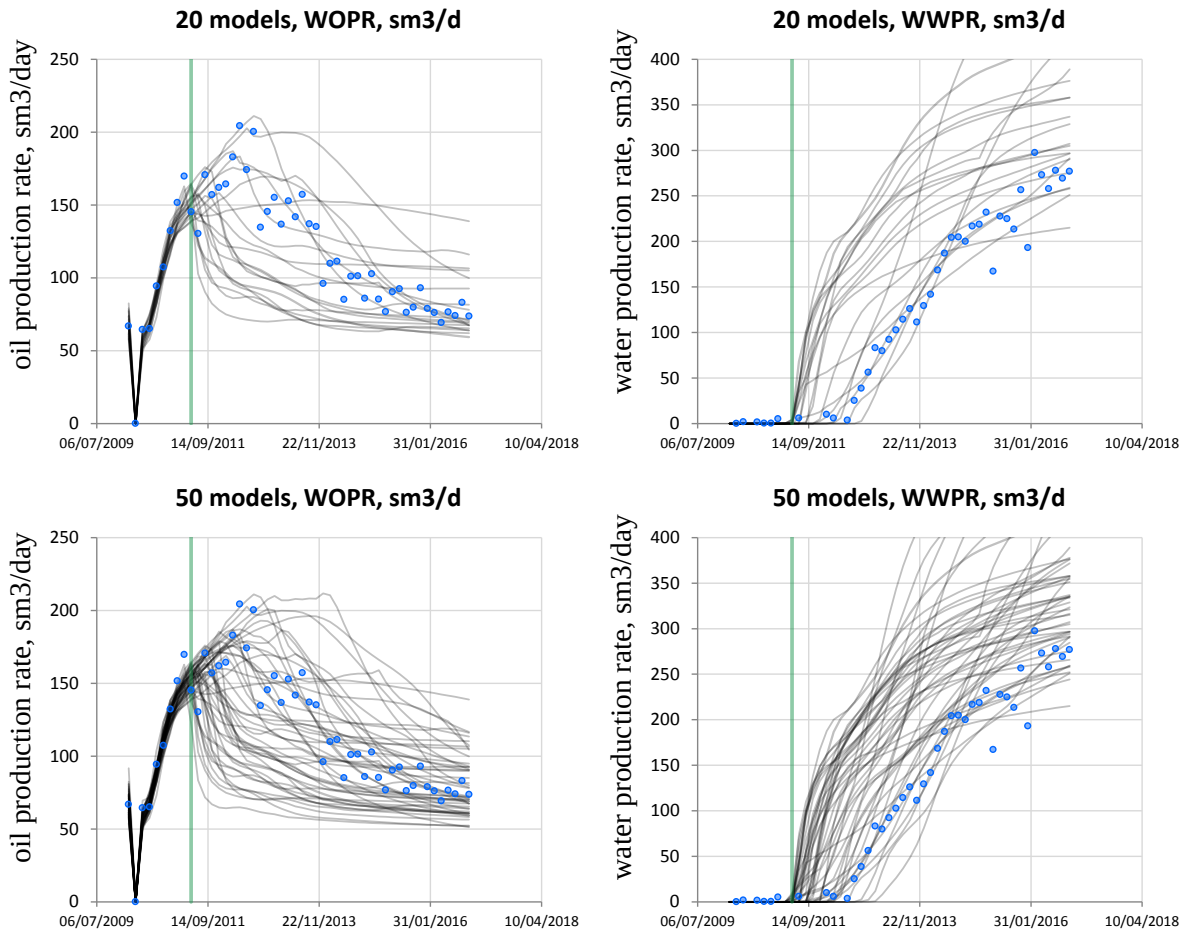

Figure 5.10 RML-matched models for setup #1. Blue circles are the observed data, grey lines are the data from the RML-matched models. The vertical green line shows the end of history (start of prediction), at the same point the seismic monitor is taken. *Top row*: 20 models, *bottom row*: 50 models. *Left column*: oil production rate, *right column*: water production rate.

To estimate how many RML-matched models are necessary for a history matching setup to give a realistic uncertainty picture, I considered the possible options of 5, 10, 20, 50 models per bundle, and it was found that 20 models is a reasonable choice. To illustrate this, a comparison of the results for 20 models and 50 models is given in Figure 5.10, where it can be seen that 50 models essentially produce the same picture as 20 models, although making it more "saturated". If one looked at the **mean** and **std** calculated from the separate trajectories displayed here, these quantities would also be very close for the 20 and 50 models cases.

Before moving further it is worth looking at the example of the 4D seismic attribute maps generated during seismic HM by the regression procedure introduced in Chapter 4. Figure 5.11 displays the input attribute map and two maps produced for the models from setups #2 and #3. As can be seen, the maps show high similarity and the main 4D features corresponding to the water saturation change and gas saturation change are reproduced reasonably well. Thus, regression between the time-lapse seismic maps and the reservoir dynamic property maps can be regarded as an adequate simulator-to-seismic tool in the context of history matching.

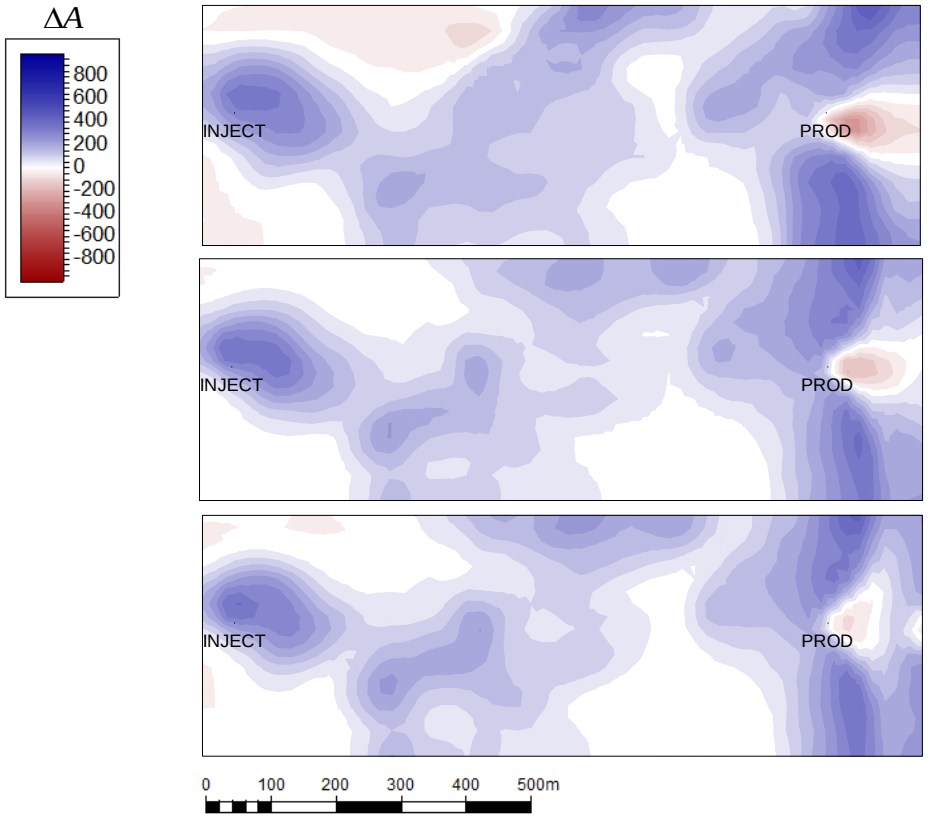

Figure 5.11 4D seismic attribute maps: the noiseless input map (*top*), output map from a RML-matched model of setup #2 (*middle*), output map of a RML-matched model of setup #3 (*bottom*).

Now we can turn to the results of uncertainty estimation with RML for each history matching setup. Figures 5.12 and 5.15 show the different modelled well data (oil and water production rates, water injection rate) both for the historic and the prediction periods. The plots of GOR are not displayed here because its major fluctuations due to the reservoir depressurisation and gas cap depletion occur during the historic period and are grasped by history matching, whereas in the prediction period all the HM setups show rather small GOR uncertainty and good forecasts.

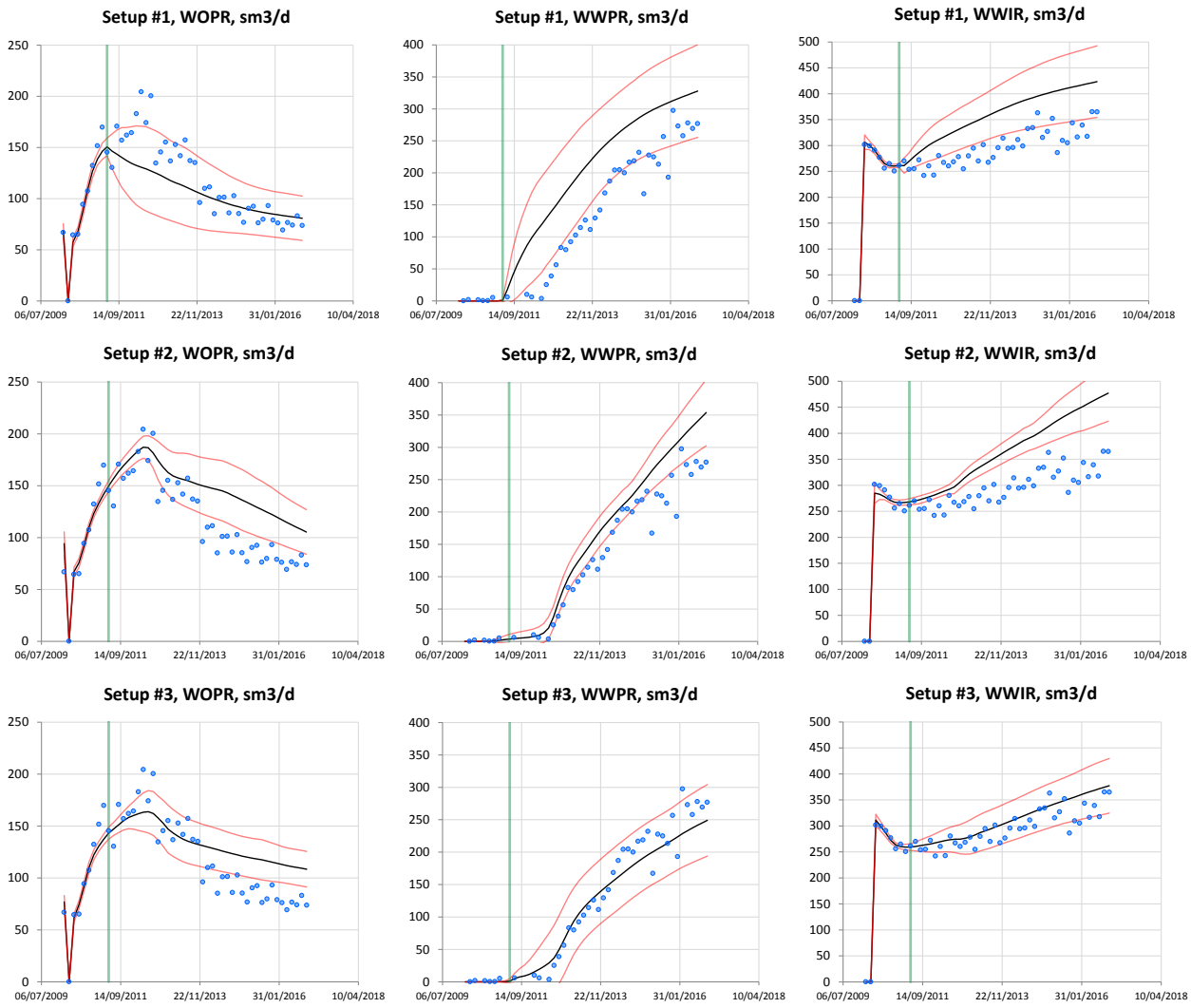

Figure 5.12 Plots of oil production rate (*left column*), water production rate (*middle column*), water injection rate (*right column*) for HM setups 1 – 3 (*rows*). *Blue circles* are the observed data, *black line* is the **mean**, *red lines* show **mean** ± **std**, *the vertical green line* shows the end of the 500 days history. The vertical axis scaling is identical across the three HM setups.

To display the uncertainty estimate, instead of plotting the separate trajectories from the RML-matched models as in Figure 5.10, I calculated the **mean** and **std** of each well

data vector, and the corridor of **mean** ± **std** is shown on the plots. For each HM setup this calculation involved the bundle of 20 models generated by RML. The observations (blue circles on the plots) are the well data from the original fine-scale model with the added perturbations.

For HM setups 1 – 3 all the history matching runs show a good well data match for the historical period, but I am interested in the behaviour at the prediction period which is located on the right of the vertical green line on the plots. The conventional well HM (setup #1) shows moderate uncertainty, and the stripe **mean** ± **std** generally covers the observations. There is a bias of the estimated mean value compared to the original well data observations which might be regarded as an indication that the whole procedure is faulty; however, there seem to be no theoretical reasons why this bias should not exist. When the seismic data without correlations are introduced (setup #2), the **std**'s notably decrease, but at the same time the **means** shift upwards, especially for the water injection rate for which the prediction mostly fails.

Adding the correlations of the seismic data errors (setup #3) leads to some increase in **std**'s compared to the non-correlated case, however there is still an improvement of the **std** compared to the conventional well HM. This is shown in Figure 5.13 by the plots of **std** for different well data during the prediction period, and the plots if **std** ratio for setups #1 and #3. Note that the improvement is more pronounced at the early stages of prediction, with **std** ratio values starting from 3 and then decreasing to 1.5 – 1.3.

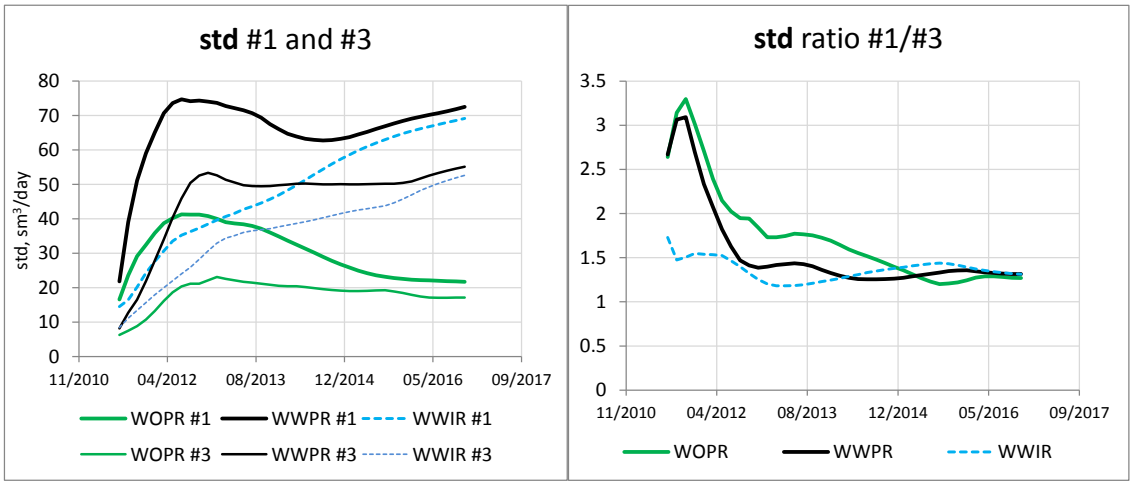

Figure 5.13 *Left*: plots of **std** for the well data at the prediction period (starting from 500 days) from setups #1 and #3. *Right*: plots of the **std** ratio, which equals **std** from setup #1 divided by **std** from setup #3.

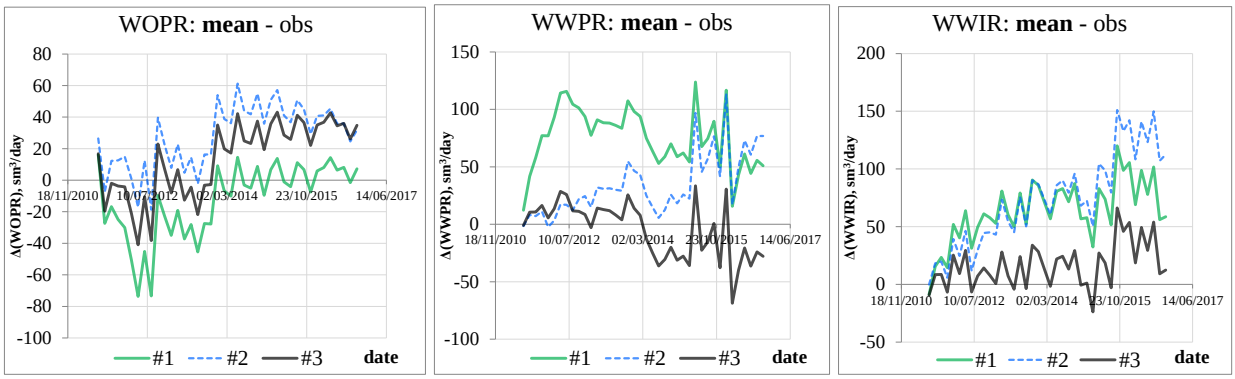

Figure 5.14 Difference between the **mean** estimated by setups #1, #2, #3, and the observations. *Left to right*: WOPR, WWPR, WWIR. On each plot *X* axis is the date (starting from 500 days), *Y* axis is the **mean** minus the observations. The different series on each plot correspond to the three HM setups.

Another enhancement from introduction of the correlations in seismic concerns the **mean** trajectories which became less biased for setup #3 than for the uncorrelated setup #2. The bias has also decreased compared to the ordinary well history matching (setup #1). This is seen most markedly for the water injection and production rates. For the oil production rate setup #3 also gives fine forecasts in the early prediction period, however some bias builds up in the late period.

As the illustration, the plots of the difference ("bias") between the **mean** estimated by setups #1 – #3 and the observed data are shown in Figure 5.14. The RMS values of these differences are provided in Table 5.3. As can be seen, history matching setup #3 has the lowest RMS values of the "bias", which are up to 3 times lower than the values for setups #1 and #2.

setup	RMS(ΔWOPR), sm^3/day	RMS(ΔWWPR), sm^3/day	RMS(ΔWWIR), sm^3/day
#1	26.3	79.1	68.9
#2	34.2	43.6	83.7
#3	27.1	24.6	25.4

Table 5.3 RMS values for the difference between the **mean** and the observations shown in Figure 5.14. The *columns* correspond to the different vectors: WOPR, WWPR, WWIR. The *rows* correspond to the different setups.

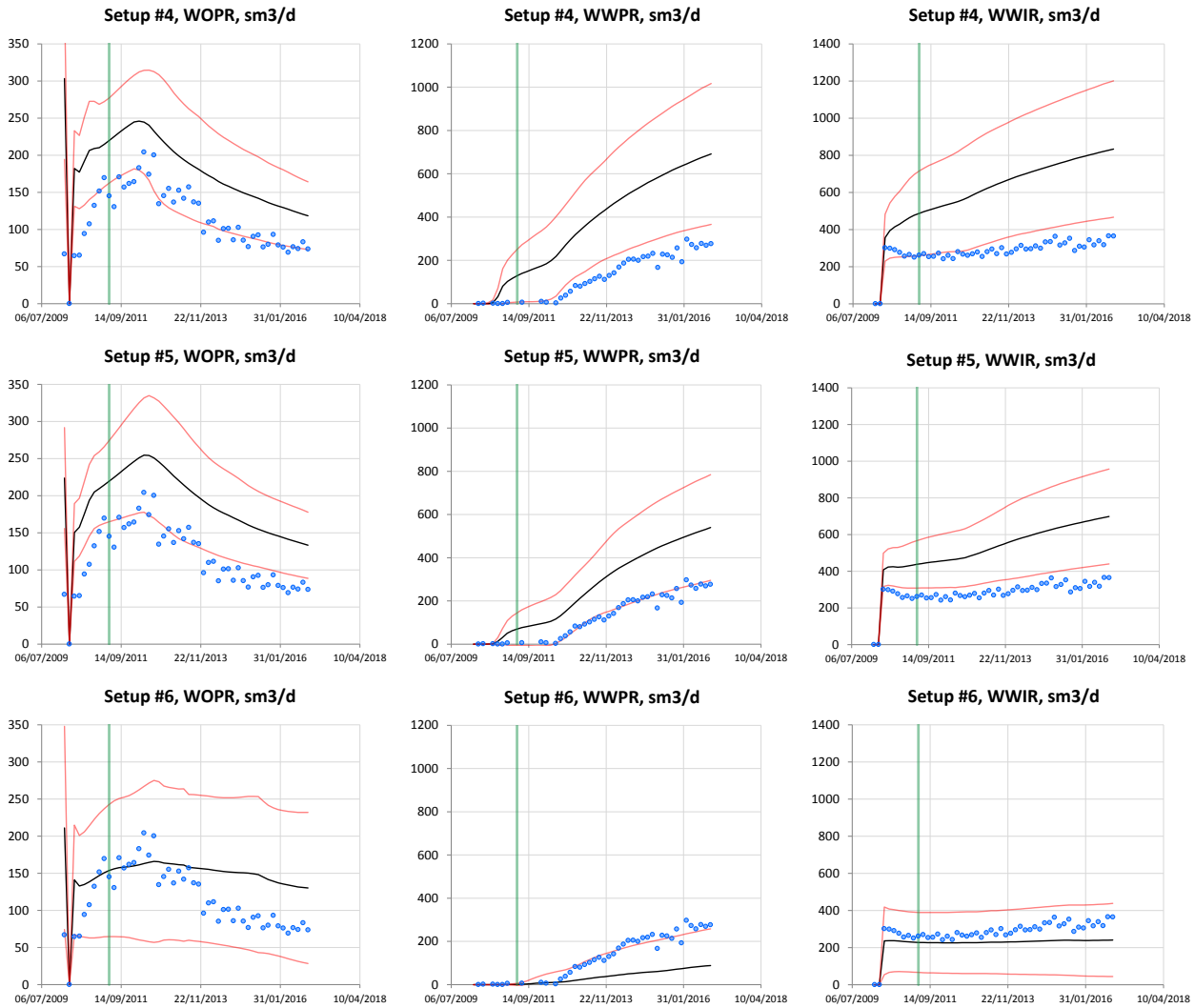

Figure 5.15 Plots of oil production rate (*left column*), water production rate (*middle column*), water injection rate (*right column*) for HM setups 4 – 6 (*rows*). *Blue circles* are the observed data, *black line* is the **mean**, *red lines* show **mean** ± **std**, *the vertical green line* shows the end of the 500 days history. The vertical axis scaling is identical across the three HM setups, but is different from that in Figure 5.12.

For HM setups 4 – 6, where the well data are not incorporated into the history matching loop, the forecasts have significant uncertainty at both historic and prediction periods (Figure 5.15). For the seismic-only history matching (setups 4 – 5) the estimated **std**'s of the predicted well data are 2 – 9 times higher than even for the conventional well HM, as demonstrated by the **std** ratio in Figure 5.16. However, if the well data were more sparse and seismic monitors were more dense – the picture might change, but investigating this is beyond the scope of my work. Besides, the situation of very sparse well data and abundant seismic data is rather exotic and can hardly be encountered in the real reservoir engineering practice. Introduction of the correlations to the seismic

data errors in setup #5 results in some reduction of uncertainty compared to setup #4. Also, if one looked at the whole bundle of the well data trajectories, then for setup #5 a more plausible distribution would be seen, whereas for setup #4 the trajectories tend to group into two clusters, leading to some degree of bimodality. Comparing the seismic-only HM cases with the set of the unconstrained models (setup #6), we can see that introduction of seismic data makes the mean trajectories improve and follow the trends that exist in the observation data. This is another illustration of the value of 4D seismic data for constraining the reservoir uncertainties.

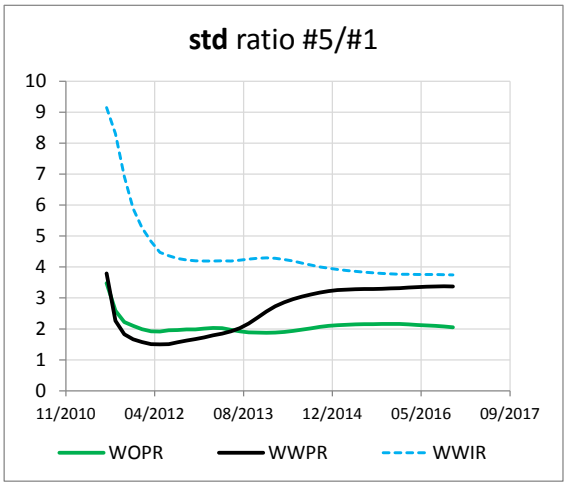

Figure 5.16 Plots of **std** ratio for the well data at the prediction period. The ratio equals **std** from setup #5 divided by **std** from setup #1.

When assessing the forecasting capabilities of a HM setup, not only should one look at how the observed data in the prediction period are covered by the **mean** ± **std** corridor. Even if such a coverage exists it may be just the averaging effect in a situation when some models overshoot the observations, while the others undershoot them, so that no single model actually predicts the observations. Even if one plots the well data in the prediction period for the whole ensemble of models (like in Figure 5.10), and finds out that the observed data are covered by the bundle of the modelled well data vectors, it may happen that there is actually no single model which reproduces *all* the observed well data vectors involved. Thus, the forecasting capabilities of the generated bundle of models should be confirmed by the presence of a few models with a good match to *all possible observed data* at the prediction period.

This criterion was checked for the setups 1 – 5 by finding the best-matching models out of the 20 generated for each setup. The found best-matching models reasonably reproduce the observations of WOPR, WWPR, WWIR, WGOR, so the criterion is met and it can be said that all the considered history matching setups have predictive power.

For setup #2 the results of the best-matching model are slightly worse for the water production and water injection rates, showing the bias similar to that in Figure 5.12. For setup #3 an illustration of performance of the best found model is shown in Figure 5.17. Some error exists here for WOPR at the late prediction period similar to what was observed in Figure 5.12. For setups 4 – 5 the existence of the best-matching models acceptably reproducing the observations confirms that the seismic-only history matching is also capable of predicting the future well data, albeit with high uncertainties. For the case of the unconstrained models (setup #6) all of them showed too significant mismatch to the observed data, meaning that the bundle of these models has no practical predictive capabilities.

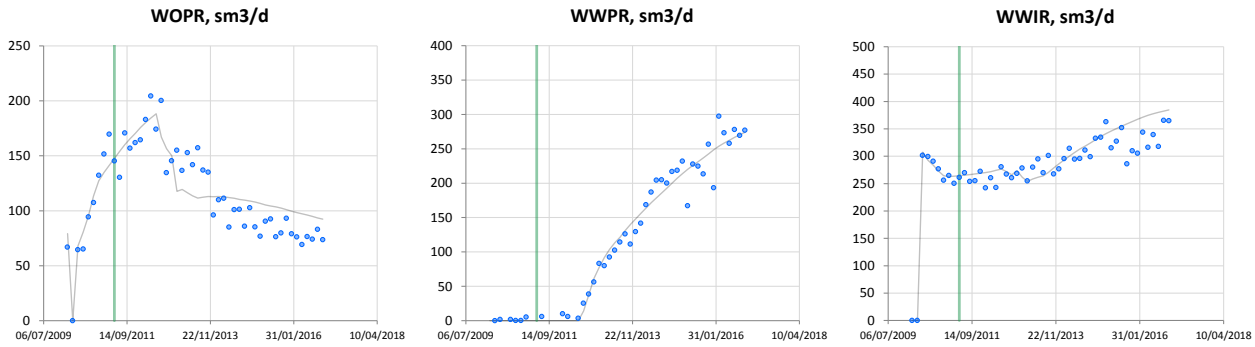

Figure 5.17 The best-matching model for setup #3 (displayed by the grey lines). The plots show: oil production rate (*left*), water production rate (*middle*), water injection rate (*right*).

Summarising the history matching exercises of this section, introduction of the 4D seismic into the history matching reduces the overall forecast uncertainties and improves the forecasts, especially at the early prediction period. This can be regarded as a proof of validity of the seismic history matching procedure proposed in Chapter 4. Moreover, when seismic data are treated more properly in terms of accounting for the spatial error correlations, the results become less biased and possess higher forecasting capacity. This supports the importance of carefully addressing the question of the seismic covariance matrices, since inappropriate covariance matrices, like the diagonal one in HM setup #2 may result in wrong uncertainty estimates with the lack of predictive power.

5.7 Summary

To estimate uncertainties in history matching, the Bayesian framework was adopted. I assumed uniform prior models distribution and a likelihood function with the Gaussian data errors. The errors (measurement, modelling, or total) are essentially described by the covariance matrix. Two uncertainty estimation techniques were considered. The first one is based on the Monte-Carlo integration with weights which takes place during CMA-ES optimisation. Although the procedure worked normally with very low dimensional problems, it underestimated uncertainty for the problems of realistic dimensionality, and was not used further. The second technique is the randomised maximum likelihood method (RML) which samples models from the posterior PDF, and is reasonably well known in the literature. However, in this work the method was implemented in a simpler way, by taking the uniform prior model distribution instead of Gaussian.

The errors in well data and seismic data were treated with the general-form covariance matrices, which are not necessarily diagonal, and allow accounting for the correlations in the data. Correlations in the seismic data errors are present in both measurement and modelling error constituents. Correlations in the well data errors result essentially from the modelling errors, as the measurement error correlation range is reported to be generally shorter than 1 month. To estimate the data error covariance matrix, a procedure was outlined which takes steps such as firstly making a rough preliminary history matching, then finding the errors in data, calculating the autocovariance vector (for wells) or map (for seismic), and then visually assessing the correlation range (or an ellipse, with two ranges, for the seismic case). Knowing the range, the correlation matrix is calculated using some idealised covariance function, e.g. the spherical one. Finally, to get the covariance matrix, the standard deviations are estimated based on engineering judgement and the χ^2 criterion outlined in Chapter 4.

The history matching technique together with the RML uncertainty estimation was applied to a three-phase heterogeneous synthetic model. A range of history matching setups were considered with the present/absent well data, the present/absent seismic data, and the present/absent correlations in the seismic data. Addition of the seismic data to history matching reduced uncertainties in all the well data types in the prediction period. A notable improvement could be observed especially in the early prediction period where the results of the seismic history matching were both more accurate in

terms of the **mean** values and less uncertain in terms of the **std** than those of the well-only HM case. Proper inclusion of the seismic error correlations resulted in the improvement of the forecasted mean values for the whole prediction period (the *bias* has decreased up to 3 times), making the history matching case with the *well + correlated seismic* data the most favourable one in terms of the forecasts precision and constraining the uncertainties. The exercises with *seismic-only* history matching showed that the seismic data alone is capable of calibrating the reservoir simulation model such that it can make future forecasts, although with high uncertainty. Generally speaking, all the seismic history matching exercises are a successful test of the proposed procedure for treating the 4D seismic which was described in Chapter 4. This procedure will be applied in the next chapter, where the history matching for a North Sea reservoir will be considered.

5.8 List of codes

For the studies described in this chapter the following programs were coded:

1. **Estimation of the autocovariances for the errors in well data**. The program takes the modelled and the observed well data from a history matched model, and calculates the autocovariance function for each well data vector by (5.12).
   Coding language: C++.

2. **Estimation of the 2D autocovariance for the error in seismic data**. The program takes the modelled and the observed seismic attribute from a history matched model, and calculates the 2D autocovariance map by (5.16).
   Coding language: C++.

3. **Automated seismic history matching with RML**. The program generates a model from the defined posterior distribution by the RML method described in section 5.3. The code is the extension of the automated seismic history matching code implemented for Chapter 4, and inherits the majority of the settings and input from it. The extension consists of adding the perturbation to the observed data (well and seismic) prior to starting the optimisation. The data perturbations are generated based on Cholesky decomposition of the corresponding covariance matrices.
   Coding language: C++.

Chapter 6 History matching for Schiehallion dataset

In the previous chapters a seismic history matching procedure was introduced which showed favourable results on the synthetic dataset in terms of the higher forecast precision and smaller forecast uncertainties of the history matched models – as compared to the conventional well history matching. In this chapter the techniques developed so far are applied to the Schiehallion reservoir. Within the chapter I will overview the general information on the field and the dataset, make an express assessment of the 4D seismic noise, set up the history matching workflow, and analyse the results of the conventional well HM and the well-seismic HM. The two history matching setups will be compared in terms of the estimated forecast uncertainties. It will be demonstrated that the reservoir models history matched using both well data and 4D seismic data have less prediction uncertainties (versus conventional well HM) for the wells located close to the moderate or strong 4D signals. This observation will serve as a proof of validity of the devised seismic history matching algorithm.

6.1 Field background

To introduce Schiehallion field, a brief background on it is presented below, which is essentially a compilation of a few papers on the subject [66], [67], [68], [69], plus some data inferred from the simulation model. The Schiehallion field is located at the Atlantic margin of the UK continental shelf, 200 km to the west of Shetland Islands, in water depths of approximately 400 m, see Figure 6.1 (*left*). The Schiehallion FPSO[36] vessel performed[37] development of this field and the satellite Loyal field. These two fields together have more than 2 billion barrels of initial oil in place, and historic production rates reaching 140 Mstb/day. The field consists of a range of reservoirs from the "T-sequence": T25, T28, T31a, T31b, T34, T35, with T31 (*a* and *b*) being the main reservoir. These are made up of the Tertiary age turbidites, and lie at depths 1700 – 2400 m. The productive sands range from channels to sheet-like sands with different patterns of overlap and connectivity. The generic geological model of the field is shown on Figure 6.1 (*right*). Apart from compartmentalisation caused by turbidite

[36] Floating production, storage and offloading (vessel).

[37] The FPSO worked until 2013, when it ceased production, and the new FPSO is under construction as of 2014. The operation of the first FPSO fully covers the time framework I consider in this thesis.

sedimentology and facies change, the field is further segmented by the east-west trending normal faults. Based on faulting, four segments are defined by the operator, with the two southernmost segments – 1 and 4 containing the majority of the original oil in place, see Figure 6.2, Figure 6.3. This study is focused on segment 4 which is separated from the northern segment 1 by a fault with large throw which is believed to be sealing, as suggested by the extended well test (see below). The reservoir is sealed from the South by a fault with a large throw exceeding the reservoir thickness. The seal from the East is provided by the pinch-out of the reservoir sands. At the West the structural dip works as the trapping mechanism [67].

The reservoir porosity and permeability are good, with average values equal to 0.27 and 600 mD respectively. The initial reservoir pressure P_{init} = 2907 psi (at depth 1940 m TVDSS) is close to the bubble point pressure P_{bub} = 2800 psi. There is a limited aquifer at the western part of the field which provides little natural support, plus small local gas caps. These characteristics result in the necessity of water injection for efficient oil recovery. The complex connectivity pattern between the sand geobodies imposes the challenge of appropriate placement of the producing and injecting wells for good pressure support. In Schiehallion field the drilled producers are horizontal so as to ensure sufficiently high production rates, and the water injectors are sub-vertical.

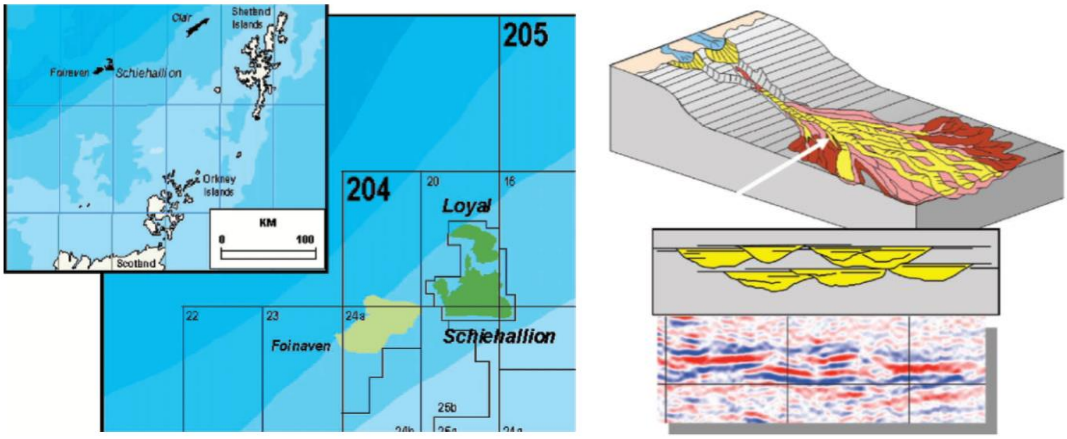

Figure 6.1 *Left*: location of Schiehallion field, *right*: generic scheme of turbidite deposits with seismic section from Schiehallion field (*below*). Pictures were adopted from [69].

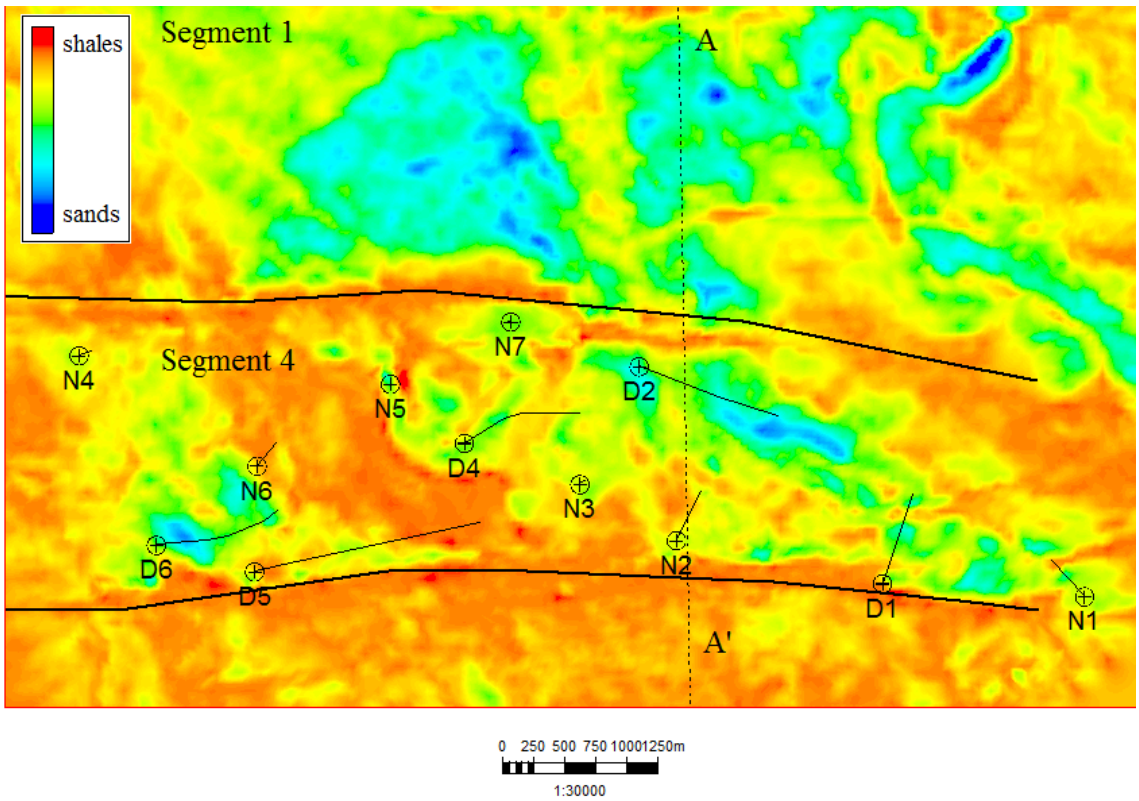

Figure 6.2 Map of the sum of negative amplitudes attribute for T31 reservoir, with sands corresponding to blue colours, shales – red colours (1996 seismic survey). The field's major segments 1 and 4 are displayed, together with the two major East-West faults (solid black lines). The wells completed in T31 reservoir of segment 4 are also shown.

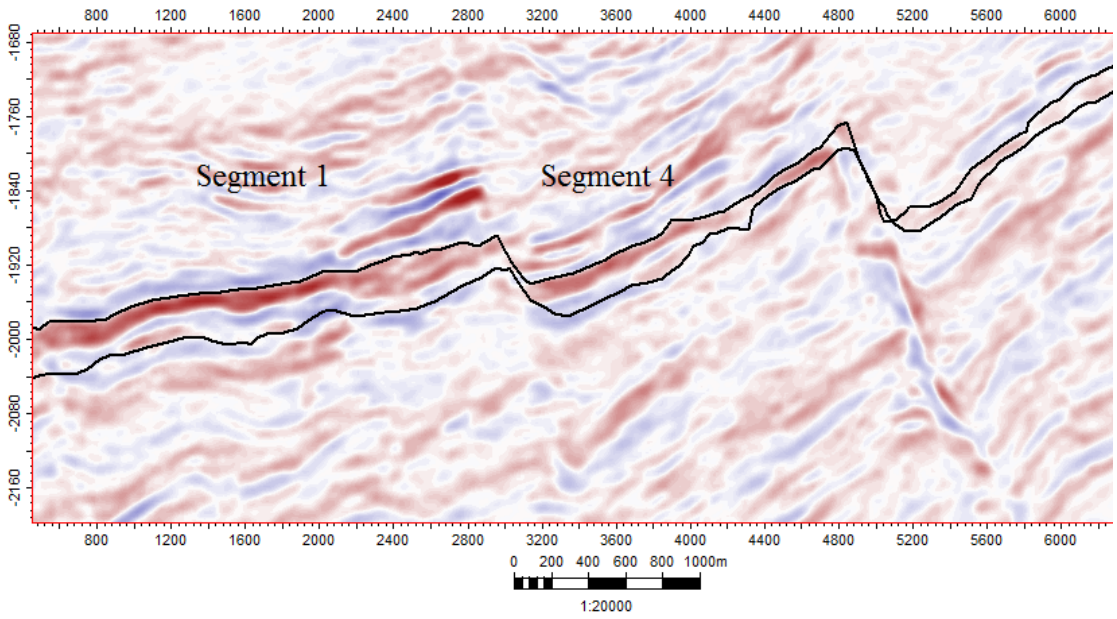

Figure 6.3 Cross-section AA' (North-South), top and base horizons of T31 are shown in black. Horizontal axis is in meters, vertical axis is two-way-time in *ms*. The normal faults bounding segment 4 from North and South are clearly seen.

Seven wells were used to appraise the field, revealing that the net oil sand could be accurately predicted from the seismic data [68]. The initial appraisal of the reservoir connectivity was done by an extended well test (EWT) performed in segment 1 in 1995, and it suggested that the reservoir was well connected [66]. The wells subsequently drilled in segment 4 showed no depletion of the initial pressure by the EWT, meaning absent or, at most, very limited communication between segments 1 and 4. The ensuing tank-based material balance studies also implied no connectivity between the two segments. Later it was found that the field connectivity is much poorer than was anticipated initially, and the EWT was actually affected by a nearby small gas cap. The initial production strategy was to place producers and injectors in different sand channels to maximise the sweep. However, due to insufficient connectivity the producers did not have appropriate pressure support. This resulted in high production GOR and so in the first 3 – 4 years of the field life the focus of the reservoir management was on managing gas. The infill drilling programme was implemented together with the improved water injection management, which allowed decreasing the production GOR to normal values. The infill drilling decisions were driven by the effective use of 4D seismic and pressure data. As the field matured, the water production increased and the reservoir management shifted to managing sweep and water cut.

To evaluate the reservoir connectivity, several data types were used. 3D seismic data allowed identifying the structural discontinuities in the reservoir resulting from normal faulting. It was found that 3D seismic may also be used for fairly accurate mapping of the net pay, [67], [68], and is a good indicator of the turbidite channel boundaries. Moreover, the seismic was employed for imaging the reservoir sands and creating a 3D reservoir model consisting of several hundred seismically-derived sand geobodies. This reservoir model was provided by the operator as part of the Schiehallion dataset and will be used in the history matching study of this chapter. 3D preproduction seismic survey was acquired at 1996, and 4D seismic monitor surveys were shot at years 1999, 2000, 2002, 2004, 2006, 2008 (and continuing, not considered in this thesis). The surveys allowed imaging the areas with gas breakout and water encroachment. These qualitative data were helpful in constraining the simpler material balance models or more complex reservoir simulation models.

The other data which allowed estimating the connectivity and sweep efficiency is the radioactive and chemical tracers which were used in all the injectors. Altogether, 13 different tracers were injected in 21 wells.

Pressure profiles measured at wells at the time of drilling gave valuable indication of connectivity of the new wells with the existing ones. For example, overpressure or depletion in excess of 400 psi at the new well is a signal of a sufficient connectivity with the other wells, whereas pressures close to the initial reservoir pressure may indicate poor connectivity [69]. There are permanent pressure gauges in all but one wells in the field. They allow pressure-transient analysis to infer the current formation permeability, skin factors and extrapolated reservoir pressure. The late-time transient pressure behaviour in Schiehallion usually indicates a channel flow model, but this does not provide much information due to the non-uniqueness of the parameters. For rapid evaluation of pressure trends and assessment of connectivity the tank-based material balance modelling was performed, for which the wells were grouped into tanks using a number of data, including e.g. the geochemical analysis of the reservoir oil samples. These material balance models helped in quick assessment of different reservoir connectivity hypotheses. The hypotheses found plausible were then further investigated by the full field reservoir simulation model [68].

6.2 Schiehallion dataset

In this study only segment 4 is examined, which is considered to be isolated from the adjacent segment 1. The data which I use are provided by the operator and include:

1. Reservoir simulation model (not history matched), which has dimensions $209 \times 57 \times 120$ cells for segment 4. The model contains the main reservoir T31 plus the overlying and underlying reservoirs connected to it.
2. Seismic cubes (coloured inversion, full offset stack) acquired at 1996, 2002, 2004, 2006, 2008. The 1996 seismic is the preproduction one and will be used as a baseline for the time-lapse studies. To assess the 4D seismic non-repeatability, normalized RMS was calculated in the overburden for the difference between surveys 1996 and 2004, see Figure 6.4. The details on this calculation can be found below, in section 6.3. The resulting mean NRMS is 0.36, which is quite close to the estimate 0.31 reported in [70].

3. Seismic horizons (top and base) for reservoir T31. Since only these horizons are available, for seismic history matching I will only use the attributes calculated for T31, which will be compared to the reservoir dynamic property maps averaged over *T31 cell layers* of the simulation model. Apart from T31, the simulation model also contains the reservoirs above (T34, T35) and below (T25, T28), see Figure 6.5. The sands of layers T25, T28, T34, T35 are developed predominantly in the western part of segment 4.
4. Historic well data for the period from 16/07/1998 (start of production) to 20/02/2008, including production and injection rates, water cuts, gas/oil ratios, well bottom whole pressures. The historical production rates for the entire segment can be seen in Figure 6.6. Eight producers (D1 – D8) and eight injectors (N1 – N8) worked during this period in segment 4. The trajectories of their perforated sections are shown in Figure 6.4. Some of the wells were completed in the reservoirs above or below T31, as reported in Table 6.1.
5. Well logs, including gamma ray, deep resistivity, neutron porosity, density, sonic and caliper logs.

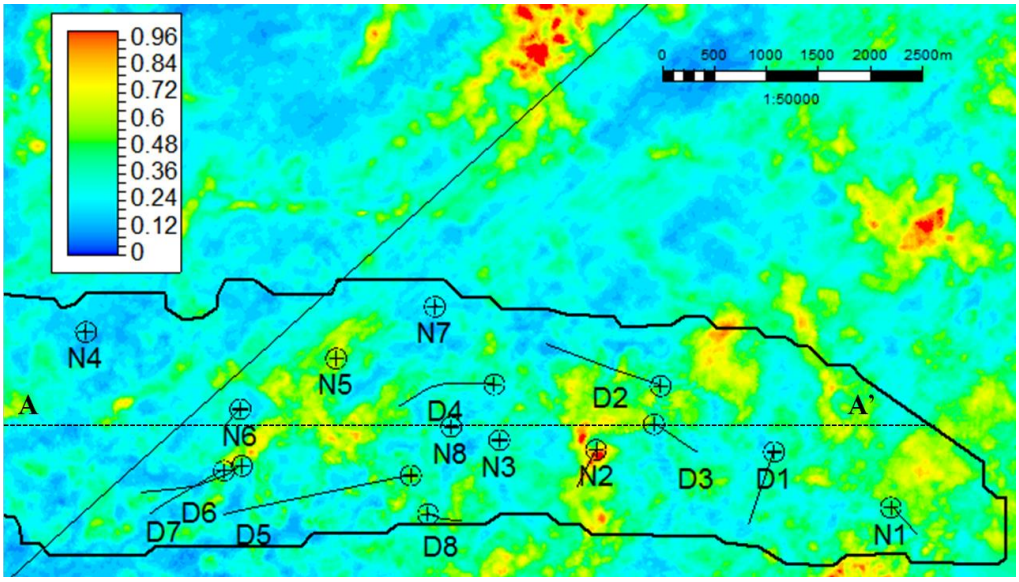

Figure 6.4 Overburden *NRMS* map for the difference between seismic cubes 1996 and 2004. The black contour line shows the boundary of segment 4. The inclined black line shows the direction of the seismic in-lines. The cross-section AA' shown by the dotted line is displayed in Figure 6.5. All the wells completed in segment 4 are displayed.

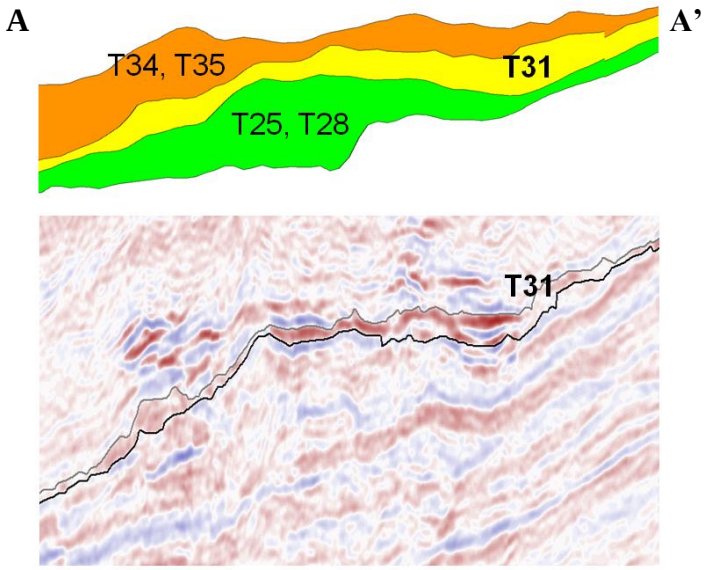

Figure 6.5 *Top*: a West-East cross section through segment 4 showing the main zones in the simulation model (upper reservoirs, T31 reservoir, lower reservoirs). *Bottom*: the corresponding seismic section with T31 top and base horizons.

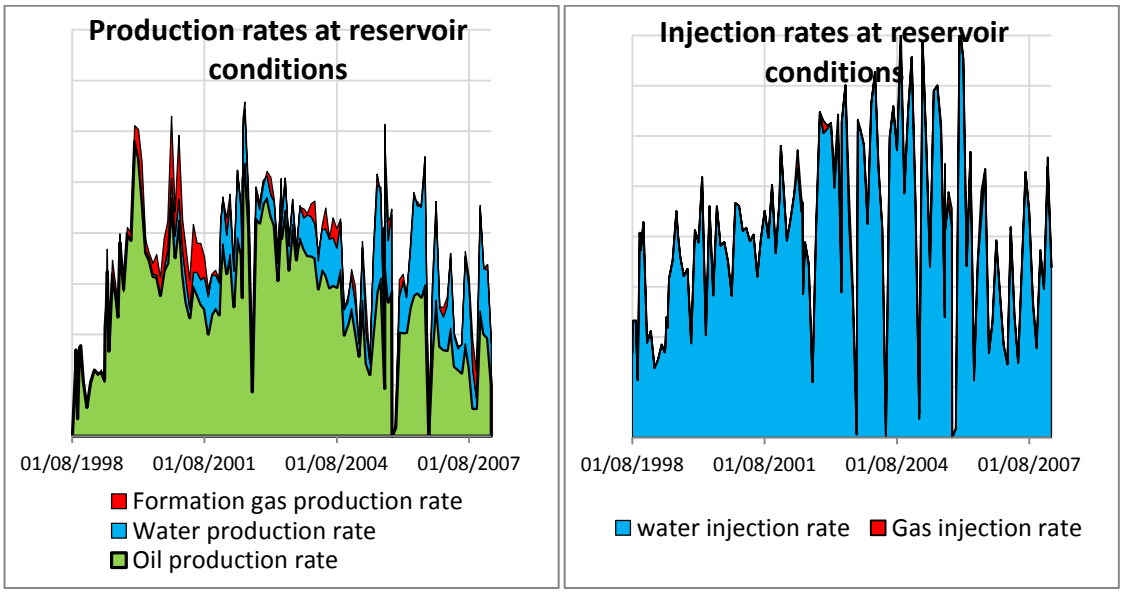

Figure 6.6 Production (*left*) and injection (*right*) rates for the entire segment 4. The vertical scale is hidden for confidentiality but is the same for the two plots. All the rates are converted to the reservoir conditions. Marginal gas injection is occasionally performed through producer D3 completed above T31 reservoir.

well	D1	D2	D3	D4	D5	D6	D7	D8	N1	N2	N3	N4	N5	N6	N7	N8
above T31			V		V		V			V		V		V		
in T13	V	V		V	V	V			V	V	V	V	V	V	V	
below T31					V			V				V		V		V

Table 6.1 Completion of the segment 4 wells: above T31 reservoir, in T31 reservoir, below T31 reservoir (completions are marked by "V").

The well data from the original fine-scale simulation model as compared to the history are displayed in Figure 6.7. As can be seen from the cross-plots, the model significantly overestimates the reservoir connectivity and permeability, so that the bottom-hole pressure of the injectors is underestimated, and bottom-hole pressure of the producers is overestimated by the model. Too high BHP at the producers also results in underestimation of the gas production. Underestimation of water production by the model may mean incorrect phase relative permeabilities together with too high sweep efficiency (delayed water breakthrough).

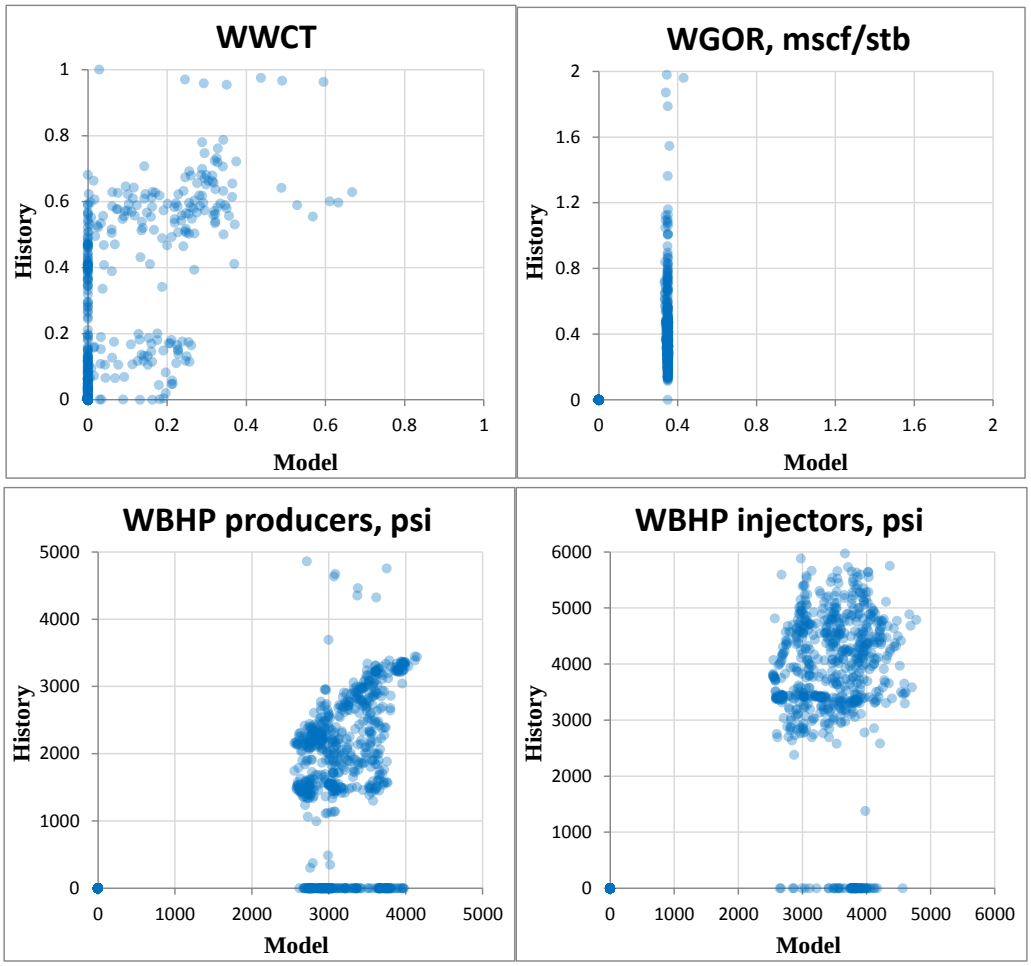

Figure 6.7 Well data cross-plots for the original fine-scale model vs. historic data. *Top, left to right*: water cut (all wells), gas/oil ratio (all wells); *bottom, left to right*: BHP at producers, BHP at injectors.

6.3 Estimation of noise to 4D signal ratio

As a part of the analysis of the input data I assessed the level of noise present in the 4D seismic data. The resulting estimate will not be used quantitatively for the history

matching purposes, and is done only for reference. One of such references is made in Chapter 3 when I produce a statement about the levels of noise for which the pressure map becomes useless for permeability inversion. When dealing with 4D noise, the common way to estimate it is to calculate the normalised RMS in the overburden for the difference of the baseline and monitor seismic cubes. However, such *NRMS* measures seismic non-repeatability, and essentially shows the ratio of the 4D noise to the baseline 3D signal in the overburden. I am interested in the different quantity – the ratio of the noise to the 4D signal in the reservoir.

The overburden, where the 4D *non-repeatability* noise is estimated, produces stronger seismic wave reflections than the reservoir where the 4D signal is found. This difference in the reflectivity can be expressed by the factor α, so that if the 3D seismic signal at the reservoir equals *G*, then the overburden 3D signal is αG. Assuming that the same scaling applies to the seismic noise, with the noise at the reservoir *N* we have noise in the overburden αN. Finally, there is 4D seismic signal in the reservoir equal to *S*. With this notation the monitor 3D seismic for the overburden can be expressed as $\alpha G + \alpha N$, and for the reservoir as $G + N + S$. The *NRMS* is calculated using the formula [71]

$$NRMS = \frac{2 \cdot RMS(M - B)}{RMS(M) + RMS(B)}, \tag{6.1}$$

where *M* denotes monitor seismic cube, *B* denotes baseline seismic cube, the root mean square (*RMS*) is calculated as a surface attribute over some window, so each $RMS(\cdot)$ in the formula above is a map. I calculate *NRMS* for the overburden in the 300 ms window, which is separated by approximately 400 ms from the top horizon of the reservoir T31. To estimate the 4D signal within the reservoir, *NRMS* is calculated between the reservoir top and base horizons (these are separated by 10 – 60 ms). Assuming that the baseline 3D seismic signal *G* is stronger than the 4D signal *S*, and the latter is stronger than the noise *N*, the following approximate expressions for the overburden *NRMS* and the reservoir *NRMS* can be set forth:

$$\begin{aligned} NRMS_{ovb} &\approx \frac{\alpha N}{\alpha G} = \frac{N}{G}, \\ NRMS_{res} &\approx \frac{S + N}{G} \approx \frac{S}{G}. \end{aligned} \tag{6.2}$$

Dividing the former by the latter, I get the ratio of the 4D noise in the reservoir to the 4D signal in the reservoir: $N/S = NRMS_{ovb} / NRMS_{res}$. The estimate of $NRMS_{res}$

shows the relative strength of the 4D signal in the reservoir, and it may be misleading for the areas with low net sand. In such areas both the baseline signal *G* and the time-lapse signal *S* are weak, so the calculated ratio (6.1) may become too high for the low denominator values. Since the 4D signal is weak in this case, $NRMS_{res} \approx N/G$, and essentially has the same meaning as $NRMS_{ovb}$. Denote *n* and *d* the numerator and denominator of (6.1). To avoid very low values of *d*, I assume that in the low net sand areas $NRMS_{res}$ should approximately equal the mean $NRMS_{ovb} = 0.36$, and hence I derive the minimum constraint $d_{\min}$ on *d*.

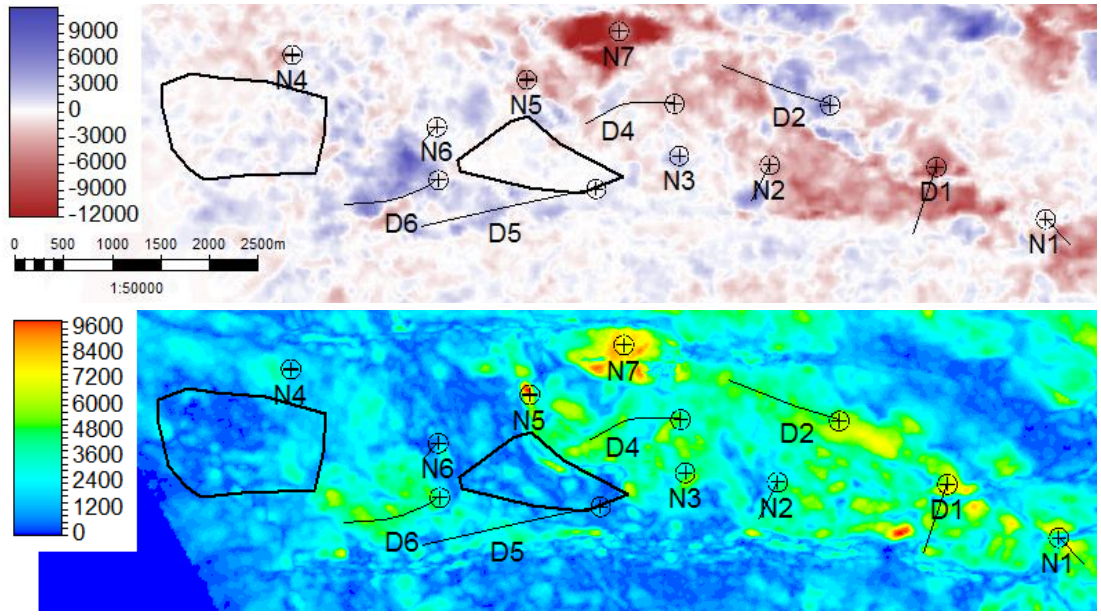

Figure 6.8 *Top*: time-lapse attribute (sum of negative amplitudes for T31), between monitor *M* at 2004 and the baseline *B*. Positive values (*blue*) correspond to reservoir hardening, negative (*red*) – to reservoir softening. *Bottom*: $RMS(M) + RMS(B)$ calculated for the T31 interval. The black contours outline the areas with small net sand. The wells shown are those completed in T31 reservoir.

Two distinctly visible low net sand areas were considered, as shown in Figure 6.8 by the black contours. The average value of *n* in these areas equals 600, so I can estimate the sought constraint $d_{\min} = 600/0.36 \approx 1700$. Then, take $d_{new} = \max(d_{\min}, d)$, so it does not become lower than the selected minimum. The corrected map of $NRMS_{res}$ is finally calculated as n/d_{new}. Dividing $NRMS_{ovb}$ map (Figure 6.4) by the corrected $NRMS_{res}$ map, I obtain the noise to signal ratio for the reservoir, which is shown in Figure 6.9. The ratio is high, reaching 100% – 200% in the areas with weak 4D signal. In the areas

with distinct 4D signal, that are outlined by the black contours in the figure, the mean value of N/S is 91%, the median is 80%, the mode is 60%. In the area close to well N7 where a strong pressure-up 4D signal is seen the N/S ratio is close to 0.36 – the average noise to signal ratio found in the overburden.

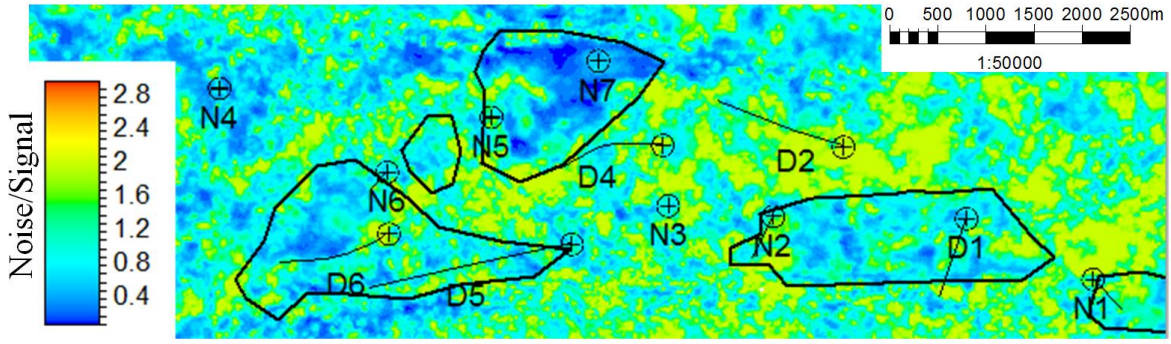

Figure 6.9 Noise/Signal ratio for T31 reservoir for the monitor 2004. The outlined areas are those with the stronger 4D signal. The wells shown are those completed in T31 reservoir.

6.4 Simulation model upscaling

Since I use a stochastic CMA-ES optimisation algorithm for the automated history matching which relies on a large amount of forward modelling, a fast-running simulation model is essential. The original model which contains 360,000 active cells takes 21,800 seconds to run the full history from 1998 to 2008. This is obviously not acceptable for the history matching workflow involving hundreds and thousands of the models runs. The model was severely upscaled (see Figure 6.10) to a coarse 70 x 22 x 30 cells model with 8,700 active cells and a full history run time 41 seconds. Horizontally, the cell size was upscaled from 50 x 50 meters to 150 x 150 meters. Vertically, the variable upscaled cell size was taken, with the following average values: 17 m for the main reservoir T31; 18 m for the overlying reservoir, where gas flow may be important; 44 m for the predominantly water-saturated underlying reservoir. The average cell thickness for the original model is 3.3 m.

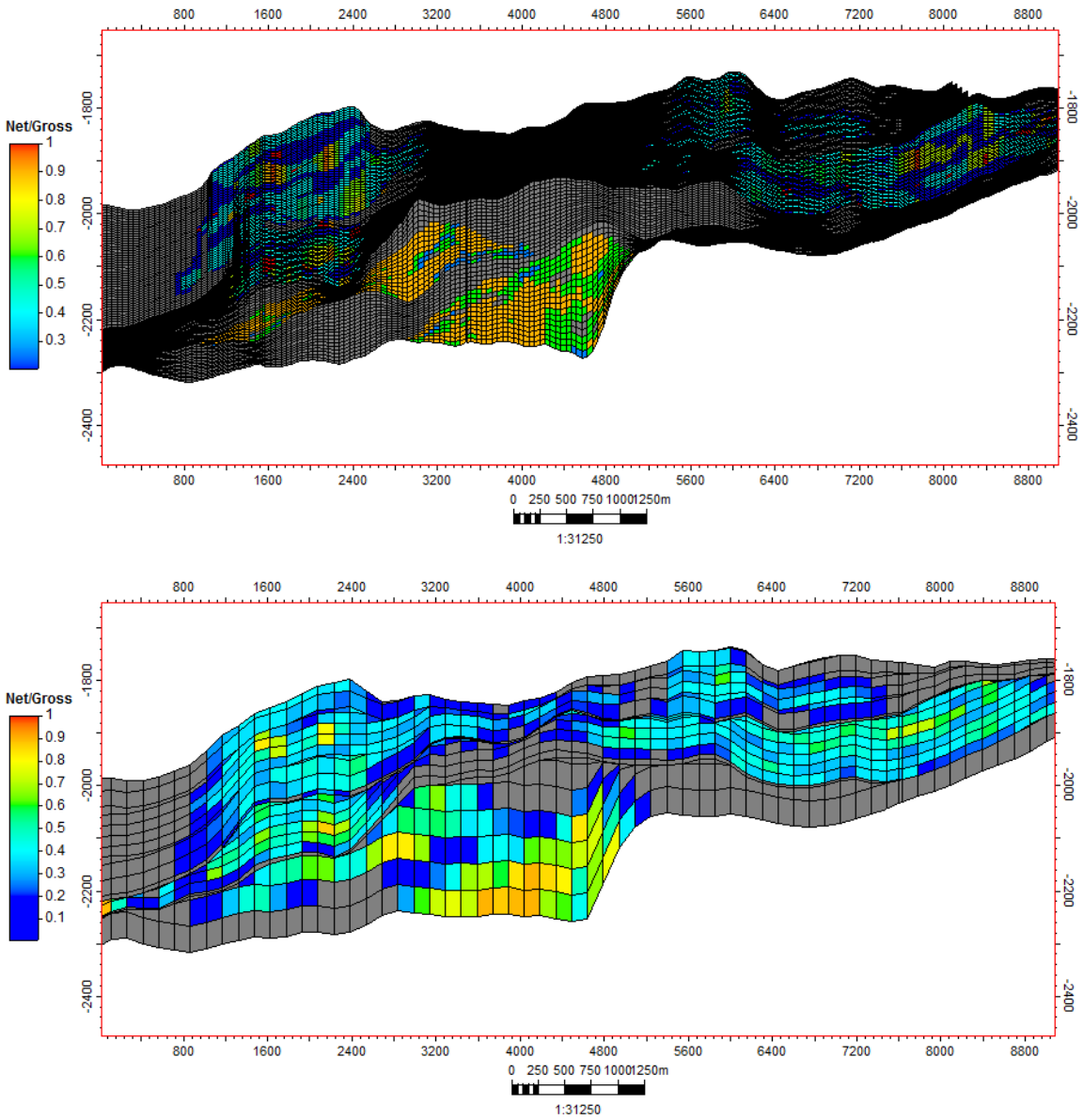

Figure 6.10 A West-East cross-section showing the NTG cube. *Top*: the original fine-scale model, *bottom* – upscaled model. All the gridlines are displayed to highlight the cell sizes.

Upscaling of the properties (NTG, porosity, permeability) was achieved by arithmetic averaging with pore volume weighting. Additionally, porosity and permeability during upscaling were weighted by NTG to preserve the pore volumes and transmissibilities between the coarse cells. Upscaling of the discrete properties (equilibration regions, geobody indices) was performed using the "most of" averaging. To check how upscaling affected the simulation model behaviour, the results from the original and the coarse models were compared, see Figure 6.11. As can be seen, the relative discrepancy in the field total oil production and total gas production is reasonably low, however the relative discrepancy in the total water production is quite high. With respect to the

model volumetrics, the relative difference in the initial oil in place between the coarse and fine models is $(OIP_{fine} - OIP_{coarse}) / OIP_{fine} = 0.54\%$, the differences in the total pore volume and water in place are even smaller, see Table 6.2. The high relative difference for the free gas is due to the very small sizes of the gas caps, which are sensitive to the cells coarsening[38].

	fine	**coarse**	**difference**
PORV, *x* rb	95.37	95.55	0.19%
OIP, *x* stb	9.44	9.49	0.54%
WIP, *x* stb	84.07	84.18	0.12%
FGIP , *x* mscf	0.038	0.065	71.23%

Table 6.2 Comparison of fluids in place for the fine and coarse models. *Rows, top to bottom*: pore volume, oil in place, water in place (including aquifer), free gas in place. All numbers are multiples of *x*, and the real values are hidden for confidentiality.

Although the discrepancies between the models are not too high, they cannot be called negligible, meaning the upscaling is rather rough and it may be challenging to transfer the updates applied to the history matched model back to the original fine model. In this work I estimate the uncertainties with RML algorithm, which is applied directly to the coarse model to generate the ensemble of the models from the posterior distribution, and then make the future well data forecasts. Direct transfer of the updates to the fine scale model does not guarantee that it will also follow the posterior distribution, and ideally the fine model should be history matched under the RML conditions. Given those complexities, in this work I do not target at transferring the updates back to the fine model.

[38] The gas caps in the coarse model are only 1-2 cells thick in the vertical dimension. The model gas saturations are initialised based on the predefined depths of the gas-oil contact, using the zero gas-oil capillary pressure, i.e. each cell is essentially assigned either zero or maximum gas saturation. Because of this, the resulting gas volumes may become inconsistent between the fine scale and the coarse scale models.

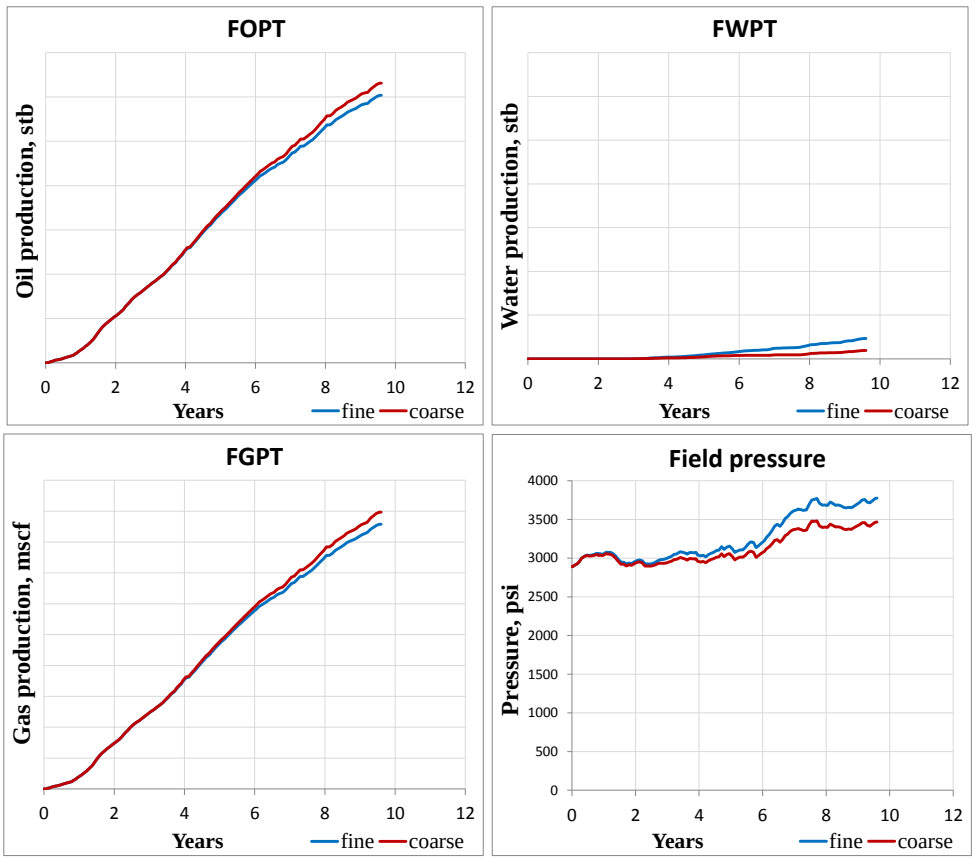

Figure 6.11 Comparison of the field production data for the fine and coarse models. *Top, left to right*: total oil production, total water production; *bottom, left to right*: total gas production, field average pressure. The values of production data are hidden for confidentiality. *Y* axes for FOPT and FWPT have the same range.

6.5 Setting up the history matching: parameterisation

One of the major uncertainties for Schiehallion is the reservoir connectivity, as mentioned earlier. Inspection of the original fine-scale simulation model also suggested that the reservoir connectivity should be reduced in order to match the well data. I selected two main controls over the connectivity to be used as parameters: firstly, *transmissibility multipliers* between certain regions of the model, and secondly, *permeability multipliers* within the regions. The natural choice of these regions is provided by the seismically-mapped geobodies present in the original simulation model, see Figure 6.12. The majority of these geobodies have localised "pancake" or channel-like shape. Each single geobody can be regarded as corresponding to an "elementary" episode in deposition and thus having relatively constant porosity-permeability properties. This makes it geologically-reasonable using a single permeability multiplier per geobody.

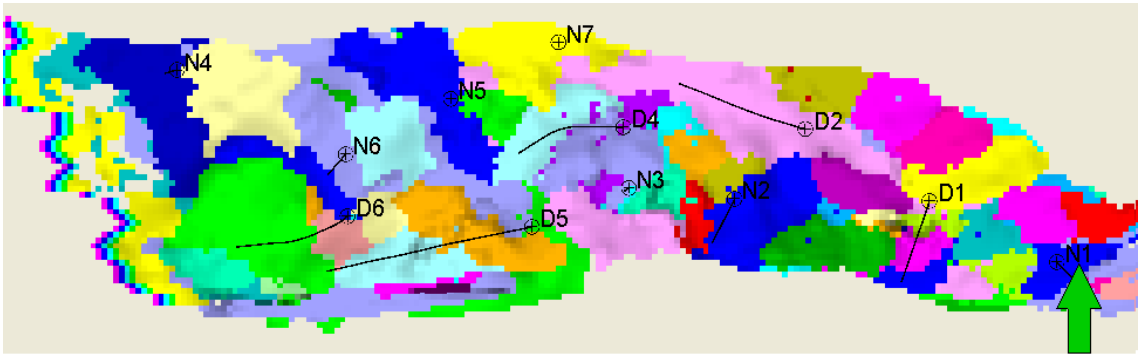

Figure 6.12 The fine 3D grid with seismically-mapped geobodies, showing the top of T31 reservoir.

On the other hand, separate geobodies are likely to have shale draping around them which acts as a thin connectivity barrier between the adjacent geobodies, cf. Figure 6.13. Such thin barriers are naturally represented in the simulation model by transmissibility multipliers. The original model has 147 geobodies in segment 4, which make the total number of permeability and transmissibility multipliers too large to be handled by the history matching procedure. To reduce this number the geobodies were amalgamated resulting in the total of 35 geobodies for the whole model. To perform such an amalgamation, the original smaller geobodies were grouped around each well based on the "closest neighbour" principle. The groups were further corrected to be more consistent with the maps of 3D and 4D seismic attributes. A few small faults present in segment 4 were also used to cut the groups into parts. Finally, each resulting group of the original geobodies produced a single amalgamated geobody, see Figure 6.14.

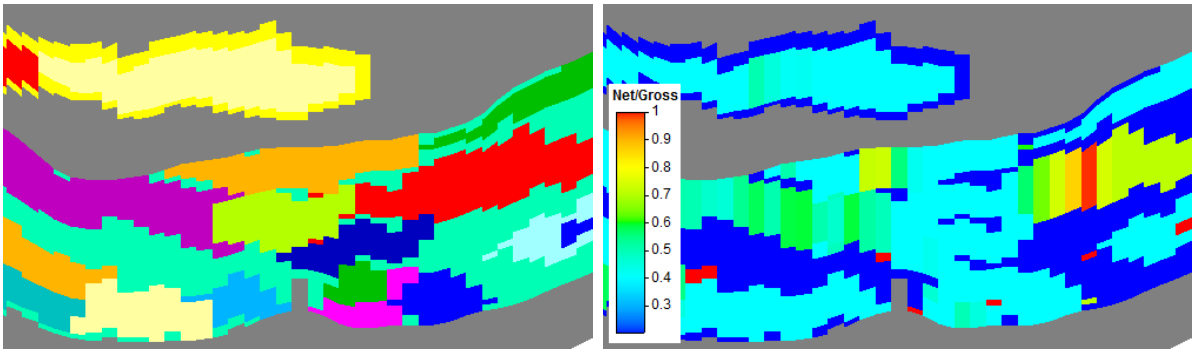

Figure 6.13 A cross-section of the original fine-scale simulation model showing the geobodies (*left*) and the corresponding NTG (*right*).

The procedure described allowed me to keep the number of parameters at feasible levels and at the same time adopt to a certain degree the geological information contained in the original model. For the specified 35 geobodies I took 33 permeability multipliers and 40 transmissibility multipliers (very often a single multiplier was used for the

connections of a particular geobody with all its neighbours). On top of that, a single *z*-permeability multiplier (i.e. k_v/k_h ratio) for the whole model was taken.

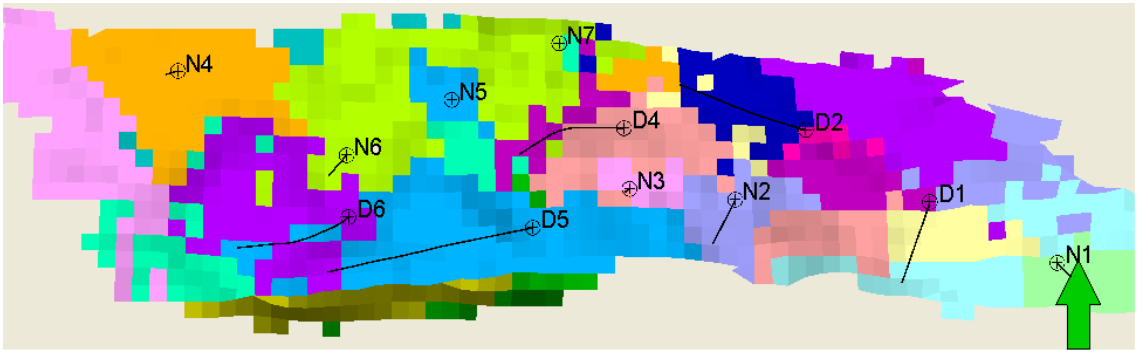

Figure 6.14 The coarse 3D grid with seismically-mapped geobodies after amalgamation, showing the top of T31 reservoir (when comparing with Figure 6.12, note that the colour codes of the geobodies are different).

For some of the wells where it was challenging to match the bottom-hole pressure (wells N7, N1, D3, D5, D7), I added a pore volume multiplier for the geobody(s) associated with that well. One more pore volume multiplier was used for the leftmost geobody of T31 which is used for numerical modelling of the aquifer both in the original fine-scale model and in the upscaled model. The relative change of the initial OIP for the resulting history matched models due to the pore volume change and the fluid contacts change (see below) is from -7% to +1%. Well D1 is completed in three adjacent geobodies which have poor connectivity: 18, 16, 14. To make the parameterisation more flexible, skin factors were introduced for the completions in geobodies 18 and 14. In the same manner for well D5 which is completed in the main reservoir T31, in the upper reservoir T34, T35 and in the lower reservoir T25, T28, two skin factors were introduced – for the completions in the *upper* and *lower* reservoirs. Schiehallion field development results in the depressurisation and re-pressurisation cycles with the associated gas exsolution and dissolution. Because of that a parameter which controls the gas dissolution rate $\partial Rs / \partial t$ was added. The latter quantity represents the maximum rate of increase of the solution gas/oil ratio *Rs* in the grid cells. A number of parameters were employed to control the oil-water and gas-oil relative permeabilities. These are: (for the water-oil system) the critical water saturation S_{wcr}, the maximum relative permeability of water in oil k_{rw0}, and two Corey exponents N_w, N_{ow}; (for the gas-oil system) the critical gas saturation S_{gcr} and two Corey exponents N_g, N_{og}. Finally, three parameters were used for the initial fluid contacts: one for the oil-water contact (OWC) in the whole segment, one for the gas-oil contact (GOC) in the

reservoir below T31 which delimits a small gas cap near producer D8, and the last one for the GOC delimiting a small gas cap near injector N1. The two small gas caps mentioned above were not penetrated by the wells and were mapped based on 3D seismic data, so their GOC's are rather uncertain.

Parameter	*min*	*max*	**Parameter**	*min*	*max*
S_{wcr}	0.177	0.42	Tr mult 17	1.E-07	1
k_{rw0}	0.1	1	Tr mult 37	1.E-07	1
N_{ow}	0.5	8	Tr mult 18	1.E-03	1
N_w	0.5	8	Tr mult 40	1.E-07	1
S_{gcr}	0	0.15	Tr mult 42	1.E-05	1
N_{og}	0.5	8	Tr mult 41	1.E-07	1
N_g	0.5	8	Tr mult 19	1.E-03	1
OWC, ft	6660.1	6774.9	Tr mult 11	1.E-03	1
GOC-D8, ft	6348.4	6561.7	Tr mult 10	1.E-05	1
GOC-N1, ft	5593.9	6003.9	Tr mult 12	1.E-02	1
K mult 1	0.1	1.1	Tr mult 13-14,17	1.E-07	1
K mult 2	0.1	1.1	Tr mult 32	1.E-03	1
K mult 3	0.1	1.1	Tr mult 33	1.E-03	1
K mult 4	0.1	1.1	Tr mult 9	1.E-05	1
K mult 5	0.1	1.1	Tr mult 7	1.E-05	1
K mult 6	0.1	1.1	Tr mult 6-all	1.E-07	1
K mult 7	0.1	1.1	Tr mult 8	1.E-03	1
K mult 8	0.1	1.1	Tr mult 34	1.E-07	1
K mult 9	0.1	1.1	Tr mult 35	1.E-03	1
K mult 10	0.1	1.1	Tr mult 29	1.E-03	1
K mult 11	0.1	1.1	Tr mult 1	1.E-03	1
K mult 12	0.1	1.1	Tr mult 2	1.E-03	1
K mult 13	0.1	1.1	Tr mult 4-5	1.E-07	1
K mult 14	0.1	1.1	Tr mult 5-6	1.E-07	1
K mult 15	0.1	1.1	Tr mult 20	1.E-05	1
K mult 16, 17	0.1	1.1	Tr mult 21	1.E-05	1
K mult 18	0.1	1.1	Tr mult 13-18,30	1.E-03	1
K mult 19	0.1	1.1	Tr mult 13-19,40	1.E-05	1
K mult 20	0.1	1.1	Tr mult 13-12,32	1.E-05	1
K mult 21	0.1	1.1	Tr mult 5-41,32	1.E-05	1
K mult 22	0.1	1.1	Tr mult 5-12,13	1.E-05	1
K mult 29	0.1	1.1	Tr mult 8-34,42	1.E-07	1
K mult 30, 31	0.1	1.1	Tr mult 9-8,42	1.E-07	1
K mult 32	0.1	1.1	Tr mult 17,16 - 18,19,31	1.E-05	1
K mult 33	0.1	1.1	Tr mult 15-14	1.E-05	1
K mult 34	0.1	1.1	Tr mult 13-5	1.E-07	1
K mult 35	0.1	1.1	PV mult N7	0.48	1.6
K mult 36	0.1	1.1	PV mult N1	0.48	1.6
K mult 37	0.1	1.1	PV mult D3	0.48	1.6
K mult 38	0.1	1.1	PV mult D5	0.48	1.6
K mult 40	0.1	1.1	PV mult D7	0.48	1.6
K mult 41	0.1	1.1	PV mult aquifer	6	20
K mult 42	0.1	1.1	skin D1 - 18	0	200
mult Kz	0.2	4	skin D1 - 14	0	1000
Tr mult 15	1E-10	1	dRs/dt, Mscf/stb/day	0	0.5
Tr mult 14	1E-10	1	skin D5 - upper	0	2000
Tr mult 38	1E-07	1	skin D5 - lower	0	500
Tr mult 16	1E-07	1			

Table 6.3 Ranges of parameters used for history matching (total number of parameters: 95).

The ranges used for all the parameters are presented in Table 6.3. The names of the parameters in this table should be generally clear from the description above. E.g. "GOC-D8" is the GOC for the gas cap near well D8; "K mult 16, 17" is the permeability multiplier for geobodies 16, 17; "Tr mult" is the transmissibility multiplier of the specified geobody with its neighbours, or between the listed geobodies; "PV mult N7" is pore volume multiplier for the geobody(s) associated with well N7; "skin D1 - 18" is the skin factor for the completion of well D1 in geobody 18. These ranges were selected generally based on engineering judgement, so that the perturbed model remains geologically and physically meaningful and consistent with the *a priori* understanding of the field. The following comments are however necessary.

1. The critical water saturation S_{wcr} was taken to range from the connate water saturation equal to 0.177 to the critical water saturation of the *original fine scale model* equal to 0.42.
2. The range for the OWC was established based on the analysis of gamma ray and deep resistivity logs at the sub-vertical injection wells N3, N4, N5, N6, N7 which penetrate both the oil-saturated sands and water-saturated sands. The chosen range for the OWC is essentially from the highest "definite water" TVDSS to the lowest "definite oil" TVDSS.
3. The ranges for the two GOC's were defined such that the minimum contact depth corresponds to an absent gas cap, and the maximum contact depth corresponds to the gas cap height twice as large as that in the original simulation model.
4. The ranges for permeability and transmissibility multipliers were taken such that these multipliers will be generally less than 1, thus reducing the total reservoir connectivity which is known to be overestimated in the original model.
5. The action of the pore volume multipliers for the geobodies associated with wells N7, N1, D3, D5, D7 can be regarded as modification of their net/gross ratios. The unperturbed average NTG of these geobodies equals, respectively, 0.27, 0.28, 0.19, 0.28, 0.40, so multiplying it by a number from 0.48 to 1.6 will not cause a severe un-geological change.
6. The maximum bound for $\partial Rs / \partial t$ was taken equal to 0.5 Mscf/stb/day so that the initial gas/oil ratio Rs = 0.35 Mscf/stb could be reached in approximately one day of gas dissolution.

6.6 Setting up the history matching: objective function

Two history matching setups will be considered: *conventional well history matching* which uses only the well data, and *seismic history matching* which uses the same well data plus 4D seismic data. The total period for which the well measurements are available is 9½ years, however only a limited initial part of it – from the start of production at 1998 till August 2004 – will be taken as a *historic period* to perform history matching. The remaining part will be used as a *prediction period* to assess the predictive capabilities of the history matched models.

The well part of the objective function f_1 is defined by formula (4.2) – a quadratic function with non-diagonal covariance matrix C_w. For the history matching purposes the production wells in the model are controlled by the liquid production rate to better honour the material balance. The historic well data used in the objective function are the water cuts and GOR's for production wells, and bottom-hole pressures for all wells. To calculate the covariance matrix C_w, I follow the steps outlined in Chapter 5: making the preliminary history matching of the model, defining the correlation ranges, and defining the standard deviations. After estimating the error between the preliminary model and the observations, the autocovariance functions were estimated. For better confidence, a few preliminary history-matched models were analysed and the average autocovariance for each data vector was taken. The correlation range for the error is then found visually, by superimposing a spherical covariance function appropriately stretched. Examples of the autocovariance functions for estimation of the correlation ranges are shown in Figure 6.15.

The ranges found for all the data vectors are listed in Table 6.4. Higher correlation ranges, e.g. 400 days, indicate that the modelling error dominates the total error, while the lower ranges, e.g. 100 days, are more typical for the vectors with higher measurement noise. The former situation is the case for the water cut vectors, the latter situation – for the GOR vectors. Higher measurement noise for the GOR does make sense because gas production from the wells producing below the bubble point is a relatively irregular and instable process involving accumulation of the gas volumes near the well and their spontaneous discharge to the well. The ranges for the BHP at producers are larger than those at injectors, which is consistent with the fact that the scatter of the BHP data at the injectors is visually higher than that at the producers. This is presumably related to the more stable flow conditions at the producers where gas

lift is implemented (hence, a softer flow control), as opposed to the water injectors where the flow conditions are affected directly by the water pumps (more rigid flow control).

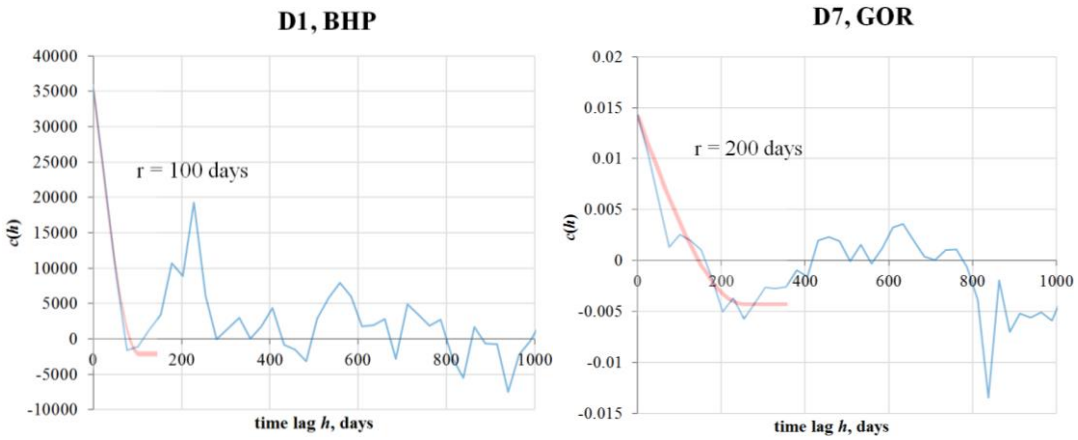

Figure 6.15 Autocovariance functions for the error between the model and observations (*blue graph*). The fitted spherical covariance function is shown by the *red line*. *Left*: autocovariance for BHP error of well D1, *right*: autocovariance for GOR error of well D7.

For well D3 no GOR measurements were used, since it tends to have high and unstable GOR with large peaks during the model simulation. This is because well D3 is occasionally used to inject gas for local gas storage [69] with subsequent production of that gas. Such well behaviour makes it difficult to incorporate gas production information in the form of GOR vectors – the high peaks make the misfit associated with this vector dominate over the other vectors, which unfavourably biases the whole optimisation workflow. However gas production can be incorporated by using the quantity that behaves more smoothly – the vector of the total gas production WGPT. Only one measurement of WGPT for well D3 was used – the one at the end of historic period at 01/08/2004. The error for this measurement is assumed to be not correlated with the other errors, and only the standard deviation σ_k is defined for it, taken equal to 10% of the corresponding observed WGPT at this date. No more dates with WGPT measurements were considered to avoid handling the correlations of data errors which arise for the cumulative well production quantities. Producer D8 and injector N8 do not work during the historic period, so they are not included into the error model. However, these wells will appear in the prediction period, and will be used in the forecasts calculation. For well D4 no BHP measurements were used because of their absence.

well	water cut		GOR	
	sigma	**correlation range**, days	**sigma**, mscf/stb	**correlation range**, days
D1	0.10	300	0.30	100
D2	0.15	300	0.15	350
D3	0.10	300	--	--
D4	0.15	400	0.20	100
D5	0.15	400	0.20	300
D6	0.15	300	0.10	300
D7	0.15	300	0.20	200

Bottom-hole pressure					
well (producer)	**sigma**, psi	**correlation range**, days	**well** (injector)	**sigma**, psi	**correlation range**, days
D1	300	100	*N1*	700	100
D2	300	400	*N2*	500	150
D3	400	250	*N3*	700	100
D4	--	--	*N4*	700	150
D5	300	400	*N5*	900	150
D6	300	250	*N6*	700	100
D7	400	150	*N7*	400	100

Table 6.4 Standard deviations σ_k and correlation ranges of the well data errors.

After defining the correlation ranges, the standard deviations of the well data errors σ_k were estimated for all well data vectors. For each vector the standard deviation was taken constant over all time steps, and is shown in Table 6.4. The definition of the sigmas was performed by applying the χ^2 criterion to each group of vectors (the groups are: WWCT's for all wells, WGOR's for all wells, WBHP's for producers, WBHP's for injectors). The 95 model parameters were allocated in equal proportions between the 4 groups. The target was to get approximately the same σ_k for each vector in the group, however for some wells this value might be increased or decreased, subject to keeping the group objective function in line with the χ^2 criterion directives. The decision on increasing or decreasing σ_k for a particular vector was based on engineering judgement and visual inspection of the observed scatter of the well data. The relative impact of each data vector on the objective function during the preliminary history matching runs was also factored into adjusting the sigmas. E.g., the BHP of injector N5 was assigned a higher sigma – for this well the high measurement error is evident, as seen on the initial well shut-in period (Figure 6.16).

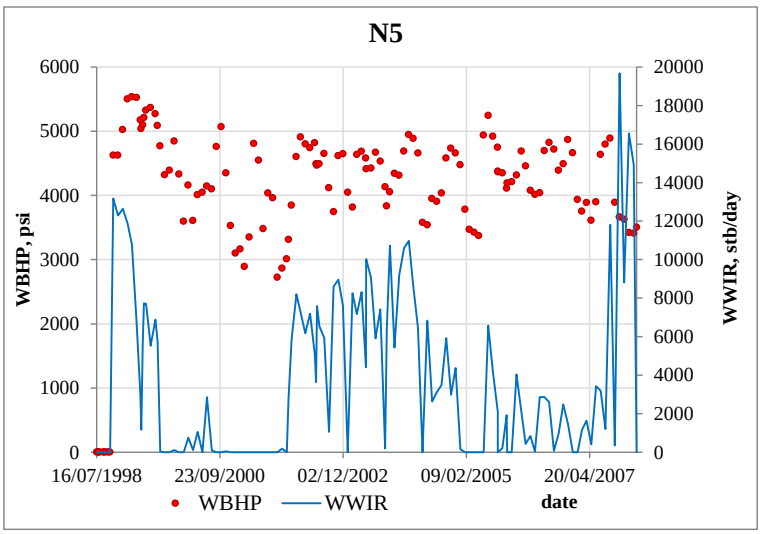

Figure 6.16 Historic water injection rate and bottom hole pressure for well N5.

As can be seen from Table 6.4, the sigma values for the BHP of injectors are higher than those for the BHP of producers. This can be explained, firstly, by the absolute BHPs at injectors (4000 psi – 5000 psi) being higher than those at producers (1500 psi – 3000 psi). In practice, matching the higher values is more difficult and results in higher modelling errors. Secondly, as was discussed above, the scatter of the historic BHP data at some injectors is larger than at producers, which can be regarded as higher measurement noise, cf. Figure 6.16. Thus, the injectors have smaller correlation ranges, but larger standard deviations for the BHP errors.

The seismic part of objective function f_2 is defined by formula (4.12). For the considered historic period 1998 – 2004 two seismic monitors are taken: at July 2002 and August 2004. The seismic attribute I use is the sum of negative amplitudes between the reservoir top and base horizons. The time-lapse attribute maps for the two monitors are shown in Figure 6.18. To define the covariance matrix for the seismic errors, the steps outlined in Chapter 5, section 5.5 were followed. From the 10 preliminary history matching runs with diagonal covariance matrix the seismic errors were found, and 2D autocovariance map was calculated as the average autocovariance over the 10 models and over 2 monitors, see Figure 6.17. For the ellipse seen on the map, the rotation angle was taken as 0 degrees. The major and minor correlation ranges were both estimated to equal 400 m, or 2.7 grid cells. While analysing the autocovariance map, more emphasis was put on the very central area, while the values more distant from the centre were ignored.

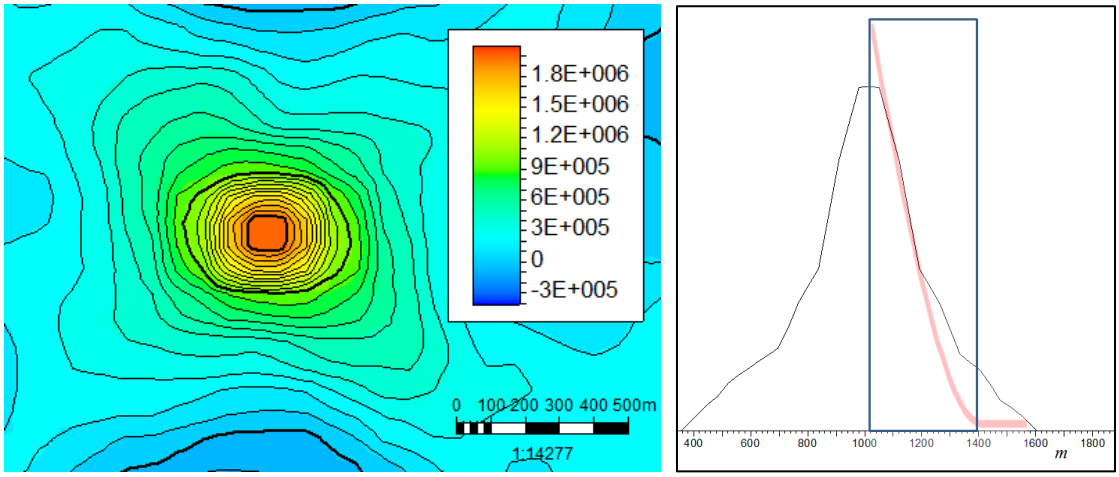

Figure 6.17 *Left*: 2D autocovariance map of seismic errors for the segment 4 simulation model. *Right*: autocovariance along the minor (North-South) axis. The red line shows the stretched spherical covariance function. The blue rectangle shows the estimated range equal to 400 m.

To define the standard deviation σ_s, χ^2 criterion was applied. With the number of well data equal to 1429, and the number of seismic data equal to 1364, the 95 parameters were allocated equally between the well and seismic data. The resulting seismic standard deviation equals $\sigma_s = 1670$, while the RMS for the time-lapse attribute data equals 1940. The regression procedure applied to the seismic data used six (all possible) quadratic terms: $\Delta P^2, \Delta Sw^2, \Delta Sg^2, \Delta P\Delta Sw, \Delta P\Delta Sg, \Delta Sw\Delta Sg$. For scaling in equation (4.8), the baseline attribute map was employed (Figure 6.2). As mentioned in section 6.2, 4D seismic is to be compared with the reservoir dynamic parameters averaged over layer T31 only, ignoring the overlying and underlying layers. Furthermore, the water-saturated zone of reservoir T31 is also excluded from consideration because it exhibits a seismic response quite different from the oil-saturated zone due to the different saturation character. As can be seen in Figure 6.18, the water saturated zone (outside the black contour) shows a very weak time-lapse response. Comparing the injection well N4 located there with injector N1 from the oil zone, we can notice different time-lapse seismic signal near these wells. This difference can hardly be attributed to the different net pay at the well locations, since the baseline seismic attribute for both wells is similar (Figure 6.2). The bottom-hole pressure changes for the two wells are also very close as reported in Table 6.5, so the only likely explanation for the different 4D signal is different initial saturations.

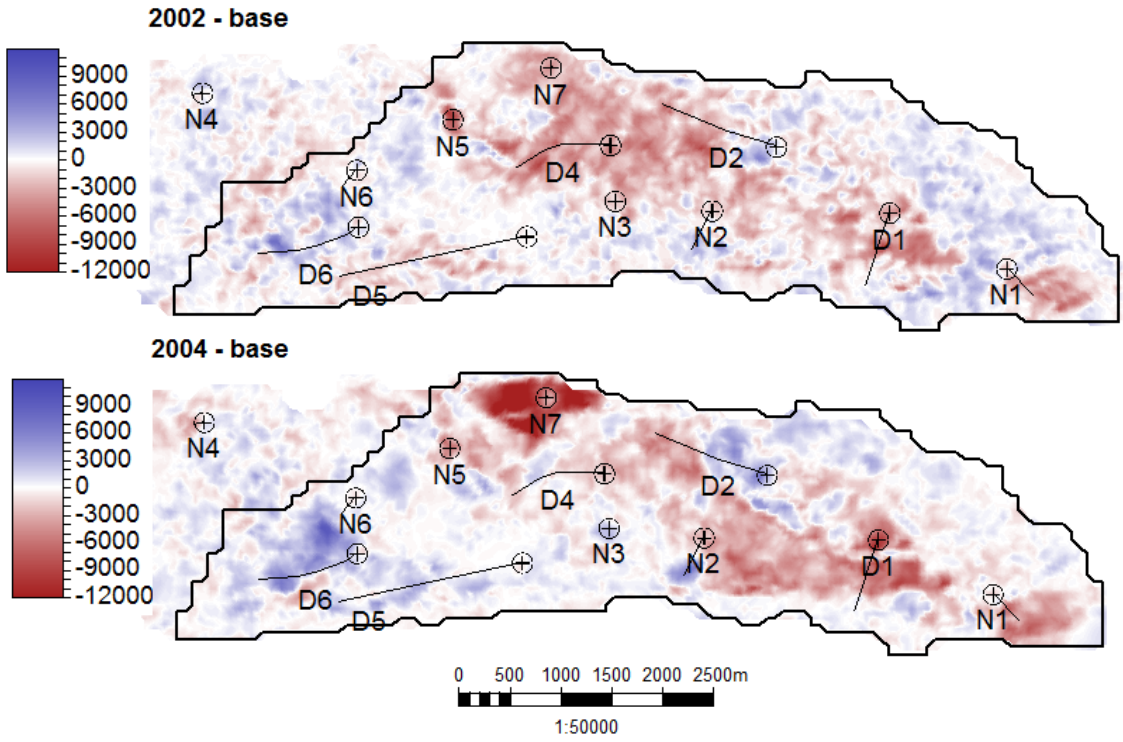

Figure 6.18 Segment 4 time-lapse attributes: 2002 – 1996 (*top*), 2004 – 1996 (*bottom*). The oil-saturated zone is outlined with the black solid line. *Red colours* correspond to the reservoir softening, *blue colours* correspond to the reservoir hardening.

	BHP change, psi	
well	**2002 - initial**	**2004 - initial**
N1	841	687
N4	767	777

Table 6.5 Bottom-hole pressure changes (monitor minus initial), in *psi*, for injectors N1, N4.

For each of the history matching setups (well and seismic) 20 reservoir models from the posterior distribution were generated by the RML approach[39]. Each RML run involved a CMA-ES optimisation run, where the following settings were used:

1. Population size λ = 25. For a problem with the search space dimension n = 95 which I have, the CMA-ES literature recommends using $\lambda = 4 + 3\ln(n) \approx 18$. A slightly higher λ was taken to make the search more global, since the available parallel computing resources easily allowed that.
2. 25000 total models evaluated, 1000 generations in total. This number of generations was a reasonable choice to make sure the CMA-ES converges to

[39] See Chapter 5, section 5.3 for details.

certain minimum. The typical behaviour of the objective function progress in the RML setting both for conventional well history matching and for seismic history matching is shown in Figure 6.19. Here it can be seen that the objective function decrease notably slows down as the generation number approaches 1000. For the seismic history matching case the same picture shows the progress plots for both parts of objective function: f_1 and f_2.

3. The starting point for CMA-ES was selected as a uniform random point within the parameter ranges specified in Table 6.3 in order to diversify the local minima found.

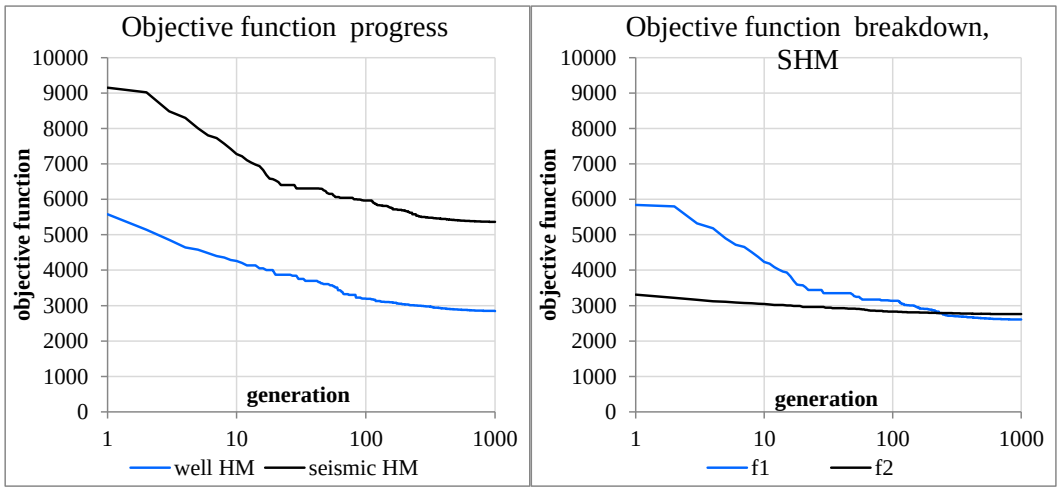

Figure 6.19 Objective function progress (best-so-far value) vs. generation. *Left*: for one RML optimisation from conventional well HM (*blue line*) and one RML optimisation from seismic HM (*black line*). *Right*: wells part of objective function (f_1, *blue line*) and seismic part of objective function (f_2, *black line*) for the seismic HM optimisation.

Since the CMA-ES optimisation did not always result in a good history match, i.e. it converged to an inappropriate local minimum[40], I needed to generate around 30 models for each HM setup using the RML. The inappropriate models were then rejected, so as to finally get 20 models that were regarded as following the posterior distribution. To

[40] These poor convergence results are the consequence of the challenging optimisation problem rather than the choice of the optimisation algorithm. The optimisation problem has 95 parameters and is further complicated by the use of non-diagonal covariance matrices (better convergence was observed for the diagonal covariances). As was examined in Chapter 4 on a simpler optimisation problem, the other algorithms, like PSO, may converge faster, but generally they deliver the final solution of the same quality as CMA-ES, provided the sufficient number of iterations. For the Schiehallion history matching case study a large number of CMA-ES iterations were used to ensure the algorithm always converges to certain local minimum.

decide on whether the model was history matched or not, the first option would be to check the χ^2 criterion given by (5.9). If for some model generated by RML the value of $0.5 f_{\min}$ exceeds the bound $\upsilon + 5\sqrt{2\upsilon}$ then the optimisation for the model can be considered as not fully converged. However, for all the models generated for the well and seismic HM setups the final objective functions turned out to be reasonably small, with $0.5 f_{\min}$ not exceeding $\upsilon + 3\sqrt{2\upsilon}$. Thus, a different approach was taken. For rejecting the models I used the direct visual inspection of the modelled well data, comparing it with the observations. If significant discrepancy of the modelled data and the observations was noticed during the *historic period* (until 01/08/2004), then the model was regarded as not history matched appropriately. An example of this is given in Figure 6.20 which displays the water cut of well D2 for 20 models generated by the RML, with one of the models showing the water cut notably below the observations.

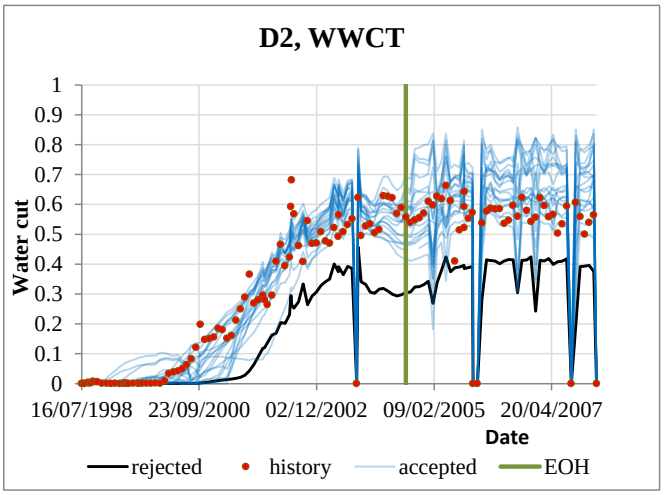

Figure 6.20 Screening the models with unacceptable match to the historic data, well D2 water cut example. *Red circles* show the history, *blue lines* show the accepted models, *black line* shows the rejected model. The *vertical green line* shows the end of history (EOH, 01/08/2004).

6.7 Results

After running the history matching with RML and rejecting the inappropriate models, I obtained 20 models for each HM setup: *well* and *seismic*. These models were then run for the prediction period staring at 01/08/2004 with wells controlled by the actual[41] liquid rates. The calculated well data at prediction period: water cuts, GOR's,

[41] The actual field observations are meant.

cumulative production of oil, water, and gas were then compared with the corresponding actual observations. Three questions are of interest here:

1. How well is the historic data matched for both HM setups?
2. How well is the well data at the prediction period forecasted?
3. Does the introduction of the 4D seismic reduce the uncertainties?

For the seismic HM setup I am also interested in the question of how well are the observed 4D seismic attributes reproduced by the history matched models, which use the linear combination of the reservoir dynamic property maps to model the seismic data. To simplify the analysis, for each HM setup the **mean** and **std** of each well data vector were calculated from the 20 models. All the subsequent discussion is done based on these **mean** and **std**. In terms of matching the historic data and reproducing the predictions both well and seismic HM gave close results, so the following applies equally to both HM cases.

For the historical period for some wells it was a bit challenging to match the historic GOR's: wells D1, D2, D7 (see Figure 6.21 for the well D7 GOR). Here it should be noted that matching the wells gas production for a reservoir producing below the bubble point may be a tricky problem, especially if a rather coarse simulation model is used. For wells D5, D6 located at the South-East part of segment 4 the historic GOR (0.3 – 0.2 mscf/stb) is below the initial reservoir GOR (0.35 mscf/stb) used in the original simulation model provided by the operator. For that reason the generated models overestimated the WGOR and WGPT for these two wells (see the same figure).

For the prediction period, both history matching setups could not properly forecast the BHP of well D1, see Figure 6.22. The generated models showed a notable decrease of the BHP at years 2005 – 2008 which is consistent with the increased production rate. Yet, the observed BHP during this period increases. On the other hand the high observed BHP at 01/12/2005 is not consistent with the increased observed GOR, which may mean errors present in the data. Prediction of water cut for well D1 also failed, because the well does not produce water in the historical period, and the 4D seismic attribute maps do not show any clear water front approaching the well, see Figure 6.25, (*d*). Any water signal in the time-lapse seismic in that area has likely been obfuscated by the gas signal. Because of the poor WWCT forecasts, the vectors of WOPT, WWPT for well D1 also did not predict the actual observations. The challenges with history matching the GOR for a number of wells continued in predicting the future GOR, so the GOR forecast failed for wells D2, D4 – D7. BHP of injectors N1, N5 was not properly

predicted, although the prediction errors were smaller than for the BHP of well D1. See Figure 6.29 for the BHP of injector N1.

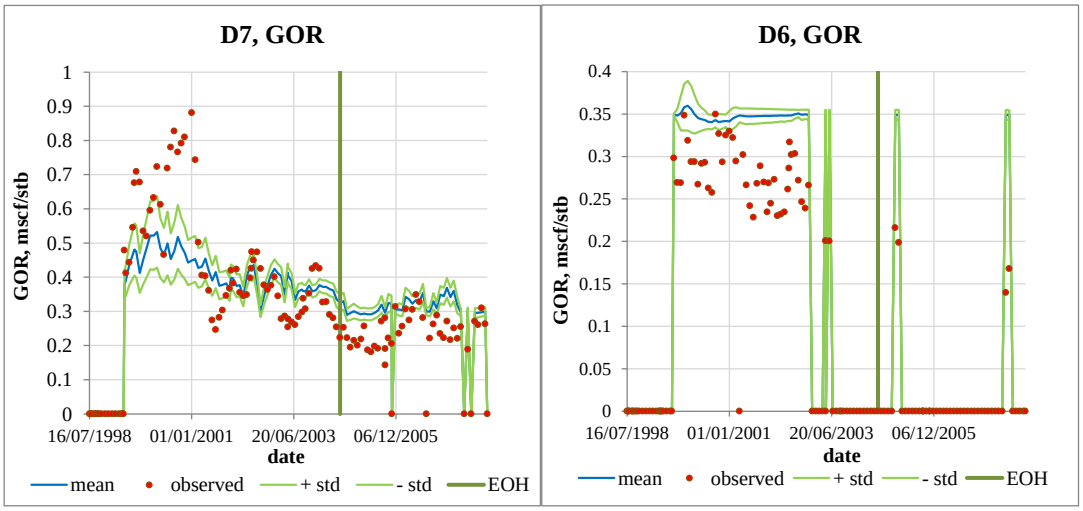

Figure 6.21 Examples of poor history matching. *Left to right*: GOR of well D7, GOR of well D6. The observations are shown by the *red circles*, the estimated **mean** – by the *blue line*, **mean** ± **std** – by the *green lines*. The *vertical green line* shows the end of history (01/08/2004). The estimates are taken from the conventional well HM case.

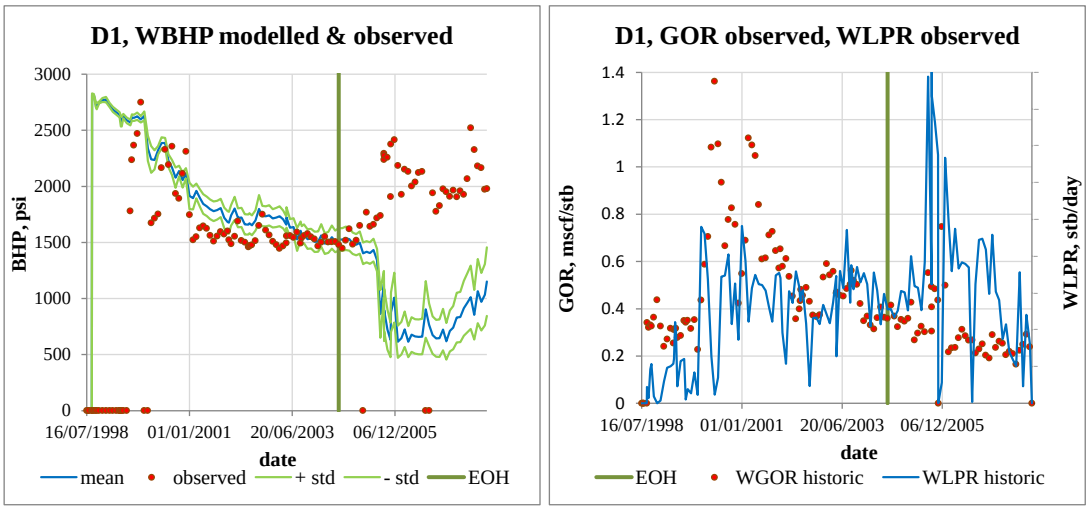

Figure 6.22 Challenges of predicting the BHP for well D1. *Left*: bottom-hole pressure. The observations are shown by the *red circles*, the estimated **mean** – by the *blue line*, **mean** ± **std** – by the *green lines*. The estimates are taken from the conventional well HM case. *Right*: observed well liquid production rate (blue line) and observed GOR (red circles). The *vertical green line* shows the end of history (EOH, 01/08/2004).

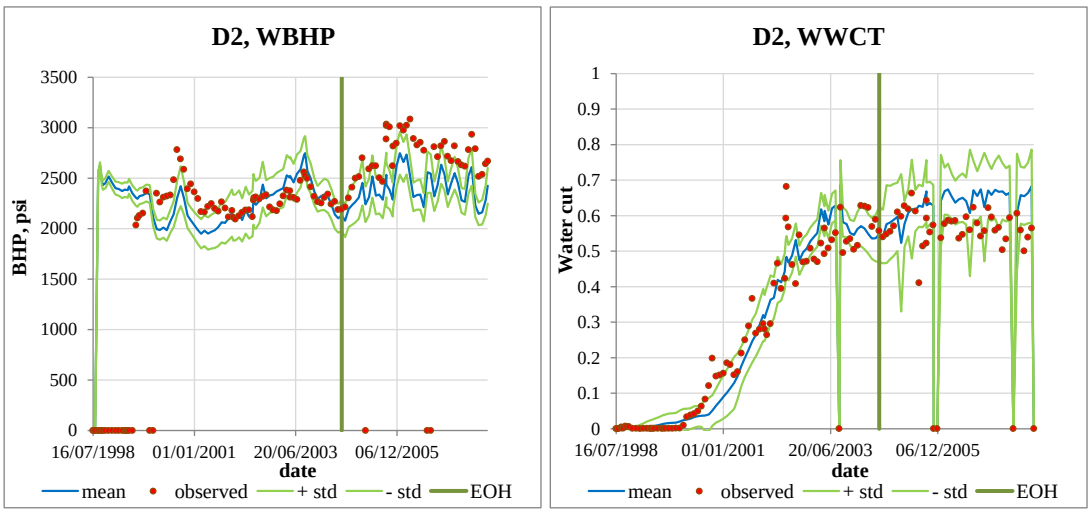

Figure 6.23 Example of a reasonable history match and forecast. *Left*: bottom-hole pressure of well D2, *right*: water cut of well D2. The observations are shown by the *red circles*, the estimated **mean** – by the *blue line*, **mean** ± **std** – by the *green lines*. The *vertical green line* shows the end of history (EOH, 01/08/2004). The estimates are taken from the conventional well HM case.

All the other vectors (among WBHP, WWCT, WGOR, WOPT, WWPT, WGOR) were history matched reasonably well, and besides showed the behaviour in the prediction period consistent with the observations, which means that the future observations are contained within the estimated **mean** ± 3·**std**[42]. The example of such vectors is given in Figure 6.23, where the BHP and the water cut of well D2 are displayed.

For the seismic history matching case we can also look at the quality of history match of the 4D attributes. For that, the observed time-lapse attributes are to be compared with the modelled attributes, i.e. those calculated from the maps of the dynamic reservoir properties by linear regression (4.8). The modelled 4D attributes for the monitors 2002 and 2004 for one of the models generated by RML in the seismic HM setup are shown in Figure 6.24. The determination coefficient for the maps regression in this case equals $R^2 = 0.38$, which is not quite large, but still is reasonable given the noise level present in the 4D signal. The modelled 4D attribute maps reproduce the main features on the input attribute maps (Figure 6.25): the gas softening signal and pressure-up softening at 2002 and 2004. Only very weak waterflood hardening signal can be seen near wells D6 and N2. The maps look smoother and have lower amplitude of the values than the observed 4D attribute maps. This is natural since the linear regression is used for the

[42] Mean ± 3·std is one of the typical ranges considered for the normally distributed quantities. This particular range contains 99.7% of the values of this quantity.

attribute modelling, and it looks at the general picture and smooths out any inconsistencies between the dependent and independent variables.

The same figure shows the modelled time-lapse seismic map for the 2006 monitor, i.e. gives the future forecast of the 4D map. To calculate it, the coefficients a_i obtained from the seismic history matching with monitors 2002, 2004 were used in equation (4.8) together with the time-lapse maps of the forecasted reservoir dynamic parameters corresponding to monitor 2006. As can be seen, the calculated 4D attribute does not predict the actual observed 4D attribute shown in Figure 6.25. The mismatch can be explained as follows. Firstly, the calculated time-lapse attribute is dominated by the gas signal spanning the Eastern area between producers D1 and D2, see contour (*a*) in Figure 6.24. This is of little surprise, because the time-lapse seismic attributes at 2004 and especially 2002 are dominated by the gas signal, so the data-driven equation (4.8) was calibrated to honour predominantly gas which came out of solution in the reservoir. At monitor 2006, as displayed in Figure 6.22 and discussed above, the modelled BHP of well D1 had significant decrease, which is an obvious forecasting failure and also is a trigger for the model to have large amounts of free gas around this producer in 2006. The modelled mispredicted gas signal is clearly seen on the modelled 2006 time-lapse attribute map.

Secondly, the water saturation in the time-lapse maps of 2002 and 2004 (Figure 6.25) is rather small and local, and there are only weak manifestations of it on the modelled attribute maps (Figure 6.24). The calibrated equation (4.8) does not focus much on this signal. The similar weak reservoir hardening spot is also seen on the predicted attribute map for 2006 near well N2, see contour (*b*) in Figure 6.24. Finally, the discrepancies in the pressure signal should be explained. The notable observed pressure-up signal at 2006 is seen around injectors N3, N5, see contour (*c*) in Figure 6.25. At 2004 however, these two wells do not show the same pressure-up signal, although the measured BHP for the wells almost did not change between 2004 and 2006 monitors. For well N3 the BHP decreased by 150 psi from 2004 to 2006, for N5 it increased by 130 psi, which is quite small compared to the BHP increase of 1200 psi between the initial pressure and the BHP measured at the monitor (2004 or 2006). Thus, the strong pressure up signal on the observed 2006 time-lapse seismic map may be erroneous, and the more moderate pressure response seen on the predicted attribute map (Figure 6.24, contour (*c*)) may be deemed reasonable (the BHP prediction at 2006 monitor for the two wells by the

considered model is quite accurate: for N3 the model overestimates the observations by 340 psi, for N5 the overestimation is 20 psi).

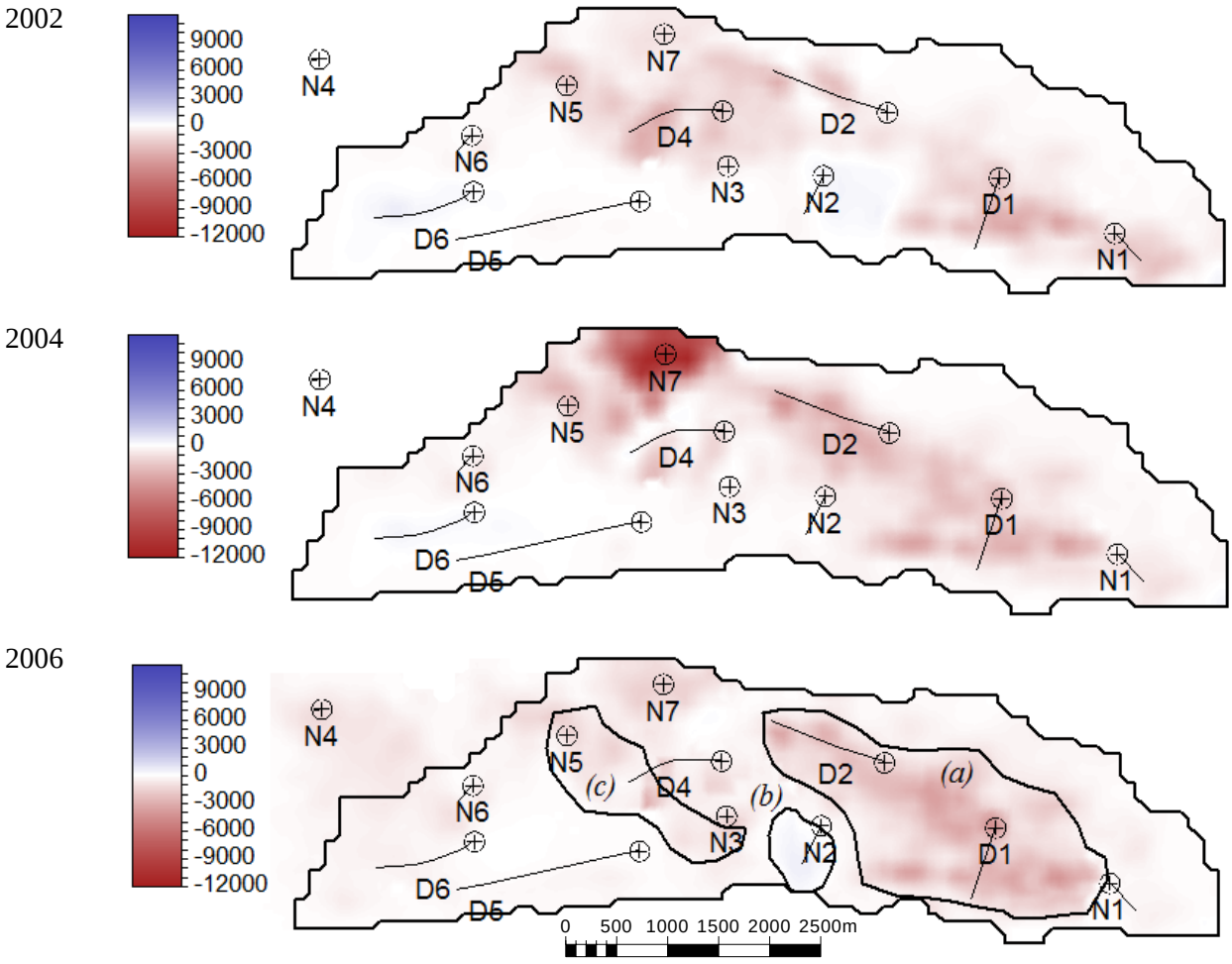

Figure 6.24 4D attribute maps produced by the history matched model (seismic HM setup). *Top to bottom*: monitor 2002 (historical), monitor 2004 (historical), monitor 2006 (predicted). The contours and letters (*a*), (*b*), (*c*) spot certain signals which are discussed in the text.

To check whether the model after seismic history matching reproduces the time-lapse seismic attributes better than a non-history matched model (no-HM) or a model history matched to the well data only (WHM), time-lapse attributes were generated for the latter two models. This was made by the same regression-based procedure as used in the seismic history matching workflow, but applied to the dynamic model parameters from the no-HM and WHM models. The resulting attributes are shown in Figure 6.26. For convenience, the same figure displays the attributes for the seismic HM model (same as in Figure 6.24), and observed seismic attributes which were obtained by upscaling the original fine-scale attributes (Figure 6.25) to the simulation model grid. It should be

noted that seismic history matching actually used the coarse-scale attributes displayed in Figure 6.26.

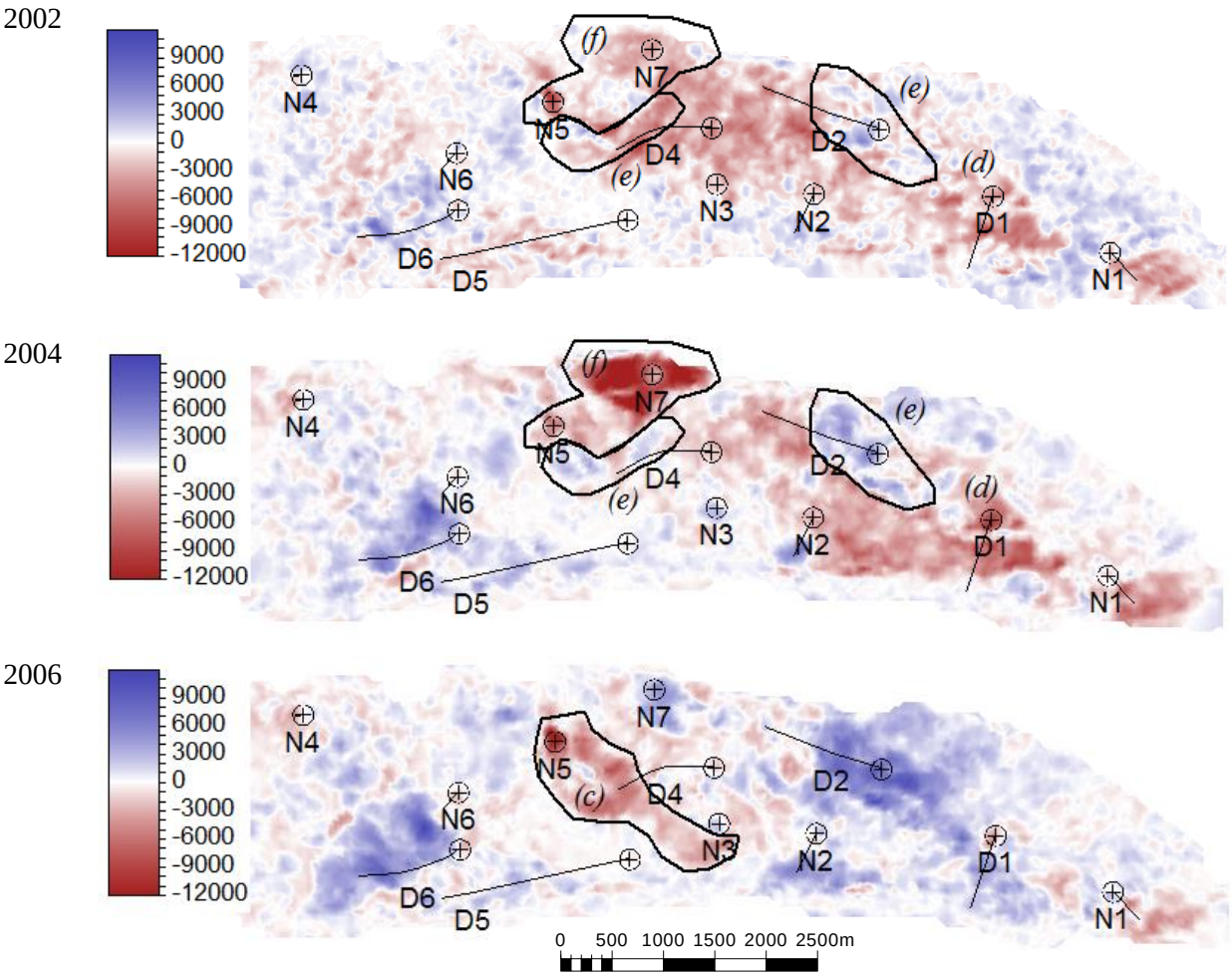

Figure 6.25 Observed 4D attribute maps. *Top to bottom*: monitor 2002 (historical), monitor 2004 (historical), monitor 2006 (future). The contours and letters (*c*), (*d*), (*e*), (*f*) spot certain signals which are discussed in the text.

Both no-HM and WHM models gave a small determination coefficient in regression between the seismic data and simulation model data, approximately equal to $R^2 = 0.08$ for both cases, which is small compared to $R^2 = 0.38$ for SHM model. On the maps, we can also see a worse reproduction of the observed seismic by the two models. E.g. for the no-HM model there are notable mismatches for the observed seismic signals near wells N2, N3, D4, D1, N1, however all these signals are reasonably reproduced by the SHM model. For the WHM model the seismic mismatch is associated essentially with the same regions. Also, seismic response for this model contains a number of localised sharp softening spots originating from local accumulations of gas in the model. Thus, the SHM model is more accurate in reproducing the observed time-lapse

seismic attributes than the models which did not incorporate seismic data into the history matching loop.

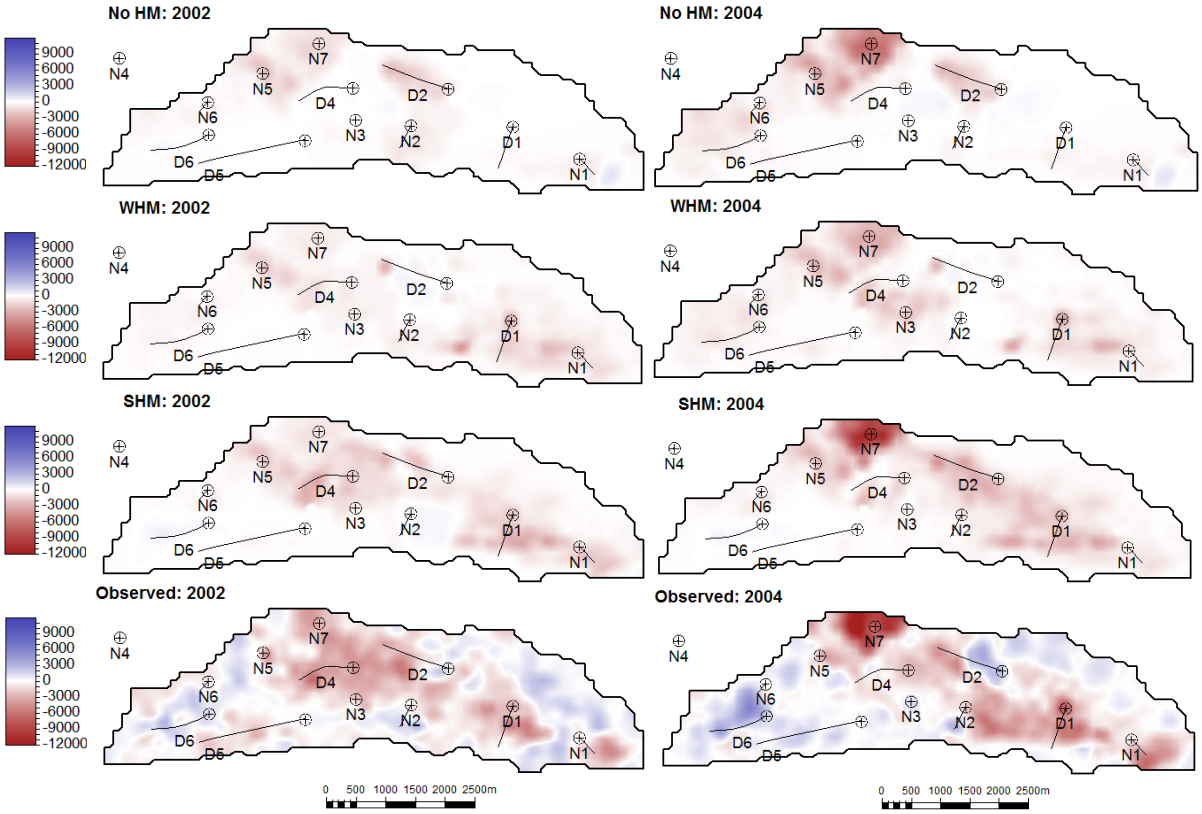

Figure 6.26 Modelled and observed time-lapse seismic attributes. *Columns, left to right*: 2002-baseline, 2004-baseline. *Row, top to bottom*: not history matched model (no-HM), model history matched to well data only (well HM), model history matched to well and seismic data (seismic HM), observed seismic (coarsened to the simulation model grid).

Now that the history match quality and prediction quality in general have been discussed, let us turn to comparing the two history matching setups with respect to the reduction (or increase) of the estimated uncertainties, and the quality of the predictions. The first thing to look at is the **std** ratio between the two setups, i.e. $\mathbf{std}_{well} / \mathbf{std}_{seismic}$. This quantity, if it is greater than 1, shows how much the prediction uncertainties reduced after introduction of the 4D seismic data into history matching. The **std** ratio for all vectors is displayed in Figure 6.27. Looking at the **std** ratio of the water cut affected vectors (WWCT and WOPT) at the prediction period, we can notice the uncertainties increase for the seismic HM case for wells D3, D5, D7, D8. All these wells are completed either above reservoir T31, or below it (D5 is completed above, below and in T31). The 4D seismic attributes, on the other hand, were calculated only for T31 interval, and constrain the fluid flow essentially for this reservoir. So, the

seismic HM setup provided tighter control over the wells completed only in T31, while the control over the other wells was somewhat loosened. This situation will be also observed for some other vectors related to the wells completed above or below T31.

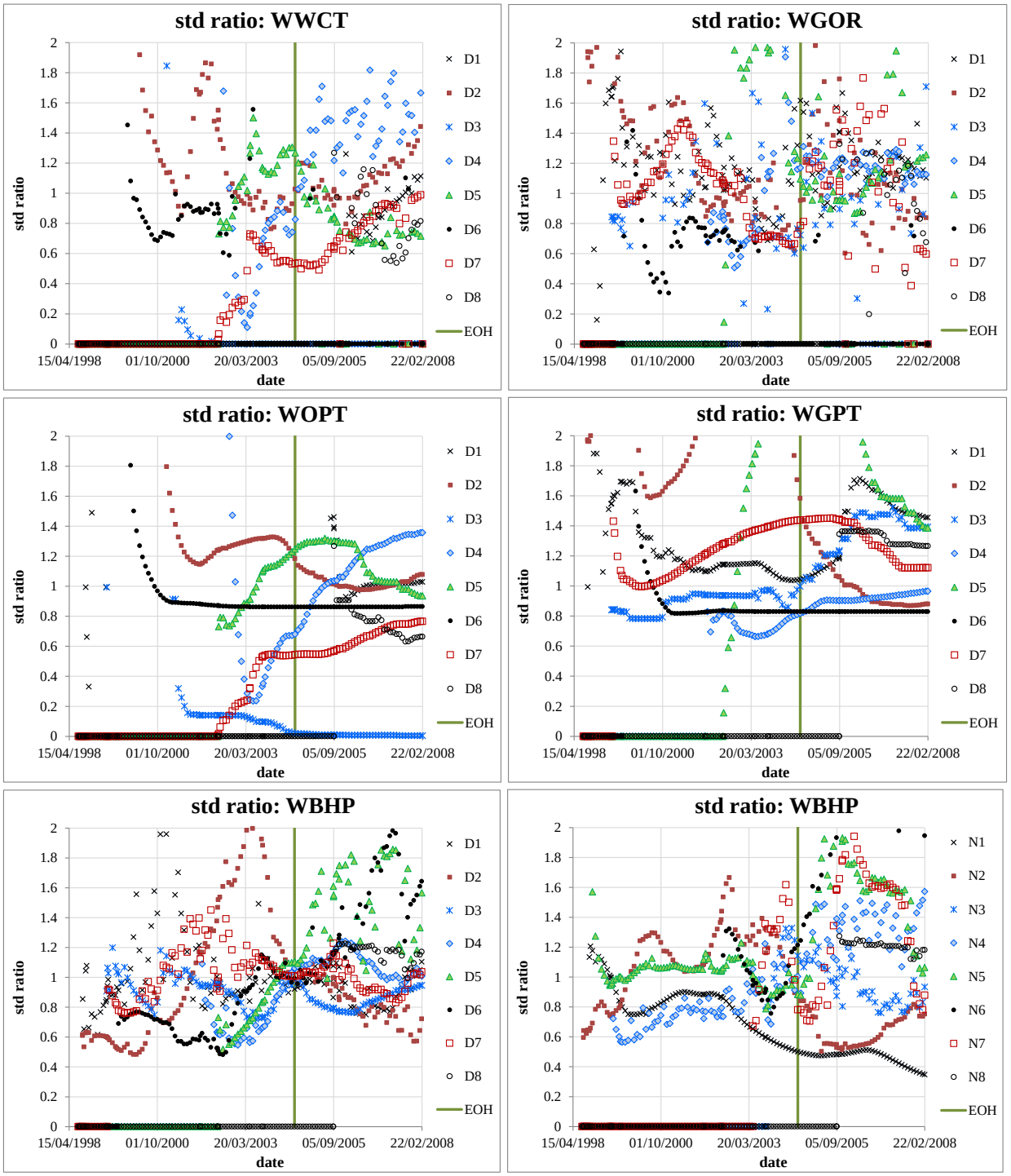

Figure 6.27 The ratio $\mathbf{std}_{well} / \mathbf{std}_{seismic}$ for the two HM setups. Each plot shows a group of data vectors (WWCT, WGOR, WOPT, WGPR, WBHP) for different wells. The *vertical green line* on the plots marks the end of history (01/08/2004). The plausible values of **std** ratio are those above 1, as they indicate decreased uncertainty for the seismic HM setup.

Well D3 for which the WWCT and WOPT **std** ratio is close to zero almost did not produce water in the conventional well HM, so $\mathbf{std}_{well} \approx 0$. At the same time for the seismic HM the forecasted water production is non-zero and reasonably follows the actual future water cut, besides, due to dispersion of the models $\mathbf{std}_{seismic} > 0$. Given that, the **std** ratio is close to zero. The uncertainties of WWCT and WOPT decreased for wells D2 and D4 which are completed in T31 and for which the 4D seismic maps show the water saturation signal nearby (Figure 6.25, contours (*e*)). The vectors affected by the gas/oil ratio (WGOR and WGPT) generally show uncertainty decrease for all wells. This is consistent with the fact that the historic 4D seismic maps show a lot of reservoir softening signals due to the gas coming out of solution. Thus, the 4D seismic data allows better constraining the model behaviour with respect to the gas production.

Comparing the histograms and standard deviations of the model parameters resolved by the two HM cases, it was difficult to say whether a particular HM setup resolved the parameters with smaller uncertainties. As an example, the histograms for the parameters which affect the gas behaviour – critical gas saturation *Sgrc*, Corey exponents for the gas-oil relative permeabilities *No*, *Ng*, and gas dissolution rate $\partial Rs / \partial t$ – are shown in Figure 6.28. The conventional well HM gives smaller uncertainty (smaller deviations on the histograms) for *Sgcr* and $\partial Rs / \partial t$, whereas the seismic HM produced smaller uncertainty for both Corey exponents. The smaller uncertainties of the gas production forecast for the seismic HM are not accompanied by the uncertainty decrease of the displayed parameters. It may be the case that some of the considered parameters have stronger impact on gas production than the others, or that the combinations of parameters should be examined instead of looking at each parameter separately. It should be also noted that with the small number of data points used for the histograms (20 points), the sample size is not sufficient to produce histograms representative of the actual posterior distributions.

Considering the histogram of *Sgcr*, I remark that it is consistent with the estimate made in [70]. In that paper the authors assessed the critical gas saturation for segment 1 of the Schiehallion reservoir by comparing the 4D seismic signals resulting from the critical gas saturation with those from the secondary gas caps. The estimated *Sgcr* ranged from 0.0055 to 0.04. In the seismic history matching output considered here the uncertainty range for *Sgcr* is from 0.00064 to 0.0407.

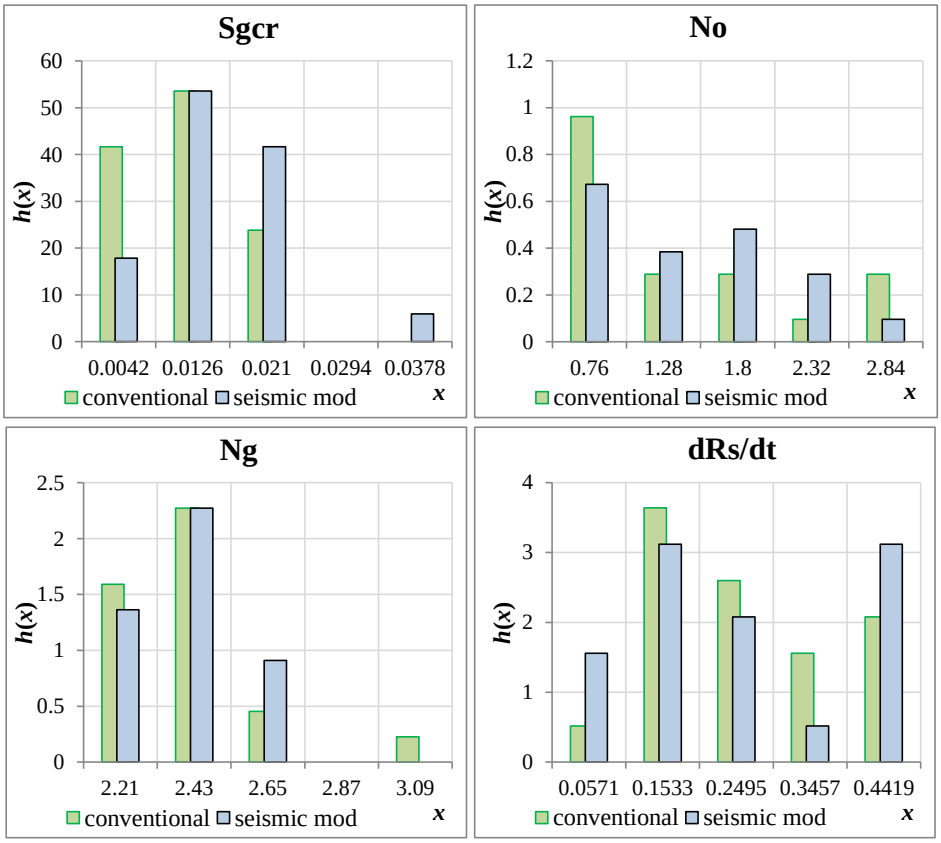

Figure 6.28 Histograms (normalised to give the integral equal one) for some model parameters resolved by the well and seismic HM setups. The parameters involved are: critical gas saturation *Sgcr*, Corey exponents for gas-oil relative permeabilities *No*, *Ng*, gas dissolution rate $\partial Rs / \partial t$.

Looking at the **std** ratio of the producers WBHP in Figure 6.27, we can see that it became worse for wells D2 and D3. The 4D signature near well D2 is quite complex as one half of the well shows reservoir hardening signal from the encroached water , the other half shows the reservoir softening due to gas. The pressure signal most likely was totally masked by these two, and pressure prediction became worse. Well D3 is completed above T31 reservoir. Reduction of uncertainties in the WBHP forecast can be seen for wells D4, D8, and more notably for wells D5, D6. The latter two wells are located in the South-West part of segment 4, and the 4D seismic indicates reservoir hardening due to water saturation increase in their vicinity. So, absence of the softening signal in that area was probably beneficial for constraining the pressure behaviour of the producers.

The injectors WBHP shows uncertainty increase for wells N1 and N2. For well N1 the conventional well HM case resulted in a smaller **std**, but the forecast did not reproduce properly the actual BHP observations. The seismic HM also did not reproduce the

future observations, but gave larger **std**, which means that it made a more reasonable estimate of the future BHP behaviour, see Figure 6.29, and also Figure 6.30. Well N2 is completed both in T31 and above it. The improvement of the WBHP uncertainty of injectors can be seen for wells N4, N8, and especially for wells N5, N6, N7. Uncertainty decrease for N5 and N7 is natural since the 4D maps show notable pressure-up signal for these wells, see Figure 6.25, contour (*f*).

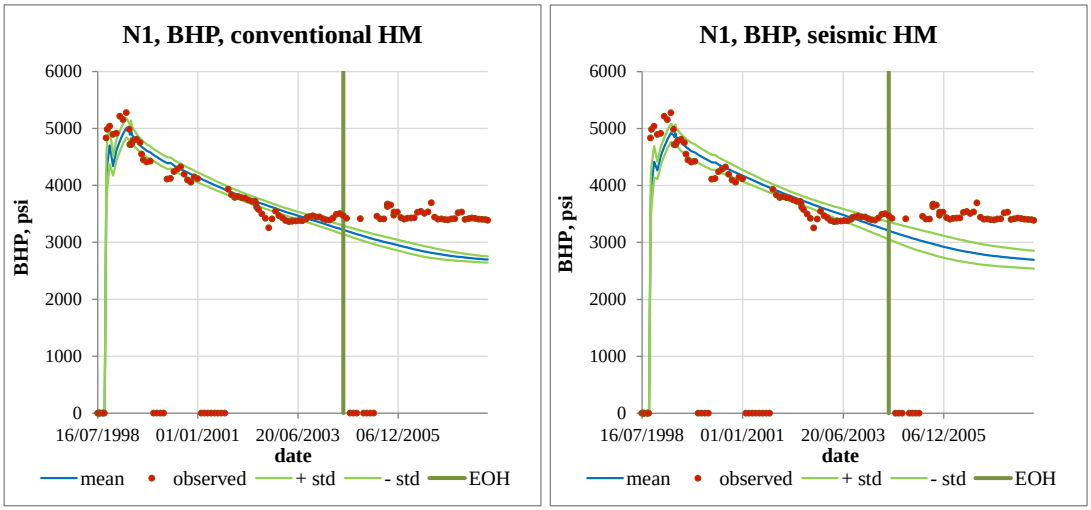

Figure 6.29 Prediction of BHP for injector N1. *Left*: conventional well HM, *right*: seismic HM. The *vertical green line* shows the end of history (01/08/2004).

When examining the uncertainties of the forecasted well data not only should one look at the decrease or increase of the standard deviations between two history matching cases, but also at the precision of the forecasts. Consider some predicted well data vector *d*, and denote by d^* its actual observations (true values), d_{mean} – the estimated **mean**, σ – the estimated standard deviation. The **std** assessed by a HM setup can be regarded as a "promise" of the HM setup that the forecasted error $e = d^* - d_{mean}$ will not exceed 3σ (or other reasonable multiple of σ). If the HM case "promised" smaller **std** but did not deliver on that promise by producing a large prediction error, then the uncertainties estimated cannot be trusted, and it makes little point to report any "uncertainty reduction". Thus, for the two HM setups considered in this work, apart from checking how the **std**'s changed after introducing 4D seismic data into history matching, I also examined how both HM setups deliver on their promises. For that, I calculated e/σ for each predicted well data vector and plotted it versus the standard deviation σ. The quantity e/σ shows the un-reliability of the forecasts, the smaller it is, the more the estimate d_{mean} is consistent with the true data d^* for the given σ.

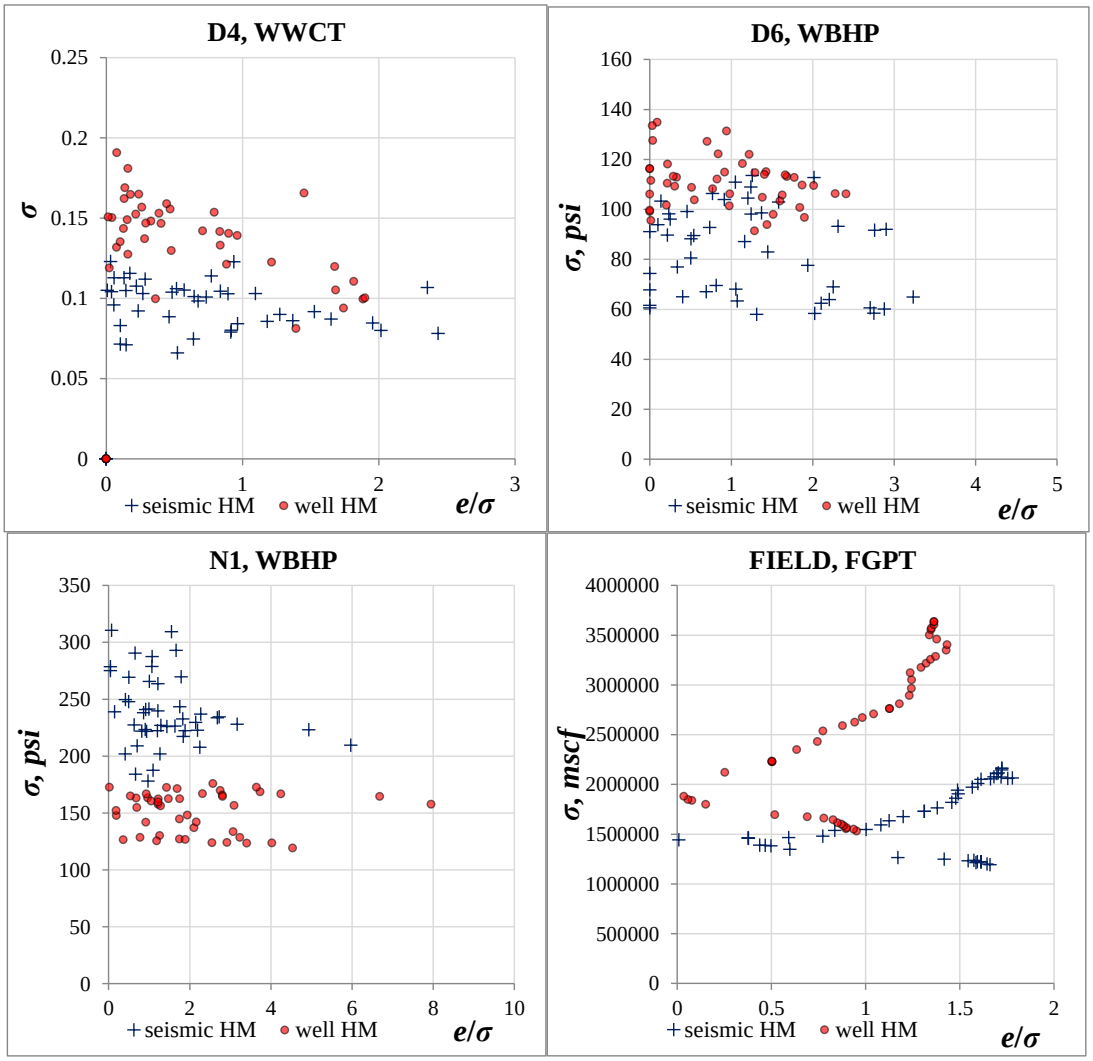

Figure 6.30 Crossplots of the forecasts un-reliability e/σ versus standard deviation σ for the conventional well HM and seismic HM cases. The names of the well data vectors are given in the plots titles.

The crossplots of e/σ versus σ showed the following (see Figure 6.30 for the examples):

1. e/σ is generally less than 3 except for the few well data vectors where the prediction obviously failed (see the discussion above). This is a quantitative confirmation of the statement made before that the majority of the vectors reasonably predicted the actual future observations.
2. For the majority of vectors like WWCT, WGOR, WBHP (not the cumulative ones) the un-reliability of the forecasts e/σ for the two HM cases is approximately the same, whereas the uncertainty σ may differ. This simplifies comparison of the HM cases as essentially σ's should be compared.

To give an example, Figure 6.30 shows the crossplots for vectors D4 WWCT and D6 WBHP, for which the seismic HM resulted in lower uncertainties, whereas the forecasts un-reliability e/σ basically did not change. A counterexample is provided in the same figure by the crossplot of N1 WBHP discussed above, for which seismic HM produced higher **std**, but at the same time lower forecasts un-reliability.

3. For the cumulative vectors (WOPT, WWPT, WGPT) the situation was observed more often when one HM setup shows smaller **std**'s, but higher e/σ than the other HM setup, see the crossplot for the Field Gas Production Total in the same figure. In this case it may be challenging to decide on what HM setup resulted in a more plausible uncertainty estimation.

Having considered the different aspects of uncertainty and predictions, let me conclude on the conducted history matching exercise. I have obtained the history matched models which both reasonably match the historic data and provide a sensible forecast for the future production. Introduction of the 4D seismic data has resulted in reduction of the forecast uncertainties where expected – i.e. for the wells completed in T31 reservoir for which there exist notable 4D seismic signals nearby associated with water saturation increase or pressure increase. The gas signal widely present in the time-lapse seismic maps helped in reducing the overall gas production uncertainty, however accurate prediction of the gas production itself remained the unresolved challenge for both well and seismic history matching cases.

6.8 Summary

In this chapter I considered an approach to history matching and the associated uncertainty estimation for segment 4 of Schiehallion field. The turbidite reservoir of this field has complex connectivity, which was overestimated by the operator during the initial field appraisal. As a result too few wells were drilled originally, leading to the deficient pressure maintenance, and excessive gas production. The situation was corrected by the subsequent infill drilling guided by the 4D seismic and the well pressure data.

The dataset provided by the operator included the reservoir simulation model with 8 producers and 8 injectors in segment 4, well production data and a number of seismic surveys made prior to the field production and during its course. The original model

was not history matched and overestimated the reservoir connectivity and sweep efficiency. For the history matching purposes it was upscaled from the 360,000 active cells fine model to the 8,700 active cells coarse model. The estimated ratio of the 4D noise to the 4D signal in the reservoir appeared to be rather high, with the median value of 80% in the areas with distinct 4D signal, and higher values elsewhere (for 2004 monitor).

The model parameterisation involved 95 parameters, the major part of them controlling the reservoir connectivity: transmissibility multipliers for the neighbour geobodies and geobody permeability multipliers. When defining the objective function, two history matching setups were considered: conventional well history matching and well-seismic history matching. Both setups used a restricted historic period until 01/08/2004, followed by the prediction period where the future forecasts are made and analysed. To define the objective function for the well HM case, the temporal correlation ranges and the standard deviations of the well data errors were estimated. The former were assessed by the visual inspection of the autocorrelation functions, the latter – using the χ^2 criterion. The seismic HM case employed the same well part of the objective function plus the seismic part, for which the spatial correlation ranges (major and minor) and the standard deviation were estimated using the similar principles.

For each history matching setup 20 models from the posterior distribution were generated by the RML algorithm. For both setups the resulting models showed reasonable match of the observations at the historical period. Rather poor match was found only for WGOR of 5 wells. The forecasts made by the models for the prediction period were quite good except WWCT of D1, WBHP of D1, N1, N5, and WGOR of 5 wells. The modelled 4D seismic showed a sensible match of the historic 4D seismic attribute maps of 2002 and 2004. Essentially, the softening gas signal and pressure-up signal were reproduced. The attempt to forecast the time-lapse attribute at 2006 did not show a good result, as the model forecasted too much gas – and hence the strong softening signal which was absent in the observed 4D attribute.

To compare the forecast uncertainties of the two HM cases, the **std** ratio for the predicted well data vectors was analysed. It showed the increase of uncertainty for the seismic HM case for the number of wells completed above or below T31 reservoir. This makes sense, because the considered time-lapse attributes are only effective for the T31 interval. There was decrease of uncertainty for some wells located close to the

distinct 4D seismic signals: reservoir hardening due to the water saturation increase and reservoir softening due to the pressure growth. The gas signal which is widespread in the historic 4D seismic maps decreased to some extent the GOR forecast uncertainty for almost all wells. However, it should be noted that the GOR prediction was challenging and involved quite large errors for both HM setups. Overall, the predictions made by the history matched models had reasonable quality, and effect of the introduction of 4D seismic, although somewhat marginal, was in line with the expectations. This allows me to state that the history matching approach set forth in Chapter 4 together with the uncertainty estimation algorithm were successful in application to the real dataset.

At this point I conclude the main part of the thesis where I posed the problems, suggested the solutions and examined the results, and turn to overviewing the whole work and discussing the possible ways of the further research, which is the subject of the next chapter.

Chapter 7 Discussion and future recommendations

Throughout the thesis I considered different aspects of the quantitative coupling of 4D seismic and reservoir engineering for thin reservoirs, including approaches to fast-track saturation forecasts, fast permeability estimation, and seismic history matching. In this chapter I overview and discuss the methods and results obtained in the previous chapters, and also suggest the recommendations for the future research which might stem from the studies undertaken in this work.

7.1 Fast saturation forecasting

The research started with considering the problem of forecasting the waterflood development from the current reservoir state estimated from 4D seismic (Chapter 2). To tackle the problem, the principles of saturation transport along the streamlines were employed. The algorithm proposed considers the reservoir properties in the 2D map sense, which is appropriate if the reservoir is thin. To predict the future saturation, the algorithm takes the input consisting of the current pressure and saturation maps, and a saturation map from the previous time step. These maps can be thought of as the result of inversion from the 4D seismic attributes. The method works under the assumption of steady-state pressure, and this condition can be regarded to be roughly satisfied if the time intervals between the successive saturation maps are small, which may be the case for the frequently acquired seismic monitors. The algorithm involves three procedures: tracking the streamlines, analysing the velocities, and propagating the saturation fronts forward. The streamline tracking is performed in a straightforward way, by directing the small line elements parallel to the pressure gradient. While doing this, the pressure map itself is interpolated between the mesh nodes to get a smoother picture. The wells are surrounded by ellipses in their vicinity, so that the streamlines are terminated at these ellipses. For each streamline the flow velocity is then analysed, accounting for the effective reservoir thickness, porosity and geometrical spread of the streamlines. Another component of the velocity analysis is tracking the distance each saturation point travelled between two successive time steps. Once the velocities have been estimated, the current saturation profile can be moved forward, assuming the velocities will not change in the future.

For the purposes of saturation propagation the total flow rate for a given streamline q is not estimated, and only acts as a component of the relative saturation velocity U_0. However, as was shown in Chapter 3, the flow rate can be calculated if the relative permeabilities are known (or at least can be estimated by some regression technique). Having the values of q for each streamline would allow forecasting not only the saturation maps, but also the watercut development for the producing wells. The anticipated procedure would take all the streamlines entering the producer, and sum up the watercut profiles supplied by them, weighting these by each streamline's flow rate. In such a procedure the starting points of the streamlines should be reconsidered however, since currently they are taken only to accomplish the velocity analysis, whereas for watercut estimation at wells the streamlines should be areally representative of the flow that enters the well.

The saturation forecasting procedure was tested on a number of models, from simple 2D models to the complex 3D ones. It showed good results for a simple 2D quarter five-spot model. For a heterogeneous 2D model with a more intricate streamline pattern the prediction quality worsened. The first reason for that is in the increased numerical errors in the velocity analysis for the streamlines which cross the saturation fronts at small (nearly tangent) angles. The second reason is the movement of saturation fronts transverse to the streamlines, which may happen because of the violation of the steady-state pressure conditions, and also due to numerical dispersion existing in the finite difference simulator. For the input pressure and saturation maps taken by vertical averaging of the properties of 3D models the prediction quality turned out to be rather poor, which is the result of treating the underlying 3D flow with 2D streamlines. Since these average pressure and saturation maps can be regarded as the pressure and saturation from some effective 2D flow contaminated by some *noise*, the problem of the prediction quality degrading is actually the problem of the noise in the input. For example, the map of the averaged 3D pressure may contain numerous local peaks and troughs not associated with the wells. The streamlines will be terminated at these peaks, becoming too short for a reliable velocity analysis and saturation propagation.

Handling the input noise by the map smoothing does not solve the problem to the desired extent, since the streamlines calculated from the smoothed pressure map do not capture properly the underlying fluid flow, and deviate towards the streamlines corresponding to the homogeneous permeability map. The necessary degree of smoothing which should be applied to the input maps is also an open question. For each

specific case where the exact future saturation is known the optimum smoothing which minimises the prediction errors can be found. However no simple solution was established for the situation where no future information is known and one needs to choose some smoothing to enhance the forecast.

Considering the problem of 3D flow prediction by 2D streamlines, the following principal issue may exist. If the averaged 3D saturation S_1 (map) is expressed as a sum of saturation from the effective 2D flow and a "noise", $S_1 = S_1^{2D} + \tilde{S}_1$, it may be considered that the 2D streamlines approach can forecast the 2D component of the saturation, i.e. obtain S_3^{2D} from S_1^{2D} and S_2^{2D}. But in the case where the fluid flow in the different reservoir sublayers occurs in different directions, or where the vertical fluxes are significant, the 3D flow may notably diverge from its corresponding effective 2D flow. This is what happened for Model 3 considered in Chapter 2: the model has fluvial channelised geology, the stacked channels go in different directions, and so does the fluid flow. In this situation the saturation maps S_i are dominated by their "noise" components $\tilde{S}_i$, which cannot be predicted by the 2D streamlines. Thus, the streamlines will essentially fail to predict the average maps S_i as well. An additional study should be conducted to address the issue of 2D representation of the 3D fluid flow, and discriminate the cases and geologies where such representation may work effectively, so that reservoirs which are *thin* from the reservoir engineering perspective can be distinguished. The answers to the above questions will likely be scale-dependent, and from the point of view of application to the 2D flow modelling, the reservoir-thickness scale will be of particular interest. The reservoirs which are likely to be thin in the reservoir engineering sense are those with laterally continuous properties (e.g. having shallow marine depositional environment), and the inverse holds for the reservoirs with abrupt facies changes which have the channelised geology with poorly connected stacked channels (e.g. having fluvial or turbidite depositional environment). The fluid flow rates in the reservoir should also be accounted for since they affect the balance between the viscous and gravity forces, and hence the rates of the vertical segregation of fluids.

The assumption of the steady-state pressure conditions made for the proposed method of saturation prediction also reduces its flexibility, since the method cannot account for the changing well controls. This restriction led me to further consideration of the fast methods of permeability estimation, to open the possibility of calculating the pressure maps for the changing well conditions.

7.2 Fast permeability estimation

In Chapter 3 three methods were studied that allow estimation of the permeability map for a 2D reservoir based on the input maps of pressure and saturation, which could be obtained by inverting the time-lapse seismic attributes. However, in testing these procedures I concentrated entirely on the reservoir engineering side, rather than the seismic side. A variety of synthetic reservoir simulation models were considered to check the different aspects of the methods. At this stage, high sensitivity to the input noise was revealed, so the further testing of the full cycle *from* inversion of pressure and saturation from 4D seismic *to* permeability map estimation was not attempted, as the noise in the real 4D seismic data normally exceeds the noise tolerated by the permeability calculation procedures considered.

The **first permeability estimation method** naturally follows from the saturation front prediction algorithm implemented before. After estimating the saturation propagation velocities along the streamlines, the corresponding flow rates are found using the phase relative permeabilities. The latter can be defined from some source (e.g. the special core analysis) or assessed from the observed saturation velocities along the streamlines. Finally, knowing the flow rates the permeability is calculated by Darcy's law. The procedure works on the streamline-by-streamline basis, which results in permeability map estimates that look somewhat noisy. To improve that, more coupling between the streamlines could be introduced to the method. One way of doing that is to consider a single set of the relative permeability curves, or consider relative permeabilities with gradually changing Corey parameters across the map, as contrasted to the present method where the phase relative permeabilities are estimated for each streamline independently. The other way of making the inversion more coupled is to impose some smoothness constraints on the whole permeability map. Since in this case the number of unknowns that are resolved simultaneously increases considerably, e.g. 6 unknown Corey parameters per streamline times the number of streamlines (100 – 1000), a gradient-based optimisation algorithm, e.g. BFGS, should be employed to treat the high-dimensional problem. Such an inversion will handle simultaneously all the streamlines, so it is also possible to assign each streamline a different weight, like it was done in the subsequent method #3. The weight would depend on the quality of the velocity analysis for the streamline, so that the streamlines with potentially erroneously estimated velocities are suppressed in contributing to the objective function.

The implemented procedure was tested on 2D and 3D models. Just like the saturation front forecasting method considered above, the procedure gave plausible results for simple 2D models. For the 2D models with more complex fluid flow more noticeable errors emerged due to the problems in velocity estimation. The errors became even higher for the complex 3D model where the 2D streamlines do not capture properly the underlying 3D flow. Introduction of noise to the pressure maps[43] also impairs the method's performance, so that it can resolve to some extent only the permeability features that are aligned with the streamlines. The permeability maps estimated in this way lack geological realism, as they have a strong imprint of the streamlines geometry. To improve this, it can be suggested to impose additional conditions on the permeability map to make it look more geological, e.g. the geostatistical condition of having certain correlation ranges in the relevant directions. Imposing this would require inverting the permeability from all streamlines simultaneously using a gradient optimiser.

The **second permeability estimation method** considered is based on the steady-state flow equation, and follows the ideas proposed by Vasco [8]. The regularisation aspects, the usage of the multiple pressure maps input and treatment of the wells were considered in more detail than in this paper, and testing of the method was done more thoroughly. The method works with the input of pressure maps and the associated well flow rates. By discretising the steady state flow equation it is possible to obtain a linear system of equations for the grid of unknown permeabilities. The system is solved after adding the regularisation conditions which force the output permeability map to be smoother and suppress the output noise. The algorithm works with a series of pressure maps that are supposed to be the instantaneous snapshots of a steady-state flow. While the real flow in the reservoir may consist of the steady-state flow contaminated by the transient effects, there may as well be a problem of getting the instantaneous snapshots of the reservoir with 4D seismic if the seismic acquisition time is quite long. E.g., the acquisition time for Schiehallion field considered in Chapter 6 is 1.5 – 2.5 months, as follows from the reports provided by the operator. This time is long enough for the pressure fluctuations occurring at the wells to travel some distance through the reservoir. As a result, the different parts of a 4D seismic attribute map may be related to the different states of the reservoir pressure. Thus, we get a snapshot with a long exposure time instead of the instantaneous one.

[43] The noisy pressure map should be reasonably smoothed before it can be handled by the algorithm.

The second permeability estimation approach was tested on a range of the synthetic 2D models. It was revealed that the method resolves the underlying permeability quite well, provided the input is not noisy. It was confirmed that using the multiple pressure maps, especially those related to the well activity in the different parts of the reservoir, is beneficial for estimating the whole permeability map. At the same time resolution of the permeability features located far from wells and not connected to them may be challenging for the procedure. The noise in the input pressure maps[44] was found to highly affect the method's performance. Depending on the case, it may stop working appropriately for the noise levels as low as 5% – 10%. The permeability maps obtained for the high noise input typically show reasonable values only close to the wells, while the rest of the map is filled with the erroneous very low values. Even if the algorithm gives a visually appealing permeability estimate, this map is likely to produce poor predictions of the saturation front, which is natural, since no saturation information is accounted for by the procedure. The direction in which the method could be studied further is omitting the boundary conditions (currently I use the zero permeability gradient normal to the boundary), and omitting the condition of the constant permeability on the discrete elliptical contours around the wells. Both these can be done because the regularisation is imposed in any case, so the main (not regularised) system of equations can be left underdetermined.

The permeability map can be represented as a linear combination of some basis functions which range from the high frequency to low frequency ones. In this way, the regularisation can done by considering only a certain number of the low frequency functions when solving the discretised flow equation, instead of introducing the smoothing terms to the objective function. Apart from regularisation done by smoothing, a different sort of constraints could be applied, which would account for the geostatistical information by biasing the permeability map towards a higher-frequency map with certain correlation ranges. Since the numerical noise which emerges in the output in the case of weak smoothing has very high frequency, using the geostatistical constraints with a reasonable variogram model and correlation ranges is anticipated to be able to suppress the said noise, while the resulting permeability map would look more geological rather than that conditioned just by smoothing. Introducing the prior permeability values for the whole map or a part of it could also be studied with respect to its ability to improve the method's performance.

[44] The noisy pressure maps should be smoothed prior to the method's application.

High sensitivity of the approach to the input noise seeded another study of how the lateral permeability heterogeneity affects the pressure signal. By doing this, I put the pressure response from the *constant (average) component* of the permeability map aside, and only considered how the *heterogeneous component* affects the pressure response. From a number of 2D models considered it was established that the lateral permeability variations have effect on pressure ranging from 17% to 73% of the total pressure signal, where the pressure signal is the time-lapse pressure difference: the monitor pressure minus the initial pressure. This result means that once the error in the pressure map (arising from the 4D noise or inaccuracy of the pressure inversion procedure) exceeds the quoted noise levels, the pressure map becomes useless in resolving the permeability map, except for the average permeability values around the wells which can be estimated from the well flow rates and the bottom-hole pressures.

Nevertheless, the noisy pressure maps extracted from time-lapse seismic can be used for estimating the fault transmissibility and connectivity of the different reservoir compartments. Pressure signal of an *over-pressurised* reservoir compartment is often clearly seen on the 4D seismic attribute map. The transmissibilities of the boundaries of the highlighted compartment can then be estimated. Estimating the pressure signal for a *depleted* compartment may be more challenging, since it is likely to be masked by the gas signal of the gas which came out of solution. Estimation of the fault or barrier transmissibilities, or, more precisely, transmissibility multipliers can be easily incorporated into the described procedure.

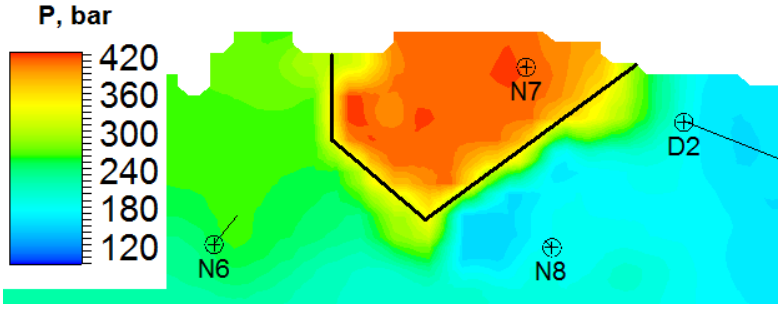

Figure 7.1 Pressure map showing a partially sealed compartment pressurised by injection from well N7. The thick black lines show the barriers with the transmissibility multipliers to be estimated.

For that, the barriers should first be introduced as lines on the map, and each barrier is assigned an unknown transmissibility multiplier, see Figure 7.1. The potential barriers are the faults interpreted from the 3D seismic or the boundaries of the sealed compartments highlighted on the 4D seismic map by the pressure-up signal. The map

of permeability which is to be inverted should be subject to a strong smoothing regularisation so that the barrier transmissibilities become resolved rather than the permeability map details. Instead of the smoothing regularisation, a different parameterisation of the permeability map could be employed, e.g. interpolating the map based on the values at wells. To introduce the transmissibility multipliers, the first way is to treat the barrier as a thin line of grid cells, and apply the multiplier to the permeability values of these cells. The second way is to reformulate the steady state flow equations (3.8) in the discretised integral form: sum of the flows into the grid cell equals the source rate in that cell. The flow between two neighbouring cells is expressed as a product of the fluid mobility λ_{ij}, transmissibility between the cells, and the pressure drop between them, e.g. the flow rate in *x* direction from cell (i, j) to cell $(i+1, j)$ equals

$$F_{x,ij} = \lambda_{ij} T_{x,ij} (P_{i,j} - P_{i+1,j}), \tag{7.1}$$

with transmissibility given by

$$T_{x,ij} = k_{harm} \cdot (h \cdot NTG)_{arithm} \frac{\Delta y}{\Delta x}, \tag{7.2}$$

where k_{harm} is the harmonic average of permeabilities of the two cells, $(h \cdot NTG)_{arithm}$ is the arithmetic average of the effective reservoir thickness of the two cells, Δx and Δy are the cell dimensions. Since permeability is averaged harmonically in this case, the resulting system of the flow equations will contain the unknowns in non-linear form, which certainly complicates its solution. However, for such discretisation the fault or barrier consists of a series of the connected grid cell edges. Each pair of cells sharing some fault edge has certain transmissibility value (7.2), and the fault transmissibility multiplier is then directly applied to this value.

The **third permeability estimation approach** attempted to avoid the input of the pressure maps because of their decreased information content in the presence of noise. Thus, the method works entirely with the saturation maps. It is an iterative procedure starting from some initial permeability approximation, and calculating the pressure map and the corresponding streamlines on each iteration. For each streamline the total pressure drop is expressed via the grid cell permeabilities, and it is then equated to the observed pressure drop, which is essentially the pressure drop between the wells connected by the streamline. The resulting equation imposes a constraint on the permeability values, and all such equations constitute a system which is solved in the

least squares sense, with the smoothing regularisation added. The permeability determined is subsequently used in the next iteration. The system of equations is nonlinear with respect to the permeabilities, but is linear with respect to the reciprocal permeabilities. The latter formulation could greatly simplify its solution and analysis, but the preliminary testing did not give plausible results as the reciprocal permeability often approached zero, leading to very high permeability values. The research in this respect was not sufficient however, so a deeper study and testing might actually bring more insights. The starting point could be in specifying the positive minimum constraint for each reciprocal permeability value and then solving the resulting linear constrained problem by quadratic programming.

The method was tested on the maps output from the simple 2D models, and it was found that the initial permeability approximation, the regularisation settings and different parameterisation approaches may significantly affect the result, up to making it completely inacceptable in the sense that the model using the estimated permeability map cannot predict the original saturation fronts. No simple guidelines were found on selecting the initial permeability and the other settings for achieving the robust results. Even for the estimated permeabilities which give reasonable saturation predictions the permeability map itself is often not looking geological. Resolving the listed problems could be attempted in some future study. One of the main concerns with the method is that permeability in each iteration is updated for the fixed streamlines, whereas the real streamlines geometry should depend on the permeability map. This lack of coupling between the streamlines and permeability results in poor convergence of the method, so that the objective function may fluctuate around some value as the algorithm works, instead of decreasing monotonously. Restricting the maximum permeability change acceptable in each iteration led to an almost monotonous decrease of the objective function, however the associated permeability inversion results were not satisfactory, so a further study may be needed to tackle the problem of coupling between the streamlines and permeability.

7.3 Seismic history matching

As the considered fast-track procedures of using the 4D seismic products to predict the waterflood or to estimate the reservoir permeability turned out to be non-working for the realistic levels of noise and realistic levels of complexity of the reservoir fluid flow,

the research focus shifted to a more computationally demanding approach – history matching. History matching provides more coupling between the different quantities describing the fluid flow – permeabilities, pressures, and saturations. For this reason it is able to tolerate higher noise in the input data compared to the fast-track procedures, which was demonstrated on a simple 2D simulation model. This means that history matching would be a preferred method for the realistic datasets which normally have moderate to high noise levels.

In Chapter 4 I considered a history matching loop that was implemented using CMA-ES optimisation algorithm and a simplified data-driven method of treating the 4D seismic. The CMA-ES algorithm, to my knowledge, was almost not applied to history matching problems before. In this work its performance was compared with a few other black box optimisers on PUNQ-S3 dataset, and the method appeared to be reasonable, although not the fastest. Application of CMA-ES to the other history matching problems gave in general positive experience.

The implemented method of incorporating 4D seismic into history matching loop is based on a linear relationship between the maps of time-lapse seismic attributes and the average maps of reservoir dynamic parameter changes. Such relationships have already been considered in the literature, mostly for the purposes of pressure and saturation inversion. To my knowledge, they have not been applied for history matching. Since no petro-elastic or seismic trace modelling is performed in this case, the proposed approach is free from the uncertainties in the petro-elastic parameters[45]. In the literature the estimation of the coefficients a_i used in these relationships is usually done at the well locations. In my work the coefficients are calculated by linear regression on the whole maps, so there is no need for preliminary calibration to the well data. Regression on the whole maps is more robust than regression (calibration) at the well locations only, especially if the data at the well locations are of poor quality. One more advantage of using the whole maps rather than wells is that the reliable estimates of water and gas saturations at well locations are usually not available, and a separate history matching may be required to get them.

[45] Note that currently people in the industry would still eventually go to a complex petro-elastic model, even if they started from a proxy seismic modelling procedure like the one I considered here. Thus, the regression-based proxy seismic modelling should be viewed as a tool supplementary to the common PEM, rather than a complete substitute for it.

Two modifications to improve the basic linear relationships were suggested: one which multiplies the average maps of the reservoir dynamic property changes by a scaling map, and the other which introduces the quadratic terms of the dynamic properties maps. The scaling map is intended to account for the reservoir lateral heterogeneities in porosity, NTG, thickness which affect the time-lapse seismic response. It was suggested to use the baseline attribute map for scaling as it is readily available, and besides, as simple testing revealed, gave more plausible enhancement than the other considered option – the map of the pore volume per unit area. Introduction of the quadratic terms was shown to be beneficial as well, however it still remains unclear which quadratic terms to use. Although synthetic tests revealed that one or two quadratic terms may be enough, it cannot be easily established which terms are these for each specific case. A simplest solution would be to use all possible quadratic terms.

The regression between the time-lapse maps of the seismic attributes and the reservoir dynamic parameters in the simplest form only delivers the coefficient of determination R^2 which can be regarded as a measure of fit between the seismic and the simulation model. However, the underlying equations are easily transformed to include the full covariance matrix, so that the spatial correlations in the seismic data errors are rigorously accounted for. This feature is one of the advantages of the proposed method since it allows handling of the uncertainties in a proper way.

One of the issues recognized for the linear regression was the need to bound the signs of the derivatives $\partial \Delta A / \partial \Delta P$,..., $\partial \Delta A / \partial \Delta Sg$, so that the relationship between the seismic and simulation model remains physically meaningful. This was implemented by performing the regression with the imposed linear constraints, which is solved by quadratic programming. The active set method of quadratic programming was adopted, and then it was found that there exist numerical difficulties in handling the linearly dependent constraints. Amendments to the algorithm were proposed which gave reasonable practical results, but their validity was not checked theoretically. Also, it may be worth trying a different approach to handle the linearly dependent constraints.

The question of the likely value of the objective function after optimisation was studied from the literature, and was applied throughout the thesis to monitor the general validity of the standard deviations of the data errors. In the majority of the reviewed literature on history matching with uncertainty estimation there seems to be no consideration of this issue, whereas it appears to be an important check. Besides, the likely minimum of

the objective function was used in my work to roughly define the standard deviation of the well data error and seismic data error. It is quite a handy tool, because for example treatment of seismic data during history matching involves both substantial measurement errors that are difficult to estimate, and modelling errors.

The seismic attribute that was used for seismic history matching is the sum of negative amplitudes between two horizons. This attribute was used throughout the thesis both for the real dataset (Schiehallion field) and the synthetic models, where Schiehallion petro-elastic modelling and wavelet were employed. The seismic cubes available for Schiehallion dataset are the full angle stacks, so there are no separate near stacks, mid stacks and far stacks. Time shifts for this field are reported to be small. Since the seismic cubes are the coloured inversion with negative values corresponding to the reservoir units, the sum of negative amplitudes happens to be quite informative to display the reservoir changes. Still, it is worth trying the proposed history matching procedure with other attributes, and also with multiple attributes per single history matching run (e.g. near stacks and far stacks simultaneously), which can be easily incorporated into the method. For thicker reservoirs or higher frequency seismic where separate reservoir units can be resolved vertically, the map-based approach used in this work is not suitable. However, the outlined principles can still be applied in volumetric terms, e.g. the linear regression can be performed between the volumes of the inverted time-lapse impedances and the 3D reservoir dynamic property changes. If impedances are not available, or are to be avoided, then one could deal with seismic using multiple horizons – for example those horizons which can be picked from the seismic section. For each of these horizons a separate seismic attribute map can be calculated. On the simulation model side, the maps of pressure and saturations can be found by averaging the 3D properties only between the appropriate pairs of horizons, so there will be a number of average maps, some picking the properties at the reservoir top, some – in the middle, some – at the bottom. Then, the linear regression can be considered between the attributes coming from all the horizons – and the corresponding reservoir average maps.

In this thesis the proposed seismic history matching procedure based on the regression between seismic and simulation model was not compared with the other SHM procedures commonly described in the literature – e.g. those which perform petro-elastic modelling and work in the impedance domain, or those which also perform the seismic trace modelling and work in the attributes domain. It makes sense to perform

such a comparison on a real dataset where the petro-elastic model is unknown *ab initio*, to check if there is any deterioration in the results of the regression-based SHM versus traditional SHM, and whether such a deterioration is adequately compensated by saving the efforts on calibrating the petro-elastic model.

Finally, it is worth noting that it is possible to calculate gradients of the proposed seismic objective function. This would allow application of the gradient optimisation algorithms for history matching, which work faster than stochastic methods. In this work such algorithms were not considered because the reservoir simulator used did not provide the derivatives of the output variables (well data, dynamic property cubes) with respect to the model parameters. If such derivatives were available then the derivatives of the seismic part of objective function f_2 could be also found. The sketch of this is given below, using the notation of Appendix E. Assume that the derivatives of the average maps ΔP, ΔSw, ΔSg with respect to some parameter w[46] are known. Also assume that the relationship between the time-lapse seismic maps and the maps from the simulation model only contains the linear terms, and does not contain the quadratic terms. Given that, the constraints matrix A in (E.4) will not depend on the average dynamic maps, neither on parameter w. The derivatives $\partial P / \partial w$ of matrix P from (E.3) are easily found since its columns consist of the maps $\Delta P \cdot A_0$,..., $\Delta Sg \cdot A_0$ stretched into vectors. Then, one can find $\partial G / \partial w = P^T \cdot C_s^{-1} \cdot \partial P / \partial w + \partial P^T / \partial w \cdot C_s^{-1} \cdot P$, and $\partial g / \partial w = -\partial P^T / \partial w \cdot C_s^{-1} \cdot f$, where G and g are from the expression defining the quadratic function $q(x)$ in (E.5). Minimisation of $q(x)$ subject to inequality constraints (E.4) terminates at minimisation of $q(x)$ subject to some active (equality) constraints defined by matrix A_{act}. In terms of the reduced variables y the minimiser (see (E.9), and also recall that $b_i = c_i = 0$) is given by

$$(Z^T G Z) y^* = -Z^T g. \tag{7.3}$$

[46] Examples of w include: reservoir porosity, NTG or permeability at some grid cell or region, phase relative permeabilities, fluid contact depths etc.

As matrices A_{act}, Z do not depend[47] on w, by virtue of $x^* = Zy^*$ one can write $\partial x^* / \partial w = Z \cdot \partial y^* / \partial w$. Then, applying the chain rule, find the derivative of the quadratic function $q(x)$ at $x = x^*$

$$\left.\frac{dq}{dw}\right|_{x=x^*} = \frac{\partial q}{\partial x} \cdot \frac{\partial x}{\partial w} + \frac{\partial q}{\partial w} = \left(Gx^* + g\right)^T \cdot \frac{\partial x^*}{\partial w} + \frac{1}{2} x^{*T} \frac{\partial G}{\partial w} x^* + \frac{\partial g^T}{\partial w} x^*. \tag{7.4}$$

The first term in this expression, which corresponds to $\partial q / \partial x \cdot \partial x / \partial w$, equals zero. To check this, consider $U = (Gx^* + g)^T Z = (GZy^* + g)^T Z$. From definition (7.3) of the minimiser y^* it follows that $U^T = 0$, making the whole term $U \cdot \partial y^* / \partial w$ zero. Finally, according to (4.12) and (E.5) the seismic part of the objective function equals $f_2 = 2q(x^*) + const$, and by the last trivial step the required derivative is found:

$$\frac{\partial f_2}{\partial w} = x^{*T} \frac{\partial G}{\partial w} x^* + 2 \frac{\partial g^T}{\partial w} x^*. \tag{7.5}$$

The above derivation was sketched under assumption that only linear terms are present in the equation linking the seismic with the reservoir simulation model. The final expression, however, does not depend on matrix Z, and the situation may be the same for the quadratic terms present as well. The accurate derivation for the quadratic case might be done in some future research.

7.4 Uncertainty estimation

Testing of the proposed seismic history matching procedure was done in Chapter 5 in the context of uncertainties estimation, and it was established that the SHM results in smaller prediction uncertainties than the conventional well HM. Moreover, it was found that using non-diagonal covariance matrices of the seismic data errors is a more robust approach to treat the uncertainties, resulting in reduction of bias in the predictions.

[47] There may be some dependence of A_{act} on w in that the set of active constraints at minimiser x^* may change at some w_0. There will be different matrices A_{act} and Z for $w < w_0$ and for $w > w_0$, but the subsequent calculations give the identical results for the derivative $\partial f_2 / \partial w$, so the derivative remains continuous as w passes through w_0.

In the first place, a method of uncertainty estimation was considered which is based on Monte-Carlo integration during CMA-ES optimisation. The method was intended to make use of the numerous ensembles of models generated by CMA-ES for all of which the objective function is evaluated during CMA-ES run. Theoretically this could be done since the PDF used by CMA-ES to sample the models is known, and Monte-Carlo integrals with weights give the unbiased estimates of the required quantities – **means** and **std**'s. However, in practice, only for the very low dimensional problems did the method work at the expected precision. For the problems of reasonable dimensionality the estimates suffered from insufficient exploration of the search space and failed to gather the necessary statistics. The algorithm was thus rejected and the randomised maximum likelihood method was adopted instead. Despite this, it is worth further looking at the possibilities to use all the information generated by an ensemble-based optimisation algorithm. By default, the optimisation algorithm seeks a single optimum point by evaluating hundreds and thousands of objective function values, which are then wasted. Incorporating these values somehow into the uncertainty estimation may be a more rational way to use the computing resources. If such an approach is found, it should be tested at least on uncertainty estimation for linear problems since the exact uncertainty solution is known for them (under Gaussian assumptions), and the linear problems often provide a good approximation to many real world physical problems. It is essential to test the approach on problems of practical dimensionality, e.g. 10 – 100. The RML method which was picked up from the literature can sample models from the posterior distribution, given the Gaussian assumptions about the prior model and the data errors. This sampling is exact in the case of linear forward modelling, and approximate for the non-linear models. There are reports in the literature where correctness of the RML sampling was tested on non-linear problems, including multimodal PDFs from history matching. Generally reasonable performance of RML is reported there, although to date there is no theoretical proof or study of RML performance and applicability *in non-linear cases*.

To estimate the error model for well and seismic data – i.e. the standard deviations or, in a more general case, covariance matrices to be used in the objective function, an approach was suggested which is rather simplistic but still makes sense. Its idea is in making some preliminary history matching and then analysing the difference (residue) between the resulting modelled well or seismic data and the corresponding measurements. From the residue the autocovariance functions can be inferred, and the correlation ranges can be estimated, finally giving us the correlation matrix. Also, the

standard deviation can be calculated – either using the standard formula $\mathbf{std} = \sqrt{1/N \cdot \sum r^2}$, or by applying the χ^2 criterion to the minimum value of the objective function. The latter method was used in this work, although both of them normally give close results. While this approach of the error model definition seems to account for the total errors, no detailed study was undertaken on its correctness. A more elaborate approach might be considered, e.g. that in which a trend is firstly picked in the residue between the model and observation, and only then the remaining higher frequency noise is processed to get the correlation ranges and standard deviations. When analysing the correlation ranges and creating the correlation matrices, more complex covariance functions could be introduced instead of the spherical one that I applied. For instance, the shape of the covariance function could have two distinct slopes: steep at small lags and gentle at large lags, see Figure 7.2. Finally, for the seismic part of objective function in the case of multiple monitors my procedure employed the covariance matrix made of identical blocks for the different monitors. It is worth implementing a more flexible method where a distinct covariance matrix can be used for each seismic monitor.

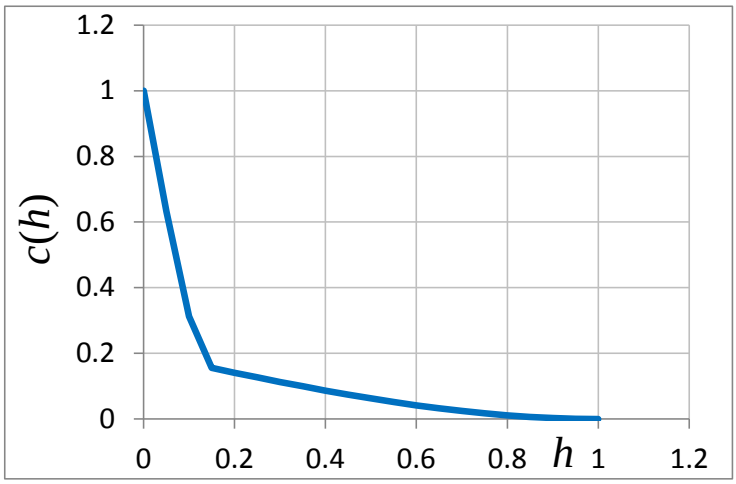

Figure 7.2 Example of a covariance function with complex shape.

Testing of history matching with uncertainty estimation was performed on a three-phase 3D synthetic model which has heterogeneously distributed rock properties, gas cap, and two wells. Considering a rather short 500 days *historical period* ensured that the model has a lot of uncertainties, even after history matching it to the well data observed at this period. The subsequent 2000 days *prediction period* was used to display the uncertain behaviour of the model. A number of history matching setups were considered, including conventional well HM, well + seismic HM, seismic-only HM, where the seismic monitor is taken at the end of the historical period. Since there is no evidence

of water breakthrough in the historical well data, the future water cut development is quite uncertain if the reservoir model is constrained to the well data alone. Introducing the 4D seismic data which areally grasps the position of the water saturation front allowed reduction of the uncertainties in oil and water production rates. This reduction (**std**'s decreased 2-3 times) is especially seen in the early prediction period when water breakthrough takes place. The success of the conducted SHM exercise also supports the validity of the seismic history matching technique introduced in Chapter 4, which links time-lapse seismic with the simulation model by means of regression between the attribute maps and the dynamic property maps. It was found that using seismic with nontrivial correlations results in less biased predictions than using seismic with diagonal covariance matrices. This observation highlights the importance of careful definition of the error model in order to get the reliable uncertainty estimates. Seismic-only history matching was shown to be capable of constraining the reservoir simulation model so that the model would predict the future well data, albeit with the uncertainties higher than in the conventional well HM case. This result is quite expected because seismic can be regarded as "soft data", whereas the well data are "hard". A further question can be addressed about the information content of the well data and seismic data – i.e. to what degree each data type reduces the reservoir uncertainties. Then, a study should be carried out on the optimal spacing of the seismic surveys in time, so that uncertainty reduction from the 4D seismic reasonably reflects the costs of the seismic acquisition and processing. The answer to the last two questions will certainly be field-specific.

7.5 SHM with uncertainty estimation for Schiehallion field

The developed seismic history matching approach together with the considered uncertainty estimation algorithm were applied in Chapter 6 to segment 4 of Schiehallion field. Schiehallion reservoir is made of Tertiary age turbidites, and features complex connectivity of the channels and the sheet-like sands, which is further complicated by the normal faulting. The initial estimates of the reservoir connectivity done after the field appraisal were overly optimistic, and led to drilling the insufficient number of wells. This resulted in the lack of pressure support and high producing GORs at the early stages of the field development. The reservoir connectivity was then reconsidered as being more poor, and the infill drilling programme was implemented with decisions

guided by the 4D seismic and the well pressure data. It helped reduce the GOR, and the reservoir engineering focus shifted on managing water cut as the field matured. At the early stages of the field life the reservoir connectivity, which is one of the key factors for the successful field development, was estimated from the 3D seismic (helps identifying faults and separate sand geobodies), pressure profiles in the newly drilled wells (the depleted or increased pressure being the signs of connectivity with the other wells), tracers injection and monitoring, and multi-tank material balance modelling (for testing the different reservoir connectivity hypotheses). The reservoir connectivity was one of the main uncertainties in the Schiehallion segment 4 history matching done in this thesis.

For history matching I used the dataset consisting of the fine scale reservoir simulation model (not history matched), well logs, well production data, and a number of seismic surveys including the preproduction baseline and the monitor 3D cubes. Only the southern segment 4 which is isolated from the rest of the field by the East-West fault was considered. The segment has 8 producers and 8 injectors for the time framework in question (1998 – 2008). The original simulation model showed the overestimated reservoir connectivity, permeability and sweep efficiency. Prior to history matching the simulation model was significantly upscaled, reducing the number of the active cells from 360,000 to 8,700. In this work I did not consider the problem of transferring the changes applied to the coarse model during history matching back to the fine scale model. Since the RML algorithm was used to sample the models from the posterior distribution, it was essential that the history matching step of the RML converges with good precision. When moving the changes back to the fine scale model, the history match quality may deteriorate (e.g. the minimum of the objective function may not satisfy the χ^2 check), and thus the fine scale model may not follow the required posterior distribution. A future research may focus on the problem of transferring the history matching changes to the fine scale model in the context of the RML algorithm application.

I made an estimate of the noise present in the 4D seismic, expressed as the ratio (N/S) of the 4D noise in the reservoir to the 4D signal in the reservoir. The estimate of N/S for the monitor 2004 showed quite high noise levels, with the median value of 80% in the areas where notable time-lapse signal is present, and even higher values elsewhere. A question may arise as to why the estimated noise level is high whereas the 4D seismic attribute (sum of negative amplitudes) shows a rather clear signal. This question was

not addressed in this work as it would involve analysis of the seismic processing and cross-equalisation of the seismic surveys, so this problem could be dealt with in a different study. The starting hypothesis I can suggest to tackle the question is that the cross-equalisation may target specifically on the part of seismic section close to the reservoir, whereas the overburden where non-repeatability is estimated may not be properly equalised.

To parameterise the model for the assisted history matching, 95 parameters were identified. The major bulk of them are the parameters controlling the reservoir connectivity – the multipliers for the transmissibility between the adjacent geobodies and permeability multipliers within the geobodies. The other parameters were the pore volume multipliers for a few geobodies (including the aquifer), skin factors for the different perforations of 2 wells completed in multiple geobodies, relative permeability parameters, and positions of the fluid contacts. The ranges of the parameters were selected so as to maintain the geological and physical realism and keep the model in line with the prior engineering understanding of the field.

In defining the objective function, two history matching setups were considered: conventional well HM, and well-seismic HM. Both setups used a limited *historical period* from the start of production to 01/08/2004 for history matching, followed by the *prediction period* where the forecasts produced by the history matched models were studied. For the objective function of the well HM I estimated the correlation range and the standard deviation for the errors in each well data vector. The correlation ranges were found visually from the autocovariance functions, and vary between 100 – 400 days. The **std**'s were estimated using the χ^2 criterion, allocating the 95 model parameters equally between the 4 groups of the well data vectors. The relatively large correlation ranges are different from the ranges commonly used in the history matching literature, which are usually small enough to be ignored, e.g. smaller than 1 month. The larger ranges produced by this approach can be explained by the fact that the total (measurement + modelling) error is accounted for, not just the measurement one. From the obtained experience with analysing the errors in data vectors I can suggest that it may be worth representing the total error as a sum of a lower frequency trend and a higher frequency error component. The trend can be seen for the situations where all the history matched models produce the same systematic error (see e.g. Figure 6.21), and this is usually the consequence of the lack of flexibility in the model parameterisation. More studies should be done with respect to such situations, and

currently their proper treatment seems to lie either in using the trends in the errors, or improving the parameterisation.

The seismic HM used the same wells objective function plus the seismic part of the objective function. To define the latter I examined the seismic error from the preliminary history matching runs, and based on it estimated the major and minor spatial correlation ranges (both equal to 400 m) and the **std**. The found **std** equals 1670, which is quite close to the RMS = 1940 of the time-lapse attributes used, and this is consistent with the high noise to 4D signal ratio estimated before. The current version of the history matching algorithm only supports the usage of the same values of the correlation ranges and standard deviation for all seismic monitors. However, Schiehallion seismic showed slightly different magnitude (RMS) of the considered 4D attributes at 2002 and 2004. So, in the future work it may be worth amending the procedure so that it can use a separate seismic covariance matrix (as defined by the correlation ranges and the **std**) for each monitor.

For each HM setup 20 models with a reasonable history match quality were generated by the RML algorithm. Since some models occasionally failed to reproduce the observed well data because of the inappropriate optimisation algorithm performance, these models were rejected, and around 30 models were actually generated to get the 20 models reproducing the history. The rejection was done in a somewhat subjective manner – by visually spotting the notable mismatches between the modelled data and the observations, as the final values of the objective function were found ineffective at discriminating failed models. As a further development, it may be worth formalising the rejection procedure to remove the bias caused by the human decision.

The resulting models showed a good match to the majority of the well data vectors, with exception for the WGOR of five wells. Improving these may be challenging and would require a deeper study of the field and access to more sources of information. For instance, for the wells D5, D6 located in the south-western part of segment 4 the measured GOR is notably below the initial solution gas oil ratio *Rs* accepted for the field (0.35 mscf/stb). This may mean incorrect GOR measurements at the wells, or, if the measurements are to be trusted, one would need to reconsider the PVT properties and specify a different PVT region in the South-West area. Alternatively, the critical gas saturation and the gas-oil phase relative permeabilities for the area in question may be reconsidered. More sources of data (like fluid samples reports, etc.) should be available to decide on which route is better.

The forecasts produced by the models for the prediction period were generally consistent with the actual observations, except WBHP and WWCT of well D1, WBHP of wells N1, N5, and WGOR of five wells. The situation with poor prediction could be potentially avoided by making the model parameterisation more flexible. For the GOR prediction of wells D5, D6 the comments made above also apply. One of the notable prediction failures is that of well D1 bottom-hole pressure: the predicted BHP shows the substantial decrease in line with the increased well flow rate, whereas the observations show the BHP increase. The measured BHP increase in not consistent with the measured well GOR which exhibits certain growth. However, the observed well D1 BHP increase is echoed by the similar BHP increase of the nearby producer D2 (Figure 6.23) which is producing with approximately stable flow rate. Thus, for the proper explanation of the well D1 behaviour the field production data should be verified and the additional sources of information should be analysed, e.g. the data on the well stimulation.

For the seismic HM setup the modelled time-lapse attributes at 2002, 2004 reasonably matched the corresponding historical attributes, reproducing essentially the reservoir softening signal of the gas exsolution and the increased pressure. Since the seismic modelling procedure employed uses the linear regression between the maps of the seismic attributes and the reservoir dynamic parameters, the modelled attributes tend to be smoother and have smaller amplitude of values than the observed attributes. Prediction of the future seismic attribute (2006) by a history matched model with the calibrated seismic modelling equation did not forecast the actual observations. This can be explained by the fact that the seismic modelling equation was calibrated to honour the gas signal abundant in the historical seismic maps. The excessive (erroneous) gas exsolution in the simulation model forecasts at 2006 thus led to the wrong modelled 4D seismic attribute. The other mismatch – corresponding to the pressure-up softening signal in the middle area is likely to be due to the erroneous 4D seismic in that location either for the historical monitors 2002, 2004, or for the prediction monitor 2006.

For the seismic history matching I examined whether the prediction uncertainties increased or decreased compared to the conventional well history matching. This was done by examining each well data vector's **std** ratio for the two HM setups. The **std** of the prediction showed an increase for some vectors (e.g. WWCT) corresponding to the wells completed above or below T31 reservoir. This behaviour seems reasonable since the observed seismic attributes were calculated for the T31 interval and only reflect the

reservoir changes in T31. The decrease of uncertainty for WWCT vectors was observed for two wells completed in T31, with distinct water saturation signal present nearby. Uncertainties for the WGOR vectors decreased for almost all producers, which is consistent with the predominance of the gas signal in the observed time-lapse seismic. The **std**'s of the producers WBHP did not change much, which is natural since the pressure decrease signal associated with the producers is usually difficult to be found on the 4D seismic attribute map because of its contamination by the gas exsolution signal. The decrease of the WBHP forecast uncertainty was present for two producers in the western part of the segment, where the time-lapse signal shows predominantly reservoir hardening. Finally, the WBHP uncertainty decreased for 5 injectors, especially those for which a notable pressure-up signal on the 4D seismic maps is observed.

Overall, the reduction of uncertainties was rather marginal, which is consistent with the high estimated level of noise compared to the 4D signal. Yet, this reduction was in line with the observed time-lapse signature, as the uncertainty decrease was established mostly for the wells which were completed in T31 reservoir and had a notable time-lapse signal nearby. Thus, application of the proposed seismic history matching workflow to the real dataset can be deemed successful. As a future work, it is worth testing the workflow on the other datasets, especially those with stronger water saturation signal, and on the compacting reservoirs. For these datasets it may be beneficial to consider multiple seismic attributes for history matching: near-, far-offset stacked amplitudes, time shifts, as they complement each other in displaying the reservoir dynamic parameters.

7.6 A brief summary of the methods

A brief summary of performance and requirements of the different methods for quantitative coupling of 4D seismic data with reservoir engineering is given in Table 7.1. The methods involved are those considered throughout Chapters 2 - 6, and range from the fast-track procedures to the full-fledged history matching.

	Method	Input	Restrictions	Noise tolerance	Speed
fast-track proceudres	Saturation front prediciton	$P_2, S_1, S_2, \varphi \cdot h \cdot NTG$	Semi-steady-state flow between the timesteps; no pressure update	Low	Very high
	Permeability estimation #1	$P_2, S_1, S_2, \varphi,\ h \cdot NTG$	Semi-steady-state flow between the timesteps	Low	High
	Permeability estimation #2	P_i, well flow rates	Instantaneous semi-steady-state flow at each timestep	Very low	High
	Permeability estimation #3	S_i, well BHPs	Semi-steady-state flow between the timesteps; may experience issues with convergence	Low	High
	Seismic history matching	Simulation model, well production history, A_i, A_{base}	--	High	Low

Table 7.1 Comparison of performance and requirements of the methods considered in this thesis. The variables in the "input" column denote different input maps according to notation in the corresponding chapters: P – pressure, S – saturation, A – seismic attribute.

7.7 Mapping the thesis ideas onto the state-of-the-art trends in industry

The concepts and workflows developed in this thesis can potentially contribute to the advanced practices and technologies which are emerging in the petroleum upstream industry and are getting a progressively wider acceptance. Two such practices/technologies will be considered here: permanent reservoir monitoring and intelligent wells. Permanent reservoir monitoring may include different monitoring systems, e.g. the permanent pressure gauges at wells which allow time-lapse pressure transient analyses [72], or permanent temperature sensors in the wells that are essential in the case of thermal recovery methods. The permanent monitoring methods which are relevant to this thesis are the Life of Field Seismic (LoFS) projects which involve installation of the ocean bottom cables (OBC) measuring the four-component[48] seismic

[48] The four components are: the hydrophone which measures the P-waves, and 3 geophones in the perpendicular directions which measure the S-waves.

signals. Such installation allows shooting the seismic surveys at shorter time intervals than the conventional offshore 4D seismic (currently the LoFS intervals are of the order of a few months). The other benefit of the OBC acquisition is the increased 4D seismic repeatability and fidelity. The examples of the oil fields with LoFS are the North Sea Valhall field [73], and Ekofisk field [74]. The increased 4D repeatability of the LoFS (and hence lower noise) opens the opportunity to apply the fast-track saturation prediction and permeability estimation methods proposed in the thesis. Besides, the higher frequency of the acquired seismic monitors will be beneficial for the fast-track procedures, since the reservoir fluid flow considered on the shorter time intervals gives a better approximation to the steady state conditions. However, currently the LoFS projects are implemented mostly for the challenging reservoirs, e.g. the two fields mentioned above are the compacting chalk reservoirs. The resulting 4D seismic signal is therefore difficult to interpret, since it involves both reservoir compaction and chalk weakening from water injection, so inversion for the saturation and pressure changes required for the fast-track methods may be problematic. In this case it may be beneficial to apply the SHM procedure devised in this thesis to integrate the large number of the 4D seismic data into the reservoir simulation model. The petro-elastic and seismic modelling may be challenging for the mentioned reservoirs, but these are not required by the SHM procedure, as it uses the regression approach instead, and this approach has the potential of capturing the complex 4D response.

The intelligent wells (IW) technology allows collecting and analysing the wellbore data (flow rates, pressures, temperatures, acoustic signals), and controlling the wellbore inflow profile by the designated components. IW's enable the recovery maximisation and production optimisation in an economically efficient way, avoiding the routine well interventions. The reservoir performance optimisation with the intelligent wells uses the feedback generated by comparison of the data acquired from the well sensors with the history matched reservoir simulation model [75]. The use of the 4D seismic data as an additional input to the history matching allows better constraint of the simulation model, which leads to more robust and confident decisions implemented for the intelligent wells. This is the area where the SHM workflow proposed in the thesis has the potential of application. The examples of 4D signals which might contribute to better constriction of the reservoir model are: water saturation signals showing the water front approaching certain completions of a horizontal IW, the pressure signals showing the lateral continuity of the overpressured/depleted zones connected to an intelligent well. In [76] an example of a horizontal producer and a horizontal injector in Ekofisk

field is provided, for which the 4D seismic signal along the wells is consistent with the pressure measured by the production logging tool (PLT). However, the analysed time-lapse seismic signal is two-dimensional, and adds more information for the reservoir engineering decisions on top of the one-dimensional data from the PLT. For optimisation of the reservoir performance with the IW the role of the simulation model will decrease if the methods of accurate reservoir characterisation and forecast are available. The potential candidates for such methods are the fast-track procedures of permeability estimation and saturation prediction developed in the thesis, provided the high quality input from the 4D seismic is available for them.

Finally, there is a trend in the petroleum reservoir development technology towards the integrated intelligent production systems. The intelligent wells constitute a part of such systems. The other part might be provided by the permanent 4D seismic monitoring together with the appropriate analysis tools which convert the 4D seismic information into the reservoir engineering domain. The range of such tools may include the fast-track procedures and the SHM workflow developed in my work.

Appendix A. Seismic modelling

In order to generate synthetic 3D and 4D seismic from a reservoir simulation model, the following procedure[49] consisting of three stages was employed. In the first stage, which is the *petro-elastic modelling*, the P and S wave velocities and density are calculated for the cellular reservoir simulation model using the petro-elastic model (PEM) parameters and current reservoir pressure and saturation. In the second stage of seismic modelling, the *reflectivity coefficients* for different incidence angles are calculated. In the third stage, seismic traces for different incidence angles are found by convolving the reflectivity coefficients with the wavelet. Then, taking the arithmetic average of traces over a certain range of incidence angles allows the stacked trace to be produced.

The petro-elastic modelling is based on a reservoir simulator output which consists of the 3D grid properties of pressure, water saturation, gas saturation, gas-oil ratio *Rs* at a number of time steps, as well as static reservoir properties: porosity and shale fractional volume (taken equal to $1-NTG$). The reservoir temperature is considered constant in my studies, however the formulae given below account for the changing temperature. The calculation starts from finding the water and brine densities ρ_W, ρ_B (g/cm^3) using polynomials depending on pressure P (MPa), temperature T (^{o}C), salinity S (weight fraction of NaCl). The polynomials employed were suggested by [5] in equations (27a), (27b):

$$\begin{aligned}\rho_W = \; & 1+10^{-6}(-80T-3.3T^2+0.00175T^3+489P-2TP \\ & +0.016T^2P-1.3\cdot10^{-5}T^3P-0.333P^2-0.002TP^2).\end{aligned} \tag{A.1}$$

$$\begin{aligned}\rho_B = \; & \rho_W+S(0.668+0.44S+10^{-6}(300P-2400PS \\ & +T(80+3T-3300S-13P+47PS))).\end{aligned} \tag{A.2}$$

The acoustic velocity in pure water at 100^{o}C and 100 MPa is calculated as a polynomial suggested by Wilson [77]:

$$V_W=\sum_{i=0}^{4}\sum_{j=0}^{3}w_{ij}T^iP^j, \tag{A.3}$$

[49] Practically, the simulator-to-seismic MATLAB code was used which was created by the previous generations of PhD students from the Edinburgh Time-Lapse Project, see e.g. the PhD thesis of Amini [95].

where constants w_{ij} are given in Table A.1. Then, the brine velocity which accounts for the temperature, pressure and salinity is given by equation (29) from [5]:

$$V_B = V_W + S(1170 - 9.6T + 0.055T^2 - 8.5\cdot 10^{-5}T^3 + 2.6P - 0.0029TP - 0.0476P^2) + S^{1.5}(780 - 10P + 0.16P^2) - 1820S^2. \quad \text{(A.4)}$$

w_{00}	1402.85	w_{21}	0.000275	w_{42}	5.23E-11
w_{10}	4.871	w_{31}	-6.5E-07	w_{03}	-1.2E-05
w_{20}	-0.04783	w_{41}	7.99E-10	w_{13}	-1.6E-06
w_{30}	0.000149	w_{02}	0.003437	w_{23}	1.24E-08
w_{40}	-2.2E-07	w_{12}	0.000174	w_{33}	1.33E-10
w_{01}	1.524	w_{22}	-2.1E-06	w_{43}	-4.61E-13
w_{11}	-0.0111	w_{32}	-1.5E-08		

Table A.1 Constants used in Wilson equation [77].

The bulk modulus of brine K_B (Pa) is calculated by

$$K_B = V_B^2 \cdot 1000\rho_B, \quad \text{(A.5)}$$

where the factor 1000 converts density from g/cm^3 to kg/m^3. To calculate the density and acoustic velocity of oil, we will require the gas/oil ratio *Rs* and oil density at standard conditions ρ_0 which is related to the API gravity by

$$API = \frac{141.5}{\rho_0} - 131.5. \quad \text{(A.6)}$$

Rs (sm^3/sm^3) is the volume ratio of the liberated gas to the remaining oil when oil is placed in the standard conditions (atmospheric pressure, T = 15.6^{o}C). This quantity is taken as output from the reservoir simulator. Then, the oil formation volume factor *Bo* (rm^3/sm^3) is calculated – either from the PVTO table from the reservoir simulator, or by equation (23) from [5]:

$$B_0 = 0.972 + 0.00038\left[2.4Rs\left(\frac{G}{\rho_0}\right)^{1/2} + T + 17.8\right]^{1.175}, \quad \text{(A.7)}$$

where *G* is specific gas gravity – the ratio of the gas density to air density at standard conditions. Based on *Bo*, the oil pseudo-density ρ', live oil density in the saturated state ρ_G, density with added pressure effect ρ_P, and finally density with added temperature effect ρ_{oil} can be found respectively by equations (22), (24), (18), (19) from [5]:

$$\rho' = \frac{\rho_0}{B_0}(1 + 0.001Rs)^{-1}, \tag{A.8}$$

$$\rho_G = (\rho_0 + 0.0012G \cdot Rs)/B_0, \tag{A.9}$$

$$\rho_P = \rho_G + (0.00277P - 1.71 \cdot 10^{-7} P^3)(\rho_G - 1.15)^2 + 3.49 \cdot 10^{-4} P, \tag{A.10}$$

$$\rho_{oil} = \rho_P / [0.972 + 3.81 \cdot 10^{-4} (T + 17.78)^{1.175}]. \tag{A.11}$$

Then, the acoustic oil velocity V_{oil} (m/s) is calculated using the pseudo-density ρ' substituted into equation (20a) from [5]:

$$V_{oil} = 2096\left(\frac{\rho'}{2.6 - \rho'}\right)^{1/2} - 3.7T + 4.64P + 0.0115\left[4.12\left(\frac{1.08}{\rho'} - 1\right)^{1/2} - 1\right]TP. \tag{A.12}$$

The bulk modulus of oil K_{oil} (Pa) is given by

$$K_{oil} = V_{oil}^2 \cdot 1000\rho_{oil}. \tag{A.13}$$

The described procedure for calculating the acoustic oil velocity from [5] is reported to overestimate the effect of *Rs* on velocity in [78]. In the latter paper a more precise approach is suggested, involving the following. Firstly, apparent liquid density of gas ρ_a is calculated at standard conditions:

$$\rho_a = 0.61731 \cdot 10^{-0.00326API} + (1.5177 - 0.54349 \cdot \log(API)) \cdot \log G. \tag{A.14}$$

Then, the velocity pseudodensity ρ_{PV} at 0^{o}C and 0.1 MPa is found as

$$\rho_{PV} = \rho_0(1 - v_g) + \varepsilon\rho_a v_g, \tag{A.15}$$

where $\varepsilon = 0.113$, and v_g is the volume fraction of apparent liquid gas. The oil acoustic velocity is given by the formula

$$V_{oil} = A - BT + CP + DTP. \tag{A.16}$$

In this formula the coefficient *A* equals the pseudoliquid velocity V_{P0} and is expressed via the velocity pseudodensity:

$$A = V_{P0} = 1900.3\rho_{PV}^{0.6477} - 256.2. \tag{A.17}$$

And finally, the coefficients *B*, *C* and *D* in (A.16) are found from

$$\begin{aligned} B &= 3.044 + 0.012 \cdot (141.5/\rho_{PV} - 131.5), \\ C &= 3 + 0.031 \cdot (141.5/\rho_{PV} - 131.5), \\ D &= 0.3356 \cdot \exp(-4.036 \cdot \rho_{PV}). \end{aligned} \tag{A.18}$$

To find the density and bulk modulus of gas, firstly calculate the pseudo-reduced pressure and temperature P_{pr}, T_{pr} by normalising the absolute pressure P and temperature $T_a = T + 273.15$ with the pseudo-critical values P_{pc}, T_{pc}, according to equations (9a), (9b) from [5]:

$$\begin{aligned} P_{pr} &= P / P_{pc} = P /(4.892 - 0.4048G), \\ T_{pr} &= T_a / T_{pc} = T_a /(94.72 + 170.75G). \end{aligned} \tag{A.19}$$

Then, for gas density the following approximation is used, according to equation (10a) in [5]:

$$\rho_g = \frac{28.8GP}{ZRT_a}, \tag{A.20}$$

where

$$\begin{aligned} Z &= [0.03 + 0.00527(3.5 - T_{pr})^3]P_{pr} + (0.642T_{pr} - 0.007T_{pr}^4 - 0.52) + E, \\ E &= 0.109(3.85 - T_{pr})^2 \exp\left(-[0.45 + 8(0.56 - 1/T_{pr})^2 P_{pr}^{1.2} / T_{pr}\right). \end{aligned} \tag{A.21}$$

The adiabatic gas modulus K_g (Pa) is calculated by equation (11a) from [5]:

$$K_g = \frac{P}{\left(1 - \frac{P_{pr}}{Z}\frac{\partial Z}{\partial P_{pr}}\right)_T}\gamma_0 \cdot 10^6, \tag{A.22}$$

where

$$\gamma_0 = 0.85 + \frac{5.6}{P_{pr} + 2} + \frac{27.1}{(P_{pr} + 3.5)^2} - 8.7\exp[-0.65(P_{pr} + 1)]. \tag{A.23}$$

and values of $\partial Z / \partial P_{pr}$ are obtained from (A.21). The factor 10^6 is needed to convert the units from MPa to Pa. Once the densities of the separate phases and their bulk moduli have been found, the properties of the mixture are calculated [5]. Densities are averaged arithmetically, and moduli are averaged harmonically (Wood's equation), see [79], [5]. In both cases the terms are weighted by the phase saturations:

$$\begin{aligned} \rho_m &= Sw\rho_B + So\rho_{oil} + Sg\rho_g, \\ \frac{1}{K_m} &= Sw\frac{1}{K_B} + So\frac{1}{K_{oil}} + Sg\frac{1}{K_g}. \end{aligned} \tag{A.24}$$

The next step is to evaluate the dry rock (sandstone) behaviour as a function of pressure. For that, the effective pressure P_{eff} will be required, which is found from the fluid pore pressure P and the confining (overburden) pressure P_{ob} [80]:

$$P_{eff} = P_{ob} - \alpha P, \tag{A.25}$$

where α is the effective stress coefficient. The overburden pressure is, in turn, calculated by $P_{ob} = d \cdot g_{ob}$ for each depth d found in the reservoir using some constant overburden stress gradient g_{ob}. Following that, the dry frame bulk and shear moduli can be calculated by equations proposed in [81]

$$\begin{aligned} K_{dry}(P_{eff}) &= \frac{K_{\inf}}{1 + E_K \exp(-P_{eff} / P_K)}, \\ \mu_{dry}(P_{eff}) &= \frac{\mu_{\inf}}{1 + E_\mu \exp(-P_{eff} / P_\mu)}. \end{aligned} \tag{A.26}$$

These equations are controlled by a number of parameters, e.g. $K_{\inf}$, $\mu_{\inf}$ (Pa) which are the bulk and shear moduli at the infinite effective pressure. After the bulk moduli of the fluid mixture K_m and dry rock frame K_{dry} have been found, the bulk modulus of the saturated rock K_{sat} can be obtained by Gassmann equation [82], [83]:

$$K_{sat} = K_{dry} + \frac{\left(1 - \frac{K_{dry}}{K_{matr}}\right)^2}{\frac{\varphi}{K_m} + \frac{1-\varphi}{K_{matr}} - \frac{K_{dry}}{K_{matr}^2}}. \tag{A.27}$$

In this equation K_{matr} is the bulk modulus of the mineral matrix, and φ is rock porosity. The rock shear modulus does not depend on the fluid content [84]:

$$\mu_{sat} = \mu_{dry}. \tag{A.28}$$

It is straightforward to find the density of the saturated rock, which is the porosity-weighted arithmetic average of the fluid mixture and the mineral matrix densities:

$$\rho_{sat} = (1-\varphi)\rho_{matr} + \varphi\rho_m. \tag{A.29}$$

The final step of the petro-elastic modelling is the sand-shale mixing whereby the effective P, S velocities V_P, V_S and density ρ of a mixture of saturated sand and shale are found. For the velocities, Backus averaging [85] is applied. The density of the sand/shale mixture is calculated by arithmetic averaging with weights f_i equal to the volumetric fraction of each rock type (saturated sand or shale).

$$\rho = \sum_{i=1}^{n} f_i \rho_i,$$
$$V_p = \sqrt{\frac{1}{\rho}\left[\sum_{i=1}^{n} \frac{f_i}{K_i + 4/3\,\mu_i}\right]^{-1}}, \qquad (A.30)$$
$$V_s = \sqrt{\frac{1}{\rho}\left[\sum_{i=1}^{n} \frac{f_i}{\mu_i}\right]^{-1}},$$

where K_i, μ_i are the bulk and shear moduli of the respective rock types, and ρ_i is their density.

Before the seismic traces can be calculated, for each trace position a vertical line is considered, and its intersections with the reservoir simulation model cell boundaries are found. Each of these intersections separates two media with different elastic properties, the upper medium with P, S velocities and density denoted as $\alpha_1, \beta_1, \rho_1$ and the lower medium with $\alpha_2, \beta_2, \rho_2$, following the notation in [86]. The reflectivity coefficient between these two media R_{PP} is the scattering matrix coefficient corresponding to the pair *incident P-wave – reflected P-wave*, and is given by [86]:

$$R_{PP}(i_1) = \left[\left(b\frac{\cos i_1}{\alpha_1} - c\frac{\cos i_2}{\alpha_2}\right)F - \left(a + d\frac{\cos i_1}{\alpha_1}\frac{\cos j_2}{\beta_2}\right)Hp^2\right] \Big/ D, \qquad (A.31)$$

where

$$D = EF + GHp^2, \qquad (A.32)$$

$$E = b\frac{\cos i_1}{\alpha_1} + c\frac{\cos i_2}{\alpha_2}, \quad F = b\frac{\cos j_1}{\beta_1} + c\frac{\cos j_2}{\beta_2},$$
$$G = a - d\frac{\cos i_1}{\alpha_1}\frac{\cos j_2}{\beta_2}, \quad H = a - d\frac{\cos i_2}{\alpha_2}\frac{\cos j_1}{\beta_1}, \qquad (A.33)$$

$$a = \rho_2(1-2\beta_2^2 p^2) - \rho_1(1-2\beta_1^2 p^2), \quad b = \rho_2(1-2\beta_2^2 p^2) + 2\rho_1\beta_1^2 p^2,$$
$$c = \rho_1(1-2\beta_1^2 p^2) + 2\rho_2\beta_2^2 p^2, \quad d = 2(\rho_2\beta_2^2 - \rho_1\beta_1^2). \qquad (A.34)$$

In these formulae i_1 is the incident angle of the P-wave, which equals the angle of the reflected (upgoing) P-wave, j_1 - angle of the reflected (upgoing) S-wave, i_2 - angle of the refracted (downgoing) P-wave, j_2 - angle of the refracted (downgoing) S-wave. All the angles are measured relative to the vertical line, which corresponds to angle zero. The angles are linked with the respective wave velocities by Snell's law, stating that the *ray parameter* (horizontal slowness) *p* is constant along the ray:

$$p = \frac{\sin i_1}{\alpha_1} = \frac{\sin i_2}{\alpha_2} = \frac{\sin j_1}{\beta_1} = \frac{\sin j_2}{\beta_2}. \qquad \text{(A.35)}$$

In this way the reflectivity coefficient can be calculated for different P-wave incidence angles. If seismic modelling is required to stack traces over a range of angles from θ_1 to θ_2, then the reflectivity coefficients are found for different angles in $[\theta_1, \theta_2]$, usually taken with increment 1^o, and their arithmetic average is taken, producing the stacked reflectivity coefficient *R*. Finally, the seismic trace can be calculated by convolving the series of the stacked reflectivity coefficients *R*(*t*) with wavelet *w*(*t*), for which fast Fourier transform (FFT) and inverse FFT are employed. Because of linearity of the convolution operation it is more computationally efficient to perform stacking of the reflectivity coefficients, instead of stacking of the seismic traces.

	parameter	unit	value
fluids	oil API		25
	S (salinity)	ppm	18000
	T (temperature)	^{o}C	57.8
	G (gas gravity)		0.586
mineral matrix	K_{matr}	GPa	38
	ρ_{matr}	kg/m^3	2680
rock stress sensitivities	K_{inf}	GPa	7.65
	P_k	MPa	5.62
	E_k		1.128
	μ_{inf}	GPa	5.14
	P_μ	MPa	7.97
	E_μ		1.083
	α (Biot coefficient)		1
shales	V_p	m/s	2811
	V_s	m/s	1289
	ρ	kg/m^3	2349
	g_{ob}	MPa/m	0.0206

Table A.2 Petro-elastic parameters used for synthetic seismic modelling.

All synthetic seismic modelling done in this work used the petro-elastic parameters specified in Table A.2. The wavelet used for calculation of seismic traces is shown in Figure A.1. The PEM parameters and the wavelet considered here are typical for synthetic seismic modelling for Schiehallion field, and were obtained from personal communication with other PhD students working with this field. The wavelet was originally extracted from the Schiehallion coloured inversion full-stack seismic. For the time-lapse studies based on the Schiehallion seismic the attribute equal to the *sum of negative amplitudes* between the top and base horizons was found appropriate [6].

Therefore, while using the Schiehallion wavelet for seismic modelling, I also used the sum of negative amplitudes as the 4D attribute.

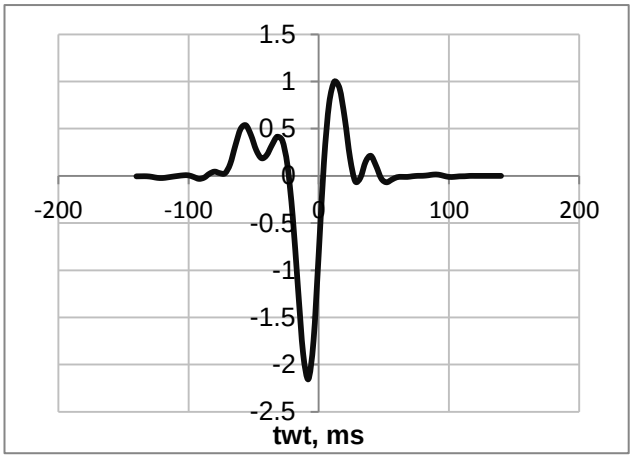

Figure A.1 Wavelet used for synthetic seismic modelling.

Appendix B. CMA-ES

This appendix briefly describes the working principles of the CMA-ES (evolution strategy with covariance matrix adaptation) algorithm [57], [58]. The source code of the algorithm in different languages, including C and MATLAB, can be downloaded from the website: https://www.lri.fr/~hansen/cmaes_inmatlab.html. At the same website one can find the presentations, a tutorial and a more exhaustive list of literature.

CMA-ES is a black box optimiser, and is capable of minimising diverse objective functions – including the non-convex and noisy ones, using only the objective function values, but not the gradients. The algorithm works with a population of models (or individuals) with fixed population size λ. Each iteration starts from sampling a new generation of individuals using a normal distribution. Then the objective function (fitness) values of the models are calculated, in the case of history matching this involves performing forward modelling for each individual. Finally, the obtained information is analysed and the parameters of the sampling normal distribution are updated so as to increase the probability of sampling the next generation with lower objective function values. The sampling of the individuals $x_k^{(g+1)}$ for generation $g+1$ and $k = 1,...,\lambda$ is described by the formula

$$x_k^{(g+1)} \sim m^{(g)} + \sigma^{(g)} N(0, C^{(g)}), \tag{B.1}$$

where $m^{(g)}$ is the mean value, $\sigma^{(g)^2} C^{(g)}$ is the covariance matrix which is split into a scalar part $\sigma^{(g)}$, also referred to as *step size* and matrix part $C^{(g)}$. This matrix part is called the *covariance matrix* in the CMA-ES literature, I will use the same terminology, italicising these words to avoid confusion with the covariance matrix in the usual sense. The step size controls the scale of the distribution, and *covariance matrix* controls the shape of the distribution ellipsoid. The initial mean value $m^{(0)}$ is some vector supplied by the user. The initial *covariance matrix* $C^{(0)}$ is diagonal and its diagonal entries are also supplied by the user.

Strictly speaking, the sampling procedure also involves checking whether the model parameters – or coordinates of the vector $x_k^{(g+1)}$ – satisfy the imposed constraints, the simplest case of such constraints being the minimum and maximum value of each parameter. Whenever a model does not satisfy them, it becomes rejected. Thus, the accepted models do not follow the pure normal distribution defined by formula (B.1),

but instead follow the normal distribution truncated to some region. The model rejection is usually strong at the beginning of optimisation when the step size is large, and becomes small at later iterations with the smaller step size.

Once the new generation has been sampled and the objective functions have been calculated, any evolution strategy performs selection and recombination of the individuals. In CMA-ES this is done by updating the mean and covariance. To update the mean, the individuals are firstly ranked according to the objective function values:

$$f(x_{1:\lambda}^{(g+1)}) \le f(x_{2:\lambda}^{(g+1)}) \le \ldots \le f(x_{\lambda:\lambda}^{(g+1)}). \tag{B.2}$$

Then the μ best individuals are selected and the updated mean is taken as the weighted sum of them

$$m^{(g+1)} = w_1 x_{1:\lambda}^{(g+1)} + \ldots + w_\mu x_{\mu:\lambda}^{(g+1)}. \tag{B.3}$$

The value of μ is usually taken as $\lambda/2$. The positive weights w_i sum up to 1, and are non-increasing so that the fittest individuals make the biggest contributions to the updated mean $m^{(g+1)}$:

$$\begin{aligned} &\sum_{i=1}^{\mu} w_i = 1 \\ &w_1 \ge w_2 \ge \ldots \ge w_\mu > 0. \end{aligned} \tag{B.4}$$

The weights can be chosen e.g. to be equal, linearly decreasing, or logarithmically decreasing. The update of the *covariance matrix* is more complex and there is a lot of discussion in the literature devoted to it. There are three main terms in the updated *covariance matrix*:

$$\begin{aligned} C^{(g+1)} &= (1 - c_1 - c_\mu) C^{(g)} \\ &+ c_1 p_c^{(g+1)} p_c^{(g+1)T} \\ &+ c_\mu \sum_{i=1}^{\mu} w_i y_{i:\lambda}^{(g+1)} y_{i:\lambda}^{(g+1)T}. \end{aligned} \tag{B.5}$$

The first term is the weighted *covariance matrix* from the previous generation. This term is responsible for the accumulation of the *covariance matrix* statistics as the algorithm iterates through the generations. The weight used here discounts the information gathered from the very old generations. The second term contains the outer product of two identical vectors $p_c^{(g+1)}$ which is thus a rank-one matrix. Accordingly,

the term is called the *rank-1 update*. Vector $p_c^{(g+1)}$ is called the *evolution path* and is found by adding the steps taken by the algorithm:

$$p_c^{(g+1)} = (1-c_c)\,p_c^{(g)} + \sqrt{c_c(2-c_c)\mu_{eff}}\,\frac{m^{(g+1)} - m^{(g)}}{\sigma^{(g)}}. \tag{B.6}$$

The steps $m^{(g+1)} - m^{(g)}$ are normalised by the corresponding step sizes $\sigma^{(g)}$. The exponential smoothing with weight $1-c_c$ is also used here to discount the information from the older generations. The subtleties of the weights $1-c_c$, $\sqrt{c_c(2-c_c)\mu_{eff}}$ can be searched in the literature. The initial evolution path is taken to be zero: $p_c^{(0)} = 0$. The idea behind the evolution path is that it accounts for the correlations between the successive step directions taken by the algorithm. If such correlations exist, the corresponding direction will be accumulated in $p_c^{(g+1)}$. Existence of such correlations means that the algorithm was successfully moving approximately in this direction in the previous steps, so the direction is likely to remain successful in the next step. Thus, the direction is "added" to the covariance matrix by the second term in (B.5). If there were no correlations between the successive steps, the resulting evolution path vector will be small and will not contribute much.

The third term in the update (B.5) is a sum of μ rank-one matrices, and is thus a matrix of rank $\min(n, \mu)$ with probability one, where *n* is the search space dimension. For this reason the term is called *rank-μ update*. The vectors $y_{i:\lambda}^{(g+1)}$ are the sampled steps $x_{i:\lambda}^{(g+1)} - m^{(g)}$ with normalisation by the *step size*, so they are defined by $y_{i:\lambda}^{(g+1)} = (x_{i:\lambda}^{(g+1)} - m^{(g)})/\sigma^{(g)}$. As can be seen, the rank-μ update is a weighted sum over the μ steps corresponding to the fittest models in the current generation. If one ignores $\sigma^{(g)}$ in the definition of $y_{i:\lambda}^{(g+1)}$, then rank-μ update is just the estimate of the *covariance matrix* by the best μ points. Including $\sigma^{(g)}$ makes the rank-μ estimates comparable across the different generations, so that accumulation in the first term of (B.5) makes sense. Since the rank-μ update is performed with only the currently-best μ steps, this allows us to include only their directions in the estimate, and ignore the directions of the unsuccessful steps. If the current successful steps will be unsuccessful in the future generations, they will become gradually "forgotten" by the *covariance matrix* because of the discounting factor in the first term in (B.5).

Finally, the step size $\sigma^{(g)}$ is updated based on the analysis on the evolution path, using the following logic. If the evolution path is too short, the successive steps go in approximately opposite directions, so they are "anti-correlated". In this case the step size should be decreased. If the evolution path is too long, the successive steps have approximately the same direction and are therefore "correlated". A few such steps could be replaced by a single step of larger length, and this is the reason to increase the step size. The "ideal" situation when there is no need to change the step size is the case of uncorrelated consecutive steps. More rigorously, the *conjugate evolution path* $p_\sigma^{(g+1)}$ is constructed, starting from $p_\sigma^{(0)} = 0$, using expression similar to (B.6):

$$p_\sigma^{(g+1)} = (1-c_\sigma)\, p_\sigma^{(g)} + \sqrt{c_\sigma (2-c_\sigma)\mu_{eff}}\, C^{(g)^{-\frac{1}{2}}} \cdot \frac{m^{(g+1)} - m^{(g)}}{\sigma^{(g)}}. \tag{B.7}$$

By means of $C^{(g)^{-\frac{1}{2}}}$ transform the expected length of the conjugate evolution path does not depend on its direction, and for independent consecutive steps we will have $p_\sigma^{(g+1)} \sim N(0, I)$. Comparing the length of $p_\sigma^{(g+1)}$ with the expected length $E\|N(0,I)\| =$ $= \sqrt{2} \cdot \Gamma\left(\frac{n+1}{2}\right) \Big/ \Gamma\left(\frac{n}{2}\right)$, the update of the step size can be performed:

$$\ln \sigma^{(g+1)} = \ln \sigma^{(g)} + \frac{c_\sigma}{d_\sigma E\|N(0,I)\|} \left(\left\| p_\sigma^{(g+1)} \right\| - E\|N(0,I)\| \right), \tag{B.8}$$

where $d_\sigma \approx 1$ is an auxiliary damping parameter. It can be noted that for $\left\| p_\sigma^{(g+1)} \right\| = E\|N(0,I)\|$ the step size will remain unchanged. For a longer conjugate evolution path the step size will increase, and for a shorter path it will decrease as suggested above. More in-depth explanations should be searched in the literature.

Once the mean, *covariance matrix* and the step size have been updated, a new generation of models can be sampled and the algorithm turns to the next iteration. Since all the update procedures do not explicitly use the values of the objective function except for ranking the individuals in (B.2), CMA-ES will behave identically if any strictly monotonic (order-preserving) transformation is applied to the objective function. This is one of the invariance properties of the algorithm which allows the generalisations of the empirical results to be made. The other invariance properties of CMA-ES include e.g. invariance to rotation, reflection and translation of the search space.

Appendix C. Parameterisation of the phase relative permeabilities

There are several ways to parameterise the phase relative permeability curves as can be found in the literature. Three of them were implemented in this work, and any of the three can be used for parameterisation in history matching. I start from the oil-water relative permeabilities. *Corey* parameterisation [87] was adopted closely to that used in [88], i.e.

$$\begin{aligned} k_{row} &= (1-S)^{No}, \\ k_{rw} &= k_{rw0} \cdot S^{Nw}, \\ S &= \frac{S_w - S_{wcr}}{1 - S_{wcr} - S_{orw}}. \end{aligned} \tag{C.1}$$

In these formulae the shape of the curves is defined by 5 parameters: critical water saturation S_{wcr} (which should be greater than or equal to the connate water saturation S_{wc}), residual saturation of oil in water S_{orw}, maximum relative permeability of water in oil k_{rw0}, and two exponents N_w, N_o. In (C.1) the water saturation S_w ranges between S_{wcr} and 1- S_{orw}, and is the input argument for the functions of oil relative permeability in water k_{row} and water relative permeability k_{rw}. For water saturation values between S_{wc} and S_{wcr} the relative permeabilities are set constant: k_{row} = 1, k_{rw} = 0. For S_w > 1- S_{orw} the water relative permeability is linearly extrapolated to 1 at S_w = 1, and k_{row} = 0.

Chierici parameterisation [89] is defined by

$$\begin{aligned} k_{row} &= \exp(-AR_w^L), \\ k_{rw} &= k_{rw0} \cdot \exp(-BR_w^{-M}), \\ R_w &= \frac{S_w - S_{wcr}}{1 - S_{orw} - S_w}, \\ A, B, M, L &> 0, \end{aligned} \tag{C.2}$$

where the meaning of the parameters is the same as in Corey parameterisation above, except for the new parameters *A, B, M, L* replacing the two Corey exponents, resulting in 7 parameters in total.

LET, or *Lomeland-Ebeltoft-Thomas* parameterisation [90] uses the following relationships:

$$
\begin{aligned}
k_{row} &= \frac{(1-S)^{Lo}}{(1-S)^{Lo} + E_o S^{To}}, \\
k_{rw} &= k_{rw0} \cdot \frac{S^{Lw}}{S^{Lw} + E_w (1-S)^{Tw}}, \\
S &= \frac{S_w - S_{wcr}}{1 - S_{wcr} - S_{orw}}.
\end{aligned}
\tag{C.3}
$$

S_{wcr}, S_{orw}, k_{rw0} have the meaning as before, supplemented by the 6 new parameters: L_o, E_o, T_o, L_w, E_w, T_w, giving in total 9 parameters. Using a parameterisation with more parameters, e.g. LET, as opposed to Corey, allows more flexible definition of the relative permeability curves, however, increasing the number of parameters may slow down convergence of the optimisation algorithm.

Formulae (C.1) – (C.3) work for the water-oil system. The corresponding relationships for the gas-oil system are similar, with the following differences. While in Corey and LET parameterisation a single rescaled saturation S is used for the oil-water system, two such rescaled variables will be used for the gas-oil system:

$$
\begin{aligned}
S^o &= \frac{S_g - S_{gc}}{S_{g\max} - S_{gc}}, \\
S^g &= \frac{S_g - S_{gcr}}{S_{g\max} - S_{gcr}}.
\end{aligned}
\tag{C.4}
$$

The difference between the two variables is that for $\boldsymbol{S^o}$ the current gas saturation S_g can vary between the connate gas saturation S_{gc} (which is usually 0)[50] and the maximum gas saturation $S_{g\max}$. For $\boldsymbol{S^g}$, the current gas saturation S_g varies between the critical gas saturation S_{gcr} and $S_{g\max}$. To convert formulae (C.1), (C.3) to gas-oil case, firstly replace everywhere "water" with "gas", and then use $\boldsymbol{S^o}$ in the definition of the oil relative permeability in gas k_{rog}, and $\boldsymbol{S^g}$ in the definition of the gas relative permeability k_{rg}. Chierici formulas (C.2) are converted using similar principles. This usage of the two rescaled saturations allows defining the gas-oil relative permeabilities such that on the segment between the connate gas saturation and critical gas saturation the gas relative permeability remains zero, whereas the oil relative permeability decreases from 1 to some smaller value.

[50] Whereas it may be challenging to give a physical meaning to the *connate gas saturation*, such a quantity is mentioned in the Technical Description for Schlumberger Eclipse simulator. When Eclipse performs the initialisation of the simulation model by EQUIL keyword, it sets the gas saturation to this value in the grid blocks lying below the gas contact.

Whatever parameterisation is chosen, the parameters S_{wcr}, S_{gcr}, $S_{g\max}$, S_{orw} should also satisfy the following consistency requirements:

$$\begin{aligned} &S_{wc} \le S_{wcr}, \\ &S_{wcr} < 1 - S_{orw}, \\ &S_{gcr} \ge 0, \\ &S_{gcr} < S_{g\max}, \\ &S_{g\max} \le 1 - S_{wc}. \end{aligned} \tag{C.5}$$

These inequalities are used as additional constraints on the model parameters during optimisation whenever the quantities from (C.5) participate in parameterisation of the history matching problem.

Appendix D. Parameterisation with pilot points and kriging

The pilot points method with interpolation of values by ordinary kriging was adopted as one of the ways of parameterisation of 2D and 3D grids for history matching. This appendix describes the underlying principles, following in most part [91]. Any interpolation method from the kriging family aims at approximating the values of some *random function* $Z(x)$ based on the values $z(x_i)$ defined at *pilot points* $x_1,...,x_n$. In application to history matching, function $Z(x)$ can represent e.g. the 2D map or 3D grid of permeability, porosity, or NTG. Quantities $z(x_i)$ can be interpreted as values of a random outcome of Z at the corresponding points. The kriging estimate also requires the knowledge of the mean $m(x)$ and covariance $C(h)$ of the random function Z, which is considered to be the second order stationary function. The variogram $\gamma(h)$ can also be used instead of covariance.

$$\begin{aligned} m(x) &= E[Z(x)], \\ C(h) &= Cov[Z(x), Z(x+h)], \\ \gamma(h) &= \frac{1}{2} E[(Z(x+h) - Z(x))^2]. \end{aligned} \tag{D.1}$$

The estimate of *ordinary kriging* $Z^*(x)$ used in this work is built as a linear combination of the input data

$$Z^*(x) = \sum_{i=1}^{n} \lambda_i(x) Z(x_i). \tag{D.2}$$

For simplicity, only global kriging estimates are considered here, so all the existing n pilot points take part in the estimate. A more advanced approach would use a local estimate based on $n(x)$ data points from some neighbourhood of the point in question x. All kriging estimates are defined so as to minimise the variance of the estimate error

$$\sigma^2(x) \equiv Var[Z^*(x) - Z(x)] \to \min, \tag{D.3}$$

with the additional condition that Z^* should be the unbiased estimate of Z

$$E[Z^*(x) - Z(x)] = 0. \tag{D.4}$$

For ordinary kriging the mean value $m(x)$ is assumed to be a constant m, albeit an unknown one. Based on this, the condition of unbiased behaviour (D.4) converts into

$$\left(\sum_{i=1}^{n} \lambda_i(x) - 1 \right) \cdot m = 0, \tag{D.5}$$

so that the sum of all weights λ_i should equal one. Following the definition (D.2), the variance from (D.3) can be written as

$$\begin{aligned}\sigma^2(x) &= Var[Z^*(x)] - 2Cov[Z^*(x), Z(x)] + Var[Z(x)] = \\ &= \sum_{i,j=1}^{n} \lambda_i(x)\lambda_j(x)C_{ij} - 2\sum_{i=1}^{n} \lambda_i(x)C_{i0} + Var[Z(x)],\end{aligned} \tag{D.6}$$

where $C_{ij} = Cov[Z(x_i), Z(x_j)]$, $C_{i0} = Cov[Z(x_i), Z(x)]$. Minimising this variance conditioned to (D.5) can be done by minimising the Lagrangian $L(x)$ with Lagrange multiplier $\mu(x)$:

$$L(x) = \sum_{i,j=1}^{n} \lambda_i(x)\lambda_j(x)C_{ij} - 2\sum_{i=1}^{n} \lambda_i(x)C_{i0} + 2\mu(x)\cdot\left(\sum_{i=1}^{n} \lambda_i(x) - 1\right) \to \min. \tag{D.7}$$

To minimise $L(x)$, one should take its derivatives with respect to λ_i and μ and equate them to zero, arriving at the linear system with $n + 1$ equations and $n + 1$ unknowns – the equations of ordinary kriging:

$$\begin{cases} \sum_{j=1}^{n} \lambda_j(x)C_{ij} + \mu(x) = C_{i0} \quad i = 1,...,n \\ \sum_{i=1}^{n} \lambda_i(x) = 1. \end{cases} \tag{D.8}$$

Having found the weights λ_i, the ultimate kriging estimate (D.2) can be evaluated. To use the ordinary kriging with variogram $\gamma(h)$ instead of the covariance function $C(h)$, system (D.8) can be transformed by virtue of $\gamma(h) = C(0) - C(h)$, arriving at

$$\begin{cases} \sum_{j=1}^{n} \lambda_j(x)\gamma_{ij} - \mu(x) = \gamma_{i0} \quad i = 1,...,n \\ \sum_{i=1}^{n} \lambda_i(x) = 1. \end{cases} \tag{D.9}$$

The kriging estimate obtained has the following properties:

1. Estimate Z^* is exact, i.e. $Z^*(x_i) = Z(x_i)$ for all pilot points x_i. This follows from the solution of system (D.8) or (D.9) at $x = x_i$, for which case it can be found that only one $\lambda_i = 1$, and the other $\lambda_j = 0$ for all $j \neq i$.

2. The weights λ_i do not depend on the values of Z at pilot points x_i, but depend only on the pilot points locations and the spatial correlations described by $C(h)$ or $\gamma(h)$. During history matching the kriging interpolations are to be made with different sets of values $Z(x_i)$ as defined by the parameterisation, but the same

pilot points and the same spatial correlations. This allows solving the kriging equations only once to find the weights, and then evaluating expression (D.2) multiple times with the appropriate sets of $Z(x_i)$.

Since kriging in history matching parameterisation is applied to produce such properties as porosities or permeabilities which are meant to be non-negative, the following constraints should be imposed on the parameters $p_i \equiv Z(x_i)$:

$$Z^*(y_k) \equiv \sum_{i=1}^{n} \lambda_i(y_k) p_i \geq 0. \tag{D.10}$$

This linear constraint can be used as soon as the kriging equations have been solved and the weights λ_i have been found. It delimis the feasible and infeasible regions for parameters $\{p_i\}$, and for every grid point y_k where the value of Z^* is to be calculated such a constraint should be added. Without this, there is no guarantee that the values of Z^* will be non-negative even if all p_i are non-negative. In this research kriging is used to create 2D maps which are then converted into 3D grids with values taken equal along the vertical axis. To handle the 2D maps, i.e. to define $\gamma(\vec{h})$ for a two-dimensional vector $\vec{h}$, the elliptical variogram model is adopted. It is defined by a 2D ellipse that has major and minor radii R, r and is rotated at angle χ, see Figure D.1.

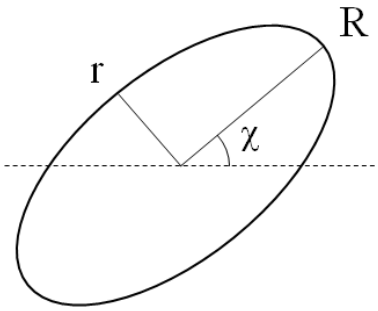

Figure D.1 Variogram ellipse with major radius R, minor radius r, rotation angle χ.

Apart from that, 1D variogram functions should be considered, e.g. the *spherical* variogram

$$\gamma_{1D}(h) = \begin{cases} (s-n)(1.5h - 0.5h^3) + n, & h \leq 1 \\ s, & h > 1, \end{cases} \tag{D.11}$$

exponential variogram

$$\gamma_{1D}(h) = (s-n)(1-\exp(-3h)) + n, \tag{D.12}$$

or *Gaussian* variogram

$$\gamma_{1D}(h) = (s-n)(1-\exp(-3h^2)) + n. \tag{D.13}$$

In these formulae s is **sill**, n is **nugget**, and the **range** is taken equal to 1 since the range is already handled by the variogram ellipse above. The plots of the three 1D variogram functions can be seen in Figure D.2.

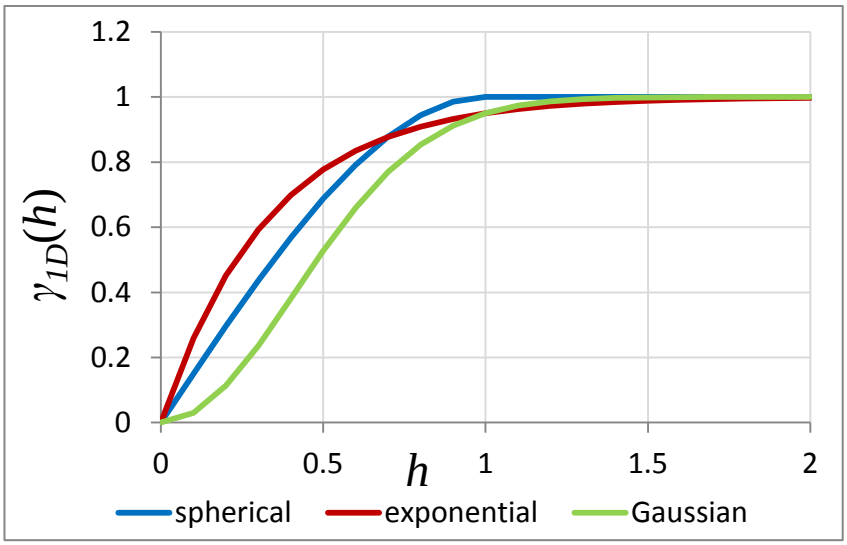

Figure D.2 1D variograms: spherical, exponential and Gaussian. Range = 1, nugget = 0, sill = 1.

Finally, to find the 2D variogram value for vector $\vec{h} = (h_1, h_2)^T$, first apply a transform to $\vec{h}$ which maps the ellipse to the unit circle:

$$\vec{g} = \begin{pmatrix} 1/R & 0 \\ 0 & 1/r \end{pmatrix} \begin{pmatrix} \cos\chi & \sin\chi \\ -\sin\chi & \cos\chi \end{pmatrix} \begin{pmatrix} h_1 \\ h_2 \end{pmatrix}, \tag{D.14}$$

and then take $\gamma(\vec{h}) = \gamma_{1D}(\|\vec{g}\|)$.

Appendix E. Linear regression with constraints, active set method

As described in Chapter 4, seismic is incorporated into history matching by performing a linear regression between the time-lapse attribute maps and the average maps of the dynamic reservoir parameters. In other words, one of the equations (4.6) – (4.8) is solved in the least squares sense. If the full covariance matrix is employed, which is usually the case, then the equations (4.6) – (4.8) are solved such that the quantity f_2 in (4.12) is minimised, where ΔA and ΔB are the left hand side and the right hand side of (4.6) – (4.8). To maintain the physically meaningful signs of the derivatives of ΔA with respect to ΔP, ΔSw, ΔSg, the appropriate constraints should be introduced. E.g. if one considers equation of type (4.8) written as

$$\Delta A = (a_P \Delta P + a_{Sw} \Delta Sw + a_{Sg} \Delta Sg + a_{PP} \Delta P^2 + a_{PSw} \Delta P \Delta Sw + a_{SgSg} \Delta Sg^2) \cdot A_0, \quad \text{(E.1)}$$

then the constraints $\partial \Delta A / \partial \Delta P \le 0$, $\partial \Delta A / \partial \Delta Sw \ge 0$, $\partial \Delta A / \partial \Delta Sg \le 0$ will be written as:

$$\begin{aligned} &a_P A_0 + 2a_{PP} \Delta P A_0 + a_{PSw} \Delta Sw A_0 \le 0, \\ &a_{Sw} A_0 + a_{PSw} \Delta P A_0 \ge 0, \\ &a_{Sg} A_0 + 2a_{SgSg} \Delta Sg A_0 \le 0. \end{aligned} \quad \text{(E.2)}$$

Equation (E.1) is formulated for all the points existing on the maps, over all time steps. Essentially, there are *m* equations corresponding to the *m* points. For brevity, they can be written in a matrix form as

$$Px = f, \quad \text{(E.3)}$$

where P is m x d matrix with columns equal to $\Delta P \cdot A_0, \Delta Sw \cdot A_0$, etc (these maps are stretched into column-vectors). The right hand side f is a m x 1 vector equal to ΔA from (E.1), and the vector of unknowns x consists of d variables $a_P, a_{Sw}, a_{Sg}, a_{PP}$, etc. Constraints (E.2) are applied for each of the m points. In the considered case, e.g., there are $3m$ constraints altogether. If the reservoir contained no gas, there would be $2m$ constraints. If some of the reservoir dynamic parameters, e.g. *Sw*, was only present in (E.1) as a linear term, the associated m constraints $a_{Sw} A_0 \ge 0$ would all be equivalent[51] and could be reduced to a single constraint. For brevity, (E.2) can be written as

[51] For this equivalence the map A_0 is required to have a constant sign, which can be expected, since A_0 is supposed to resemble the pore volume map. A_0 map used in this work for history matching is the sum of negative amplitudes between two horizons, and maintains the negative sign.

$$A^T x \geq b, \tag{E.4}$$

where each column a_i of matrix A represents a separate constraint. Vector b in this case is zero, but for generality I will keep denoting it b. Equation (E.3) is solved by minimising the quantity $(Px - f)^T C_s^{-1}(Px - f)$, in other words the following quadratic function is minimised:

$$q(x) = \frac{1}{2} x^T G x + g^T x \rightarrow \min, \tag{E.5}$$

where $G = P^T C_s^{-1} P$, $g = -P^T C_s^{-1} f$. To minimise this function subject to constraints (E.4), an *active set method* is applied, as described in [36]. The method is briefly outlined below.

Inequalities (E.4) divide the parameter space into the *feasible* region containing the points which satisfy the inequalities (or equalities), and *infeasible* region containing all the remaining points. The algorithm starts in some feasible point $x^{(0)}$ and performs a number of minimising steps, not leaving the feasible region, to arrive at the final solution. For a current feasible point $x^{(k)}$, constraints (E.4) can be divided into two categories: *active* constraints $a_i, i \in I$, for which the equality $a_i^T x^{(k)} = b_i$ holds, and *inactive* constraints a_j for which the strict inequality holds: $a_j^T x^{(k)} > b_j$. The current active constraints are indexed by I which is called the *active set*, and can contain from 0 to d indices (since the search space is d-dimensional, maximum d constraints can be active). At each iteration the algorithm minimises the quadratic function $q(x)$ subject only to the active constraints (equalities) and ignoring the inactive ones (inequalities). Thus, the following *equality problem* is solved:

$$\begin{cases} \frac{1}{2} x^T G x + g^T x & \rightarrow \min \\ a_i^T x = b_i, & i \in I. \end{cases} \tag{E.6}$$

Shifting the origin to $x^{(k)}$ by taking $x = x^{(k)} + \delta$, we arrive at the equivalent problem

$$\begin{cases} \frac{1}{2} \delta^T G \delta + \delta^T g^{(k)} & \rightarrow \min \\ a_i^T \delta = c_i = 0, & i \in I, \end{cases} \tag{E.7}$$

where $g^{(k)} = g + G x^{(k)} = \nabla q(x^{(k)})$. Vector $c = \{c_i\}$ in this particular equality problem is strictly zero, and finally this will simplify the procedure, but in the meanwhile I will keep denoting it c to show how a general equality problem can be solved. To solve the

equality problem, a generalised elimination method is applied. Denoting A_{act} the matrix of equality constraints which consists of columns $a_i, i \in I$, find two matrices Y and Z such that $[Y \mid Z]$ is a square full rank matrix, $A_{act}^T Y = I$, $A_{act}^T Z = 0$. Then all the points δ satisfying the constraints $A_{act}^T \delta = c$ can be represented as $\delta = Yc + Zy$, where vector y can be regarded as the reduced coordinates vector. Substituting it to the quadratic function, we arrive at the equivalent minimisation problem

$$\frac{1}{2} y^T Z^T G Z y + (GYc + g^{(k)})^T Z y \to \min. \tag{E.8}$$

If $Z^T G Z$ is positive definite, the unique minimiser y^* is given by

$$(Z^T G Z) y^* = -Z^T (GYc + g^{(k)}). \tag{E.9}$$

Then, the solution of (E.7) is given by $\delta^* = Yc + Zy^* = Zy^*$. The Lagrange multipliers for the equality problem are given by equation $A_{act} \lambda^* = G\delta^* + g^{(k)}$, and can now also be calculated. For that, pre-multiply this equation by Y^T, which gives

$$\lambda^* = Y^T (G\delta^* + g^{(k)}). \tag{E.10}$$

To find matrices Y and Z, QR factorisation of matrix A_{act} was performed using the Householder reflections method

$$A_{act} = [Q_1 Q_2] \cdot \begin{bmatrix} R \\ 0 \end{bmatrix} = Q_1 R, \tag{E.11}$$

where $[Q_1 Q_2]$ is orthogonal matrix and R is square upper triangular. Then, it is easy to establish that the matrices $Y = Q_1 R^{-T}$, $Z = Q_2$ possess the required properties. Equation (E.10) can now be written as a triangular system $R\lambda^* = Q_1^T (G\delta^* + g^{(k)})$. If the found solution of the equality problem δ^* is feasible with respect to the main constraints (E.4), then the new iterate is taken as $x^{(k+1)} = x^{(k)} + \delta^*$. It may happen, however, that some constraint is violated as one moves from $x^{(k)}$ to $x^{(k)} + \delta^*$. To find the first constraint $a_i^T x \geq b_i$ violated by $x = x^{(k)} + \beta\delta^*$ in this way, find

$$\beta^* = \min \frac{b_i - a_i^T x^{(k)}}{a_i^T \delta^*}, \tag{E.12}$$

where the minimum is taken over all inactive indices $i \notin I$ for which $a_i^T \delta^* < 0$, and β^* is only sought on the segment [0, 1]. The constraint index corresponding to the found

minimum β^* is then added to the active set *I*, the equality problem with the new set of constraints is solved, and the process is repeated until a feasible $x^{(k+1)} = x^{(k)} + \delta^*$ is found.

Once we have $x^{(k+1)}$ - the feasible minimiser of the equality problem, examine the Lagrange multipliers λ^* corresponding to it. If all of them are non-negative, then the current point is the global minimum of the original quadratic function (E.5) subject to constraints (E.4). If, however, there exists $\lambda_j^* < 0$ for some active constraint $j \in I$, further reduction of the quadratic function is possible if the constraint *j* is set inactive. Thus, index *j* is removed from *I* and the algorithm continues with the new equality problem. If multiple negative λ_j^* are found, then the constraint is removed which corresponds to the minimum of them.

Practice has revealed that due to numerical errors the (almost) linearly dependent columns can occur in the active constraints matrix A_{act}. This, in turn, may lead to the algorithm getting stuck when the same indices are added to the active set and removed from it in a circular manner. To circumvent this problem two modifications were made:

1. At the step (E.12), where a new constraint is added, instead of condition $a_i^T \delta^* < 0$, I use $a_i^T \delta^* < \varepsilon$ where ε is a negative number with a small absolute value, e.g. $\varepsilon = -10^{-18}$. The whole constrained minimisation problem is attempted to be solved with this ε, and if it gets stuck, multiply ε by 10 and attempt to solve the problem again.
2. While calculating β^*, its value is permitted to become negative. This may happen if, due to the previous numerical inaccuracies resulting from the *modification 1* above, the current point $x^{(k)}$ has violated some constraint. Negative β^* allow getting rid of this situation. However, the negative β^* also means that the new iterate will increase the quadratic function value. Besides, there is no guarantee that some other constraints will not become violated by the step with such β^*. Nevertheless, the practical application of the algorithm revealed that the final solution x^* of the constrained minimisation only violates the original constraints (E.4) up to machine arithmetic precision. E.g. the worst violated constraint $a_i^T x^* - b_i$ may reach -10^{-12} for $\|a_i\| \sim 10^1$, $\|x^*\| \sim 10^4$.

Typically there is a difference of at least 16 orders of magnitude between $\|a_i\| \cdot \|x^*\|$ and $\left|a_i^T x^* - b_i\right|$ for the worst negative $a_i^T x^* - b_i$.

The other useful pre- and post-processing step for the algorithm is normalisation of the components of vector *x* in (E.3). The need for that arises because matrix *P* has column-vectors with distinctly different magnitudes, the most prominent examples being the column-vector with very large values $\Delta P^2 \cdot A_0$ and the one with very small values $\Delta Sg^2 \cdot A_0$. Before any solution takes place the columns of *P* are made to have similar magnitude, and the components of the constraints matrix *A* and vector *x* are normalised accordingly. Once the constrained minimisation is finished, the re-normalisation is applied to recover the actual solution *x*.

References

1 Brevik, I. (1999). Rock model based inversion of saturation and pressure changes from time lapse seismic data. In *69th Annual International Meeting, Society of Exploration Geophysicists*.

2 Landrø, M. (2001). Discrimination between pressure and fluid saturation changes from time-lapse seismic data. *Geophysics*, 66, 3, 836-844.

3 Cole, S., Lumley, D., Meadows, M., Tura, A. (2002). Pressure and Saturation Inversion of 4D Seismic Data by Rock Physics Forward Modeling. In *SEG International Exposition and 72nd Annual Meeting* (Salt Lake City).

4 Gassmann, F. (1951). Elastic waves through a packing of spheres. *Geophysics*, 16, 673-685.

5 Batzle, M., Wang, Zh. (1992). Seismic properties of pore fluids. *Geophysics*, 57, 11, 1396-1408.

6 MacBeth C., Floricich, M., Soldo, J. (2006). Going quantitative with 4D seismic analysis. *Geophysical Prospecting*, 54, 303-317.

7 Floricich, M., MacBeth, C., Stammeijer, J., Staples, R., Dijksman, C. (2006). A New Technique for Pressure - Saturation Separation from Time-Lapse Seismic - Schiehallion Case Study. In *EAGE 68th Conference & Exhibition* (Vienna).

8 Vasco, D. (2004). Seismic imaging of reservoir flow properties: Time-lapse pressure changes. *Geophysics*, 69, 511-521.

9 Vasco, D.W., Datta-Gupta, A., He, Z., Behrens, R., Rickett, J., Condon, P. (2003). Reconciling time-lapse seismic and production data using streamline models: the Bay Marchand field, Gulf of Mexico, SPE-84568.

10 Vasco, D., Datta-Gupta, A. et al. Seismic imaging of reservoir flow properties: Time-lapse amplitude changes. *Geophysics*, 69 (November-December 2004), 1425-1442.

11 Rodrigues, J.R.P. (2006). Combining Adjoint Calculations and Quasi-Newton Methods for Automatic History Matching, SPE-99996.

12 Arenas, E., Kruijsdijk, C., Oldenziel, T. (2001). Semi-Automatic History Matching Using the Pilot Point Method Including Time-Lapse Seismic Data, SPE-71634.

13 Makhlouf, E.M., Chen, W.H., Wasserman, M.L., Seinfeld, J.H. (1993). A General History Matching Algorithm for Three-Phase Three-Dimensional Petroleum Reservoirs, SPE-20383.

14 Landa, J.L., Horne, R.N. (1997). A Procedure to Integrate Well Test Data, Reservoir Performance History and 4-D Seismic Information into a Reservoir Description, SPE-38653.

15 Shah, P.C., Gavalas, G.R., Seinfeld, J.H. (1978). Error analysis in history matching: the optimum level of parameterization, SPE-6508.

16 Oliver, D.S., Chen, Y. (2011). Recent progress on reservoir history matching: a review. *Computational Geosciences*, 185-221.

17 Landa, J.L., Kamal, M.M., Jenkins, C.D., Horne, R.N. (1996). Reservoir Characterization Constrained to Well Test Data: A Field Example, SPE-36511.

18 Husebey, O.K., Valestrand, R., Naevdal, G., Sagen, J. (2009). Natural and Conventional Tracers for Improving Reservoir Models Using the EnKF Approach, SPE-121190.

19 Jin, L., Alpak, F.O., Hoek, P., Pirmez, C., Fehintola, T., Tendo, F., Olaniyan, E.E. (2011). A Comparison of Stochastic Data-Integration Algorithms for the Joint History Matching of Production and Time-Lapse Seismic Data, SPE-146418.

20 Davolio, A., Maschio, C., Schiozer, D.J. (2011). Incorporating 4D Seismic Attributes into History Matching Process through an Inversion Scheme, SPE-142946.

21 Huang, X., Meister, L., Workman, R. (1997). Reservoir Characterization by Integration of Time-Lapse Seismic and Production Data, SPE-38695.

22 Gosselin, O., Berg, S., Cominelli, A. (2001). Integrated History-Matching of Production and 4D Seismic Data, SPE-71599.

23 Gosselin, O., Aanonsen, S.I., Aavatsmark, I., Cominelli, A., Gonard, R., Kolasinski, M., Ferdinandi, F., Kovacic, L., Neylon, K. (2003). History matching Using Time-lapse Seismic (HUTS), SPE-84464.

24 Reiso, E., Haver, M.C., Aga, M. (2005). Integrated Workflow for Quantitative Use of Time-Lapse Seismic Data in History Matching: A North Sea Field Case, SPE-94453.

25 Roggero, F., Ding, D.Y., Berthet, P., Lerat, O., Cap, J., Schreiber, P.E. (2007). Matching of Production History and 4D Seismic Data - Application to the Girassol Field, Offshore Angola, SPE-109929.

26 Emerick, A.A., Moraes, R.J., Rodrigues, J.R.P. (2007). History Matching 4D Seismic Data with Efficient Gradient Based Methods, SPE-107179.

27 Fahimuddin, A., Aanonsen, S.I., Skjervheim, J.-A. (2010). Ensemble Based 4D Seismic History Matching: Integration of Different Levels and Types of Seismic

Data, SPE-131453.

28 Waggoner, J.R., Cominelli, A., Seymour, R.H. (2002). Improved Reservoir Modeling With Time-Lapse Seismic in a Gulf of Mexico Gas Condensate Reservoir, SPE-77956.

29 Kjelstadli, R.M., Lane, H.S., Johnson, D.T., Barkved, O.I., Buer, K., Kristiansen, T.G. (2005). Quantitative History Match of 4D Seismic Response and Production Data in the Valhall Field, SPE-96317.

30 Kennedy, J., Eberhart, R.C. (1995). Particle swarm optimization. In *IEEE International Conference on Neural Networks* (), IEEE Press, 1942–1948.

31 Fernández-Martínez, J.L., García-Gonzalo, E. (2009). Stochastic stability analysis of the linear continuous and discrete PSO models.

32 Hajizadeh, Y. (2010). Ants Can Do History Matching, SPE-141137.

33 Sambridge, M. (1999). Geophysical Inversion with a Neighbourhood Algorithm - I. Searching a Parameter Space. *Geophysics Journal International*, 138, 479-494.

34 Abdollahzadeh, A., Reynolds, A., Christie, M., Corne, D.W., Davies, B.J., Williams, G.J.J. (2011). Bayesian Optimization Algorithm Applied to Uncertainty Quantification, SPE-143290.

35 Hajizadeh, Y., Demyanov, V., Mohamed, L., Christie, M. (2011). Comparison of Evolutionary and Swarm Intelligence Methods for History Matching and Uncertainty Quantification in Petroleum Reservoir Models. In *Intelligent Computational Optimization in Engineering*.

36 Fletcher, R. (1986). *Practical methods of optimization*.

37 Gao, G., Reynolds, A.C. (2006). An Improved Implementation of the LBFGS Algorithm for Automatic History Matching, SPE-90058.

38 Ding, D.Y. (2010). Development of a Data Partition Technique for Gradient-Based Optimization Methods in History Matching, SPE-130473.

39 Kaku, A. (2011). *Implementation of High Precision Arithmetic in the BFGS Method for Nonsmooth Optimization (MSc thesis)*.

40 Rodrigues, J.R.P. (2006). Calculating derivatives for automatic history matching. *Computational Geosciences*, 10, 119-136.

41 Lépine, O.J., Bissell, R.C., Aanonsen, S.I., Pallister, I.C., Barker, J.W. (1999). Uncertainty analysis in predictive reservoir simulation using gradient information, SPE-57594.

42 Oliver, D.S., Reynolds, A.C., Liu, N. (2008). *Inverse Theory for Petroleum Reservoir Characterization and History Matching*. Cambridge University Press, Cambridge.

43 Oliver, D.S., He, N., and Reynolds, A.C. (1996). Conditioning Permeability Fields to Pressure Data. In *5th European Conference on the Mathematics of Oil Recovery* (Leoben, Austria).

44 Liu, N., Oliver, D.S. (2003). Evaluation of Monte Carlo methods for assessing uncertainty, SPE-84936.

45 Gao, G., Zafari, M., Reynolds, A.C. (2006). Quantifying uncertainty for the PUNQ-S3 problem in a Bayesian setting with RML and EnKF, SPE-93324.

46 Sambridge, M. (1999). Geophysical Inversion with a Neighbourhood Algorithm - II. Appraising the Ensemble. *Geophysics Journal International*, 138, 727–745.

47 Zafari, M., Reynolds, A.C. (2007). Assessing the uncertainty in reservoir description and performance predictions with the ensemble Kalman filter, SPE-95750.

48 Liu, N., Oliver, D.S. (2005). Critical Evaluation of the Ensemble Kalman Filter on History Matching of Geologic Facies, SPE-92867.

49 Emerick, A.A., Reynolds, A.C. (2011). Combining the Ensemble Kalman Filter with Markov Chain Monte Carlo for Improved History Matching and Uncertainty Characterization, SPE-141336.

50 Aanonsen, S.I., Naevdal, G., Oliver, D.S., Reynolds, A.C., Valles, B. (2009). The Ensemble Kalman Filter in Reservoir Engineering - a Review, SPE-117274.

51 Emerick, A.A., Reynolds, A.C. (2011). History Matching a Field Case Using the Ensemble Kalman Filter with Covariance Localization, SPE-141216.

52 Watanabe, S., Datta-Gupta, A. (2011). Use of Phase Streamlines for Covariance Localization in Ensemble Kalman Filter for Three-Phase History Matching, SPE-144579.

53 Tong, Y., Zhang, Y., Oliver, D.S. (2011). Adaptive Regularization in the Ensemble Kalman Filter for Reservoir History Matching, SPE-141059.

54 Oldenziel, T. (2003). *Time-lapse seismic within reservoir engineering, PhD thesis*.

55 Osako, I., Datta-Gupta, A., King, M.J. (2004). Timestep Selection During Streamline Simulation Through Transverse Flux Correction, SPE-79688.

56 Tarantola, A. (2005). *Inverse Problem Theory and Methods for Model Parameter Estimation*. SIAM.

57 Hansen, N., Ostermeier, A. (1996). Adapting arbitrary normal mutation distributions in evolution strategies: The covariance matrix adaptation. In *IEEE Conference on Evolutionary Computation* (), 312-317.

58 Hansen, N., Ostermeier, A. (2001). Completely derandomized self-adaptation in evolution strategies. *Evolutionary Computation*, 9(2), 159–195.

59 Jastrebski, G.A., Arnold D.V. (2006). Improving evolution strategies through active covariance matrix adaptation. In *IEEE World Congress on Computational Intelligence* (), 9719-9726.

60 Igel, C., Suttorp, T., Hansen, N. (2006). A computational efficient covariance matrix update and a (1+1)-CMA for evolution strategies. In *Genetic and Evolutionary Computation Conference* (), 453-460.

61 Falahat, R., Shams, A., MacBeth, C. (2013). Adaptive scaling for an enhanced dynamic interpretation of 4D seismic data. *Geophysical Prospecting*, 61.

62 Alvarez, E., MacBeth, C. (2014). An insightful parametrization for the flatlander's interpretation of time-lapsed seismic data. *Geophysical Prospecting*, 62, 75-96.

63 Aanonsen, S.I., Aavatsmark, I., Barkve, T., Cominelli, A., Gonard, R., Gosselin, O., Kolasinski, M., Rene, H. (2003). Effect of Scale Dependent Data Correlations in an Integrated History Matching Loop Combining Production Data and 4D Seismic Data, SPE-79665.

64 Schlumberger. *SimOpt user guide 2010.2*.

65 Fang, J., Tacher, L. (2003). An efficient and accurate algorithm for generating spatially-correlated random felds. *Communications in Numerical Methods in Engineering*, 801-808.

66 Richardson, S.M., Herbert, N., Leach, H.M. (1997). How well connected is the Schiehallion reservoir?, SPE-38560.

67 Leach, H.M., Herbert, N., Los, A., Smith, R.L. (1999). The Schiehallion development. In *Petroleum Geology Conference* (), The Geological Society of London, 683-692.

68 Dobbyn, A., Marsh, M. (2001). Material Balance: A Powerful Tool for Understanding The Early Performance of The Schiehallion Field, SPE-71819.

69 Govan, A.H., Primmer, T., Douglas, C.C., Moodie, N., Davies, M., Nieuwland, F. (2005). Reservoir management in a deepwater subsea field - the Schiehallion experience, SPE-96610.

70 Falahat, R., Obidegwu, D., Shams, A., MacBeth, C. (2014). The interpretation of amplitude changes in 4D seismic data arising from gas exsolution and dissolution.

Petroleum Geoscience, 20, 303-320.

71 Kragh, E., Christie, P. (2002). Seismic repeatability, normalized RMS, and predictability. *The Leading Edge*, 21, 640-647.

72 Shchipanov, A.A. Berenblyum, R., Kollbotn, L. (2014). Pressure Transient Analysis as an Element of Permanent Reservoir Monitoring, SPE-170740.

73 Gestel, J.P., Best, K.D., Barkved, O.I., Kommedal, J.H. (2007). Valhall Life of Field Seismic Automated Workflow. In *SEG* (San Antonio).

74 Wang, Y., Wallace, K., Zhang, H., Bertrand, A., Shen, Y. (2013). Acoustic full waveform inversion using reflection energy: a case study from the Ekofisk LoFS ocean bottom dataset. In *SEG* (Houston).

75 Robinson, M. (2003). Intelligent Well Completions, SPE-80993.

76 Tolstukhin, E., Lyngnes, B., Sudan, H.H. (2012). Ekofisk 4D Seismic - Seismic History Matching Workflow, SPE-154347.

77 Wilson, W. D. (1959). Speed of sound in distilled water as a function of temperature and pressure. *J. Acoust. Soc. Am.*, 1067-1072.

78 Han, D.H., Batzle, M. (2000). Velocity, Density and Modulus of Hydrocarbon Fluids - Empirical Modeling. In *SEG* ().

79 Berryman, J.G. (1995). Mixture Theories for Rock Properties. In *American Geophysical Union Handbook of Physical Constants*.

80 Biot, M.A. (1941). General theory of three-dimensional consolidation. *Journal of applied physics*, 12, 155-164.

81 MacBeth, C. (2004). A classification for the pressure-sensitivity properties of a sandstone rock frame. *Geophysics*, 69, 497-510.

82 Gassmann, F. (1951). Über die elastizität poröser medien. *Viertel. Naturforsch. Ges.*

83 Smith, T.M., Sondergeld, C.H., Rai, C.S. (2003). Gassmann fluid substitutions: A tutorial. *Geophysics*, 68, 430-440.

84 Berryman, J.G. (1999). *Origin of Gassmann's equations*.

85 Backus, G.E. (1962). Long-wave elastic anisotropy produced by horizontal layering. *Journal of Geophysical Research*, 67, 11, 4427-4440.

86 Aki, K., Richards, P.G. (2002). *Quantitative Seismology*.

87 Corey, A. (1954). The Interrelation between Gas and Oil Relative Permeability.

Producers Monthly, 19.

88 Ghedan, S.G. (2007). Dynamic rock types for generating reliable and consistent saturation functions for simulation models, SPE-111295.

89 Chierici, G.L. (1984). Novel relations for drainage and imbibition relative permeabilities, SPE-10165.

90 Lomeland, F., Ebeltoft, E., Thomas, W.H. (2005). A new versatile relative permeability correlation. In *International Symposium of the Society of Core Analysts* (Toronto).

91 Demyanov, V., Savelieva, E. (2010). *Geostatistics: theory and practice*. Nauka, Moscow.

92 Barroso Viseras, F.J., Blanchais, S., Verdiere, S., Bouzarkouna, Z., Schaeffner, A., Jannes, P. (2014). Non-Deterministic Approach to Define a Robust Development Plan: a Complex Mature Carbonate Field Case Study, SPE-171904.

93 Schulze-Riegert, R.W., Krosche, M., Pajonk, O., Mustafa, H. (2009). Data Assimilation Coupled to Evolutionary Algorithms - A Case Example in History Matching, SPE-125512.

94 Awotunde, A.A., Naranjo, C. (2014). Well Placement Optimization Constrained to Minimum Well Spacing, SPE-169272.

95 Amini, H. (2014). *A pragmatic approach to simulator-to-seismic modelling for 4D seismic interpretation, PhD thesis*.